

**ÉCOLE DOCTORALE DES SCIENCES CHIMIQUES**

**UMR-7006**

# THÈSE

présentée par :

**Marco Carroli**

soutenue le: **25 Juin 2020**

pour obtenir le grade de : **Docteur de l'université de Strasbourg**

Spécialité : Chimie Physique

## **Dispositifs électroniques multifonctionnels à base organique**

**Utilisation d'un mélange organique bi-composant pour des  
mémoires non volatiles**

**THÈSE dirigée par :**

**M. Samorì Paolo**

Professeur, Université de Strasbourg, Strasbourg, France

**M. Orgiu Emanuele**

Professeur, Institut national de la recherche scientifique,  
Varenes (Québec), Canada

**RAPPORTEURS :**

**M. Biscarini Fabio**

Professeur, Università degli Studi di Modena e Reggio Emilia, Modena, Italy

**M. Vuillaume Dominique**

Directeur de recherche, Institut d'Électronique de Microélectronique et de  
Nanotechnologie, Villeneuve d'Ascq, France

**AUTRES MEMBRES DU JURY :**

**M. Heiser Thomas**

Professeur, Laboratoire des sciences de l'ingénieur, de l'informatique et de  
l'imagerie (ICube), Strasbourg, France

**Mme. Ismailova Esma**

Directeur de recherche, Department of Bioelectronics (BEL), Centre  
Microélectronique de Provence, Gardanne, France

## Résumé de these

Le stockage d'information est une fonctionnalité de base requise pour la plupart des dispositifs électroniques. Parmi ses indicateurs de performance clés, la quantité de données pouvant être stockées revêt une importance capitale. À cet égard, cette thèse se concentre sur la mise en place d'un dispositif de type transistor à effet de champ organique (*organic field-effect transistor* ou OFET) dont la réponse optique repose sur un mélange bicomposant semi-conducteur/molécule photochromique qui confère une capacité de stockage au dispositif grâce à une réponse électrique non volatile à plusieurs niveaux. Ce mélange est intégré dans un dispositif à mémoire rémanente qui exploite également la ferroélectricité de la couche diélectrique pour augmenter la capacité de stockage. Les dispositifs organiques multicomposants constituent une approche prometteuse pour le développement d'une technologie de mémoire à faible coût.

Les semi-conducteurs organiques ont fait l'objet d'études approfondies au cours des trois dernières décennies en raison de leurs propriétés physiques modifiables par synthèse chimique, de leur traitement à faible coût et de leur intégration sur des supports flexibles.<sup>[1-3]</sup> Leurs propriétés uniques ont attiré l'attention de plusieurs entreprises qui ont exploité ces matériaux pour des écrans à cristaux liquides, des dispositifs de stockage de données, des batteries portables, des écrans électroluminescents et des cellules photovoltaïques.<sup>[4-8]</sup> Le développement de matériaux organiques multi-composants capables de combiner un ensemble de propriétés conduit à de nouveaux dispositifs multifonctionnels <sup>[9-10]</sup> et ouvre la voie à un nouveau progrès technologique à l'ère de l'*Internet of Everything* (IoE).<sup>[11]</sup>

Les chaînes de polymères conjugués interagissent faiblement entre elles, ce qui entraîne de nombreux degrés de liberté structurelle qui conduisent à une micro-structuration complexe de la couche à l'état condensé. La compréhension et le contrôle de la microstructure de tels systèmes, qui comportent des phases amorphes et ordonnées présentant des degrés d'ordre variables, permettent une meilleure intégration avec différentes petites molécules conférant une nouvelle fonctionnalité.<sup>[12]</sup> Le contrôle structurel de ces matériaux moléculaires ainsi que la connaissance des processus physiques de base entre les différents composants, a donné lieu à des percées en matière d'ingénierie et de conception rationnelle des dispositifs.<sup>[13]</sup> Récemment, la possibilité de combiner un processus peu coûteux avec des capacités d'intégration plus élevées tout en développant

les propriétés optoélectroniques a suscité un grand intérêt vers les mélanges de polymères semi-conducteurs.<sup>[14]</sup>

Dans ce contexte, la fonctionnalité des OFET fabriqués par solution a été améliorée grâce au développement d'un nouveau mélange multicomposant incorporant des molécules fonctionnelles dans des matrices semi-conductrices. Parmi les nombreuses classes de molécules, les molécules photochromiques sont des candidates idéales pour une intégration dans la prochaine génération de dispositifs optoélectroniques, car elles peuvent être contrôlées optiquement avec une haute résolution spatio-temporelle sans générer de déchets.<sup>[15]</sup> La commutation induite optiquement entre deux états adressables indépendamment l'un de l'autre entraîne des changements à la fois à l'échelle moléculaire et à l'échelle macroscopique. Des changements structuraux et électroniques réversibles de la géométrie, des moments dipolaires, de la conjugaison  $\pi$  et de la bande interdite sont induits au niveau moléculaire. Des changements de forme, de comportement d'agrégation et de conductance sont observés à l'échelle macroscopique. Les dérivés photochromiques du diaryléthène (DAE) se sont révélés les meilleurs candidats car ils présentent une grande stabilité thermique et une commutation en solution presque sans fatigue. Les DAE-Me ont été synthétisés, dans le cadre d'une collaboration à long terme, par le groupe du professeur Stefan Hecht à l'Université Humboldt de Berlin.<sup>[16-17]</sup> Afin de conférer aux transistors à couche mince la capacité de répondre à un stimulus optique, les molécules de DAE ont été dispersées dans une matrice semi-conductrice polymérique. Les DAE utilisées au sein de ce travail, dites DAE-Me, ont été conçues de façon telle à avoir leur HOMO permettant une interaction électronique sélective avec la plupart des semi-conducteurs de type p. Lorsque le diaryléthène est dans sa forme dite *ouverte*, sa HOMO ne permet pas d'interaction électronique entre les polarons dans la matrice polymérique et le DAE. Dans ce cas, les DAE agissent comme de centres de scattering pour les charges (polarons) transportées au travers de la matrice semi-conductrice hôte. En revanche, lorsque le diaryléthène est sous forme dite *fermée*, les charges transportées à travers la couche semi-conductrice peuvent être piégées, réduisant ainsi le courant de sortie. Comme le diaryléthène est thermodynamiquement stable dans ses deux formes, cet effet a été utilisé pour stocker de l'information et construire des mémoires multiniveaux.<sup>[18]</sup>

De nombreux polymères semi-conducteurs à haute performance présentent des propriétés adaptées à l'interaction avec le DAE dans les dispositifs à plusieurs composants. Une

évaluation correcte de l'intégration du DAE nécessite de tester électriquement et optiquement les performances de photo-commutation des couches bi-composants permettant d'identifier le polymère le plus approprié. En particulier, l'amplitude de commutation et la fatigue par rapport à la mobilité dans les FET sont les principaux critères de sélection de la paire DAE/polymère la plus prometteuse pour une application dans le domaine de l'optoélectronique. Alors que le poly(3-hexylthiophène (P3HT) est l'un des semi-conducteurs de type p les plus utilisés pour l'électronique organique et l'un des composants les plus reconnus pour ces applications, plusieurs matériaux ont été développés ces dernières années, en affichant des performances électriques et une stabilité à l'air supérieures. Parmi ceux-ci, le PDVT-8 et le PCD-TTP sont choisis comme matériaux hôtes alternatifs car ils présentent un degré de cristallinité et une microstructure totalement différents de ceux du P3HT.<sup>[12,19]</sup> Bien que les dispositifs PDVT-8 et PCD-TPT présentent des performances électriques supérieures, les OFET basés sur le mélange P3HT ont démontré une capacité de photo-commutation exceptionnelle, les deux états étant extrêmement stables pendant plusieurs mois. Au vu de cette analyse préliminaire, le mélange utilisant du P3HT représente le meilleur candidat pour étudier tout ce qui concerne l'ingénierie des microstructures.

Comme les performances du dispositif multiniveaux sont liées au degré d'interaction électronique entre le polaron transporté dans les régions conjuguées de la couche et le niveau accepteur des DAE, la réponse du dispositif aux stimuli optiques ne peut qu'augmenter encore grâce à une optimisation de la microstructure du mélange. Afin d'optimiser les deux, la capacité du DAE-Me à piéger les porteurs de charge transportés dans la matrice de P3HT lorsque les DAE se trouvent dans l'état fermé et à les dé-piéger lorsqu'ils sont ramenés dans l'isomère ouvert, l'absence de séparation de phase entre les deux composants à l'échelle mésoscopique est nécessaire. La corrélation entre la morphologie et les performances optoélectroniques des transistors organiques à couche mince basés sur des mélanges de diaryléthènes (DAE) photochromiques et de P3HT est étudiée en faisant varier la masse moléculaire ( $M_w=20-100$  kDa) et la régiorégularité du polymère conjugué ainsi que la température de recuit thermique (TA-160 °C) dans les couches minces.

Les architectures semi-cristallines des mélanges P3HT/DAE comprennent des domaines cristallins, assurant un transport de charge efficace, et des régions moins agrégées, où les DAE sont situés en raison de leur expulsion spontanée des domaines cristallins lors de

l'auto-assemblage. Le meilleur compromis entre la mobilité de l'effet de champ ( $\mu$ ) et les capacités de commutation a été observé dans des mélanges contenant du P3HT avec  $M_w=50$  kDa, présentant des  $\mu$  aussi élevés que  $1 \times 10^{-3} \text{ cm}^2 \text{V}^{-1} \text{s}^{-1}$  combinés à un taux de commutation induit par un stimulus optique supérieure à 50 %. Une  $M_w$  supérieure ou inférieure à 50 kDa s'est avérée préjudiciable à la mobilité de l'effet de champ et a entraîné une réduction de la commutabilité du courant de l'appareil. Les couches réalisées avec le P3HT possédant une régiorégularité plus élevée présentent des performances électriques améliorées, mais s'accompagnent d'une réponse aux stimuli optiques plus modeste que dans le cas du P3HT régio-random. La microstructure du mélange régio-régulaire de P3HT s'est avérée sensible à la température de recuit thermique, une augmentation en  $\mu$  et une diminution de la modulation du courant étant observées en réponse au stimulus lumineux. Une réduction de la photoréaction est mesurée pour les températures de recuit supérieures à 80 °C. Le modèle Spano ainsi que les mesures d'absorption UV-vis et les observations de rendement quantique suggèrent que la performance de commutation est réduite, peut-être parce que la présence de DAE-Me\_o abaisse la température de fusion du P3HT, ce qui contribue à augmenter l'épaisseur du cristal lamellaire sans nécessairement affecter le degré global de cristallinité pendant le recuit thermique. Enfin, à une température supérieure à 140 °C, la photoréponse des courbes de transfert est perdue en raison de la fusion du DAE-Me\_o. Cette étude offre un aperçu important sur les dispositifs bi-fonctionnels exploitant le P3HT/DAE-Me\_o.

Par la suite, les connaissances acquises sur les mélanges multi-composants sont utilisées comme point de départ pour la conception et la réalisation d'un nouveau concept de dispositif multifonctionnel. Dans cette optique, le mélange semi-conducteur/molécules photochromiques le plus performant est combiné à un isolant de grille ferroélectriques afin d'obtenir un stockage de données multi-bits. En effet, la commutation de polarisation ferroélectrique peut être utilisée comme un mécanisme supplémentaire pour contrôler le stockage de données non volatiles dans les mémoires organiques.<sup>[20]</sup> Alors que dans les condensateurs ferroélectriques, la lecture de la charge de polarisation est destructive, dans les OFET ferroélectriques, la lecture est basée sur une commutation résistive. L'idée est de développer un dispositif dans lequel les propriétés favorables des matériaux ferroélectriques, telles que la bi-stabilité et la non-volatilité, peuvent être combinées aux propriétés bénéfiques offertes par le mélange de semi-conducteurs, telles que la conductivité, la rectification et la réponse optique. L'un des matériaux organiques ferroélectriques les plus prometteurs est le poly(fluorure de vinylidène-trifluoroéthylène)

(P(VDF-TrFE)) qui présente les propriétés avantageuses d'une polarisation résiduelle relativement importante sans fatigue, d'un temps de commutation court et d'une bonne stabilité thermique.<sup>[21]</sup> Une fois déterminées les meilleures conditions pour la réalisation d'une couche mince de PVDF-TrFE, celles-ci sont utilisées pour la fabrication de la couche isolante de grille dans un transistor à effet de champ ferroélectrique (FeFET). Tout d'abord, les propriétés électriques et optiques du dispositif multi-composant sont testées séparément. Pour prouver que la conductivité du dispositif peut être modulée de manière non volatile par la polarisation partielle de la couche isolante ferroélectrique, la tension de grille du dispositif est balayée. Si la couche ferroélectrique est polarisée négativement, elle peut induire une couche d'accumulation permanente dans le semi-conducteur. Cela signifie que lorsqu'une tension de drain non nulle est appliquée, un courant peut être mesuré même si la tension de grille est nulle. Au contraire, si la couche ferroélectrique est polarisée positivement, le canal du transistor est appauvri en charges et aucun courant de drain significatif ne peut être mesuré si une tension de drain est appliquée. Au moins six niveaux de courant de drain distincts (y compris l'état OFF) peuvent être programmés dans le FeFET. Chaque niveau de courant est stable dans le temps et est reproductible sur des cycles. De plus, on n'observe aucune fatigue dans la cyclabilité.

Afin de prouver les propriétés optiques du FeFET, une mesure de commutation dynamique est effectuée en exploitant une configuration de sonde lumineuse faite sur mesure lors d'un détachement à l'Université de Nova Gorica. Un deuxième objectif de cette expérience est de mesurer le nombre maximum de niveaux de courant par état de polarisation. Tout d'abord, la couche ferroélectrique du FeFET a été entièrement polarisée négativement. Ensuite, le courant de drain est mesuré dans le temps pendant que l'appareil est irradié à une fréquence de 0,1 Hz par une impulsion laser UV de 3ns de long ( $\lambda = 310$  nm) à une intensité donnée. Cette procédure a conduit à une diminution progressive du courant contrôlée par le nombre d'impulsions. Chaque impulsion génère un niveau de courant en raison du nombre croissant de molécules de diaryléthène sous forme ouverte qui sont transformées en leur forme fermée. Au total, on peut distinguer plus de 600 niveaux de courant pour l'état de polarisation ferroélectrique complet. Le nombre total de niveaux de courant augmente ou diminue en fonction de l'intensité lumineuse. Par conséquent, nous prouvons qu'en utilisant des filtres, la hauteur des pas de courant peut être contrôlée puisque le nombre de molécules subissant une isomérisation est directement lié à la densité des photons frappant la zone active du dispositif. L'augmentation de la densité de puissance surfacique constitue une méthode simple pour améliorer le rapport signal/bruit

(*signal to noise ratio*, SNR) de la variation de courant, ce qui permet de mieux stocker les données.

Enfin, nous poursuivons en démontrant qu'une combinaison des propriétés électriques et optiques de ce FeFET multi-composant peut être exploitée pour le stockage futur de données à haute densité. Nous montrons que ce nouveau concept de dispositif permet un stockage réversible à plusieurs niveaux dans une seule cellule, en utilisant des cycles de programmation/effacement (P/E) de la lumière simple mais extrêmement efficaces pour chaque état de polarisation. Les rayonnements UV/lumière verte avec une impulsion définie sont capables de déplacer de manière réversible et fiable l'état de la cellule entre les niveaux intermédiaires (définis par le balayage de la tension de grille) avec une grande répétabilité. Ce fonctionnement à plusieurs niveaux dépend des états de polarisation partielle librement accessibles du PVDF-TrFE comme niveaux de base pour les états de conductivité intermédiaires en raison de la fermeture consécutive des molécules de DAE. En effet, ces états mixtes présentent des valeurs de courant comprises entre celles induites par la polarisation partielle ferroélectrique. Le nombre maximum de niveaux mixtes possibles pour chaque état de polarisation est défini par la différence entre deux états de polarisation partielle consécutifs divisée par la variation minimale de courant distinguable induite par la lumière UV. Six niveaux photo-induits distinguables sont programmés avec des impulsions UV de 2 min à partir de chaque état de polarisation principal. Ces niveaux ont été écrits en série et ensuite effacés à l'état initial à l'aide de la lumière verte. L'expérience démontre que chaque niveau peut être atteint dans les deux sens, induisant la fermeture ainsi que l'ouverture des molécules d'EAD. Cela implique que tout niveau est accessible à partir de tous les autres, avec un contrôle très précis des niveaux actuels et une répétabilité remarquable, simplement en appliquant l'impulsion d'écriture ou d'effacement appropriée. De telles capacités constituent un énorme bond en avant en termes de fonctionnalité et seront cruciales pour la réalisation de mémoires hybrides praticables.

En résumé, en faisant varier la masse moléculaire et la régiorégularité du P3HT dans le mélange, il a été possible de conclure que la ségrégation de phase DAE-Me<sub>0</sub> au sein d'une matrice P3HT est fortement corrélée aux propriétés optoélectroniques du FET bi-fonctionnel. La microstructure du mélange régio-régulaire de P3HT s'est révélé être sensible à la température de recuit thermique, une augmentation en  $\mu$  et une diminution de la modulation du courant étant observées en réponse à la stimulation lumineuse, probablement due à un accroissement de la ségrégation P3HT-DAE, ce qui entrave

partiellement la photo-isomérisation du DAE. Nos résultats démontrent l'importance d'un réglage fin de la structure et de la morphologie des couches bicomposantes pour exploiter la nature multifonctionnelle des dispositifs optoélectroniques. La régularité et la température de recuit pendant la fabrication du processus doivent être choisies/contrôlées afin de régler les propriétés du dispositif résultant. En outre, la technologie future basée sur ce mélange doit tenir compte de la fenêtre de température à laquelle les dispositifs peuvent fonctionner tout en conservant les caractéristiques initiales.

Nous avons également fait la démonstration du premier prototype d'une mémoire hybride, photochromique-ferroélectrique, non volatile, qui permet un stockage multi-niveau (jusqu'à 3000 niveaux, soit plus de 11 bits) dans un seul transistor. La fonctionnalité du dispositif a été augmentée en exploitant la polarisation partielle ferroélectrique en combinaison avec la commutation optique. Les transistors de mémoire sont commutés entre les états de mémoire par des stimuli indépendants: impulsions laser ou balayage de tension. Notre nouveau concept de mémoire ferroélectrique-photochromique permet une extensibilité totale puisque les unités de commutation photochromique ne font que quelques nm de long et que les dispositifs ferroélectriques organiques PVDF-TrFE ont montré une tendance intéressante au niveau de réduction d'échelle ces dernières années. De nouvelles améliorations ne peuvent être obtenues qu'en utilisant soit un matériau ferroélectrique présentant une plus grande polarisation résiduelle, soit un polymère semi-conducteur à plus grande mobilité.

À l'ère de l'IoE, où les objets seront intégrés les uns aux autres et aux humains, la nécessité de stocker des informations à l'aide de la lumière sur un substrat flexible va devenir une nécessité. L'interaction continue entre les objets et les êtres humains exigera l'intégration d'un plus grand nombre de capteurs dans les applications futures. Compte tenu des fonctionnalités supplémentaires requises pour le développement futur des communications, les ordinateurs portables, les drones et les véhicules autonomes, la demande totale de bande passante mémoire et de stockage augmente. À cet égard, la transmission optique des données permet un débit plus élevé que son homologue électrique. Par conséquent, malgré des performances qui ne sont pas encore au niveau de celles mises en œuvre par la technologie de mémoire à faible coût à base de silicium, l'électronique organique offre un grand potentiel pour le développement de dispositifs de mémoire capables d'assurer la liaison entre les stimulations électriques et optiques. L'amélioration d'une mémoire ferroélectrique photochromique est une étape importante

dans ce sens, en permettant de stocker des informations multi-bits dans une cellule de mémoire à un seul transistor. En utilisant un mélange d'un polymère semi-conducteur avec une petite molécule photochromique et en combinant la couche résultante avec un matériau organique ferroélectrique, nous avons pu réaliser un dispositif à trois électrodes avec une capacité de stockage élevée. Le contrôle optique fin de 3ns sur ses états de courant électrique le rend adapté à l'électronique de demain. De plus, la longue conservation des données et leur bonne fiabilité après les cycles de programmation/effacement rendent cette approche idéale pour les applications non volatiles. Tout a été possible grâce à une sélection minutieuse des conditions de traitement et à une analyse détaillée des microstructures de la couche. Cette thèse a démontré la polyvalence de l'électronique organique en exploitant la méthode de mélange comme une approche efficace pour conférer des fonctionnalités supplémentaires aux matériaux, en réduisant les coûts et en utilisant des procédés de fabrication peu complexes.

## Summary

Information storage is a basic functionality required in most electronic devices. Among its key performance indicators, the amount of data that can be stored holds a paramount importance. In this regard, this thesis focuses on the realization of an optically responsive organic field-effect transistor (OFET) device based on a bicomponent semiconductor/photochromic blend that imparts storage capability to the device through a multi-level non-volatile electrical response. Such blend is integrated in a non-volatile memory device which also exploits the ferroelectricity of the dielectric layer to boost storage capacity. Multi-component organic devices are a promising approach towards the development of a low-cost memory technology.

Organic semiconductors have been extensively investigated in the past three decades because of their tunable physical properties via chemical functionalization, their low-cost processing and their integration onto flexible supports.<sup>[1-3]</sup> Their unique properties have attracted the attention of several companies which have exploited these materials for applications such as liquid crystal displays, data storage devices, portable batteries, light-emitting displays and photovoltaic cells.<sup>[4-8]</sup> The development of multi-component organic materials that can combine a set of properties leads to new multi-functional devices<sup>[9-10]</sup> and paves the way for a further technology advancement in the era of Internet of Everything (IoE).<sup>[11]</sup>

Conjugated polymer chains interact weakly among each other resulting in many degrees of structural freedom which lead to a complex film micro-structuring in the condensed state. Understanding and controlling the microstructure of such systems, which have amorphous and ordered phases exhibiting varying degrees of order, allows a better integration with different small molecules imparting new functionality.<sup>[12]</sup> Structural control at the appropriate length scales combined with knowledge of basic physical processes between the components have given rise to engineering breakthroughs and rational design of devices.<sup>[13]</sup> Recently, the potential to combine low-cost process and higher integration capabilities while engineering optoelectronic properties has attracted great interest on semiconducting polymer blends.<sup>[14]</sup>

In this context, the functionality of solution-processed OFETs has been enhanced with the development of new multi-component blend incorporating functional molecules in semiconducting matrices. Among various classes of molecules, photochromic molecules are ideal candidates to integrate in the next generation of opto-electronic devices as they

can be optically controlled with high spatiotemporal resolution without the generation of waste products.<sup>[15]</sup> The optically induced switching between two independently addressable states leads to changes both at the molecular and the macroscopic scale. Reversible structural and electronic changes in the geometry, dipole moments,  $\pi$ -conjugation, bandgap is induced at the molecular level. Changes in shape, aggregation behavior and conductance are observed at the macroscopic scale. Photochromic DAE derivatives (DAE-Me) were selected as best candidate since they display a high thermal stability and almost fatigue-free switching in solution. DAE-Me were synthesized, in the frame of a long-term collaboration, by the group of Prof. Stefan Hecht at Humboldt University of Berlin.<sup>[16-17]</sup> In order to confer a light responsive nature to thin-film transistors, DAE molecules were dispersed in a polymeric semiconducting matrix. DAE-Me were designed to have HOMO energy levels which allow selective electronic interaction with most of p-type semiconductor. When the diarylethene is in open form, its HOMO acts as a scattering center for charges, i.e. no electronic interaction occurs between DAE and the host semiconducting matrix. On the other hand, when the diarylethene is in the closed form, charges transported across the semiconductor film can get trapped reducing thereby the output current. Since the diarylethene is thermodynamically stable in both forms, this effect was used in order to store information and build multilevel memories.<sup>[18]</sup> Many high-performance semiconducting polymers exhibit properties suitable for interaction with DAE in multi-component devices. A correct assessment of DAE integration requires to test electrically and optically the photo-switching performances of bi-component films allowing to determine the most suitable polymer. In particular, switching amplitude and fatigue with respect to mobility in FET are employed as the major figures of merit to pick the most promising DAE/polymer pair for optoelectronic application. While P3HT remains one of the most used p-type semiconductors for organic electronics and one of the more established building blocks for these applications, in the last few years several materials have successfully challenged it, by displaying greater electrical performances and air stability. Among those, PDVT-8 and PCD-TTP are chosen as alternative host materials since they exhibit totally different degree of crystallinity and microstructure than P3HT.<sup>[12, 19]</sup> Although PDVT-8 and PCD-TPT devices showed higher electric performances, OFET based on P3HT blend display outstanding photo-switchable capability with the two states being extremely stable over the timescale of several days. Considering this preliminary analysis, P3HT blend is selected as best candidate to conduct deeper investigation on micro-structure engineering.

Since the multi-level device performances are related to the degree of electronic interaction between the polaron transported in the conjugated portions of the film and the accepting DAE levels, the device photoresponse can only further increase through an optimization of the blend microstructure. In order to maximize both, the capability of DAE-Me to trap the charge carriers transported within the P3HT matrix when in the closed isomer and to de-trap them when toggled back to the open isomer, the absence of phase separation at the mesoscale between the two components is required. The correlation between morphology and opto-electronic performance in organic thin-film transistors based on blends of photochromic diarylethenes (DAE) and poly(3-hexylthiophene) (P3HT) is investigated by varying molecular weight ( $M_w=20-100$  kDa) and regioregularity of the conjugated polymer as well as the temperature of thermal annealing (rt-160 °C) in thin films. Semi-crystalline architectures of P3HT/DAE blends comprise crystalline domains, ensuring efficient charge transport, and less aggregated regions, where DAEs are located as a result of their spontaneous expulsion from the crystalline domains during the self-assembly. The best compromise between field-effect mobility ( $\mu$ ) and switching capabilities was observed in blends containing P3HT with  $M_w=50$  kDa, exhibiting  $\mu$  as high as  $1 \times 10^{-3} \text{ cm}^2 \text{V}^{-1} \text{s}^{-1}$  combined with a  $> 50\%$  photoswitching ratio. Higher or lower  $M_w$  than 50 kDa were found to be detrimental for field-effect mobility and to lead to reduced device current switchability. The films made with P3HT possessing higher regioregularity exhibit lower electrical performance accompanied by a more modest photo-response than regiorandom P3HT. The microstructure of the regioregular P3HT blend was found to be sensitive to the thermal annealing temperature, with an increase in  $\mu$  and a decrease in current modulation being observed as a response to the light-stimulus. Reduced photoresponse is measured for annealing temperatures higher than 80 °C. The Spano model together with UV-vis absorption measurements and quantum yield observations suggests that the switching performance is lowered possibly because the presence of DAE-Me<sub>o</sub> lowers the P3HT melting temperature, assisting in increasing the lamellar crystal thickness without necessarily affecting the overall degree of crystallinity during thermal annealing. Finally, at higher temperature than 140 °C, the photoresponse of the transfer curves is lost due to the melting of DAE-Me<sub>o</sub>. This study offers an important insight on bi-functional devices exploiting P3HT/DAE-Me<sub>o</sub>.

As follow-up, the knowledge acquired on multicomponent blend is exploited as starting point for the design and realization of a new device concept with increased functionality. In this concern, the best performing semiconductor-photochromic blend is combined with

ferroelectric materials in order to achieve multi-bit data retention. Indeed, ferroelectric polarization switching can be used as an additional mechanism to control non-volatile data retention in organic memory devices.<sup>[20]</sup> While in ferroelectric capacitors the readout of the polarization charge is destructive, in ferroelectric OFET the readout is based on resistive switching. The idea is to develop a device in which the favorable properties of ferroelectrics such as bi-stability and non-volatility can be combined with the beneficial properties provided by the semiconductor blend such as conductivity, rectification and optically response. One of the most promising organic ferroelectric material is poly(vinylidene fluoride-trifluoroethylene) (P(VDF-TrFE)) which has the advantageous properties of a relatively large fatigue-free remnant polarization, short switching time and a good thermal stability.<sup>[21]</sup> First, the solution process and the film deposition of the P(VDF-TrFE) have been studied by fabricating and characterizing ferroelectric capacitor. Once the best conditions have been found for the realization of a PVDF-TrFE thin film, they are used for the fabrication of the gate insulation layer in a ferroelectric field-effect transistor FeFET. Firstly, the electrical and optical properties of the multi-component device are tested separately. To prove that the device conductivity can be modulated in a non-volatile way by the partial polarization of the ferroelectric layer, gate voltage sweeps are applied to the device. If the ferroelectric layer is negatively polarized, it can induce a permanent accumulation layer in semiconducting film. This means that when a non-zero drain voltage is applied, a current can be measured even if the gate voltage is zero. On the contrary if ferroelectric layer is positively polarized, the channel of the transistor is depleted from charges and no significant drain current can be measured if a drain voltage is applied. At least 6 distinct drain current levels (including Off state) can be programmed in FeFET. Each current level is stable over time and it is reproducible over cycles. Moreover, no fatigue in cyclability is observed.

In order to prove the optical properties of the FeFET, a dynamic switching measurement is performed exploiting a custom-made light probe setup during a secondment at the University of Nova Gorica. A second objective for this experiment is to measure the maximum number of current steps per polarization state. First, the ferroelectric layer of FeFET were fully negatively polarized. Then, the drain current is measured over time while the device is irradiated at a frequency of 0.1 Hz with a 3-ns long UV ( $\lambda = 310$  nm) laser pulse at a given intensity. Such procedure led to a progressive current decrease controlled by the number of pulses. Each pulse generated a current step due to the increasing number of diarylethene molecules in the open form which are turned into their closed form. In total,

more than 600 current levels are distinguishable for the full ferroelectric polarization state. The overall number of current steps increases or reduces depending on the light intensity. Therefore, we prove that using filters the current step height can be controlled since the number of molecules undergoing isomerization is directly linked to the density of the photons hitting the active area of the device. Increasing the areal power density provides an easy method to improve the signal to noise ratio (SNR) of the current variation resulting in better data storage capabilities.

Finally, we follow up by demonstrating that a combination of the electrical and optical properties of this multi-component FeFET can be exploited for future high-density data storage. We show that this new device concept allows reversible multi-level storage in a single cell, using simple but extremely effective light program/erase (P/E) cycles for each polarization state. UV/green light irradiations with defined pulse are able to reversibly and reliably move the cell status between intermediate levels (defined by gate voltage sweep) with high repeatability. This multi-level operation depends on the freely accessible partial polarization states of PVDF-TrFE as ground levels for intermediate conductivity states due to consequently closure of DAE molecules. Indeed, these mixed states exhibit current values lying between those induced by the ferroelectric partial polarization. The maximum number of possible mixed levels for each polarization state is defined by the difference between two consecutive partial polarization states divided by the minimum distinguishable current variation induced by UV light. Six distinguishable photo-induced levels are programmed with 2 min UV pulses starting from each main polarization state. These levels were written in a serial manner and subsequently erased to the initial state using green light. The experiment demonstrate that each level can be reached from both directions inducing the closure as well as the opening of the DAE molecules. This implies that any level is accessible from all others, with very accurate control of the current levels and remarkable repeatability, just by applying the appropriate Write or Erase pulse. Such capabilities provide a huge leap forward in terms of functionality and will be crucial for the realization of practicable hybrid memories.

In summary, upon varying molecular weight and regioregularity of the P3HT in the blend, it was possible to conclude that DAE-Me<sub>0</sub> phase segregation within a P3HT matrix is strongly correlated to the opto-electronic properties of the bi-functional FET. The microstructure of the regioregular P3HT blend was found to be sensitive to the thermal annealing temperature, with an increase in  $\mu$  and a decrease in current modulation being observed as a response to the light-stimulus likely due to an increased P3HT-DAE

segregation, partially hindering the DAE photoisomerization. Our findings demonstrate the paramount importance of fine tuning the structure and morphology of bicomponent films for leveraging the multifunctional nature of opto-electronic devices. The regioregularity and annealing temperature during process fabrication have to be chosen/controlled in order to tune the resulting device properties. Moreover, future technology based on such blend must consider the temperature window where devices can operate while retaining the initial characteristics. We have also demonstrated the first prototype of a hybrid, photochromic-ferroelectric, non-volatile memory that provides multi-level (up to 3000 levels, i.e. over 11 bits) storage in a single transistor. The device functionality was increased by exploiting ferroelectric partial polarization in combination with optical switching. The memory transistors are switched between memory states by independent stimuli: laser pulses or voltage sweep. Our new concept of ferroelectric-photochromic memory allows fully scalability since the photochromic switching units are just few nm long and PVDF-TrFE organic ferroelectric devices have seen an interesting scaling trend in recent years. Further improvements can be only obtained by using either a ferroelectric material exhibiting higher remnant polarization or semiconducting polymer with higher mobility.

In the era of Internet of Everything in which objects will be seamless connected each other and to humans, the need to store information using light on a flexible substrate will become a requirement. The continuous interaction between objects and living entities will require a higher number of sensors to be embedded in future applications. Considering the additional functionality required for tomorrow's communications, wearable computers, autonomous drones and vehicles, the total memory bandwidth and storage demand is increasing. In this regard, optical data transmission allows faster data rate if compared with its electrical counterpart. Hence, in spite of performances which are still not at the level of those implemented through low-cost silicon-based memory technology, organic electronics holds a great potential for developing memory devices able to act as liaison between electrical and optical stimuli. The improvement of a photochromic ferroelectric memory is an important step forward in this direction which allows to store multi-bit information in a single transistor memory cell. By blending a semiconducting polymer with a photochromic small molecule and combining the resulting film with an organic ferroelectric material, we were able to realize a three-terminal device with impressive storage capabilities. The fine 3ns optical control over its electrical current states makes it suitable for future electronics. Moreover, the long data-retention and good reliability after

program/erase cycles makes this approach ideal for non-volatile applications. Everything was possible thanks to a careful selection of process conditions and a detailed analysis of the film microstructures. This thesis has demonstrated the versatility of organic electronics exploiting the blending method as efficient approach to impart additional functionalities to materials, reducing costs and avoiding high process pitfalls.

## References

- [1] A. V. Teplyakov, S. F. Bent, *Journal of Vacuum Science & Technology A: Vacuum, Surfaces, and Films* **2013**, 31, 050810.
- [2] A. Facchetti, M. H. Yoon, T. J. Marks, *Adv Mater* **2005**, 17, 1705.
- [3] M. J. Griffith, N. P. Holmes, D. C. Elkington, S. Cottam, J. Stamenkovic, A. D. Kilcoyne, T. R. Andersen, *Nanotechnology* **2019**, 31, 092002.
- [4] I. McCulloch, M. Heeney, C. Bailey, K. Genevicius, I. MacDonald, M. Shkunov, D. Sparrowe, S. Tierney, R. Wagner, W. Zhang, *Nat Mater* **2006**, 5, 328.
- [5] S. Ono, S. Seki, R. Hirahara, Y. Tominari, J. Takeya, *Appl Phys Lett* **2008**, 92, 93.
- [6] S. Möller, C. Perlov, W. Jackson, C. Taussig, S. R. Forrest, *Nature* **2003**, 426, 166.
- [7] A. Facchetti, *Chem Mater* **2011**, 23, 733.
- [8] H. Uoyama, K. Goushi, K. Shizu, H. Nomura, C. Adachi, *Nature* **2012**, 492, 234.
- [9] M. He, F. Qiu, Z. Lin, *The journal of physical chemistry letters* **2013**, 4, 1788.
- [10] B. Nketia-Yawson, Y.-Y. Noh, *Macromolecular Research* **2017**, 25, 489.
- [11] M. Hermann, T. Pentek, B. Otto, in *Proceedings of the 49th Annual Hawaii International Conference on System Sciences*, DOI: 10.1109/hicss.2016.488 (Eds: T. X. Bui, R. H. Sprague), Ieee Computer Soc, Los Alamitos **2016**, p. 3928.
- [12] R. Noriega, J. Rivnay, K. Vandewal, F. P. V. Koch, N. Stingelin, P. Smith, M. F. Toney, A. Salleo, *Nat Mater* **2013**, 12, 1038.
- [13] P. Chen, G. Yang, T. Liu, T. Li, M. Wang, W. Huang, *Polymer international* **2006**, 55, 473.
- [14] E. Moons, *Journal of Physics: Condensed Matter* **2002**, 14, 12235.
- [15] E. Orgiu, P. Samori, *Adv Mater* **2014**, 26, 1827.
- [16] M. Herder, F. Eisenreich, A. Bonasera, A. Grafl, L. Grubert, M. Pätzelt, J. Schwarz, S. Hecht, *Chemistry—A European Journal* **2017**, 23, 3743.
- [17] M. Herder, B. M. Schmidt, L. Grubert, M. Patzelt, J. Schwarz, S. Hecht, *J Am Chem Soc* **2015**, 137, 2738.
- [18] T. Leydecker, M. Herder, E. Pavlica, G. Bratina, S. Hecht, E. Orgiu, P. Samori, *Nat Nanotechnol* **2016**, 11, 769.
- [19] T. Leydecker, M. A. Squillaci, F. Liscio, E. Orgiu, P. Samorì, *Chem Mater* **2018**, 31, 6491.
- [20] R. C. Naber, K. Asadi, P. W. Blom, D. M. de Leeuw, B. de Boer, *Adv Mater* **2010**, 22, 933.
- [21] D. Zhao, I. Katsouras, M. Li, K. Asadi, J. Tsurumi, G. Glasser, J. Takeya, P. W. Blom, D. M. De Leeuw, *Sci Rep-Uk* **2014**, 4, 5075.

## Table of Contents

Résumé de these.....	i
Summary.....	ix
Chapter 1. Introduction .....	1
1.1 Motivation and aim of the thesis.....	1
1.2 Organic semiconducting polymers.....	3
1.2.1 Structural and energetic profile characteristics .....	4
1.2.2 Transport models in organic semiconductors.....	6
1.2.3 General structure-electrical properties relationship in organic semiconductors .....	10
1.2.4 Polarons and bipolarons in semiconducting polymers.....	15
1.3 Photochromism .....	19
1.3.1 Organic photochromic molecules .....	20
1.4 Ferroelectricity.....	22
1.4.1 Organic ferroelectrics .....	24
Chapter 2. Organic Devices .....	31
2.1 Role of interfaces in organic devices.....	31
2.2 Charge injection in organic semiconductor devices .....	35
2.2.1 Charge injection models .....	36
2.3 Surface functionalization to improve charge transport - semiconductor/dielectric interface.....	38
2.3.1 Effect on impurities in the semiconductor: Trapping and doping .....	39
2.4 Organic Field-effect Transistors (OFETs).....	40
2.4.1 OFET architectures .....	41
2.4.2 OFETs operation modes .....	43
2.4.3 Measurement of electrical characteristics and parameters extraction .....	45
2.5 Photochromism in organic devices.....	48
2.6 Ferroelectric Organic Devices – Ferroelectric Memories .....	50
Chapter 3. Materials and Experimental Techniques .....	59
3.1 Employed Semiconductors.....	59
3.1.1 Poly (3-Hexylthiophene) (P3HT).....	59
3.1.2 Other polymers employed: PDVT-8 and PCD-TPT.....	60
3.2 Preparation of OFETs and their characterization .....	62

3.2.1	Methods for solution deposition.....	62
3.2.2	Substrates for OFET .....	64
3.2.3	UV-Ozone treatment.....	65
3.2.4	Design of device's electrodes by photolithography.....	65
3.2.5	Electrodes deposition.....	67
3.2.6	Self-assembled monolayer functionalization.....	68
3.2.7	Preparation of solutions for spin-coating.....	68
3.3	Characterization techniques .....	70
3.3.1	Surface Characterization .....	70
3.3.2	Electrical Characterization .....	72
Chapter 4. Investigation of DAE trapping mechanism using Charge Modulation Spectroscopy (CMS) .....		75
4.1	Charge modulation spectroscopy (CMS): Basic working principles .....	75
4.2	Experimental setup and measurement technique.....	78
4.3	Device fabrication and characterization.....	79
4.4	CMS spectra acquired on pristine P3HT-based devices.....	81
4.5	CMS spectra acquired on P3HT/DAE blends .....	84
4.6	Conclusions.....	87
Chapter 5. A close look at the photo-switching properties of transistors based on a photochromic molecule / p-type polymer semiconductor blend .....		92
5.1	The role of morphology in optically switchable transistors based on DAE/P3HT blend.....	94
5.1.1	Role of molecular weight and regioregularity.....	95
5.1.2	Annealing temperature.....	100
5.2	Blend of DAE with other p-type copolymers – Preliminary study .....	108
5.3	Conclusions.....	113
Chapter 6. Optically Switchable Ferroelectric Field-effect Transistors (OS-FeFET) based on P3HT/DAE blend semiconductor layer and organic ferroelectric gate insulator .....		117
6.1	Results and Discussions.....	119
6.2	Conclusions and Outlook.....	127
Chapter 7. Conclusion and Outlook .....		131
Appendix A1- Experimental section of Chapter 5.....		135
Appendix A2– Experimental section of Chapter 6 .....		139

Acknowledgements..... 147

# Chapter 1. Introduction

## 1.1 Motivation and aim of the thesis

The storage and transmission of information is essential for many aspects of the human life. Looking back from cave paintings till contemporary digital technology, the human evolution was always driven by our capability of sharing and storing information in an accessible way. The fourth industrial revolution which has its fundamental in digital technology led in the recent years to innovative concepts like Internet of Things (IoT)<sup>[1]</sup> or Artificial intelligence.<sup>[2]</sup> Such breakthroughs will not be possible without a huge leap forward in performance of memory devices. By 2025, the total amount of data will reach at more than 160 ZB ( $10^9$  TB), which is 4 times higher than the prediction made in 2012.<sup>[3]</sup> The recent unfortunate event, COVID-19 outbreak, has pushed this prediction even higher given the higher demand coming from a larger number of people being constantly connected from remote. Therefore, the huge gap between the amount of daily-created data and the capacities of existing storage medium in a close future will be the main bottleneck for further improvements. These considerations are motivating scientists to study physical phenomena that are able to store information over long time, possibly leading in future to a more efficient and reliable memories. So far, to boost the data storage capabilities of memory devices, the most common approach has relied on the continuous scaling down, ensuring the integration of more memory cells per unit area. TSMC's 5nm Fin Field-Effect Transistor (FinFET) process technology is the most recent example.<sup>[4]</sup> However, this strategy has intrinsic photolithographic limits thus the scaling-down trend driven by the Moore's law will reach to its bottleneck by 2022.<sup>[5]</sup>

On top of that, a more general concept which includes human interface has to be taken into account when designing the future technology revolution. The Internet of Everything (IoE) is an extension of the above-mentioned IoT which involves the seamless interconnection and autonomous coordination of massive number of computing elements and sensors together with living entities.<sup>[6]</sup> An example of IoE that is quickly developing during the recent years is the idea of self-driving cars. Autonomous drive cannot rely only on more and more sophisticated car embedded sensor systems, but next-generation advanced driver-assistance systems (ADAS) will increasingly leverage on an improved connectivity by using car-to-car (also known as Vehicle to Vehicle, or V2V), car-to-infrastructure (also known as Vehicle to Infrastructure, or V2X) and finally car-to-person

data. In this big picture, human beings enter as the third and more complex variable of the system. Therefore, wearing sensors will be a requirement for humans to be part of such complex network together with autonomous vehicles and infrastructures. In this outlook, flexible, transparent organic electronics opens interesting alternatives for devices suitable for an easy integration in IoE.

Organic material offers a simple way to implement multifunctionality in a single device relying on the combination of different organic components, with each of them imparting a distinct property to the resulting hybrid material and device thereof.<sup>[7]</sup> The functionality of organic field-effect transistors (OFET) has been enhanced during the past years with the development of multi-component systems incorporating functional molecules in semiconducting matrices.<sup>[8-23]</sup> Benefiting from flexibility, low-cost and multilevel data storage, organic memory devices exhibit attractive future for built-in non-volatile memories at human interface. However, in terms of production costs, polymer non-volatile memories have not an easy path since they would have to compete with Flash memory technology. A new organic memory technology would be able to take a share of the actual global market (currently a multibillion-euro market)<sup>[24]</sup> only by implementing new functionality such as interaction with light. Compared with electrically operated memory, light modulated memories in which electrical read-out are orthogonal to photo-programming operation promises new alternatives for future applications. Photochromic organic memories could widen the devices function and integrate various photo-devices, such as light-emitting diodes, photovoltaics, or photo-sensor platforms.

In this concern, this thesis reports a novel approach for realization of an organic multifunctional nonvolatile memory device by combining a ferroelectric polymer with a photochromic molecules-semiconducting polymer blend. First, we have investigated the nature of the interaction between photochromic molecules and polarons. Second, we show the studies exploited to improve the photo-switchable capabilities and electrical performances of the organic semiconducting blends on silicon-oxide gated transistors. Then, we follow-up by exploiting these results to address the development of a radical new ferroelectric memory. To provide the basic knowledge on materials, physical properties and concepts employed in the rest of this thesis, this chapter is dedicated to an introduction. We first introduce conjugated polymer semiconductors with main focus on their charge transport properties. This is followed by an introduction of photochromic

molecules and then ferroelectric polymers, concepts that will be recalled during the discussion of results.

## 1.2 Organic semiconducting polymers

Over the last 20 years, under the drive of the Nobel Prize in Chemistry in 2000,<sup>[25]</sup> a growing interest in organic semiconductors has led to new technological developments in organic electronics.<sup>[26]</sup> Polymers are widely used for inexpensive, disposable products due to their favorable versatility, ease of manufacture and low-cost.<sup>[27-29]</sup> The conjugated polymers differ from the crystalline inorganic semiconductor systems due to the basics of the molecular interaction. Films with complex morphologies and different degree of order can be realized from polymeric semiconductor thanks to the interplay of non-covalent interactions. In particular, most of the unique properties of these materials come from conjugation that is the alternation of single and double bonds between carbon atoms. Their molecular structure originates from sp<sup>2</sup>-hybridized carbon atoms linked together in creating a backbone that is therefore characterized by  $\pi$ -atomic orbital. The overlapping of these  $\pi$ -atomic orbital results in delocalized  $\pi$  molecular orbitals that defines the HOMO and LUMO electronic levels and characterizes the strength of the inter-molecular electronic couplings, which represent the key parameter governing charge transport. While inorganic semiconductors feature large charge carrier mobilities (typically on the order of  $10^3 \text{ cm}^2 \text{ V}^{-1} \text{ s}^{-1}$ )<sup>[30]</sup> due to the covalent nature of the bonds between atoms, in organic semiconductor the weak nature of interactions leads to modest carrier mobilities (typically on the order of max.  $10^{-3}$ - $1 \text{ cm}^2 \text{ V}^{-1} \text{ s}^{-1}$ ).<sup>[31-37]</sup> The weakness of the electronic coupling due to the large thermal lattice fluctuations induces (transient) charge carrier localization and formation of carriers with high mass, commonly called polarons; transport then relies on polaronic hopping from chain to chain. As a result, the charge carrier mobilities are highly affected by film morphology and can range over several orders of magnitude when going from highly disordered amorphous films (typically,  $10^{-6}$  to  $10^{-3} \text{ cm}^2 \text{ V}^{-1} \text{ s}^{-1}$ ) to highly ordered crystalline materials ( $> 1 \text{ cm}^2 \text{ V}^{-1} \text{ s}^{-1}$ ).<sup>[38]</sup> The nature of charge transport in conjugated polymers is therefore much more complex than for inorganic semiconductors. At first, it is important to discuss basic concepts of organic semiconductors in order to understand the nature of charge transport. Thus, a detailed description of charge transport in conjugated polymers and their unique properties will be presented in this chapter.

### 1.2.1 Structural and energetic profile characteristics

Semiconducting polymers are defined in relation to the energy bands that arise from the bonding and anti-bonding energy levels associated with the  $\sigma$ -bonds between adjacent carbon atoms (formed from the  $sp^2$  wavefunctions) and the orthogonal  $\pi$ -bonds that originate from the  $p_z$  wavefunctions (refer to **Figure 1.1** for details). While the  $\sigma$ -bonds hold the structure together, the  $\pi$ -bonds are those that confer specific properties to conjugated polymers, among which their semiconductivity. [39]

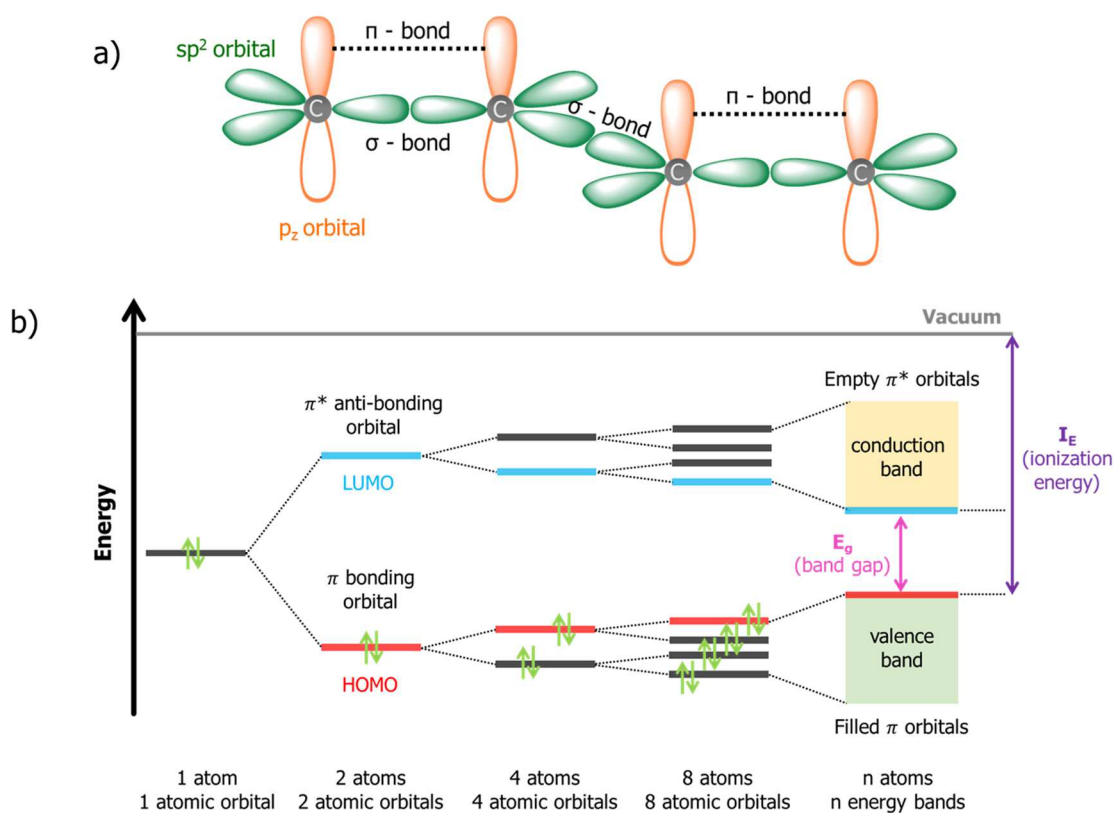


**Figure 1.1:** a) Schematic view of  $\pi$  or  $\sigma$  bonds. b) Representative sketch of the formation of conduction and valence bands for  $\pi$ -conjugated polymers based on Linear Combination of Atomic Orbitals (LCAO) method.

The energy of the highest occupied molecular orbital (HOMO) matches with the top of the highest energy  $\pi$ -band (valence band), and the energy of the lowest unoccupied molecular orbital (LUMO) corresponds to the bottom of the lowest energy  $\pi^*$ -band (conduction band). The energy gap ( $E_g$ ) between the highest occupied energy band and the lowest unoccupied energy band defines the properties of the material. Since  $E_g$  is the threshold

energy barrier for an electron in the HOMO to be promoted to the LUMO, it is a fundamental property which determines the electronic behavior of materials. Conductors have no band gap, while insulators have a large band gap as shown in **Figure 1.2**.

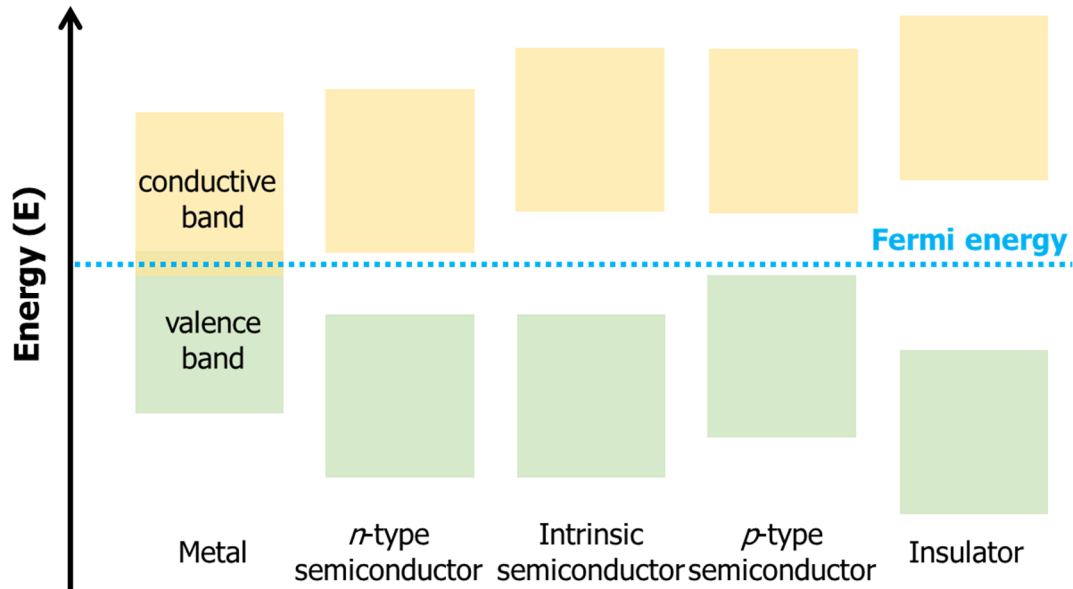


**Figure 1.2:** Band diagrams for metal, semiconductor and insulator.

Instead, semiconductor is defined as a material with a narrow band gap having the Fermi level sitting in between, where Fermi level ( $E_f$ ) is defined as the highest energy level occupied by an electron at 0 K. If the Fermi level is exactly at the middle of the  $E_g$ , the semiconductor is called intrinsic and electrons and holes have equal probability to populate the conduction and valence band, respectively. If the  $E_f$  is closer to the valence band, the latter is more easily populated by holes than conduction band by electrons. Such unbalance gives origin to a more favored hole conduction and the semiconductor is called p-type. Vice versa, if the Fermi level is situated closer to the conduction band, the electron conduction is predominant over hole conduction and the semiconductor is called n-type.

The Fermi-Dirac distribution describes how the electrons are statistically distributed around the Fermi level:<sup>[40]</sup>

$$n_i = \frac{g_i}{e^{\frac{E_i - \mu}{k_B T}} + 1}$$

where  $n_i$  is the number of particles in the state with  $E_i$  having a degeneracy  $g_i$ ,  $k_B$  is the Boltzmann constant,  $\mu$  is the chemical potential (or Fermi Level) and  $T$  is the temperature.

For semiconductor, the ionization energy IE is the energy required to extract an electron from the valence band maximum (i.e. the HOMO) to the vacuum level and electron affinity EA from conduction band (i.e. the LUMO).<sup>[41]</sup> For metals the Fermi level is usually considered to sit in the middle of the metallic band, therefore IE corresponds to the value of work function ( $W_f$ ) where  $W_f$  corresponds to the energy required to extract an electron from the Fermi level  $E_f$  to the vacuum level.

### 1.2.2 Transport models in organic semiconductors

Over the past few years scientists have deeply studied the transport physics in several systems relying on small molecules and conjugated polymers of high mobility, thus allowing to understand the complex factors influencing the charge carrier mobility of these materials. Historically the main models which are generally applied to depict charge transport in organic semiconductors include i) hopping transport or ii) multiple trapping and release. Most often such models have been tailored from the investigation on inorganic semiconductor. While in inorganic semiconductors atoms are strongly localized on their equilibrium lattice sites, conjugated polymers are macromolecules characterized by weak bonds, having numerous degrees of conformational freedom. This leads to different microstructures within the polymers, which range from completely amorphous to crystalline.

In general, semicrystalline conjugated polymers show a characteristic crystalline packing which include ordered lamellae. Such ordered lamellae consist of co-facially stacked molecules displaying strong  $\pi$ -orbital overlap. In such ordered environments, the charge transport mechanisms mainly consist of two processes: intrachain, interchain transport (**Figure 1.3**).<sup>[42]</sup> Intrachain transport is the delocalization of electrons within the polymer backbone and it requires only a small amount of activation energy due to a strong interaction between the  $\pi$ -orbitals between neighboring molecules. In this case, electrons are almost free to move inside the conjugation length, or in other words electrons can move as long as the conjugation length is not interrupted. Interchain transport on the other hand, involves the moving of charge carriers between the neighboring polymer chains and needs more energy to be accomplished due to a weak Van der Waals interaction between polymer chains. This kind of transport is affected by the so-called transfer integral of a molecular system, which define the overlapping of molecular orbitals between adjacent molecules. Higher transfer integral means higher probable tunneling effect between two

sites.<sup>[42]</sup> Finally, inter-grain transport that is the hopping of charges between crystalline domains can occur in the case of polycrystalline films.

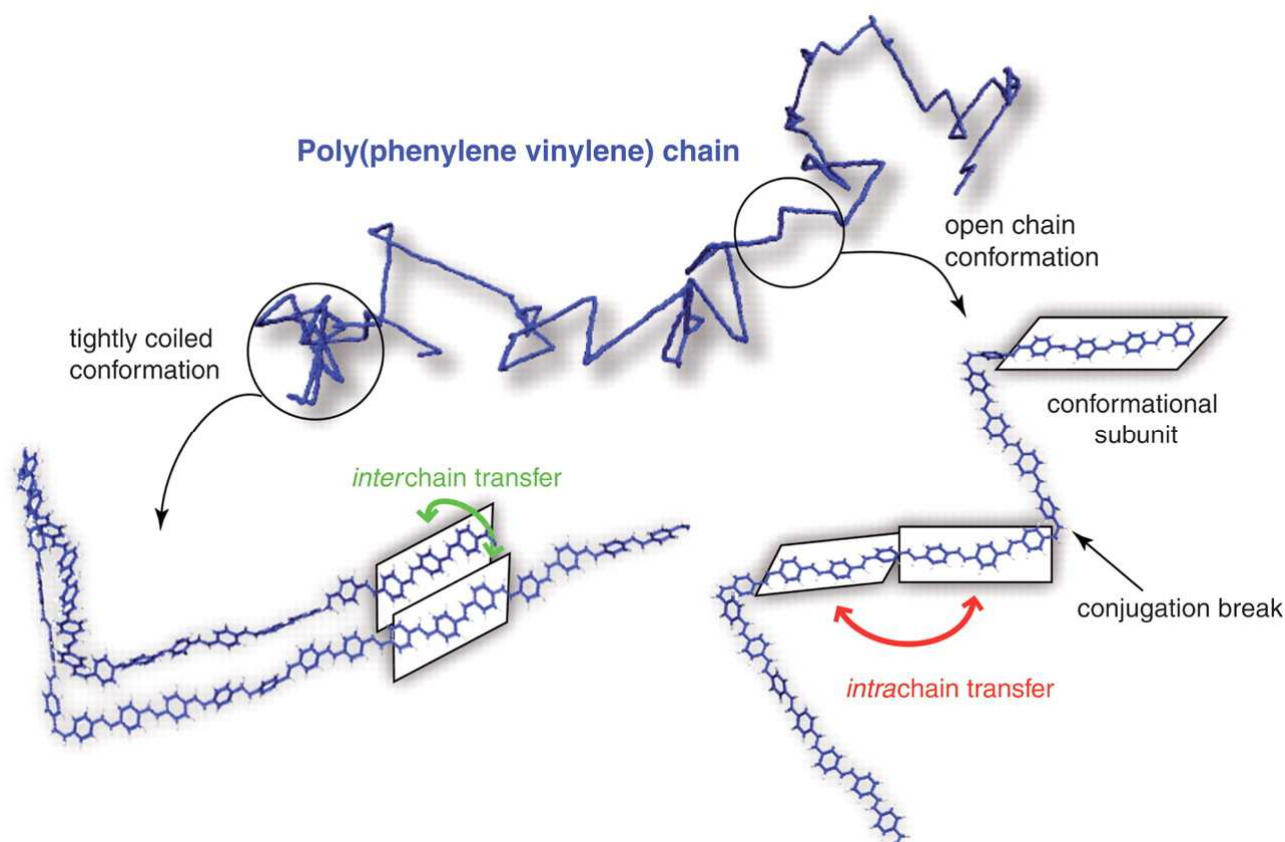


**Figure 1.3:** Schematics of intrachain, interchain transports. Example for poly(phenylene vinylene).<sup>[42]</sup>

These considerations explain why generally charge transport in semicrystalline semiconductor is better than amorphous semiconductors. Yet, this does not seem to be always valid for organic semiconductors. Indeed, new polymers which rely on increasingly complex monomers does not seem to follow the same paradigm; i.e high regioregularity, texture, or crystallinity have been considered over the past years prerequisites to achieve high mobility. Surprisingly, nowadays highly disordered polymers are as efficient as semicrystalline materials. Materials having an intermediate order-disorder scale between crystalline and amorphous can even perform better than materials having high degree of crystallinity. The mutual relationship between microstructure and electrical properties needs to be considered in designing high mobility polymers by increasing their tolerance to an inevitably large amount of disorder within the aggregates and, therefore, allowing more efficient intra and intermolecular charge transport/transfer at the segmental level.

In the following paragraphs, the main transport models applied for organic semiconductors will be introduced together with the latest advances in the physical understanding of the relationship between structural disorder, charge transport and dynamics in conjugated polymer systems. Finally, the polaronic model and its implication in polymer microstructure investigation will be presented.

### 1.2.2.1 Variable Range Hopping model

Various charge transport models have been proposed for polymeric semiconductors. The most common transport model is the Variable Range Hopping (VRH).<sup>[43]</sup> This model is based on the assumption that charges can hop a short distance with a high activation energy or a long distance with a low activation energy. The disordered system is characterized by an exponential distribution of localized states, and the tunneling hopping is activated thermally. At high T the accessible available energy range is wider. At low temperature, hopping over long distances becomes more energetically favorable than hopping to high energies. Hence the conductivity varies with temperature. The temperature dependence of charge transport in such systems is strongly dependent on the density of localized states. Thus, an important parameter for tunneling frequency is the overlapping of states, which is directly related to polymer's crystallinity, with more crystalline polymers presenting a higher overlapping and thus higher performances. Also, this model takes into account the effect of an applied electric field on the gate of a transistor. When the device is turned on, charges fill lower energy states, and additional carriers must fill higher energy levels, resulting in a smaller activation energy to hop away from the initial state, i.e. there is a linear dependence of output current with gate applied voltage. Based on this theory Vissenberg and Matters developed a model based on percolation mechanisms.<sup>[43]</sup> It assumes that transport is governed by the tail states of the Gaussian density of states (DOS) which is approximated by an exponential distribution:

$$N(E) = \frac{N_t}{kT_0} \exp\left(-\frac{E}{kT_0}\right)$$

where  $N_t$  is the total density of localized states,  $k$  the Boltzmann constant and  $T_0$  is the width of the exponential distribution. The resulting mobility gives the following expression

$$\mu = \frac{\sigma_0}{q} \left( \frac{\pi \left(\frac{T_0}{T}\right)^3}{(2\alpha)^3 B_c \Gamma\left(\frac{1-T}{T_0}\right) \Gamma\left(\frac{1+T}{T_0}\right)} \right)^{\frac{T_0}{T}} \left[ \frac{C_i^2 (V_G - V_T)}{2kT_0 \epsilon_S} \right]^{\frac{T_0}{T-1}}$$

Here,  $\sigma_0$  is a coefficient for the conductivity,  $\alpha$  an effective overlap parameter that intervenes in the hopping of charges from site to site and  $B_c$  the critical number for the onset of percolation.  $q$  is the elemental charge and  $\epsilon_s$  the permittivity of the semiconductor. This model is able to accurately reproduce experiments and provide, by means of a single mathematical expression, a clear picture of several effects as the Poole-Frenkel-like dependence of the mobility on the electric field or the Arrhenius dependence on temperature. Another major outcome of the model is that it predicts a gate voltage dependent mobility that follows a power law, a behavior that has been indeed observed in polymeric transistors.

### 1.2.2.2 Multiple Trap and Release (MTR) model

An alternative model which describes transport of charges along the localized levels in the vicinity a delocalized band edge is the multiple trapping and release (MTR).<sup>[44]</sup> This is an extension of the classical band transport which includes the presence of localized states (generated by crystal defect or impurities) called traps. Shallow traps are the localized states in the band-gap within approx  $k_B T$  (25meV at 298K) from the edge of the transport band, while deep traps are the states further than  $k_B T$ .<sup>[45]</sup> The basic trapped by a shallow trap with a probability close to one and their release is controlled by thermally activated process. During their transit in the delocalized band, the charge carriers interact with the localized levels through trapping and thermal release.

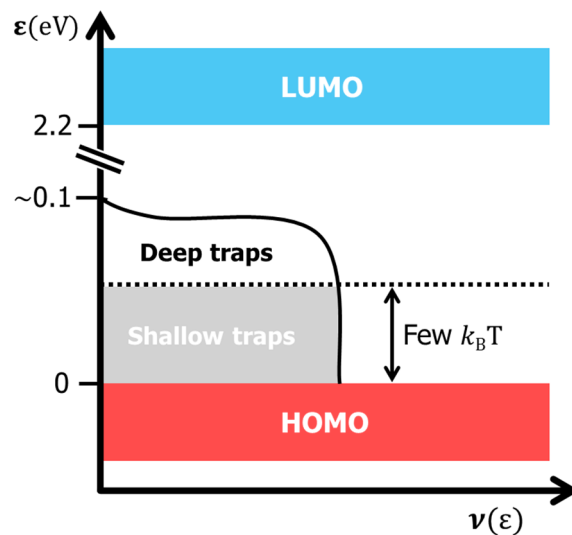


**Figure 1.4:** Electronic states distribution near the HOMO energy in the rubrene crystals. Reproduced from literature. <sup>[45]</sup>

In the case of homogenous dispersed traps, the resulting effective mobility  $\mu_{eff}$  is describe by the following equation:

$$\mu_{eff} = \mu_0 \alpha e^{-\frac{E_c - E_t}{k_B T}} \quad \text{(Equation 1.1)}$$

where  $\mu_0$  is the charge carrier mobility in absence of traps,  $\alpha$  is the ratio between the density of available delocalized states and the trap states and  $E_c - E_t$  is the energy difference between the transport band edge and the single trap level.

The MRT model is an accurate description of charge transport in organic crystals, it is applicable to ordered materials such as vapor deposited small molecules or oligothiophenes, where thermally activated charge transport is often observed. however, MRT model does not apply for disordered films.

### 1.2.3 General structure-electrical properties relationship in organic semiconductors

The molecular structure and assembly of molecular semiconductors in the solid state is directly responsible for the charge transport properties of the material. In particular, the overlap among adjacent orbitals is determined by the packaging of individual moieties within the solid state, which is describe by transfer integrals ( $J$ ); thus, defining the pathway for charge transport. If systems have one large  $J$ , a strong anisotropic transport is observed, being carrier mobilities higher only in a specific direction. Playing on the molecular packaging, the transport anisotropy in a material can be quickly adjusted. Generally, systems with isotropic distribution of transfer integrals show the highest charge carrier mobilities. In crystalline inorganic semiconductors like Si, charge carriers are defined as Block electrons with delocalized wavefunctions extended over the crystalline lattice. Some of the transport signatures observed in these types of materials are also found in molecular crystals, particularly the observation of an ideal Hall signature and the temperature dependence of the mobility, i.e. an observed increase of mobility with decreasing temperature in the temperature range between 150 K and room temperature (RT).<sup>[46]</sup> Nevertheless, using optical spectroscopy on molecular crystals, which is able to probe the electronic states of the carriers faster than those of lattice vibrations, it has been revealed that charge carriers are not spatially fully extended Block electrons in molecular semiconductors.<sup>[47]</sup> This is confirmed by charge modulation spectroscopy experiments which reveal that the induced charge absorptions have an evident molecular character and

are similar to those of radical cations/anions in solution. This suggests that the electron wavefunction is delocalized at its best over small clusters of molecules.<sup>[48]</sup>

At room temperature, high mobilities ( $\mu$ ) for organic crystalline semiconductors are reported to be in the range of 1-20 cm<sup>2</sup> V<sup>-1</sup> s<sup>-1</sup>, which is well below the lower band limit of 50 cm<sup>2</sup> V<sup>-1</sup> s<sup>-1</sup> for the application of Bloch-Boltzmann (band) transport.<sup>[49]</sup> Molecules forming this kind of materials display so large thermal vibrations which allow for quantum microscopic processes beyond the semiclassical description. If a strong molecular disorder is present, the electronic wavefunctions display a pronounced tendency to localization at short times (less than 1 ps), which leads to a sizeable suppression of the charge diffusivity.<sup>[50-51]</sup> Such physical mechanism has been named transient localization (TL). The resulting mobility is described by the following equation:<sup>[52]</sup>

$$\mu = \frac{e L^2}{k_B T 2 \tau_{vib}} \quad \text{(Equation 1.2)}$$

where  $e$  is the elementary charge,  $k_B$  is the Boltzmann constant,  $T$  is the temperature,  $L$  is the TL length and  $\tau_{vib}$  is the timescale of intermolecular motions.

**Equation 1.2** is no longer valid when the disorder becomes so strong that the carriers start to be localized on a single molecular site. In this case, a transition to a thermally activated hopping transport is likely to occur.<sup>[53]</sup> Setting  $L \approx 6 \text{ \AA}$  a typical intermolecular distance, it is possible to estimate the breakdown of the TL regime as  $\mu \lesssim 0.5 \text{ cm}^2 \text{ V}^{-1} \text{ s}^{-1}$ , by considering  $k_{BT} \approx 25 \text{ meV}$  and  $\tau_{vib} = \omega_0^{-1}$ , with  $\hbar\omega_0 \approx 5 \text{ meV}$  within the typical range of intermolecular vibration frequencies in molecular crystals.

In semiconducting polymers, generally to reach better values of carrier mobilities, higher molecular weights are preferred since polymer chains have to be sufficiently long to perform as tie chains able to interconnect adjacent crystalline domains. However, this is only valid until a threshold, exceeding this value the polymer chain twisting starts to induce a detrimental effect and such trend is reversed.<sup>[34]</sup> Generally, polymers showing the highest performances exhibit a degree of energetic disorder approximately of  $k_{BT}$ .<sup>[54-55]</sup> A possible way to quantify such energetic disorder is to determine the Urbach energy, that represents a measure of the width of the tail of the optical absorption near the bandgap. It is noteworthy that a significant lower energetic disorder was found in many high mobility D-A copolymers having a lower degree of crystallinity than well-known semicrystalline polymers such as P3HT or PBTTT. This is supposed to reflect more uniform distribution of conformations of the polymer backbone across the films.<sup>[54]</sup> However, although these

high performing polymer systems shows mobilities which are almost as high as those of the molecular crystals (discussed above), the charge transport is still thermally activated. This generally reflects the presence of a residual static energetic disorder in the density of states due to spatial variations in the conformation of the polymer chain segments that charges encounter as they hop through the network of chains.

In order to understand the charge transport in conjugated polymers, several processes across multiple length scales must be taken into account. Since length scales map onto timescales, this assumption can be deduced experimentally. Indeed, conventional time of flight measurements have demonstrated a pronounced time dependence of carrier mobility in polymers.<sup>[56-57]</sup> Looking at the molecular scale, it is fundamental that charges are capable of delocalizing and move on the chains. The transport along single chains occur in a short period of time of less than 10 ps. In terms of mobility, on-chain transport are found to be up to  $600 \text{ cm}^2 \text{ V}^{-1} \text{ s}^{-1}$  in polymers.<sup>[58]</sup> Finally, at the end of a chain or in correspondence of kinks, which serve as structural traps, charges will ultimately move from one chain to another chain. As consequence, another key aspect that influences the mobility is the mesoscale (10–100 nm) arrangement of transport paths.

### ***1.2.3.1 Charge transport in semi-crystalline polymers***

The microstructure of high molecular weight poly(3-hexylthiophene) P3HT, a well-known semicrystalline conjugated polymer, shows continuous dissimilarity in order parameters, <sup>[59-60]</sup> indeed it comprises both amorphous and semi-ordered regions. The ordered parts can consist of both small domains wherein the molecular units are ordered in a short-range manner or large domains having long-range periodicity in all three spatial dimensions such as crystallites. In semicrystalline microstructures, typically charges are mainly restricted to the ordered regions, wherein there is high conjugation length and the molecular coupling.<sup>[61]</sup> Therefore, when charges go from a crystalline regions to another one crossing the in-between amorphous region, they experience an injection barrier. On top of this, charges are slowed down by the intrinsic slower transport in amorphous microstructures than in crystallites. Thus, it is a real disadvantage in terms of transport to cross amorphous regions. Only when rather straight tie chains bridge crystallites, the latter are considered to be properly electrically connected. This implies that the distance between crystallites shall not be longer than the polymer persistence length.<sup>[62]</sup> Only in these conditions, charges can effectively go from crystal to crystal without obstacles caused by the presence of amorphous intercrystallite regions. Recently, studies on blends of

polythiophene batches having different molecular weights have revealed and confirmed the great importance of tie chains.<sup>[63]</sup> Indeed, it has been demonstrated that when the fraction of tie-chains is beyond  $\sim 10^{-4}$ , the effectiveness of transport is increased no matter the details of the chain lengths and distributions in the polymer. Furthermore, at bigger length scales of hundreds of nanometres to micrometres, a high mobility in semi-crystalline microstructures is gained when charges can go from crystal to crystal without entanglements or unexpected changes in the polymer backbone direction.

### *1.2.3.2 Effect of disorder on transport properties*

In the case of semi-crystalline polymers, charge transport occurs in ordered regions since the movement of charge from ordered to amorphous areas is hindered by a strong energy barrier. It is imperative to study the impact of structural defects inside ordered regions to comprehend the effect of disorder on electronic properties. Any inconsistencies in the structure lead to inconsistencies in energy. Furthermore, the disordered structure also has an impact on the transfer of charges between molecules. Indeed, it is not uncommon to observe charge localization as a result of disorder.<sup>[64-65]</sup> Therefore, in semiconducting polymers, it is necessary to understand the process of transportation of charges in intermediate disorder regimes. In the case of an imperfect crystal, the structural disorder is the result of the arbitrary variation in the lattice spacings, which is described by the paracrystallinity parameter  $g$ , i.e the standard deviation of local static lattice fluctuations normalized by the average value of the lattice spacing.<sup>[66]</sup> As stated above, in a polymer, the backbone direction implies the strongest electronic coupling and highest mobility. However, in any device, the polymer needs to establish intermolecular transport of charges since an individual chain will not suffice to enable transportation on a macroscopic level. Therefore, the disorder in the  $\pi$ -stacks becomes especially important as it is an extremely significant direction which favors intermolecular charge transfers. In the  $\pi$ -stacks, paracrystallinity leads to the formation of deep tails of electronic states in the bandgap of the material having energy width proportional to  $g^2$ .<sup>[67]</sup> In disordered stacks, the states that are formed due to the disorder are situated deeper in the DOS tail and are highly localized. As paracrystallinity increases, even the states which are situated within the 'delocalized band' begin to become localized. The demarcation between band and tail states begins to blur in the limit of large positional disorder ( $g \sim 10\%$ ) and, in this condition, a single broad distribution of localized states which resembles electronic structure of amorphous materials is observed.<sup>[68-69]</sup> When localized and the delocalized states coexist, an

intermediate paracrystallinity regime ( $g \sim 3-7\%$ ) is observed. This depicts the fact that in the case of paracrystalline aggregates, the transport takes place by mobile charges transiently being entrapped in localized states and the subsequent release (multiple trap and release model).<sup>[70]</sup>

### ***1.2.3.3 Paracrystallinity in conjugated polymers***

Organic solids are not intrinsically disordered system, as observed in small-molecule film. However, the paracrystallinity in the  $\pi$ -stacking direction increases going from oligomer to a high-molecular-weight polymer. The parameter  $g$  keeps increasing with the addition of monomers until the paracrystallinity becomes independent to molecular length. The high-mobility, high-molecular-weight polymers are more amorphous than crystalline in the direction of interchain transport, with  $g \sim 10-20\%$ , regardless the lamellar stacking configurational order. Indeed, the effect of high molecular weight on paracrystalline disorder substantiates that the defects are potentially a result of chain folding and entanglements.<sup>[71]</sup> The  $\pi$ -stack order may also be affected by the side-chain conformational disorder. In the low-molecular-weight connectivity-limited regime, the impact of molecular weight on disorder as well as on mobility establishes that the charge transport properties are tight associated to the lattice disorder. However, at high molecular weight, the lattice disorder as well as the carrier mobility become independent of chain length. In semi-crystalline polymers, this translate into a regime of tie-chain where long polymer chains lead to a proper transfer of charges through effective bridges between ordered regions. This regime comes together with an intrinsic high degree of disorder in the structure.

Over the past few years, not only semicrystalline conjugated polymers, which have dominated the research field for about 20 years, have been studied but also other more rigid, fused-ring polymer, especially donor-acceptor (D-A) copolymers with alternating electron-rich and electron-deficient units though the backbone of the polymer. This new class of polymers has drawn the attention of the scientific community for its apparently controversial characteristics. These polymers cannot be classified either as semicrystalline or amorphous as they exhibit a mobility similar to semicrystalline polymers, but they bear a structural resemblance to amorphous materials. Indeed, on one hand, they have a higher level of long-range disorder in comparison to semicrystalline polymers, which can be substantiated by several factors including lower diffracted intensities, a low number of diffraction peaks, along with a large breadth of their  $\pi$ -stacking peak. On the other hand,

they display characteristics similar to semi-crystalline polymers in terms of activation energies and trap width. They can be defined as semi-amorphous polymers having an adequate short-range order.<sup>[72]</sup> The latter is enough to allow an efficient charge transfer between molecules. Examples of these materials are copolymers based on more complex moieties, such as carbazoles (PCDTBT).

All these aspects result in the polymeric semiconductors being categorized into two types. The first one is the amorphous material which does not have long-range order. The charge transport is heavily restricted in amorphous materials due to the hopping between localized states in a broad DOS. In such a case, the mobility is typically limited to  $<0.1 \text{ cm}^2 \text{ V}^{-1} \text{ s}^{-1}$  while coupled with high activation energies.<sup>[73]</sup> The second category consists of materials which are capable of enabling at least short-range-order by forming interconnected aggregates. In such case, charge transport is usually described by trapping and releasing mechanism. The aggregating materials are further subcategorized based on the aggregation distance. Semi-crystalline materials usually demonstrate long-range order in the  $\pi$ -stacking direction in the range of tens of nanometers. Conversely, semi-amorphous polymers can form aggregates which enable intermolecular charge transport locally despite the disordered nature in their  $\pi$ -stacks. Such short-range order at the segmental level suffices for effective charge transportation. In the case of high-molecular-weight polymers, regardless of whether they are amorphous or semicrystalline, they consistently exhibit high disorder in the  $\pi$ -stacking direction which results to the formation of traps in the DOS.

#### 1.2.4 Polarons and bipolarons in semiconducting polymers

In the year 1977, researchers have found a way to increase polyacetylene conductivity to a high value ( $10^3 \text{ cm}^{-1}$ ) by exposing it to oxidizing or reducing agents. <sup>[74]</sup> This specific method is commonly known as ‘doping’ corresponding to the doping of inorganic semiconductors or can also be viewed as a redox reaction. ‘Doping’ involves the transfer of a neutral polymer to an ionic complex which consists of a polymeric cation or anion along with a counterion. The latter is either the reduced form of the oxidizing agent or the oxidized form of the reducing agent. In the case of inorganic semiconductors, when an oxidizing agent is used, the doping process is p-type. Similarly, the use of a reducing agent is called n-type doping. The reactions involving oxidation or reduction only affect the  $\pi$ -

electrons, while the  $\sigma$ -electrons continue to hold the polymer together. The charge is capable of moving along the  $\pi$ -conjugated chain.<sup>[75]</sup> **Figure 1.5** illustrates a schematic diagram of poly(alkylthiophene) chain's oxidation process, wherein a charge is introduced.

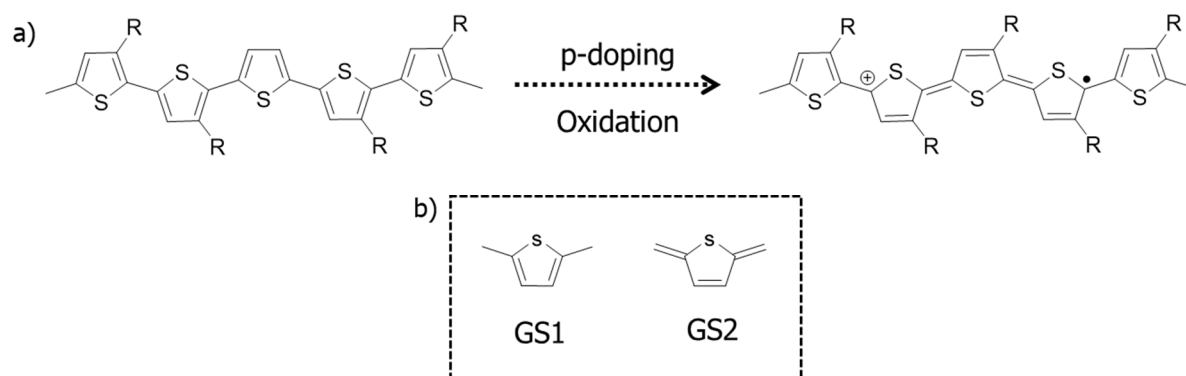


**Figure 1.5:** a) Creation of a polaron in a neutral poly(alkylthiophene) chain by oxidation (p-doping). b) Non-degenerated ground states of poly(thiophene).

In an organic semiconductor, the presence of a charge on the polymer backbone may lead to formation of a polaron, through the interaction of the charge with the surrounding environment where the former has the tendency to polarize the latter. Conjugated polymers are capable of changing the conformation near the charge, which inorganic semiconductors cannot do. The non-ionized state and the ionized state do not vary in geometry in the case of organic polymers. Thus, the polymer lattice can be distorted by introducing a charge in the polymer chain. A polaron is a quasi-particle which is used to describe the interaction between the charges and the atoms in any material. Landau<sup>[76]</sup> and Pekar<sup>[77]</sup> were the first to introduce the concept, in reference to inorganic materials. Later Holstein,<sup>[78]</sup> with the know small-polaron model, included the concept in the study of organic compounds. Therefore, polaron transport is nothing but a moving charge in an organic material which is surrounded by a polarization cloud. The polarization cloud is subjected to oscillations of multiple atoms with a specific vibration, called phonon, and leads to electron-phonon coupling. This coupling tends to act on the charge's localization length within a molecular system. A weak coupling leads to the delocalization of the charge over a few molecules whereas a strong coupling localizes the charge which decreases the charge carrier's mobility and increases the electron's effective mass.

**Figure 1.5a** shows that the backbone of polymer is divided by charge into areas having different ground states. In poly(thiophene), due to the quinoid state holding higher energy than the other ground states, the two states are not degenerated (**Figure 1.5b**). Further, it

is possible to restrict lattice degeneration to a specific number of monomeric units, hence, polarons are self-localized charged species.

If a charge is introduced in a polymer chain, one can observe a change in the energy levels of the neutral polymer chain's highest occupied molecular orbital (HOMO) and the lowest unoccupied molecular orbital (LUMO).

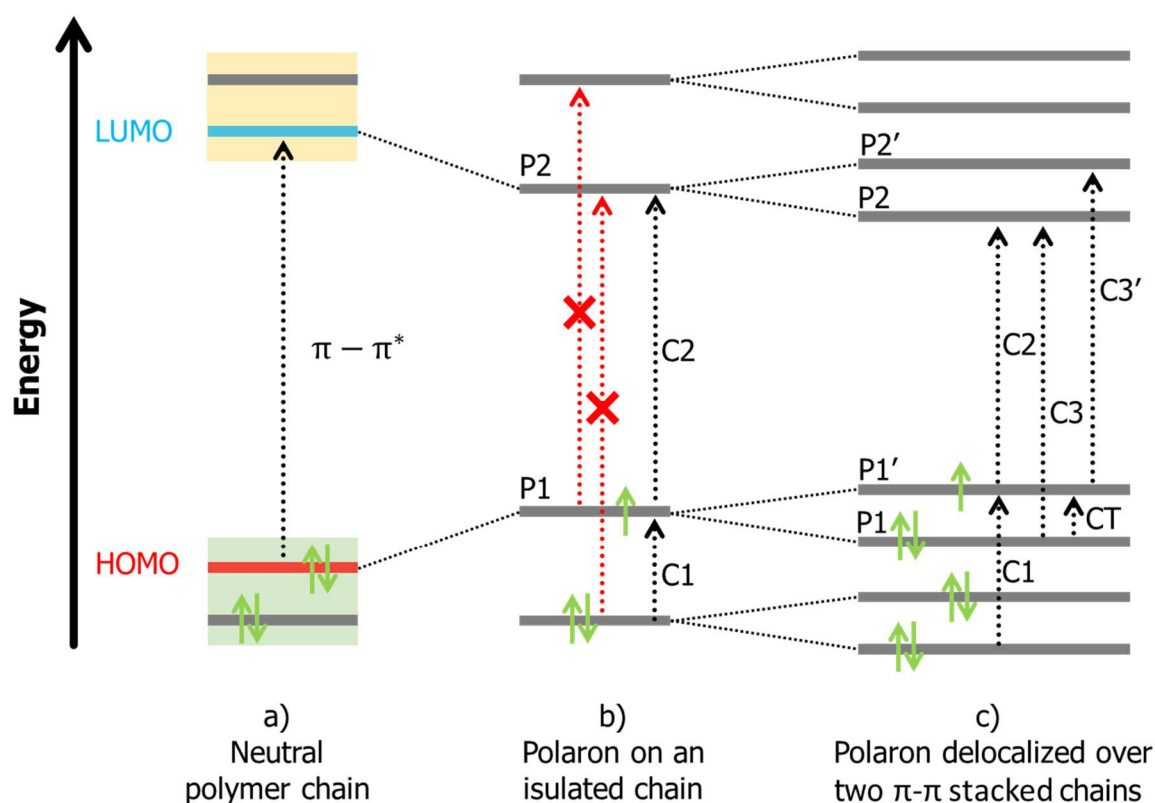


**Figure 1.6:** Energy levels diagram of a neutral polymer chain, a polaron on an isolated chain and a polaron delocalized over two  $\pi$ - $\pi$  stacked chains. Forbidden transitions are indicated with dotted red arrows. [79]

In **Figure 1.6a** one can observe a neutral thiophene chain's energy levels, along with the valence band and the conduction band. An energy gap exists between the HOMO and the LUMO wherein no states are allowed. When a transition occurs from the HOMO to the LUMO states, it is known as  $\pi$ - $\pi^*$  transition. **Figure 1.6b** depicts the process of the removal of an electron from an organic semiconductor's conjugated chain, specifically from its HOMO. This leads to the generation of a positively charged polaron. Two new electronic states, known as polaronic levels P1 and P2, are formed within the polymer's band gap. These energy states have parity which may either be even or odd. Transitions can only

occur if they also cause a change in parity. In an alkylthiophene chain with a polaron, transitions depicted in **Figure 1.6b** using slashed black arrows are permitted, while arrows using red dots are used to represent forbidden transitions. In a neutral polymer, the polaronic absorptions involves a reduction in energy as compared to a  $\pi$ - $\pi^*$  absorption in **Figure 1.6a**.

As already described in **Figure 1.4**, in polymers, the charge transport can either be intramolecular or intermolecular in nature and for the latter transition, the charge carriers need to jump from one polymer chain to another. H. Sirringhaus<sup>[80]</sup> found that, in P3HT, which is a polymer with high inter-chain interaction, polarons are spread across multiple  $\pi$ -stacked chains, instead of being restricted to just one. In the case of a dimer which is cofacial, polaron delocalizes over two chains, which causes the polaronic levels to be distributed as doublets, which is illustrated in **Figure 1.6c**. Thus, this leads to two new charge transfer transitions, CT and C3/C3'.<sup>[79]</sup> **Figure 1.6c** does not depict transitions which are forbidden symmetrically.

### 1.3 Photochromism

The word Photochromism derives from two Greek words, **φωτός** (photos) and **χρώμα** (chroma) which respectively mean light and color. <sup>[81]</sup> Not surprisingly, photochromism is defined as a light-induced reversible transformation of a chemical species between two isomers having different absorption spectra. <sup>[82-84]</sup> If we consider the two stable forms of a chemical species, X and Y, upon irradiation, the thermodynamically stable form X is transformed into form Y. Then, the back reaction from Y to X can either occur thermally, giving rise to the photochromism of type T, or photochemically, inducing the photochromism of type P. <sup>[85]</sup> Both states, X and Y, feature markedly different properties at the molecule level.<sup>[86]</sup>

In general, light is a highly interesting external stimulus due to a number of advantages: i) it is non-invasive, ii) it is an endless source of energy, iii) it can be applied over long distances and at highly speed, iv) it can easily be tuned in terms of intensity as well as photon energy, v) an exceptionally high time resolution can be achieved using laser techniques. The versatility of materials based on photochromic substances has led to their use in many useful applications, from glass lenses to trendy cosmetics and clothes.<sup>[87-89]</sup> Nowadays, with the rising of the digital age, photochromic materials are also exploited in other fields related to the transmission, release, and storage of digital data.<sup>[90-91]</sup> For instance, photochromic species meet the requirement of rewritable recording media and are thus found in CD-RW and DVD-RW, where upon request, memory bits have to swap (commute) between the two binary states (“0” and “1”).<sup>[92-94]</sup> In these devices, like in photochromic systems, light writes (and erases) information, which are then read using optical properties. Considering that the information needs to be written at erased at high speed, photochromic systems are suited for fast switching as changes take place in sub-nanosecond timescales. Another advantage of a memory device based on photochromic systems is that the memory density can potentially reach a value of more than  $10^{18}$  bitmm<sup>-3</sup>, as the elemental switching unit is the photochromic molecule itself, which is comparable to a bit and occupies less than a cubic nanometer.<sup>[95-98]</sup>

In general, to achieve functional systems of technological relevance, the employed photochromic compounds must be improved and optimized in terms of the desired property change, their switching efficiency and resistance to fatigue. i.e. the highest stress over a large number of switching cycles that a photochromic material can withstand without breaking. <sup>[7]</sup>

### 1.3.1 Organic photochromic molecules

Compared to inorganic systems, such as silicon-based materials, the broad variety of organic molecules display peculiar features, such as flexibility, transparency, solubility in various solvents and chemical reactivity.

Most of the recent studies on organic photochromism deal with a group of less than 10 families of compounds. Among these molecules, azobenzenes,<sup>[99-103]</sup> spiropyrans<sup>[104-105]</sup> and diarylethenes<sup>[90, 106-107]</sup> have been exploited in combination with organic semiconductors. They have drawn the most attention thanks to their excellent performance and extensive utility. These families of photochromic molecules typically all require the use of high-energy UV light to trigger their photochemical reactions. Azobenzenes have been particularly employed for their change in volume, upon irradiation, resulting from a trans to a bulkier cis isomerization.<sup>[108]</sup> Spiropyrans have been mostly used because they exhibit the added benefit of a solubility switch upon irradiation, i.e. a conversion from a hydrophobic to a hydrophilic form.<sup>[109]</sup> These two traditional molecules are classified into T type (thermally reversible) photochromic molecules, as the photogenerated colored isomers, upon irradiation with Ultraviolet (UV) light, are thermally unstable, and the colors disappear in the dark at room temperature (RT). On the other hand, diarylethene (DAE) molecules are classified into P-type photochromic compounds, i.e. thermally irreversible but photochemically reversible. DAEs are one of the most important families of photochromic compounds composed of two aromatic moieties, typically thiophene groups, at the two sides of an olefinic bond, which is rigidified by a cyclopentane unit (**Figure 1.7a**). Upon irradiation of the open-form isoform with UV-light, a new bond is formed, due to the delocalization in the conjugated system, with generation of the closed-form isomer. The different  $\pi$ -electronic structures of the isomers induce a marked alternation of the HOMO and LUMO energy levels, and thus the conversion from a colorless isomer (open-form isomer) into a colored one (closed-form isomer), as reported in **Figure 1.7b** for DAE-Me as example. The new photogenerated colored isoform is thermally stable, i.e. it does not return to its open colorless form in the dark at RT, but it will return to its original state upon irradiation with visible light.<sup>[110]</sup>

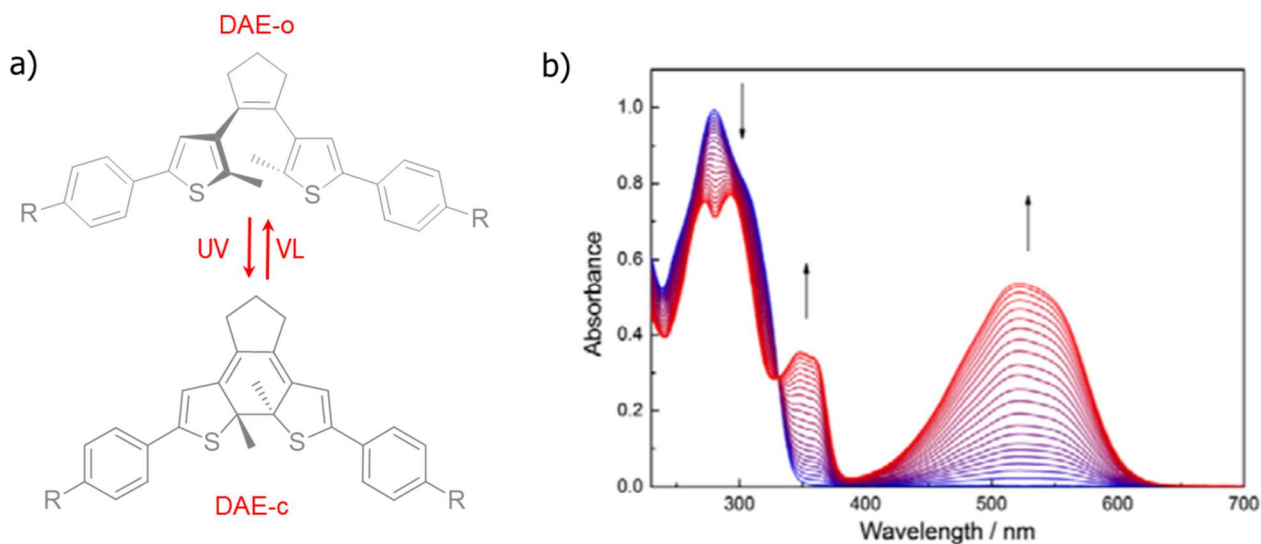


**Figure 1.7:** a) Chemical formula of the photochromic molecule DAE in the two stable switching states, DAE-opened (DAE-o) and DAE-closed (DAE-c); b) UV/Vis absorption spectra of DAE-Me during the course of irradiation ( $\lambda_{UV} = 313$  nm) until reaching the photostationary state (PSS). Reproduce from literature.<sup>[111]</sup>

In general, the photochemical interconversion between the two isoforms of DAEs is highly efficient, both isoforms are stable, and possess an outstanding fatigue resistance. In addition, DAEs only undergo a small structural change during the isomerization reaction, i.e. the geometrical difference between the ring-open isomer and the ring-closed isomer is only very small, in contrast to many other photochromic compounds such as azobenzenes. Therefore, the steric hindrance does not change, and the switching can be performed in a tightly packed space.<sup>[112-113]</sup> Overall, the outstanding feature of DAEs is the pronounced change of their  $\pi$ -electronic system during the isomerization reaction accompanied by a significant alternation of electronic levels and thus redox potentials.

## 1.4 Ferroelectricity

When a uniform external electric field is applied to a dielectric material, local dipoles are produced inside the material because negative charges are shifted in one direction while the positive ones in the opposite. This displacement of positive and negative charges results into the polarization of the dielectric material as expressed in the following equation:

$$D = \epsilon_0 E + P \quad \text{(Equation 1.3)}$$

where  $P$  is the polarizability and  $\epsilon_0$  the vacuum permittivity.

Therefore, the polarization is a measure of the electrical dipoles induced by such movement of charges inside the dielectric. The sum of all products between distance of charges and charge itself represents the electric dipole moment, while the total dipole moments per unit of volume represents the polarization  $P$ . The average charge inside the material is zero, however at the boundary perpendicular to the electric field there is a net positive (negative) charge which is not compensated. Therefore, the induced polarization creates a depolarization field that is an electric field in the opposite direction of the polarization (**Figure 1.8a**), which tends to bring the displaced charges back to their equilibrium position after removing the external field. This results in an almost linear dependency (without any significant hysteresis) of charge displacement (or polarization) versus the external electric field, as shown in **Figure 1.8b**.<sup>[114]</sup>

However, some materials can have intrinsic dipole moments that are not induced by any electric field. When an electric field is applied to such materials, a spontaneous polarization arises, that can be switched with the direction of applied field. In 1921 this previously unaccounted phenomena, subsequently called ferroelectricity, was discovered in Rochelle salt ( $\text{KNa}(\text{C}_4\text{H}_4\text{O}_6)_4\text{H}_2\text{O}$ ).<sup>[115]</sup> When the electric field is removed, ferroelectric materials exhibit a remnant polarization  $P_r$ , similarly to ferromagnetic materials. This polarization corresponds to the distortion of the spontaneous polarization loops resulting in the typical electric hysteresis as shown in **Figure 1.8c**.

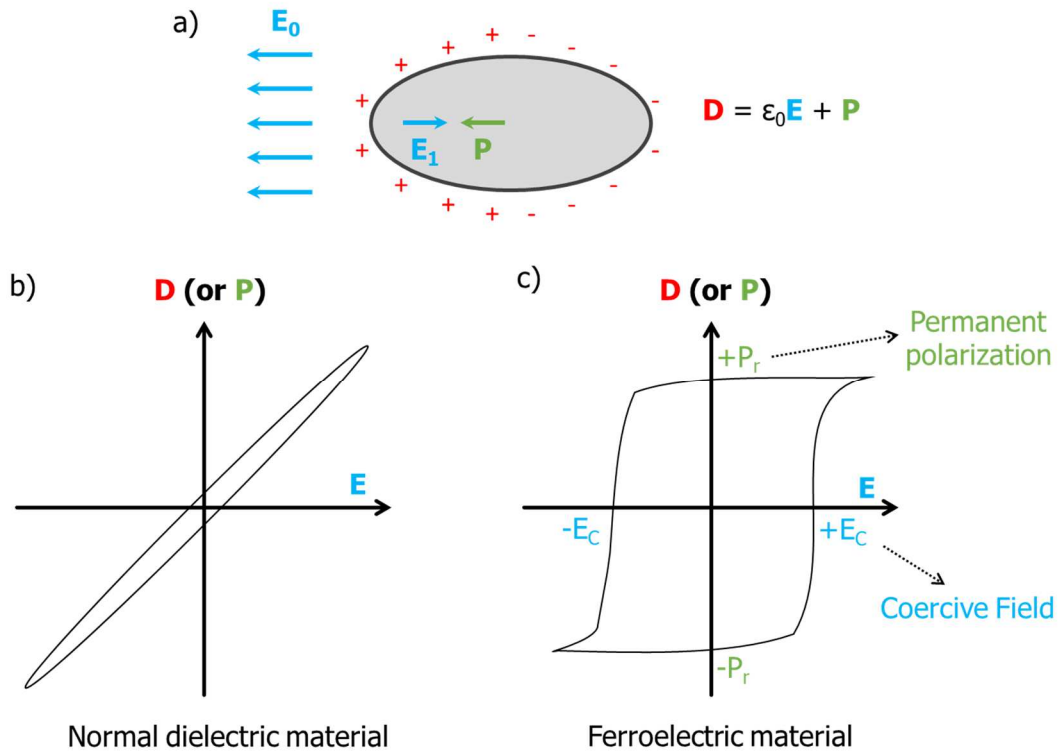


**Figure 1.8:** a) Sketch of the dielectric material exposed to external electric field  $E_0$ . Schematic plots of displacement (or polarization) loop in a) a normal dielectric, and b) a ferroelectric material.

The term “ferroelectricity” was created specifically because of the similarity between the electrical qualities of ferroelectrics and the magnetic qualities of ferromagnets. The dielectric displacement,  $D$ , and Polarization,  $P$ , of ferroelectrics generally follow the electric field  $E$  in a similar way as the magnetic field,  $B$ , and Magnetization,  $M$ , of ferromagnets transform-with the magnetizing field,  $H$ .

The remnant polarization in ferroelectric materials stems from the alignment of intrinsic dipole moments within a crystalline material.<sup>[116]</sup> On one hand, although mobile charges within a permeable dielectric can accomplish an electric hysteresis as well, these charges are not thermally stable and will go back to equilibrium after a while when one removes the field that was applied. On the other hand, intrinsic dipole moments in amorphous material will devise a random orientation, thus rendering a zero-net polarization. Therefore, only crystalline materials with such a nature that the dipole moments do not completely neutralize one another can exhibit ferroelectricity.

Certain ferroelectrics display a phase transition at elevated temperatures. At the so-called Curie temperature ( $T_c$ ), the crystalline configuration of the material changes from a low temperature polarized state to a stable high temperature unpolarized state.

Ferroelectrics comprise a coercive field ( $E_c$ ), which is basically described as the minimum field necessary to complete full polarization switching. This switching of polarization has to occur below the dielectric breakdown field of the material and it depends on temperature as well as the applied field. The switching mechanism usually includes the nucleation and growth of ferroelectric domains in which all dipole moments are evenly oriented. A spontaneous ferroelectric polarization initiates a depolarization field, similar to dielectric polarization.<sup>[114]</sup>

The ferroelectric properties of any material are observable from charge displacement versus field measurements on capacitors, as shown in **Figure 1.8c**. At low fields, the applied field is unable to initiate the domains nucleation and growth and, in such case, only a linear dielectric displacement will be observed. At field strengths close to the coercive field, the ferroelectric begins to polarize; at higher fields, it saturates since the maximum quantity of polarized domains within the material is achieved. In saturation regime, intersections with the *E*-axis and the *P*-axis in **Figure 1.8c** are respectively recognized as the coercive field and the remnant polarization of the material.

Ferroelectric material have been utilized in many applications.<sup>[117]</sup> Among them, memory application is one of the most promising. Memory devices use hysteresis by correlating the polarization states +Pr and -Pr with a Boolean 1 and 0 that forms the basis for most logic circuits utilized today.<sup>[118]</sup> The polarization states-in a ferroelectric thin-film capacitor with can fundamentally be maintained for an immeasurable length of time.<sup>[116]</sup> This facet of ferroelectricity is one of the principle reasons for its appeal in the creation of memory applications. However, in practice, there can be defective layers at the interface between ferroelectric and the metal layer that can affect the polarization retention. This depolarization effect becomes more prominent as the thickness of the ferroelectric film decreases. Ferroelectricity can also be unfavorably influenced by other factors such as conductivity within the ferroelectric or as charges that are trapped at the interfacial surface.

#### 1.4.1 Organic ferroelectrics

Most of the applications related to organic ferroelectric materials relies on PVDF [polyvinylidene fluoride;  $(\text{CH}_2\text{CF}_2)_n$ ] and its copolymer P(VDF-TrFE) [poly(vinylidene fluoride-trifluoroethylene);  $(\text{CH}_2\text{CF}_2)_n-(\text{CHF}\text{CF}_2)_m$ ]. The molecular structure of P(VDF-TrFE) is shown in **Figure 1.9a**.

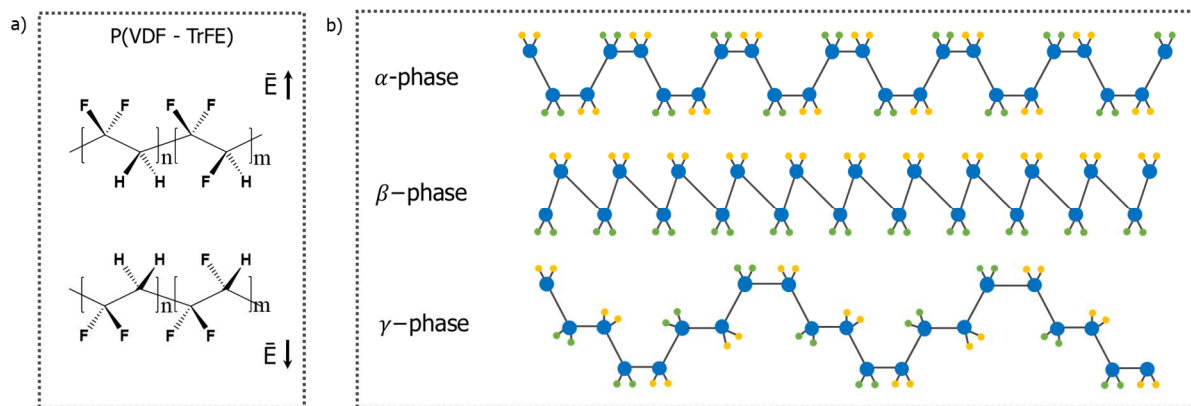


**Figure 1.9:** a) Chemical structure and b) crystalline phases of PVDF-TrFE.

A variety of additional organic ferroelectric materials do exist, but PVDF possess a number of beneficial properties, including a large remnant polarization, a short switching time and an above average thermal stability.<sup>[119]</sup> The ferroelectricity of PVDF originates from the dipole moments within in the VDF molecules that can be aligned with the applied field by rotating the polymer backbone, as shown in **Figure 1.9a**. The dipole moments primarily stem from the presence of the electro-negative fluorine atoms. A large number of references on ferroelectric properties and material features of PVDF are present in literature.<sup>[120]</sup>

Solution-processed PVDF thin-films are not ferroelectric since the crystalline structure and stereo-chemical compound are such that the dipole moments cancel each other out.<sup>[121]</sup> In order to impart ferroelectric property to the film, a stretching procedure to force the polymer into a different conformation is required. This can be done by using PVDF-TrFE instead of PVDF. Films of PVDF-TrFE are ferroelectric directly after solution deposition due to the steric hindrance coming from the additional fluorine atoms of PTrFE which induce an all-trans stereochemical conformation. Such conformation allows the direction of the dipole moments to be aligned. PVDF-TrFE thin-films do necessitate an annealing step at high temperature (higher than 130°C) in order to increase the crystalline microstructure of this material and augment its ferroelectric behavior at the same time.<sup>[122]</sup> This annealing phase does not restrict the usage of PVDF-TrFE for any applications since this temperature is compatible with a large variety of substrates and organic-electronic materials. The endurance of PVDF-TrFE and its overall viability for electronic device applications is apparent from its extensive use for piezoelectric sensors and actuators. PVDF and P VDF-TrFE need no distinctive logistic safeguards.

Prospects for the creation of a stable memory technology grounded on PVDF-TrFE already came to vision more than two decades ago.<sup>[123]</sup> However, this has not yet culminated into any profitable memory products. On the other hand, memory equipment that utilize inorganic ferroelectric materials have been commercially available for longer than a decade.<sup>[116]</sup> However, this could easily change in the next few years, given the fact that numerous companies report and patent applications highlighting the advance stage of development for ferroelectric polymer-based memory technology.<sup>[124]</sup> This upholds the stance of the technological world that there is a significant potential for organic nonvolatile memory technologies based on ferroelectricity.

## References

- [1] D. Miorandi, S. Sicari, F. De Pellegrini, I. Chlamtac, *Ad hoc networks* **2012**, 10, 1497.
- [2] A. Agrawal, J. Gans, A. Goldfarb, *What to expect from artificial intelligence*, MIT Sloan Management Review, **2017**.
- [3] Q. Zhang, Z. Xia, Y.-B. Cheng, M. Gu, *Nat Commun* **2018**, 9, 1.
- [4] G. Yeap, S. Lin, Y. Chen, H. Shang, P. Wang, H. Lin, Y. Peng, J. Sheu, M. Wang, X. Chen, presented at 2019 IEEE International Electron Devices Meeting (IEDM) **2019**.
- [5] A. P. Godse, U. Bakshi, *Solid State Devices and Circuits*, Technical Publications, **2009**.
- [6] M. H. Miraz, M. Ali, P. S. Excell, R. Picking, presented at 2015 Internet Technologies and Applications (ITA) **2015**.
- [7] E. Orgiu, P. Samori, *Adv Mater* **2014**, 26, 1827.
- [8] Q. Miao, M. Lefenfeld, T. Q. Nguyen, T. Siegrist, C. Kloc, C. Nuckolls, *Adv Mater* **2005**, 17, 407.
- [9] J. E. Anthony, *Chem Rev* **2006**, 106, 5028.
- [10] R. Schmidt, M. M. Ling, J. H. Oh, M. Winkler, M. Könemann, Z. Bao, F. Würthner, *Adv Mater* **2007**, 19, 3692.
- [11] V. Palermo, P. Samori, *Angewandte Chemie International Edition* **2007**, 46, 4428.
- [12] S. Sergeev, W. Pisula, Y. H. Geerts, *Chem Soc Rev* **2007**, 36, 1902.
- [13] I. McCulloch, M. Heeney, M. L. Chabinyc, D. DeLongchamp, R. J. Kline, M. Cölle, W. Duffy, D. Fischer, D. Gundlach, B. Hamadani, *Adv Mater* **2009**, 21, 1091.
- [14] C. Li, M. Liu, N. G. Pschirer, M. Baumgarten, K. Mullen, *Chem Rev* **2010**, 110, 6817.
- [15] M. Gsänger, J. H. Oh, M. Könemann, H. W. Höffken, A. M. Krause, Z. Bao, F. Würthner, *Angewandte Chemie International Edition* **2010**, 49, 740.
- [16] W. Y. Lee, J. H. Oh, S. L. Suraru, W. C. Chen, F. Würthner, Z. Bao, *Adv Funct Mater* **2011**, 21, 4173.
- [17] G. De Luca, W. Pisula, D. Credgington, E. Treossi, O. Fenwick, G. M. Lazzerini, R. Dabirian, E. Orgiu, A. Liscio, V. Palermo, *Adv Funct Mater* **2011**, 21, 1279.
- [18] T. M. Figueira-Duarte, K. Mullen, *Chem Rev* **2011**, 111, 7260.
- [19] Y. Diao, B. C. Tee, G. Giri, J. Xu, D. H. Kim, H. A. Becerril, R. M. Stoltenberg, T. H. Lee, G. Xue, S. C. Mannsfeld, *Nat Mater* **2013**, 12, 665.
- [20] A. Facchetti, *Nat Mater* **2013**, 12, 598.
- [21] N. D. Treat, J. A. N. Malik, O. Reid, L. Yu, C. G. Shuttle, G. Rumbles, C. J. Hawker, M. L. Chabinyc, P. Smith, N. Stingelin, *Nat Mater* **2013**, 12, 628.
- [22] C. B. Nielsen, M. Turbiez, I. McCulloch, *Adv Mater* **2013**, 25, 1859.
- [23] I. McCulloch, *Adv Mater* **2013**, 25, 1811.
- [24] K. J. Yoon, Y. Kim, C. S. Hwang, *Advanced Electronic Materials* **2019**, 5, 1800914.
- [25] R. Menon, *current science* **2000**, 79, 1632.
- [26] G. Meller, T. Grasser, *Organic electronics*, Springer, **2009**.
- [27] F. Eder, H. Klauk, M. Halik, U. Zschieschang, G. Schmid, C. Dehm, *Appl Phys Lett* **2004**, 84, 2673.
- [28] C. Drury, C. Mutsaers, C. Hart, M. Matters, D. De Leeuw, *Appl Phys Lett* **1998**, 73, 108.
- [29] W. Clemens, W. Fix, J. Ficker, A. Knobloch, A. Ullmann, *Journal of Materials Research* **2004**, 19, 1963.
- [30] G. Baccarani, P. Ostojia, *Solid State Electronics* **1975**, 18, 579.
- [31] R. J. Kline, M. D. McGehee, E. N. Kadnikova, J. S. Liu, J. M. J. Frechet, M. F. Toney, *Macromolecules* **2005**, 38, 3312.
- [32] R. J. Kline, M. D. McGehee, E. N. Kadnikova, J. S. Liu, J. M. J. Frechet, *Adv Mater* **2003**, 15, 1519.

- [33] J.-H. Huang, F.-C. Chen, C.-L. Chen, A. T. Huang, Y.-S. Hsiao, C.-M. Teng, F.-W. Yen, P. Chen, C.-W. Chu, *Org Electron* **2011**, 12, 1755.
- [34] H. Yan, Z. Chen, Y. Zheng, C. Newman, J. R. Quinn, F. Dötz, M. Kastler, A. Facchetti, *Nature* **2009**, 457, 679.
- [35] P. M. Beaujuge, H. N. Tsao, M. R. Hansen, C. M. Amb, C. Risko, J. Subbiah, K. R. Choudhury, A. Mavrinskiy, W. Pisula, J.-L. Brédas, *J Am Chem Soc* **2012**, 134, 8944.
- [36] J. Mei, D. H. Kim, A. L. Ayzner, M. F. Toney, Z. Bao, *J Am Chem Soc* **2011**, 133, 20130.
- [37] A. J. Kronemeijer, E. Gili, M. Shahid, J. Rivnay, A. Salleo, M. Heeney, H. Sirringhaus, *Adv Mater* **2012**, 24, 1558.
- [38] Y. Yamashita, *Science and technology of advanced materials* **2009**, 10, 024313.
- [39] A. J. Heeger, *Chem Soc Rev* **2010**, 39, 2354.
- [40] S. M. Sze, K. K. Ng, *Physics of semiconductor devices*, John Wiley & sons, **2006**.
- [41] G. Bieri, F. Burger, E. Heilbronner, J. P. Maier, *Helvetica Chimica Acta* **1977**, 60, 2213.
- [42] E. Collini, G. D. Scholes, *Science* **2009**, 323, 369.
- [43] M. Vissenberg, M. Matters, *Phys Rev B* **1998**, 57, 12964.
- [44] G. Horowitz, *Journal of materials research* **2004**, 19, 1946.
- [45] V. Podzorov, E. Menard, A. Borissov, V. Kiryukhin, J. A. Rogers, M. Gershenson, *Phys Rev Lett* **2004**, 93, 086602.
- [46] M. Gershenson, V. Podzorov, A. Morpurgo, *Reviews of modern physics* **2006**, 78, 973.
- [47] H. Yada, R. Uchida, H. Sekine, T. Terashige, S. Tao, Y. Matsui, N. Kida, S. Fratini, S. Ciuchi, Y. Okada, *Appl Phys Lett* **2014**, 105, 155\_1.
- [48] A. Y. Meneau, Y. Olivier, T. Backlund, M. James, D. W. Breiby, J. W. Andreasen, H. Sirringhaus, *Adv Funct Mater* **2016**, 26, 2326.
- [49] S. Fratini, S. Ciuchi, *Physical Review Research* **2020**, 2, 013001.
- [50] A. Troisi, G. Orlandi, *Phys Rev Lett* **2006**, 96, 086601.
- [51] S. Ciuchi, S. Fratini, D. Mayou, *Phys Rev B* **2011**, 83, 081202.
- [52] S. Fratini, D. Mayou, S. Ciuchi, *Adv Funct Mater* **2016**, 26, 2292.
- [53] F. Ortmann, F. Bechstedt, K. Hannewald, *physica status solidi (b)* **2011**, 248, 511.
- [54] D. Venkateshvaran, M. Nikolka, A. Sadhanala, V. Lemaire, M. Zelazny, M. Kepa, M. Hurhangee, A. J. Kronemeijer, V. Pecunia, I. Nasrallah, *Nature* **2014**, 515, 384.
- [55] Y. Xu, H. Sun, W. Li, Y. F. Lin, F. Balestra, G. Ghibaudo, Y. Y. Noh, *Adv Mater* **2017**, 29, 1702729.
- [56] A. Devižis, K. Meerholz, D. Hertel, V. Gulbinas, *Chemical Physics Letters* **2010**, 498, 302.
- [57] R. Noriega, A. Salleo, A. J. Spakowitz, *Proceedings of the National Academy of Sciences* **2013**, 110, 16315.
- [58] P. Prins, F. Grozema, J. Schins, S. Patil, U. Scherf, L. Siebbeles, *Phys Rev Lett* **2006**, 96, 146601.
- [59] B. Watts, T. Schuettfort, C. R. McNeill, *Adv Funct Mater* **2011**, 21, 1122.
- [60] B. A. Collins, J. E. Cochran, H. Yan, E. Gann, C. Hub, R. Fink, C. Wang, T. Schuettfort, C. R. McNeill, M. Chabinyc, *Nat Mater* **2012**, 11, 536.
- [61] R. Noriega, J. Rivnay, K. Vandewal, F. P. V. Koch, N. Stingelin, P. Smith, M. F. Toney, A. Salleo, *Nat Mater* **2013**, 12, 1038.
- [62] S. A. Mollinger, B. A. Krajina, R. Noriega, A. Salleo, A. J. Spakowitz, *ACS Macro Letters* **2015**, 4, 708.
- [63] K. Gu, C. R. Snyder, J. Onorato, C. K. Luscombe, A. W. Bosse, Y.-L. Loo, *ACS Macro Letters* **2018**, 7, 1333.
- [64] S. Kondov, W. McGehee, J. Zirbel, B. DeMarco, *Science* **2011**, 334, 66.

- [65] C. Gómez-Navarro, P. J. De Pablo, J. Gómez-Herrero, B. Biel, F. Garcia-Vidal, A. Rubio, F. Flores, *Nat Mater* **2005**, 4, 534.
- [66] A. Hindeleh, R. Hosemann, *Journal of Physics C: Solid State Physics* **1988**, 21, 4155.
- [67] J. Rivnay, R. Noriega, J. E. Northrup, R. J. Kline, M. F. Toney, A. Salleo, *Phys Rev B* **2011**, 83, 121306.
- [68] M. Baldo, Z. Soos, S. Forrest, *Chemical physics letters* **2001**, 347, 297.
- [69] W. Pasveer, J. Cottaar, C. Tanase, R. Coehoorn, P. Bobbert, P. Blom, D. De Leeuw, M. Michels, *Phys Rev Lett* **2005**, 94, 206601.
- [70] R. Street, J. Northrup, A. Salleo, *Phys Rev B* **2005**, 71, 165202.
- [71] M. Brinkmann, P. Rannou, *Macromolecules* **2009**, 42, 1125.
- [72] J. Clark, J. F. Chang, F. C. Spano, R. H. Friend, C. Silva, *Appl Phys Lett* **2009**, 94.
- [73] A. Troisi, *Org Electron* **2011**, 12, 1988.
- [74] J. L. Bredas, G. B. Street, *Accounts of Chemical Research* **1985**, 18, 309.
- [75] J. A. van Haare, E. E. Havinga, J. L. van Dongen, R. A. Janssen, J. Cornil, J. L. Brédas, *Chemistry—A European Journal* **1998**, 4, 1509.
- [76] J. Appel, in *Solid State Physics*, Vol. 21, Elsevier **1968**, p. 193.
- [77] S. Pekar, *SOVIET PHYSICS JETP* **1969**, 28.
- [78] A. Alexandrov, P. Kornilovitch, *Phys Rev Lett* **1999**, 82, 807.
- [79] D. Beljonne, J. Cornil, H. Sirringhaus, P. J. Brown, M. Shkunov, R. H. Friend, J. L. Brédas, *Adv Funct Mater* **2001**, 11, 229.
- [80] H. Sirringhaus, *Adv Mater* **2005**, 17, 2411.
- [81] G. Brown, Wiley-Interscience, New York, 1971.
- [82] J. M. Kelly, C. B. McArdle, M. J. d. F. Maunder, *Photochemistry and polymeric systems*, Royal Society of Chemistry Cambridge, **1993**.
- [83] M. Irie, *Photo-reactive materials for ultrahigh density optical memory: MITI research and development program on basic technologies for future industries*, Elsevier Science Inc., **1994**.
- [84] M. Irie, T. Seki, Y. Yokoyama, *New frontiers in photochromism*, Springer, **2013**.
- [85] J. Crano, R. Guglielmetti, Plenum, 1998.
- [86] H. Dürr, H. Bouas-Laurent, *Photochromism: molecules and systems*, Elsevier, **2003**.
- [87] M. Porden, presented at Ophthalmic Lens Design and Fabrication **1991**.
- [88] G. H. Carroll, Google Patents, 2002.
- [89] F. Fan, Y. Wu, *Journal of Applied Polymer Science* **2017**, 134.
- [90] M. Irie, ACS Publications, 2000.
- [91] L. Poyntz-Wright, P. S. Russell, *Electronics Letters* **1988**, 24, 1054.
- [92] M. Balistreri, A. Mijiritskii, J. T. Wilderbeek, C. Busch, B. Yin, H. Martens, Google Patents, 2006.
- [93] M. Ono, Google Patents, 1998.
- [94] K.-H. Teng, B. Huang, Google Patents, 2006.
- [95] C. C. Corredor, Z.-L. Huang, K. D. Belfield, A. R. Morales, M. V. Bondar, *Chem Mater* **2007**, 19, 5165.
- [96] S. Kawata, Y. Kawata, *Chem Rev* **2000**, 100, 1777.
- [97] D. A. Parthenopoulos, P. M. Rentzepis, *Science* **1989**, 245, 843.
- [98] K. Ogawa, *Applied Sciences* **2014**, 4, 1.
- [99] S. Shinkai, *Pure Appl Chem* **1987**, 59, 425.
- [100] Z. F. Liu, K. Hashimoto, A. Fujishima, *Nature* **1990**, 347, 658.
- [101] T. Ikeda, O. Tsutsumi, *Science* **1995**, 268, 1873.
- [102] N. Tamai, H. Miyasaka, *Chem Rev* **2000**, 100, 1875.

- [103] T. Hugel, N. B. Holland, A. Cattani, L. Moroder, M. Seitz, H. E. Gaub, *Science* **2002**, 296, 1103.
- [104] F. M. Raymo, M. Tomasulo, *Chem Soc Rev* **2005**, 34, 327.
- [105] I. Yildiz, E. Deniz, F. M. Raymo, *Chem Soc Rev* **2009**, 38, 1859.
- [106] S. L. Gilat, S. H. Kawai, J.-M. Lehn, *Journal of the Chemical Society, Chemical Communications* **1993**, 1439.
- [107] H. Tian, S. Yang, *Chem Soc Rev* **2004**, 33, 85.
- [108] N. Crivillers, A. Liscio, F. Di Stasio, C. Van Dyck, S. Osella, D. Cornil, S. Mian, G. Lazzerini, O. Fenwick, E. Orgiu, *Phys Chem Chem Phys* **2011**, 13, 14302.
- [109] H. i. Lee, W. Wu, J. K. Oh, L. Mueller, G. Sherwood, L. Peteanu, T. Kowalewski, K. Matyjaszewski, *Angewandte Chemie International Edition* **2007**, 46, 2453.
- [110] M. Irie, T. Fukaminato, K. Matsuda, S. Kobatake, *Chem Rev* **2014**, 114, 12174.
- [111] E. Orgiu, N. Crivillers, M. Herder, L. Grubert, M. Patzel, J. Frisch, E. Pavlica, D. T. Duong, G. Bratina, A. Salleo, N. Koch, S. Hecht, P. Samori, *Nat Chem* **2012**, 4, 675.
- [112] S. Kobatake, M. Irie, *Bulletin of the Chemical Society of Japan* **2004**, 77, 195.
- [113] M. Morimoto, M. Irie, *Chem Commun* **2005**, 3895.
- [114] C. Kittel, P. McEuen, P. McEuen, *Introduction to solid state physics*, Wiley New York, **1996**.
- [115] J. Valasek, *Physical review* **1921**, 17, 475.
- [116] J. Scott, *Berlin* **2000**.
- [117] J. Scott, *Science* **2007**, 315, 954.
- [118] J. C. Scott, L. D. Bozano, *Adv Mater* **2007**, 19, 1452.
- [119] H. S. Nalwa, *Ferroelectric polymers: chemistry: physics, and applications*, CRC Press, **1995**.
- [120] T. Furukawa, *Phase Transitions: A Multinational Journal* **1989**, 18, 143.
- [121] R. G. Kepler, R. Anderson, *Advances in physics* **1992**, 41, 1.
- [122] H. Kodama, Y. Takahashi, T. Furukawa, *Ferroelectrics* **1997**, 203, 433.
- [123] A. J. Lovinger, *Science* **1983**, 220, 1115.
- [124] R. C. Naber, K. Asadi, P. W. Blom, D. M. de Leeuw, B. de Boer, *Adv Mater* **2010**, 22, 933.

## Chapter 2. Organic Devices

### 2.1 Role of interfaces in organic devices

Organic thin-film structures form organic devices. They include several layers of organic materials together with contacts for electron or hole injection. To inject these charge carriers into the films and transport them through the device, metal-organic (MO) interfaces have to be crossed. Because of their importance in such processes, during the past years, metal-semiconductor interfaces have become the focus of several studies, which are aimed at achieving a better understanding on their electronic and chemical structure, at monitoring interface energy barriers, and at maximizing the injection of charge carriers.<sup>[1-2]</sup>

At first, the electronic structure of MO interfaces was believed to observe the vacuum level alignment rule, i.e. the Schottky–Mott limit, as named by scientists working in the field of metal-inorganic (MI) semiconductor interfaces. Indeed, the Mott limit, which is known to be valid for inorganic semiconductor interfaces, was initially considered for organic ones because of the hypothesis that organic surfaces, comprising closed-shell molecular units, would not have a strong interaction with the metal surface. According to this model, when a metal and a semiconductor are in contact, an interface energy barrier can be defined as the energy offset between the Fermi Energy level of the metal and the molecular orbital energy level of the semiconductor. A metal-semiconductor contact for an intrinsic semiconductor with defect free interface is shown in **Figure 2.1**.<sup>[3]</sup>

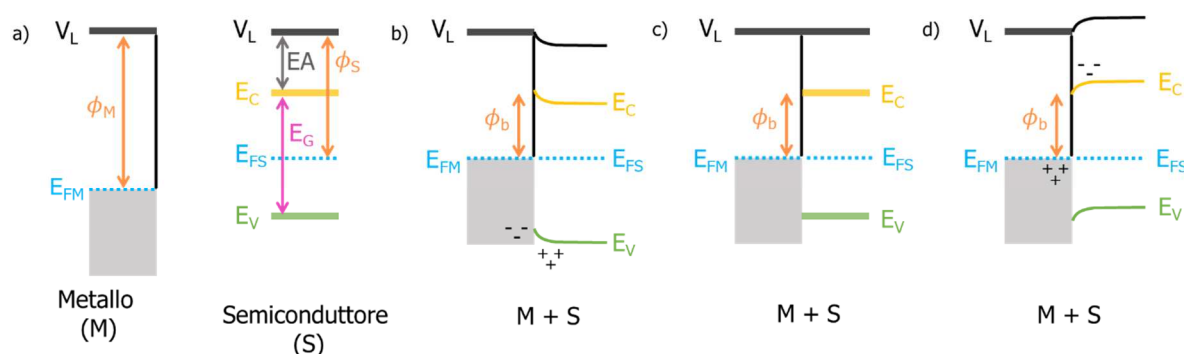


**Figure 2.1:** Schematic representation of the energy level alignment in a semiconductor-metal junction.

The conduction band  $E_C$  (LUMO energy level) of the semiconductor sits at  $EA$  (electron affinity) from the vacuum level,  $V_L$ , while the valence band  $E_V$  (HOMO energy level) at  $IE$

(ionization energy) equal to  $E_A + E_G$  (semiconductor band gap). Fermi-level,  $E_{FS}$ , is located halfway the band gap. The work function  $\Phi_S$  of a semiconductor is the energy required to remove an electron at the Fermi level, therefore  $\Phi_S = V_L - E_{FS}$ . The values of work functions are very sensitive to surface contamination. Typical values for very clean surfaces are 4.3 V for Al and 5.0 V for Au.<sup>[4]</sup> Finally, the bandgap energy  $E_g$ , is the energy difference between the conduction band energy  $E_C$  and the valence band (HOMO energy level)  $E_V$ . The work-function of the metals ( $\Phi_M$ ) on the other hand is equal to the distance between the metal's vacuum level and Fermi level  $E_{FM}$ ,  $\Phi_M = V_L - E_{FM}$ . **Figure 2.1a**, shows the energy level of metal and semiconductor energy levels when they are separated. Bringing the metal and semiconductor in contact results in the alignment of the Fermi level at thermal equilibrium. The consequent shift of the vacuum level of one with respect to the other is due to the formation of an interface dipole barrier which results from the interaction of the electronic density. The resulting energy barrier  $\Phi_b$  is the energy that a carrier needs to overcome when going from the Fermi level of the metal,  $E_{FM}$ , to into the conduction band of the semiconductor. Therefore,  $\Phi_b = E_C - E_{FM} = \Phi_M - E_A$ . There are three main contacts can theoretically arise in injecting electrons into an intrinsic semiconductor:

- (i)  $\Phi_M > \Phi_S$  corresponds with an injection limited/blocking electron contact and an ohmic hole contact;
- (ii)  $\Phi_M = \Phi_S$  correspond to a neutral contact for all the involved for both charge carries;
- (iii)  $\Phi_M < \Phi_S$  the contact will be Ohmic for electrons and will only be limited for holes.

Conversely to conventional semiconductor like Si, polymer semiconductors are highly disordered. This disorder perturbs the formation of well-defined energy bands and broadens the DOS at the HOMO and LUMO levels. This broadening makes the definition and concept of an injection barrier more difficult. Indeed, by the middle of 1990s with the work of Ishii and co-workers,<sup>[5]</sup> the study of various MO semiconductor interfaces revealed a much complex situation to model, thus breaking the previous assumption on the validity of the vacuum level alignment rule. First, MO interfaces display a more complex physics of charge injection and transport in molecular solids, compared to standard MI interfaces, thus hindering the identification of various mechanisms. As a result of the weak van der Waals bonding, as well as the small intermolecular overlap of wave functions which induce

a transport dominated by thermally activated intermolecular hopping. In such low-dielectric constant and nearly charge-depleted materials, charge transport can follow and be described according to three different models: space-charge-limited, trap-limited, or injection-limited, in light of the charge injection conditions and applied field. Second, the way MO interfaces behave depends on their morphology and chemistry. The morphology at the interface can significantly change, depending on the processing. Within the soft organic matrix, the diffusion of metal atoms and clusters can be important, resulting into charge transfer reactions, generally referred to as doping, as well as the development of organometallic complexes deep in the organic film.

As already discussed above, in order to assess the electronic structure of a metal-semiconductor interface, it is useful to compare the metal work function  $\Phi_M$  with the semiconductor EA (in case of electron injection) and semiconductor IE (in case of hole injection). However, for MO interfaces, the Schottky-Mott rule is not valid anymore because of the presence of dipoles at the interface, as shown in **Figure 2.2**.

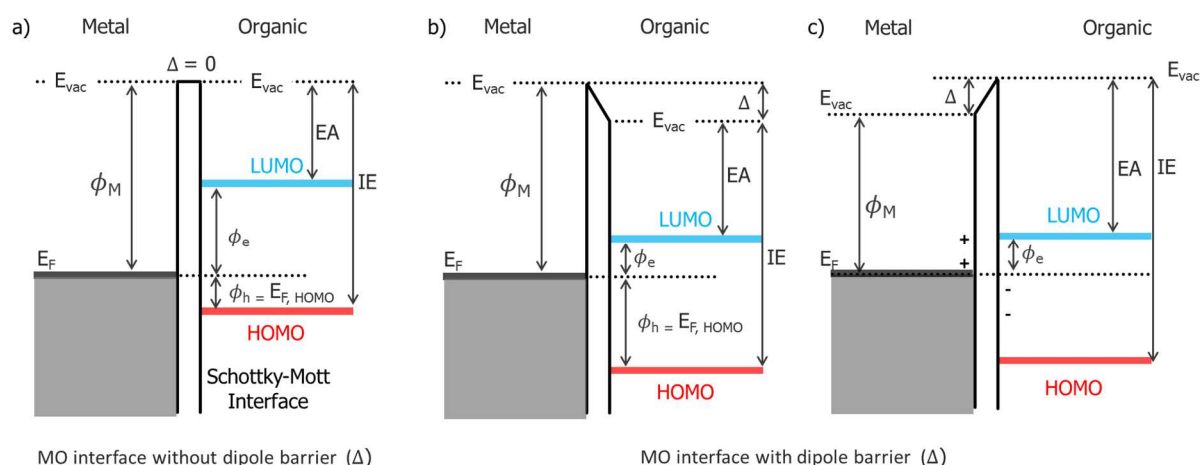


**Figure 2.2:** Energy diagram of a metal-organic semiconductor interface a) without and b) c) with a dipole barrier  $\Delta$ .

The origin of these dipoles is different and can be ascribed to three main reasons. Dipoles can originate from i) charge transfer relying on relative values of  $\Phi_M$  and the values of organic EA and IE; ii) a chemical reaction which gives rise to the development of gap states and pinning of  $E_F$  at the interface; iii) modifications induced on the metal at the molecular level.

In the first group, the metal work function  $\Phi_M$  is energetically smaller or equal to the organic EA, before the interface is formed. Thus, an electron transfer to the LUMO of the

interface molecules occurs. Consequently, a dipole barrier is generated, which is equal to an upward step of  $E_{vac}$  from the metal to the organic film. Thus, charges that move from the metal to the organic film remain localized at the interface, above the HOMO and below the  $E_F$  as shown in **Figure 2.2c**. In general, these interfaces do not show a band bending in the organic semiconductor film and the molecular level alignment is fixed at the interface with respect to the metal Fermi level.

The second group includes reactive interfaces, in which chemically induced electronic states control the alignment of the energetic levels. An example is tris(8-hydroxyquinoline) aluminum ( $Alq_3$ )/Mg interface, the Mg work function falls into the  $Alq_3$  gap. Such condition prevents the possibility of charge transfer and the consequent formation of an interface dipole. However, a dipole barrier of about 0.5 eV, which points from the metal towards the organic layer, has been shown experimentally.<sup>[6-7]</sup> Moreover, measurements have revealed that the interface electronic structure comprises interface states which arise from the generation of a new Mg: $Alq_3$  organometallic complex. At the interface of this new complex, a density of filled states is originated, having an energy which is in the previous gap of pristine  $Alq_3$ . Because of the formation of such filled states in the gap, an electron charge transfer from the organic to the metal is needed for the alignment of the Fermi level, resulting in its pinning.

Finally, the third group describes interface dipole barrier found at the interfaces, like *p*-sexiphenyl or pentacene on Au,<sup>[8]</sup> which results into a decrease of the metal work function  $\Phi_M$  by adsorbed molecules.<sup>[5, 9]</sup> Within the first monolayer of the organic material,  $\Phi_M$  decreases by a large quantity behaving like an interface dipole barrier, and substantially does not change for thicker layer. The work function of the metal corresponds to the sum of bulk and surface contributions, in other words the bulk chemical potential ( $\mu$ ) and the surface dipole (SD).<sup>[10]</sup> The structure of the surface influences significantly the SD and it is partially determined by the tail of electrons overflowing from the metal surface into the vacuum. The presence of an adsorbate modifies such SD contribution: in the presence of large adsorbates like conjugated organic molecules, the molecule electrons and the metal surface electrons repulse each other, thus compressing the electron tail (known as pillow effect) and lowering  $\Phi_M$ . This suddenly leads to the downward shift of the vacuum level from the metal towards the organic film at the interface. As a consequence of such lowering of  $\Phi_M$ , a shift of the molecular energy levels towards lower energy occurs, with an equivalent increase in the energy difference between the metal  $E_F$  and the HOMO of the

organic film, which represents the hole-injection barrier. In comparison with a vacuum level alignment situation, in this case the energy barrier is consistently higher, resulting in a substantial reduction of the hole-injection performance. On the contrary, in case of the organic molecules are physisorbed on metals, the observed shift of vacuum level due to SD contribution is smaller, which corresponds to a tiny change in  $\Phi_M$ .<sup>[11]</sup>

## 2.2 Charge injection in organic semiconductor devices

Organic devices possess values of single contact resistance which range from 10 k $\Omega$ cm to 10 M $\Omega$ cm,<sup>[12-16]</sup> much higher than their inorganic counterparts. Therefore, in general contact effects severely impact organic transistors performance. This is highlighted by various articles on fully contact-limited organic transistors,<sup>[17-19]</sup> which show transistor operation not being controlled by the modulation of the channel resistance but by the variation of the contact resistance with the gate voltage. In a transistor having a field-effect mobility  $\mu$  and a contact resistance  $R_c$ , the contact resistance is independent of the channel length  $L$  to a good approximation, although the real channel resistance depends on  $L$  and in the linear regime is equal to  $R_{ch} = L/W\mu en$ . Thus, it is possible to identify a critical channel length  $L_c = \mu en R_c$  for which  $WR_{ch} = R_c$  such that the contacts and the channel equally contribute to the total transistor resistance. A normal TFT operation can be obtained only for transistors with a channel length that is larger than  $L_c$ . On the other hand, transistors having channel length  $L \ll L_c$  turn into harshly contact limited operation, implying that the source-drain voltage instead of dropping over the transistor channel, mostly does it over the contact regions. This results into a reduction of the total transistor current.

From what stated above it is evident that understanding the physics behind the contact resistance is a requirement needed to improve the switching speeds and operation currents of organic transistors with short channels ( $< 1 \mu\text{m}$ ).<sup>[17, 20]</sup> Contact effects in organic transistors have been experimentally investigated in TFTs made of either vacuum deposited oligomers (oligothiophenes,<sup>[12, 18-19, 21-22]</sup> pentacene<sup>[23-24]</sup>) or solution processed polymers (polythiophene<sup>[25-26]</sup> F8T2<sup>[13-14, 17]</sup>). The influence of the temperature, which is a central parameter concerning charge injection has been investigated by Chwang and Frisbie.<sup>[18]</sup> They have concluded that (diffusion-limited) thermionic emission is the dominant process for injection of charge carriers in organic transistors, as also reported in several works.<sup>[14-15, 23, 27]</sup> However, the applicability of thermionic emission models to disordered organic materials in general has been questioned by several authors in later

years.<sup>[28]</sup> Alternative injection mechanisms such as thermally assisted injection into a disordered organic semiconductor may play a dominant role in the injection limited regime.<sup>[29-30]</sup>

### 2.2.1 Charge injection models

Thermionic emission is a classical injection mechanism which is founded on the relation between the velocity and kinetic energy of a delocalized charge and is used in the prediction of a current density  $J$ :

$$J = A_G T^2 e^{-\frac{\phi_b - \Delta\phi}{kT}} \quad (\text{Equation 2.1})$$

where the effective energy barrier is denoted by  $\phi_b$ , the absolute temperature is denoted by  $T$  and the effective Richardson constant is  $A_G$ . In electron emission devices, the negative bias applied to the electron emitter will induce an electric field  $F$  at the surface. Without the induced field, the barrier seen by an escaping Fermi-level electron has height equal to the metal work-function. The electric field lowers the surface barrier by an amount  $\Delta\phi$  increasing the emission current.

$$\Delta\phi = \sqrt{\frac{q^3 F}{4\pi\epsilon_0}} \quad (\text{Equation 2.2})$$

The Richardson equation can be used to describe the Schottky emission that is the electron emission that takes place at metal-semiconductor interface in the field-and-temperature-regime.<sup>[31]</sup> The barrier-lowering effect due to the band bending induced by high electric field (lower than about  $10^8 \text{ V m}^{-1}$ ) favors the charge tunneling into the semiconductor.

However, it needs to be highlighted that the thermionic emission model does not apply to low mobility semiconductors ( $\mu \leq 10^{-3} \text{ m}^2/\text{Vs}$ ).<sup>[32]</sup> Backflows are expected to occur in low mobility semiconductors due to the huge concentration of the charge carriers at the interface, as the velocity of the charge carriers that can be found in the semiconductor's bulk remain lower than the speed at the interface.<sup>[31]</sup> The charge density in the bulk and the velocity remain proportional to each other, resulting into the diffusion-limited injection following

$$J = qN_V\mu F e^{-\frac{\Phi_b - \Delta\Phi}{kT}} \quad (\text{Equation 2.3})$$

with the  $F$  being the applied electric field and the  $N_V$  being the semiconductor's effective density of states. In both diffusion-limited injection (low mobility) and thermionic emission (high mobility), the barrier height  $\Phi_b$  is crucial to define the charge injection. As the injection barrier is lowered, the current density is expected to increase exponentially.

In conjugated polymers, hopping triggered by heat among the transport sites is responsible for controlling the transport properties, meaning that charge carriers are localized. Therefore, in case of conjugated polymers it is not generally right to assume that injection is well described by the above-discussed classical model. Indeed, such models generally do not take into account the presence of delocalized charge carriers. Simulations have demonstrated that the injection is basically controlled by temperature and field dependence of the injection process.<sup>[33]</sup> Thus, the injection current can be described like a two-step process. In the first step, a carrier jumps in the semiconductor, while in the second step this carrier may escape or degenerate into the electrode.<sup>[30]</sup> The injection limited current (ILC) can be described by the following equation:

$$J \propto \int_a^\infty dx_0 \exp(-2\gamma x_0) w_{esc}(x_0) \int_{-\infty}^\infty dE Bol(E) g\left[\frac{U(x_0)}{e} - E\right] \quad (\text{Equation 2.4})$$

where  $\exp(-2\gamma x_0)$  represents the tunneling probability at distance  $x_0$ , with an inverse localization radius  $\gamma$ .

The charge injection requires the charge carrier to jump a distance  $x_0$  (larger than  $a$ , i.e the neighbor distance between to hopping states) from the contact into an arbitrary site in the conjugated polymer. The probability for a charge carrier to get to other side of the device, i.e. to fully escape, is  $w_{esc}$ . The energy contribution to the jump is given by Boltzmann function  $Bol(E)$ , reported in equation below:

$$Bol(E) = \begin{cases} \exp\left(-\frac{E}{kT}\right), & E > 0 \\ 1, & E < 0 \end{cases} \quad (\text{Equation 2.5})$$

where  $E$  is defined with reference to the Fermi-level of the metal. Finally, a Gaussian distribution of transport sites,  $g[U(x_0)/e - E]$  centered around the electrostatic potential  $U(x_0)/e$  and having an energy width  $\sigma$  describes the density of transport states within the polymer focused.

**Equation 2.4** which described the hopping based injection model, does not include any fit parameters. Indeed, the energy width ( $\sigma$ ), the dielectric constant ( $\epsilon$ ), and the nearest neighbor distance ( $a$ ), are characteristics of the semiconductor itself and can be obtained

either from measurements of mobility<sup>[34]</sup> or from admittance spectroscopy.<sup>[35]</sup>  $\gamma$ , which is the inverse localization radius results from the strength of the potential barrier,<sup>[36]</sup> while the potential barrier itself,  $\Phi_b$ , represents the difference in energy from the electrode energy level to the center of the Gaussian DOS of the polymer. It is clear that the calculated current density has an exponential dependence, with the presence of the injection barrier at the interface.

### 2.3 Surface functionalization to improve charge transport - semiconductor/dielectric interface

The interface between the semiconductor and the dielectric is important for the performance of electrical devices. Upon application of an electric field to the semiconductor, the charge carriers will travel towards the dielectric. The applied potential will determine the affected charges, i.e. holes will move towards the negative potential while electrons towards the positive one. Therefore, the charge carriers will accumulate at the interface between the dielectric and the semiconductor, forming a region where most of the charges are transported, i.e. where the electrical conduction happens. Thus, the wettability and roughness of the dielectric, especially at the interface, will deeply influence the properties of the semiconductor, impacting its crystallinity. Therefore, creating a dielectric surface adapted to charge transport is of paramount importance for optimizing the electrical performances of a device. On the one hand, the obvious approach is to decrease the roughness of the surface and remove the adsorbed impurities that could hinder charge transport. On the other hand, charge mobility may also be improved through the use of SAMs on the dielectric surface. The SAM formation on a dielectric is like the process for metal functionalization that has already been described above. In case of a dielectric of SiO<sub>2</sub>, the most commonly used in devices, the functionalization can be easily performed with molecules having a silane group. One of the family of molecules most commonly used to chemically modify SiO<sub>2</sub> surface is alkylsilane. Alkylsilanes react covalently with atoms at the surface of the dielectric forming a monolayer with methyls as terminal groups, which will increase the surface hydrophobicity (**Figure 2.3**). Thus, the choice and use of a suitable SAM on a dielectric can favor the process of crystallization of a semiconductor through the adjustment of the wettability and surface energy.

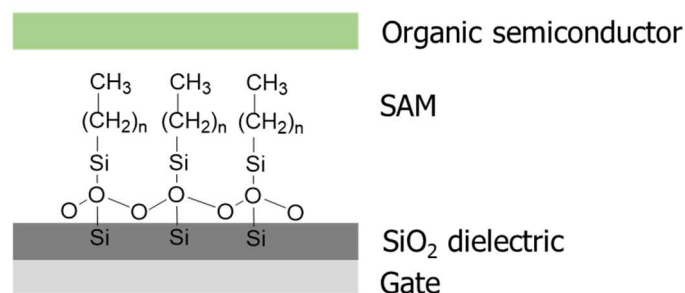


**Figure 2.3:** Schematic representation of the formation of an alkylsiloxane SAM at the SiO<sub>2</sub> dielectric surface by chemical absorption of an alkyltrichlorosilane.

### 2.3.1 Effect on impurities in the semiconductor: Trapping and doping

In general, doping consists in the introduction of small quantities of impurities (e.g. a small molecule or an ion) intentionally added into a semiconducting material with the aim of tuning its electrical properties, thus allowing some additional energy states within the band gap, that result into better conduction. Such process of doping is generally used for inorganic semiconductors. For instance, in case of silicon, small quantities of electrons acceptors, such as boron, are added for p-type doping, while small quantities of electrons donors, such as phosphorous, are introduced for n-type doping, producing states close to the valence band or to the conduction band, respectively.<sup>[37]</sup> Most of the materials used in this thesis are intrinsic organic semiconductors. Despite the organic semiconducting material has been purchased carefully purified, impurities within or at the surface of the film may remain. Such impurities can have different sources: the air in which the organic semiconductor is produced, the synthesis of the organic compound itself and/or residues coming from the lithographic process. Most of all, molecular oxygen present in the air has a major importance in the degradation of most of the organic semiconductor materials. Indeed, the presence of oxygen in an organic semiconductor material is shown to cause oxidative doping. This results in increased charge carrier concentration and altered the charge transport characteristics of the material.<sup>[38]</sup> To address this issue the most common strategy used in the lab is that to prepare devices and measure their electrical properties into a controlled atmosphere, without oxygen and humidity. Otherwise, in order to measure and store the device in air, the semiconductor is isolated from the atmosphere with a protecting layer like a polymeric film.

## 2.4 Organic Field-effect Transistors (OFETs)

Organic Field-Effect Transistors (OFETs) are field-effect transistor in which the active layer is an organic semiconductor film.<sup>[39]</sup> They are used to examine and understand bulk semiconductors when connected with metallic electrodes and dielectric surfaces or to control electronic signals in electronic application. **Figure 2.4a** shows the two-dimensional view of a typical OFET.

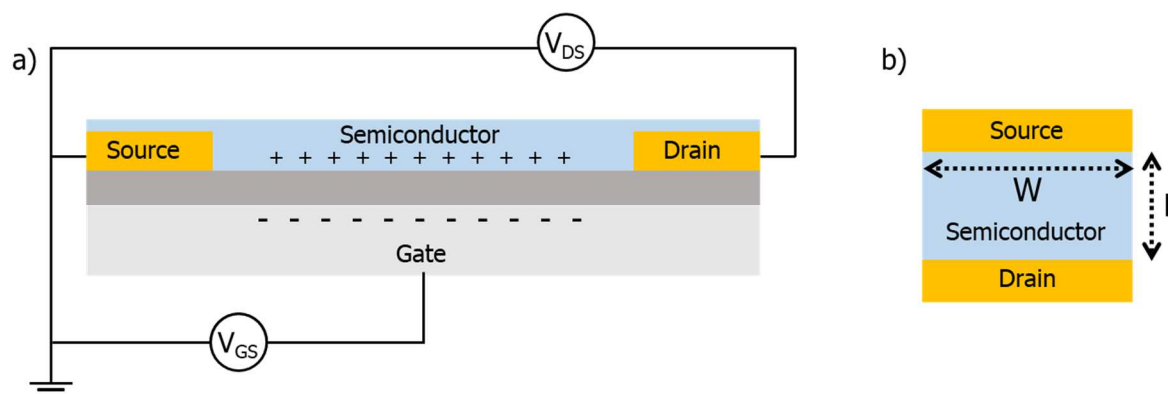


**Figure 2.4:** Schematic representation of the a) lateral view and b) top view of an OFET (example of bottom-contact and bottom-gate geometry).  $V_{DS}$  and  $V_{GS}$  are the applied drain and gate voltage respectively.

In general, an OFET consists of three main parts: metal electrodes or terminals, a semiconductor thin layer and an insulator or dielectric layer. The three terminals are called source, drain and gate. The drain current, which is the output factor, can be adjusted based on two distinct voltages, called the drain and the gate voltages,  $V_{DS}$  and  $V_{GS}$  respectively. The gate electrode is generally made of a highly doped conductive silicon. Nevertheless, other metals or conductive polymers can be employed for the same purposes in different geometries (e.g. Al, Au, Ag, Pd, Cu, Ni or PEDOT:PSS). The source and drain electrodes are comprised of noble metals like gold or silver or conducting polymers like PEDOT-PSS and they are selected according to semiconductor work function. To ensure the flexibility of substrate, a support of plastic (e.g. PET or PEN) can be used, while organic insulating polymers such as Cytop, PMMA, PVP, or PS<sup>[40-43]</sup> are used to make the dielectric in alternative to inorganic dielectric like  $\text{SiO}_2$ ,  $\text{Al}_2\text{O}_3$  or  $\text{HfO}_2$ .<sup>[44]</sup> Gate dielectric covers the gate electrode and is an insulating layer, necessary to avoid charge transport between source and drain electrodes through the gate. It is necessary that a dielectric material withstands electric fields of a minimum value of  $2 \text{ MVcm}^{-1}$  without breaking, possesses insulating properties, and has low roughness on the surface.<sup>[45]</sup>

The gate terminal effectively controls the density of the charge within the system, which is produced as a result of electrostatic coupling. Hence, it is able to turn the device on and off depending on the applied voltage. The electric potential (voltage) applied between the drain and the source terminals is the  $V_{DS}$  potential and creates an electric field which allows the charges to drift towards the electrodes which either introduce (source) or collect (drain) the current.<sup>[31]</sup> The dielectric layer shields the gate electrode from the active channel, which allows charge to be accumulated within the channel following a different physical principle from the population inversion commonly required in inorganic (silicon-based) devices. In fact, OFETs work on the principle of accumulation, wherein the channel is induced with charges which are opposite in sign to the gate potential. An organic semiconductor forms the active layer which is placed in direct contact with the two ohmic electrodes, source and drain. Two parameters must be considered concerning source-drain contacts geometry: the electrode width, which is called  $W$ , and the channel length, or  $L$ , which is their distance (**Figure 2.4b**). The area  $W \times L$  identifies where charges are transported between source and drain electrodes, i.e. the so-called channel. In principle, OFETs can be found in four different geometries, which will be briefly described in the next paragraph.

#### 2.4.1 OFET architectures

The aforementioned elements of the OFETs can be fabricated in several architectures (**Figure 2.5**) which may introduce significant differences in the device performances (mobility,  $V_{th}$  and  $I_{on}/I_{off}$ ) as a result of different charge transport and injection physics. In bottom-contact, bottom-gate geometry (**Figure 2.5a**), the flow of charges is restricted to the very first few layers of the semiconductor close to the dielectric surface, as both the source and drain electrodes are placed on the dielectric surface. In this configuration the dielectric is positioned directly on the flat gate, thus it is easier to obtain very a thin layer which ensures ideal capacitance. Moreover, its functionality can be optimized before the semiconductor is deposited. As the semiconductor is deposited in the end, the device fabrication is straightforward and usually extremely reproducible. For such reason, bottom-contact, bottom-gate geometry is the most common choice for studying semiconductor properties.

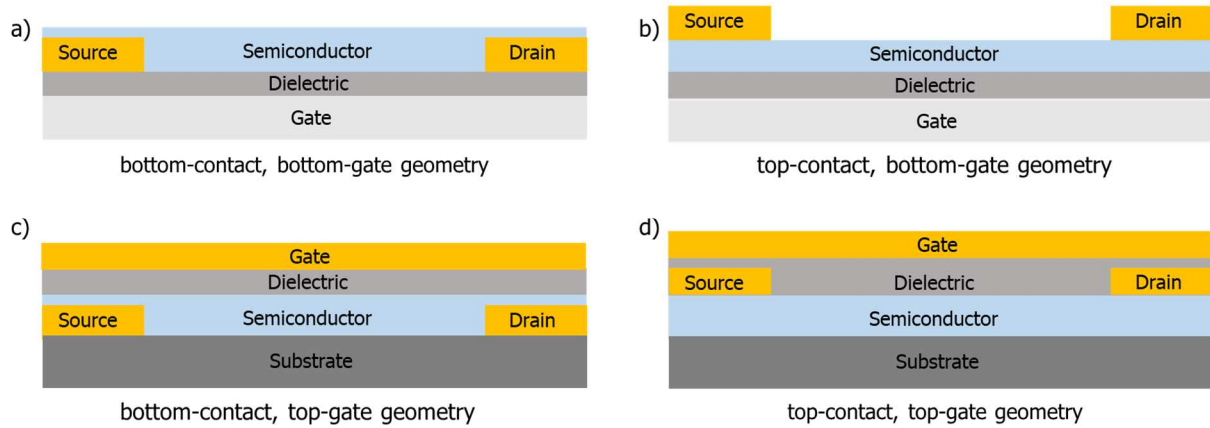


**Figure 2.5:** Schematic representation of the four different OFTF geometries: a) bottom-contact, bottom-gate geometry, b) top-contact, bottom-gate geometry, c) bottom-contact, top-gate geometry, d) top-contact, top-gate geometry.

However, to better inject charges from the source and drain electrodes into the semiconductor, one can adopt the top-contact, bottom-gate geometry (**Figure 2.5b**). In this approach, while the source and drain electrodes are placed over the semiconductor, the dielectric and gate remain at the bottom. This staggered geometry assists in the injection as there is a large contact area between the source electrode and the semiconductor.<sup>[46]</sup> Moreover, the diffusion of metal atoms within the soft active layer after thermal evaporation, allows the formation of an intimate semiconductor/electrode interface. Another possible geometry is the bottom-contact, top-gate configuration (**Figure 2.5c**). This approach relies on fabricating transistors over a substrate. Source and drain electrodes which are placed inside first, can be functionalized to ensure an optimal charge injection, while the semiconductor is deposited later. Since both the electrodes and the semiconductor are not perfectly flat films, a thicker dielectric layer is deposited above the semiconductor in order to prevent gate leakage current. Finally, the gate is placed over the dielectric. Though this geometry allows for particularly good transport at the semiconductor/dielectric interface, it has its own set of disadvantages. First, it requires higher number of production steps and is also more prone to source/gate short circuit and consequent failure.

Finally, the fourth possible geometrical approach is top-contact, top-gate configuration (**Figure 2.5d**). This geometry places the source and drain electrodes over the semiconductor. In this case, the dielectric layer between source/drain and gate electrodes

is even more prone to short circuit and hence the bottom-contact, top-gate geometry is usually recommended over this configuration.

### 2.4.2 OFETs operation modes

The gate electrode and the gate dielectric, which form the OFET core, can be regarded as a plane capacitor. As discussed earlier, application of bias at gate leads to the generation of carriers of opposite sign at the dielectric/semiconductor interface proportional in magnitude to the dielectric capacitance and the applied gate voltage, leading to the formation of a conductive channel. When a bias is applied between source-drain electrodes, charges begin to move and a current is measured.<sup>[47]</sup> It is important to highlight that organic semiconductors contain a substantial number of traps within the channel. These traps emerge from the interface between the polymer and the surface of the gate dielectric, as well as from the nature of the semiconducting material, which as an inherent defective structure. Some of the charges which are injected through the application of gate bias are required to fill the traps at the interface. Thus, a current is measured only when the gate voltage ( $V_{GS}$ ) is higher than the threshold voltage ( $V_{TH}$ ).  $V_{TH}$  is a characteristic parameter of the material and depends on the interface as well as the geometry of the device. It is the voltage value above which the formation of the conducting channel occurs and thus an OFET device turns on. As shown in **Figure 2.6** two transport regimes can occur through the semiconductor channel: the linear (a) and the saturation (b) regime. This depends on the applied drain ( $V_{DS}$ ) and gate ( $V_{GS}$ ) biases. At low drain voltage  $V_{DS} < (V_{GS} - V_{TH})$  a linear regime is observed, in which the current between source and drain ( $I_{DS}$ ) follows the Ohm's law. When the drain voltage increases and  $V_{DS} = V_{GS} - V_{TH}$ , the channel reaches a point where it is "pinched off", i.e. a depletion region is formed on the channel, which is an area depleted of charges. If a higher  $V_{DS}$  is applied, i.e.  $V_{DS} > (V_{GS} - V_{TH})$ , a narrow depletion region is formed closed to the drain electrode and the current  $I_{DS}$  tends to saturate, becoming independent of the  $V_{GS}$ . This region is called saturation regime.

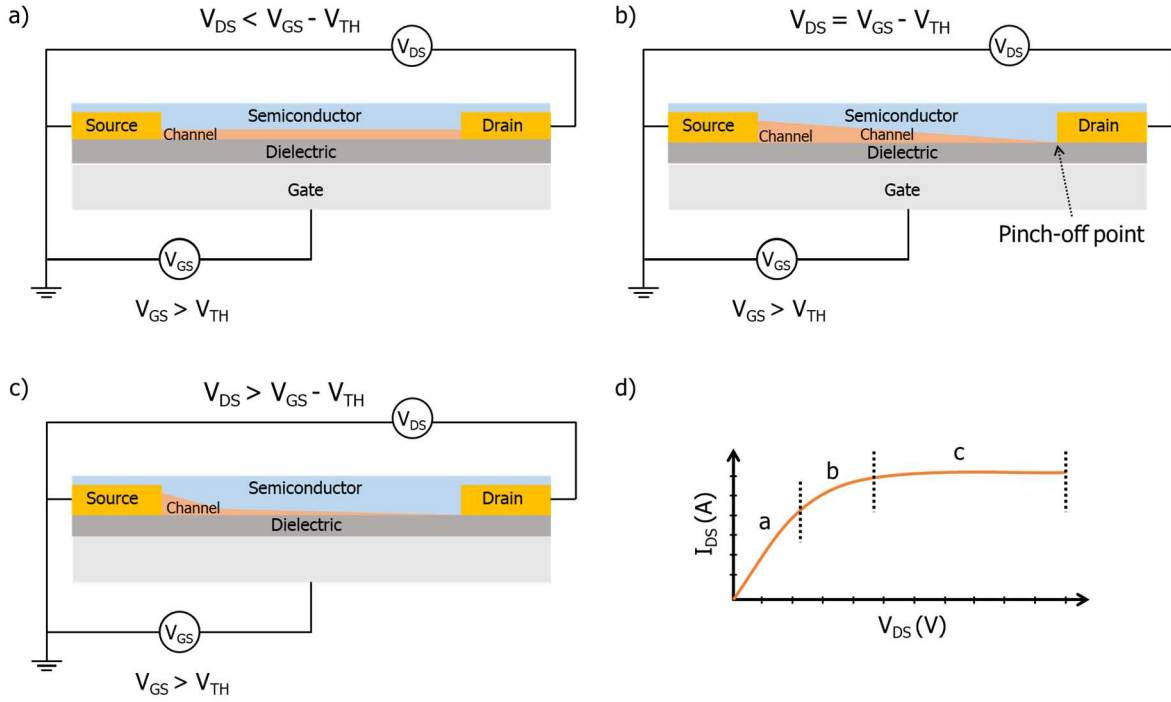


**Figure 2.6:** Schematic representation of an OFET (bottom-contact and bottom-gate geometry) operating in a) linear regime, b) at the pinch-off point, and c) in the saturation regime. The orange area is the semiconductor channel. In d) the corresponding output characteristics in the various operation regimes are represented.

In both the linear and saturation regimes, the  $I_{DS}$  depends on the capacitance of the dielectric ( $C_i$ , i.e. the capacitance per unit area of the insulator layer which depends on  $\epsilon_0$ , the permittivity of vacuum,  $\epsilon_r$ , the relative permittivity of the dielectric and  $d$ , the thickness of the dielectric layer), the threshold voltage ( $V_{TH}$ ), the field-effect carrier mobility of the semiconductor ( $\mu$ ) which depends on the operating regime (linear or saturation), the length ( $L$ ) and the width ( $W$ ) of the channel, giving the two equations reported below:

$$I_{DS} = \frac{W}{L} C_i \mu_{LIN} (V_{GS} - V_{TH}) V_{DS} \quad \text{(Equation 2.6)}$$

$$I_{DS} = \frac{W}{2L} C_i \mu_{SAT} (V_{GS} - V_{TH})^2 \quad \text{(Equation 2.7)}$$

In the two equations above, we can see that the width-to-length ratio ( $W/L$ ) influences the final value of  $I_{DS}$ . In general, the ratio  $W/L$  is maximized by an interdigitated geometry of the source and drain, because higher  $I_{DS}$  currents are experimentally easier to measure and process in output and transfer curves.

### 2.4.3 Measurement of electrical characteristics and parameters extraction

Three-terminal field-effect devices allow for two different types of measurements of (drain) current - voltage. By applying a constant  $V_{GS}$  bias, while sweeping  $V_{DS}$  and recording the resulting  $I_{DS}$ , the so-called output ( $I_{DS}$  vs  $V_{DS}$ ) curve can be obtained, as shown in **Figure 2.7c**. In general, multiple output curves for different values of  $V_{GS}$  are recorded. As already discussed above, two regions can be defined, corresponding to two operation regimes of the OFET, i.e. linear and saturation regime., depending on the applied  $V_{DS}$ . On the other hand, sweeping the  $V_{GS}$  while applying various constant  $V_{DS}$  biases, the so-called transfer curves ( $I_{DS}$  vs  $V_{GS}$ ) are obtained, represented in **Figure 2.7a-b** for a linear and saturation regime, respectively.

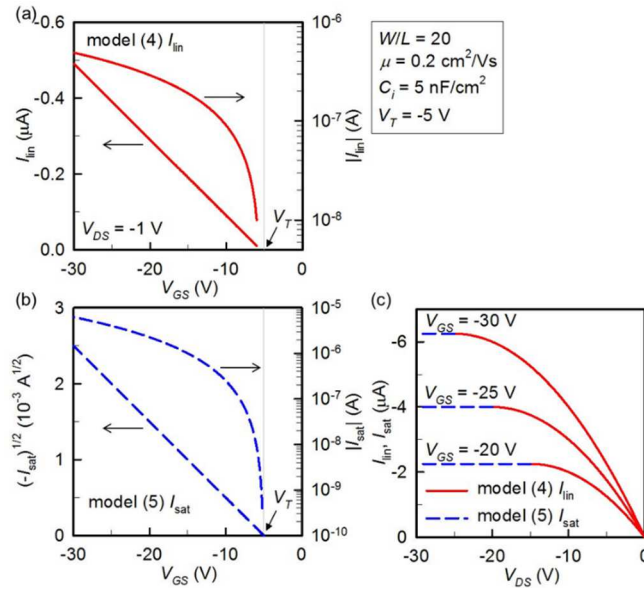


**Figure 2.7:** Example of characteristic curves for an OFET. a) Transfer curve ( $I_{DS}$  vs  $V_{GS}$ ) for a linear regime and c) saturation regime, c) output curves ( $I_{DS}$  vs  $V_{DS}$ ).<sup>[48]</sup>

These curves help to examine important parameters concerning the optimal operation of an OFET, as well as the fundamental properties of a semiconductor. These parameters are the charge carrier mobility ( $\mu$ ), the threshold voltage ( $V_{TH}$ ) and the  $I_{on}/I_{off}$  ratio.

The charge carrier mobility  $\mu$  is defined as the average drift velocity of a charge,  $v_d$ , when an electric field,  $E$ , is applied:<sup>[49]</sup>

$$\mu = \frac{v_d}{E} \quad (\text{Equation 2.8})$$

**Equations 2.6** and **2.7** allow us to extrapolate the field-effect mobility ( $\mu_{FE}$ ) for linear and saturation regime respectively, as showed in the following equations:

$$\mu_{LIN} = \frac{L}{WC_iV_{DS}} \left( \frac{\partial I_{ds}}{\partial V_{DS}} \right) \quad (\text{Equation 2.9})$$

$$\mu_{SAT} = \frac{2 \left( \frac{\partial \sqrt{I_{ds}}}{\partial V_{GS}} \right)^2}{C_i \frac{W}{L}} \quad (\text{Equation 2.10})$$

$\mu_{FE}$  is used to characterize how efficient is the charge transport in the semiconducting thin layer. However its value can be affected by the deposition technique, the semiconductor morphology, [50-51] eventual interface functionalization (e.g. SAM), and contact resistance[52].

As discussed earlier, the threshold voltage ( $V_{TH}$ ) is a measure of the voltage beyond which the formation of a conductive channel begins. It determines the state of operation of an OFET, being in on or off state. Linear regression of the  $I_{DS}$  current for liner regime and linear regression of the square root of saturation current for saturation regime can be used to determine threshold voltage. Ideally,  $V_{th}$  should be 0 in a perfect system, but due to the traps at the semiconductor/dielectric system, there is often a shift from this value.[53] The  $V_{th}$  value is directly related to the number of traps  $N_{trap}$  by:

$$V_{TH} \approx \frac{eN_{trap}}{C_{insulator}} \quad (\text{Equation 2.11})$$

in which the fundamental charge is depicted by  $e$ .

Finally, the  $I_{on}/I_{off}$  ratio is the ratio of the  $I_{DS}$  measured in the on state, i.e. when the device is fully operating and  $I_{DS}$  flowing in off state, i.e. when no current is detected in the channel. at a certain  $V_{GS}$ . As it represents the capability of an OFET to switch from the *on* state to the *off* state, and high  $I_{on}/I_{off}$  ratio is an extremely sought-after parameter. This ratio can be measured from transfer curves and is primarily dependent on device mobility, though dielectric capacitance and the semiconductor thickness can also have an impact on its measure.[54]

Another aspect to consider is that the device conductivity depends on the electrical outcome from the total resistance ( $R_{tot}$ ).  $R_{tot}$  is the sum of the resistance of the channel

region ( $R_{\text{channel}}$ ), i.e. the intrinsic resistance of the semiconductor, and the one of the electrode-semiconductor contact ( $R_{\text{contact}}$ ).  $R_{\text{contact}}$  reflects to the ability of a charge to be injected from the metallic electrode to the semiconductor. Thus, it depends on the potential energetic misalignment between the energy levels of the semiconductor, i.e. the energy barrier explained in **paragraph 2.1**. While  $R_{\text{contact}}$  is independent on the channel length  $L$ ,  $R_{\text{channel}}$  depends on it. Therefore, a high value of  $R_{\text{contact}}$  can limit the effective field-effect mobility  $\mu_{FE}$  in an OFET. Thus, the value  $\mu$  is general underestimated. A possible way to extract  $R_{\text{contact}}$  is the Transfer Length Method (TLM).<sup>[55]</sup> Similar devices with various channel lengths ( $L$ ) are built, then their total resistance  $R_{\text{tot}}$  is measured. Then, by plotting the channel length *vs.* the total resistance measured  $R_{\text{tot}}$  (**Figure 2.8**),  $R_{\text{contact}}$  is extrapolated at  $L=0$ .

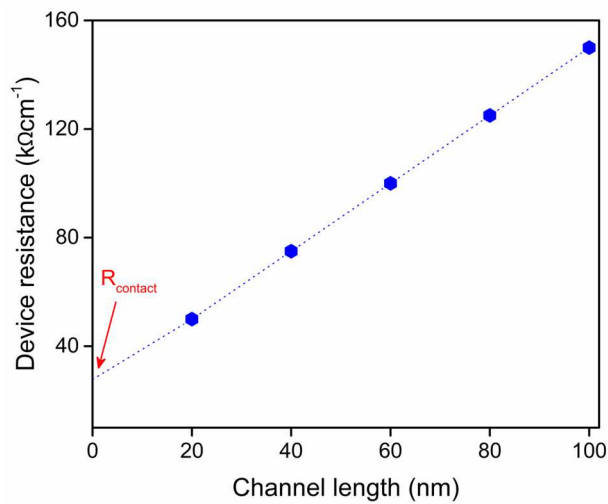


**Figure 2.8:** Example of a Transfer Length Plot (i.e. total resistance  $R_{\text{tot}}$  *vs.* channel length  $L$ ), used to extrapolate the contact resistance  $R_{\text{contact}}$ .

## 2.5 Photochromism in organic devices

In this paragraph the latest advances in the fabrication of bi- and multi-functional devices that rely on the combination of the photo-responsive nature of photochromic molecules and the (opto)electronic properties of organic and polymeric semiconductors will be reported. As stated above in **paragraph 1.3**, three are the kind of photochromic molecules that have already been exploited in combination with organic polymers, i.e. azobenzenes, spiropyrans and diarylethenes. Among them, diarylethenes (DAE) molecules do not thermally interconvert between the different states, and on the other hand, the write-erase process is robust as it can be achieved over a large number of cycles, without loss of photochromic performance. Thus, considering the emerging field of active optoelectronic materials and devices, the photochromic properties of DAEs have been demonstrated to represent key components in the construction of smart functional systems such as optical data storage<sup>[56-62]</sup> and optical switching devices.<sup>[63]</sup> Their optical readout depends on the feasibility of measuring differences in optical features between the two isomeric states in either fluorescence or absorbance. However, the main drawback is that, the optical readout is a destructive process since, when exposed to light the molecule's state is altered. The measurement of the electrical properties in molecular junctions,<sup>[64-65]</sup> where the isomerization of the photochromic molecule results into a binary conductance, could represent an alternative approach to that of the optical read out. However, single molecular junctions are not easy to fabricate and are susceptible to huge statistical fluctuations. Consequently, the process would be much more time consuming, advanced fabrication and deposition techniques would be required, as well as a tight control of the processing environment. DAE molecules have also been connected to nanoparticles or gold electrodes via the thiol groups.<sup>[66-67]</sup> However, because of the quenching of the excited state of the DAE when in close contact with the metal surface of the electrode, it has been shown that the entire photoswitchability cannot be maintained.<sup>[68]</sup>

Upon irradiation with light, significant changes of the electrical properties of bulk DAE materials, such as polymeric materials containing DAEs in their main chain<sup>[69-71]</sup>, single crystals, amorphous or polycrystalline films<sup>[72]</sup> have been detected. Therefore, in general, it is much easier to measure the conductance of these materials, but their applicability might be limited because of the poor electrical conductivity<sup>[73]</sup> or poor switching to the ring-closed isomer in the solid state.<sup>[71]</sup> In 2013, R. Hayakawa and co-workers<sup>[74]</sup> have realized an OFET exploiting a neat DAE layer as semiconductor, which has a 100-

switching ratio of the drain current between the photochemical *on*- and *off*-state. The device showed a hole mobility of only  $10^{-5} \text{ cm}^2 \text{ V}^{-1} \text{ s}^{-1}$ , though, which confirms the poor semiconducting properties of DAE. Considering this, DAE combination with organic semiconducting molecules allows a lower cost manufacturing, an easier processability; moreover, it can be applied in various device geometries. The group of K. Toshihide reported about an OFET device composed of a DAE layer within a layer of pentacene (used as semiconductor) and the dielectric with a considerably lower  $I_{\text{on}}/I_{\text{off}}$  ratio but a higher hole mobility. Such reduction in the  $I_{\text{on}}/I_{\text{off}}$  ratio was ascribed to the fact that the DAE layer scarcely was scarcely semiconducting thus resulting into a poor hole injection, upon light irradiation and isomerization to the ring-closed isomer.<sup>[75]</sup> To solve this issue and enhance the interaction of the photochrome with the organic semiconductor, F.L.E. Jakobsson and co-workers<sup>[76]</sup> theoretically suggested to blend both components into one layer. Indeed, by adjusting the energy levels of the polymer and semiconductor so that the HOMO level of the semiconductor lies below the HOMO level of the photochrome, the hole mobility within the semiconductor should decrease because of charge trapping at the photochrome sites. As a consequence of the isomerization, the HOMO level of the photochrome is decreased and the transport through the valence level of the semiconductor becomes possible. From experiments carried out on blends with F8BT<sup>[77]</sup> and polyoctylthiophene<sup>[78]</sup> as semiconducting matrices which shown a variation of photocurrent upon isomerization, it can be deduced that this principle might work also when using DAEs as photochromes. The first example in which the blending approach is used to implement DAEs in photomodulable electronic devices to reversibly photomodulate the current output was proposed by Samorì and co-workers.<sup>[79]</sup> Since then, DAE molecules have been exploited in combination with other emissive or hole- and electron-transporting layers to construct electro-optical devices such as OFETs,<sup>[80-82]</sup> OLEDs<sup>[83]</sup> and OLETs<sup>[84]</sup> that can be applied as high-density memory elements. In particular, photo-programmable transistor and OLETs based on DAE blend with semiconductor have shown a great potential to store information. Leydecker and his coworkers<sup>[85]</sup> demonstrated that over 256 (8 bit storage) distinct current levels was achievable in a single OFET device. These memory transistors exhibit robustness over 70 write–erase cycles and non-volatility exceeding 500 days. This technology was implemented on flexible substrates, therefore such devices can be possibly integrated into wearable electronics and smart nanodevices. Hou and her coworkers<sup>[84]</sup> fabricated three distinct classes of optically switchable OLETs emitting over the entire visible spectrum (green, red and blue), which can reversibly and remotely switch output

current and electroluminescence on and off by means of visible and ultraviolet light irradiation. Different emitting patterns can be written in high resolution and erased through a non-invasive and mask-free process. This technology potentially promising for optically gated highly integrated full-color displays and active optical memory.

## 2.6 Ferroelectric Organic Devices – Ferroelectric Memories

One of the major requirements for many applications of electronic devices is memory functionality. Examples of such application are RFID tags, i.e. tags which must be able to send and receive stored information, which is transmitted with radio signals.<sup>[86]</sup> RFID tags do not have a power source that is steadily available, but they derive power from the radio signal received.<sup>[87]</sup> In other words, they need to be based on a non-volatile technology which does not require memory refresh operation to prevent loss of information. Unlike write-once read-many (WORM) type of memory where the information stored using the resistive switching does not allow the device to return to its original state,<sup>[88]</sup> RFID tags and many other application requires to adjust the stored information. Therefore, in order to obtain a memory technology applicable everywhere, it is important to combine non-volatility and re-writability. So far, many attempts have been made towards non-volatile and rewritable memories able to facilitate a viable memory technology for a broad range of applications. Examples are memories based on metal-organic semiconductor-metal junctions,<sup>[89]</sup> electromechanical switches<sup>[90]</sup> and charge trapping effects in field-effect transistors.<sup>[91-92]</sup> An alternative and promising approach towards the realization of a low-cost memory technology relies on organic nonvolatile memory devices based on ferroelectricity. In the introductory chapter (**paragraph 1.4**), we introduced ferroelectricity and available organic ferroelectric materials and explained why this physical mechanism has a great potential for enabling an organic memory. In this paragraph, we bring the discussion a step ahead reviewing the most important examples of ferroelectric device, with a particular emphasis on ferroelectric capacitor and field effect transistors.

Among the different types of ferroelectric memory devices, the most straightforward is the thin film capacitor, in which the information is stored by aligning the direction of the internal polarization either up or down with an applied field. In order to retrieve the information, a switching voltage is applied to get a high or a low charge displacement current response. This read-out will depend on whether the internal polarization is aligned

or not with the direction of the applied field. Therefore, ferroelectric capacitors have a so-called destructive read-out since the stored information can be affected by the read operation. Capacitors based on the most used ferroelectric polymer P(VDF-TrFE) were investigated for electronic device applications. Given the relatively high coercive field of 50 MV/m of P(VDF-TrFE), sub-100 nm thick layers are required to arrive at a switching voltage below 10 V. Moreover, K. Kimura<sup>[93]</sup> and Y. Tajitsu<sup>[94]</sup> established that spin-coated films with a thickness below 100 nm have a remarkably slower ferroelectric response when compared to the bulk material. In other words, they figured out that P(VDF-TrFE) was not suited for low-voltage memory applications. In 1998, A. V. Bune and co.<sup>[95]</sup> showed that a ferroelectric response could be retained down to layer thicknesses of 15 nm, by preparing thin films through a Langmuir-Blodgett deposition. However, as the switching times of the aforementioned spin-coated films are longer by orders of magnitude, such films are probably even less appropriate for applications. To obtain this low-voltage switching behavior, a bottom electrode stack, including an interfacial layer of the conductive polymer PEDOT:PSS [poly(3,4-ethylenedioxythiophene):poly(styrene sulfonic acid)], and a top electrode consisting of vapor-deposited gold were employed.<sup>[96]</sup> Later, ferroelectric capacitors were demonstrated to have the same ferroelectric properties as the bulk material when the layer thickness was of 50 nm and a longer cycle endurance properties.<sup>[97]</sup> The polarization degradation, the so-called fatigue, arises to a value of 15 % after  $10^7$  cycles at an elevated temperature of 60 °C. This improvement is likely related to the use of conductive polymers as top and bottom electrodes instead of aluminum. Indeed, X-ray photoelectron spectroscopy (XPS) measurements have shown that aluminum reacts with P(VDF-TrFE) inducing the formation of non-ferroelectric or 'dead' layers near the electrode interfaces.<sup>[98-99]</sup> The appearance of such layers is shown in the slower switching kinetics. A possible way to circumvent this reaction is to use the more chemically inert element like gold. Indeed, this yielded to an improvement of the ferroelectric response of P(VDF-TrFE) thin-film capacitors as well.<sup>[100]</sup> However, a better understanding was provided by Zhao and coworkers<sup>[101]</sup> which have demonstrated that the fatigue is due to delamination of the top electrode, as shown in **Figure 2.9**. The origin is the accumulation of gases, expelled from the capacitor, under the impermeable top electrode. The gases are formed by electron-induced phase decomposition of P(VDF-TrFE). When the gas barrier is removed and the waveform is adapted, a fatigue-free ferroelectric capacitor based on P(VDF-TrFE) is realized. The capacitor can be cycled for more than  $10^8$  times, approaching the programming cycle endurance of its inorganic ferroelectric counterparts.

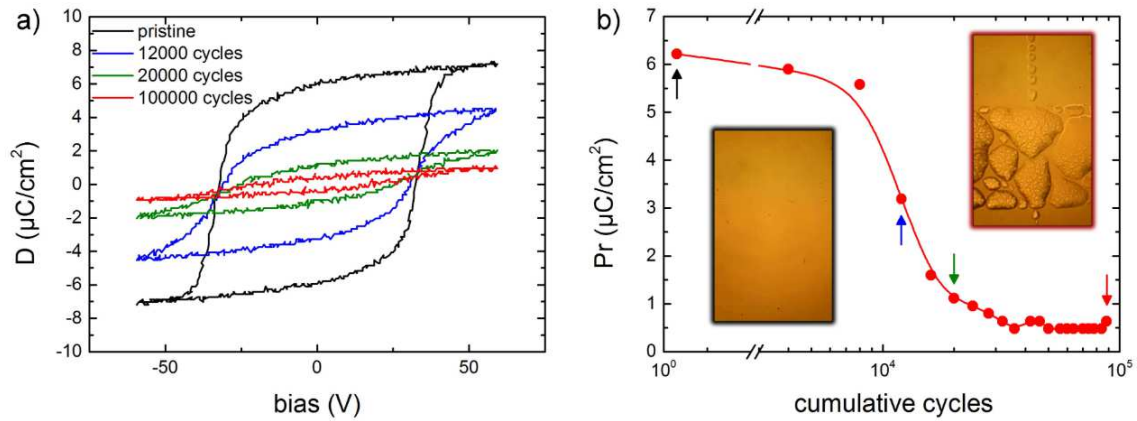


**Figure 2.9:** a) Cycling induces fatigue in ferroelectric displacement loops of a P(VDF-TrFE) ferroelectric capacitor with Au top electrode. b) The extracted remanent polarization as a function of the cumulative number of cycles. The inset shows optical micrographs of the pristine and degraded capacitor.<sup>[101]</sup>

Another drawback of ferroelectric capacitor (together with destructive read-out) that has to be taken into account while designing new memories is that the displacement current response scales with the surface area of the capacitors. This implies that at a certain point the current read-out cannot be detected anymore. A possible alternative way to overcome this scaling issue is the use of ferroelectric field-effect transistors (FeFETs). Generally, in FeFETs a ferroelectric insulator is exploited as a gate dielectric. The charge carrier density in the semiconductor channel can be controlled by the ferroelectric polarization resulting into memory functionality. Indeed, the ferroelectric spontaneous polarization aligned to the gate voltage induces either a high or a low semiconductor channel conductance that remains after removing the gate voltage. Using a low drain voltage that does not interfere with the ferroelectric polarization, the conductance can be measured at any time. In such a way, a nonvolatile memory combined with a non-destructive read-out functionality is given by FeFETs. FeFETs based on inorganic materials revealed issues with thermal stability and charge trapping at the ferroelectric-semiconductor interface.<sup>[102-103]</sup> Although the latter have been partially solved with the interposition of a thin layer of  $\text{HfO}_2$ ,<sup>[104]</sup> these remain the main issues hampering the implementation of inorganic FeFETs in commercial products. On the other hand, FeFETs based on organic material do not show particular interface problems mainly because the interactions inside the organic materials are relatively weak, i.e. *i.e.* van der Waals and/or hydrogen bonding. Nevertheless, their use requires other type of challenges.

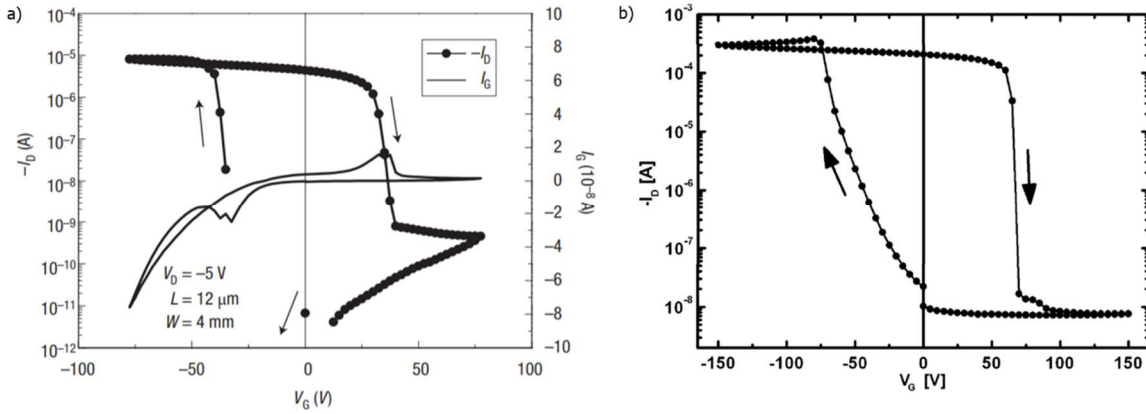


**Figure 2.10:** Hysteretic transfer characteristics for first examples of polymer FeFETs with P(VDF-TrFE) as the gate dielectric. a) Bottom-gate FeFET based on MEH-PPV semiconducting layer. The ferroelectric layer thickness is  $0.85 \mu\text{m}$ . The arrows show the clockwise hysteresis of the drain current consistent with accumulation and depletion of p-type charge carriers. The FeFETs had previously been brought into the off-state. The drain voltage  $V_D$ , channel length  $L$  and width  $W$  are  $-5 \text{ V}$ ,  $12 \mu\text{m}$  and  $4 \text{ mm}$ , respectively <sup>[105]</sup> b) Top-gate FeFET based on rr-P3HT semiconducting layer. The gate insulator layer thickness and dielectric capacitance are  $1.8 \mu\text{m}$  and  $5.5 \text{ nF/cm}^2$ , respectively. The drain voltage  $V_D$ , channel length  $L$  and width  $W$  are  $5 \text{ V}$ ,  $30 \mu\text{m}$  and  $6 \text{ mm}$ , respectively.<sup>[106]</sup>

In 2005, R. C. G. Naber et al.<sup>[105]</sup> showed the first FeFET relying on a polymer semiconductor, i.e. the amorphous polymer MEH-PPV [poly(2-methoxy,5-(2'-ethylhexyloxy)-*p*-phenylenevinylene)] wherein the observed bistability originated from the ferroelectricity of the gate dielectric. In order to quantify their memory, deeper investigation have been carried out. The switching time resulted in less than 1 millisecond. Regarding the memory retention, no variation in the drain current levels was observed throughout one week. Finally, the FeFET was able to sustain more than 1000 program and erase cycles without fatigue. Later, it was also demonstrated that the rather thick ferroelectric for this device could be thinned till having the device operating at  $15\text{V}$ .<sup>[107]</sup> In order to achieve such improvement, on one hand, P(VDF-TrFE) processing conditions were optimized to obtain high quality films appropriate for a gate dielectric. On the other hand, RR-P3HT [regioregular poly(3-hexylthiophene)] was exploited instead of MEH-PPV. In fact, its higher field-effect mobility, reaching a value of  $8 \times 10^{-3} \text{ cm}^2 \text{ V}^{-1} \text{ s}^{-1}$ , allowed the use of lower drain voltages to measure the channel conductance perturbing less the polarization state. However, compared to the previously reported values of mobility, i.e. up to  $0.1 \text{ cm}^2 \text{ V}^{-1} \text{ s}^{-1}$ , the mobility value achieved with rr-P3HT was still lower.<sup>[108]</sup> The reason

behind the obtained lower mobility is the high surface roughness of P(VDF-TrFE) films which can adversely affect the ferroelectric-semiconductor interface.<sup>[109]</sup> To solve this issue the layer stack was inverted, i.e. P(VDF-TrFE) was deposited onto rr-P3HT instead of the other way around.<sup>[106]</sup> In this way, the inherently smoother surface of rr-P3HT enables a better interface. This is an important result that eases a further reduction of the drain voltage used to sample the channel conductance during a read operation.

The major drawback for FeFET compared to other technologies is that the scaling down of the devices is hampered by a consequent increase of the depolarization field. Therefore, in order to achieve high-density memory arrays via solution-processed polymers, an alternative approach relies on the development of multi-level memories capable of programming more than two states in a cell. Therefore, the multilevel storage capacity is one of the most desirable advantages of the Fe-FET. Recently, Xiong and coworkers<sup>[110]</sup> demonstrated multilevel storage capacity on P(VDF-TrFE)/P3HT FeFET induced by partial polarization states of the ferroelectric layer. Such approach holds a great potential for the increase of data storage capacity in organic memory devices.

## References

- [1] W. R. Salaneck, S. Stafstrom, J. L. Brédas, *Conjugated polymer surfaces and interfaces: electronic and chemical structure of interfaces for polymer light emitting devices*, Cambridge University Press, **2003**.
- [2] W. R. Salaneck, K. Seki, A. Kahn, J.-J. Pireaux, *Conjugated Polymer and Molecular Interfaces: Science and Technology for Photonic and Optoelectronic Application*, CRC press, **2001**.
- [3] C. Kittel, P. McEuen, P. McEuen, *Introduction to solid state physics*, Wiley New York, **1996**.
- [4] E. Huber Jr, C. Kirk Jr, *Surface Science* **1966**, 5, 447.
- [5] H. Ishii, K. Sugiyama, E. Ito, K. Seki, *Adv Mater* **1999**, 11, 605.
- [6] C. Shen, I. G. Hill, A. Kahn, J. Schwartz, *J Am Chem Soc* **2000**, 122, 5391.
- [7] C. Shen, A. Kahn, J. Schwartz, *J Appl Phys* **2001**, 89, 449.
- [8] N. Koch, A. Kahn, J. Ghijsen, J.-J. Pireaux, J. Schwartz, R. Johnson, A. Elschner, *Appl Phys Lett* **2003**, 82, 70.
- [9] X. Crispin, V. Geskin, A. Crispin, J. Cornil, R. Lazzaroni, W. R. Salaneck, J.-L. Bredas, *J Am Chem Soc* **2002**, 124, 8131.
- [10] J. W. Niemantsverdriet, *Spectroscopy in catalysis: an introduction*, John Wiley & Sons, **2007**.
- [11] N. Koch, E. Zojer, A. Rajagopal, J. Ghijsen, R. L. Johnson, G. Leising, J. J. Pireaux, *Adv Funct Mater* **2001**, 11, 51.
- [12] L. Torsi, A. Dodabalapur, H. Katz, *J Appl Phys* **1995**, 78, 1088.
- [13] H. Sirringhaus, T. Kawase, R. Friend, T. Shimoda, M. Inbasekaran, W. Wu, E. Woo, *Science* **2000**, 290, 2123.
- [14] R. Street, A. Salleo, *Appl Phys Lett* **2002**, 81, 2887.
- [15] P. V. Necliudov, M. S. Shur, D. J. Gundlach, T. N. Jackson, *Solid State Electron* **2003**, 47, 259.
- [16] M. Waldrip, O. D. Jurchescu, D. J. Gundlach, E. G. Bittle, *Adv Funct Mater* **2019**, 1904576.
- [17] N. Stutzmann, R. H. Friend, H. Sirringhaus, *Science* **2003**, 299, 1881.
- [18] A. B. Chwang, C. D. Frisbie, *The Journal of Physical Chemistry B* **2000**, 104, 12202.
- [19] K. Seshadri, C. D. Frisbie, *Appl Phys Lett* **2001**, 78, 993.
- [20] J. Zaumseil, T. Someya, Z. Bao, Y.-L. Loo, R. Cirelli, J. A. Rogers, *Appl Phys Lett* **2003**, 82, 793.
- [21] G. Horowitz, R. Hajlaoui, D. Fichou, A. El Kassmi, *J Appl Phys* **1999**, 85, 3202.
- [22] T. W. Kelley, C. D. Frisbie, *Journal of Vacuum Science & Technology B: Microelectronics and Nanometer Structures Processing, Measurement, and Phenomena* **2000**, 18, 632.
- [23] P. Necliudov, M. Shur, D. Gundlach, T. N. Jackson, *J Appl Phys* **2000**, 88, 6594.
- [24] H. Klauk, G. Schmid, W. Radlik, W. Weber, L. Zhou, C. D. Sheraw, J. A. Nichols, T. N. Jackson, *Solid State Electron* **2003**, 47, 297.
- [25] H. Sirringhaus, N. Tessler, D. Thomas, P. Brown, R. Friend, in *Advances in Solid State Physics* 39, Springer **1999**, p. 101.
- [26] L. Bürgi, H. Sirringhaus, R. Friend, *Appl Phys Lett* **2002**, 80, 2913.
- [27] N. Tessler, Y. Roichman, *Appl Phys Lett* **2001**, 79, 2987.
- [28] T. Van Woudenberg, P. Blom, M. Vissenberg, J. Huiberts, *Appl Phys Lett* **2001**, 79, 1697.
- [29] Y. N. Gartstein, E. Conwell, *Chemical physics letters* **1996**, 255, 93.
- [30] V. Arkhipov, E. Emelianova, Y. Tak, H. Bässler, *J Appl Phys* **1998**, 84, 848.
- [31] S. M. Sze, K. K. Ng, *Physics of semiconductor devices*, John wiley & sons, **2006**.

- [32] J. Simmons, *Phys Rev Lett* **1965**, 15, 967.
- [33] U. Wolf, V. I. Arkhipov, H. Bässler, *Phys Rev B* **1999**, 59, 7507.
- [34] H. Martens, P. Blom, H. Schoo, *Phys Rev B* **2000**, 61, 7489.
- [35] H. Martens, H. Brom, P. Blom, *Phys Rev B* **1999**, 60, R8489.
- [36] E. L. Wolf, *Principles of electron tunneling spectroscopy*, Oxford University Press, **2012**.
- [37] S. Zhang, S.-H. Wei, A. Zunger, *Phys Rev B* **2001**, 63, 075205.
- [38] O. Mitrofanov, D. V. Lang, C. Kloc, J. M. Wikberg, T. Siegrist, W.-Y. So, M. Sergent, A. P. Ramirez, *Phys Rev Lett* **2006**, 97, 166601.
- [39] G. Horowitz, *Adv Mater* **1998**, 10, 365.
- [40] W. L. Kalb, T. Mathis, S. Haas, A. F. Stassen, B. Batlogg, *Appl Phys Lett* **2007**, 90, 092104.
- [41] J. H. Park, D. Hwang, J. Lee, S. Im, E. Kim, *Thin Solid Films* **2007**, 515, 4041.
- [42] F.-Y. Yang, K.-J. Chang, M.-Y. Hsu, C.-C. Liu, *J Mater Chem* **2008**, 18, 5927.
- [43] X.-H. Zhang, S. P. Tiwari, B. Kippelen, *Org Electron* **2009**, 10, 1133.
- [44] A. Kumar, M. V. Fischetti, T. H. Ning, E. Gusev, *J Appl Phys* **2003**, 94, 1728.
- [45] F. Li, A. Nathan, Y. Wu, B. S. Ong, *Organic Thin Film Transistor Integration: A Hybrid Approach*, Wiley, **2011**.
- [46] C. H. Kim, Y. Bonnassieux, G. Horowitz, *IEEE electron device letters* **2011**, 32, 1302.
- [47] J. Zaumseil, H. Sirringhaus, *Chem. Rev.* **2007**, 107, 1296.
- [48] C.-H. Kim, Y. Bonnassieux, G. Horowitz, *IEEE Transactions on Electron Devices* **2013**, 61, 278.
- [49] J. L. Z. Bao, *Organic Field-Effect Transistors*, CRC Press, New York **2007**.
- [50] O. D. Jurchescu, B. H. Hamadani, H. D. Xiong, S. K. Park, S. Subramanian, N. M. Zimmerman, J. E. Anthony, T. N. Jackson, D. J. Gundlach, *Appl. Phys. Lett.* **2008**, 92, 132103.
- [51] D. M. DeLongchamp, S. Sambasivan, D. A. Fischer, E. K. Lin, P. Chang, A. R. Murphy, J. M. J. Fréchet, V. Subramanian, *Adv. Mater.* **2005**, 17, 2340.
- [52] T. Masashi, K. Naoya, I. Shingo, N. Takashi, K. Takashi, N. Hiroyoshi, *Jpn. J. Appl. Phys.* **2014**, 53, 02BE02.
- [53] A. Wang, I. Kymissis, V. Bulović, A. I. Akinwande, *Appl. Phys. Lett.* **2006**, 89, 112109.
- [54] G. Horowitz, *Adv. Mater.* **1998**, 10, 365.
- [55] D. K. Schroder, *Semiconductor material and device characterization*, John Wiley & Sons, **2015**.
- [56] P. V. Ashrit, G. Bader, F. E. Girouard, V.-V. Truong, presented at Optical Data Storage Technologies **1991**.
- [57] Y. Ke, J. Chen, G. Lin, S. Wang, Y. Zhou, J. Yin, P. S. Lee, Y. Long, *Adv Energy Mater* **2019**, 9, 1902066.
- [58] F. Stellacci, C. Bertarelli, F. Toscano, M. C. Gallazzi, G. Zotti, G. Zerbi, *Adv Mater* **1999**, 11, 292.
- [59] D. A. Parthenopoulos, P. M. Rentzepis, *Science* **1989**, 245, 843.
- [60] S. Kawata, Y. Kawata, *Chem Rev* **2000**, 100, 1777.
- [61] A. J. Myles, N. R. Branda, *Adv Funct Mater* **2002**, 12, 167.
- [62] B. Yao, Y. Wang, N. Menke, M. Lei, Y. Zheng, L. Ren, G. Chen, Y. Chen, M. Fan, *Mol Cryst Liq Cryst* **2005**, 430, 211.
- [63] F. M. Raymo, *Adv Mater* **2002**, 14, 401.
- [64] I. Hnid, D. Frath, X. Sun, F. Lafolet, J.-C. Lacroix, *J Am Chem Soc* **2020**.
- [65] Z. Liu, S. Ren, X. Guo, in *Molecular-Scale Electronics*, Springer **2019**, p. 173.
- [66] S. Ishida, S. Kim, S. Kurihara, T. Fukaminato, presented at Molecular and Nano Machines II **2019**.

- [67] T. Mosciatti, M. G. del Rosso, M. Herder, J. Frisch, N. Koch, S. Hecht, E. Orgiu, P. Samorì, *Adv Mater* **2016**, 28, 6606.
- [68] D. Dulić, S. J. van der Molen, T. Kudernac, H. Jonkman, J. De Jong, T. Bowden, J. Van Esch, B. Feringa, B. Van Wees, *Phys Rev Lett* **2003**, 91, 207402.
- [69] T. Kawai, T. Kunitake, M. Irie, *Chem Lett* **1999**, 28, 905.
- [70] E. Kim, H. W. Lee, *J Mater Chem* **2006**, 16, 1384.
- [71] T. Kawai, Y. Nakashima, M. Irie, *Adv Mater* **2005**, 17, 309.
- [72] E. Kim, M. Kim, K. Kim, *Tetrahedron* **2006**, 62, 6814.
- [73] H. Lin, Z. Wei, J. Xiang, W. Xu, D. Zhu, *Chemphyschem* **2009**, 10, 1996.
- [74] R. Hayakawa, K. Higashiguchi, K. Matsuda, T. Chikyow, Y. Wakayama, *Acs Appl Mater Inter* **2013**, 5, 3625.
- [75] M. Yoshida, K. Suemori, S. Uemura, S. Hoshino, N. Takada, T. Kodzasa, T. Kamata, *Jpn J Appl Phys* **2010**, 49, 04DK09.
- [76] F. L. Jakobsson, P. Marsal, S. Braun, M. Fahlman, M. Berggren, J. Cornil, X. Crispin, *The Journal of Physical Chemistry C* **2009**, 113, 18396.
- [77] S. Perissinotto, M. Garbugli, D. Fazzi, C. Bertarelli, M. Carvelli, A. R. Srimath Kandada, Z. Yue, K. S. Wong, G. Lanzani, *Chemphyschem* **2011**, 12, 3619.
- [78] T. Koshido, T. Kawai, K. Yoshino, *Synthetic Met* **1995**, 73, 257.
- [79] E. Orgiu, A. M. Masillamani, J.-O. Vogel, E. Treossi, A. Kiersnowski, M. Kastler, W. Pisula, F. Dötz, V. Palermo, P. Samorì, *Chem Commun* **2012**, 48, 1562.
- [80] M. El Gemayel, K. Börjesson, M. Herder, D. T. Duong, J. A. Hutchison, C. Ruzie, G. Schweicher, A. Salleo, Y. Geerts, S. Hecht, E. Orgiu, P. Samorì, *Nat Commun* **2015**, 6.
- [81] K. Börjesson, M. Herder, L. Grubert, D. Duong, A. Salleo, S. Hecht, E. Orgiu, P. Samorì, *J Mater Chem C* **2015**, 3, 4156.
- [82] W. Rekab, T. Leydecker, L. Hou, H. Chen, M. Kirkus, C. Cendra, M. Herder, S. Hecht, A. Salleo, I. McCulloch, *Adv Funct Mater* **2019**, 1908944.
- [83] R. C. Shallcross, P. Zacharias, A. Köhnen, P. O. Körner, E. Maibach, K. Meerholz, *Adv Mater* **2013**, 25, 469.
- [84] L. Hou, X. Zhang, G. F. Cotella, G. Carnicella, M. Herder, B. M. Schmidt, M. Pätzelt, S. Hecht, F. Cacialli, P. Samorì, *Nat Nanotechnol* **2019**, 14, 347.
- [85] T. Leydecker, M. Herder, E. Pavlica, G. Bratina, S. Hecht, E. Orgiu, P. Samorì, *Nat Nanotechnol* **2016**, 11, 769.
- [86] E. Cantatore, T. C. Geuns, G. H. Gelinck, E. van Veenendaal, A. F. Gruijthuijsen, L. Schrijnemakers, S. Drews, D. M. De Leeuw, *IEEE Journal of solid-state circuits* **2006**, 42, 84.
- [87] S. Steudel, K. Myny, V. Arkhipov, C. Deibel, S. De Vusser, J. Genoe, P. Heremans, *Nat Mater* **2005**, 4, 597.
- [88] S. Möller, C. Perlov, W. Jackson, C. Taussig, S. R. Forrest, *Nature* **2003**, 426, 166.
- [89] J. C. Scott, L. D. Bozano, *Adv Mater* **2007**, 19, 1452.
- [90] Y. Li, A. Sinitskii, J. M. Tour, *Nat Mater* **2008**, 7, 966.
- [91] W. Y. Lee, H. C. Wu, C. Lu, B. D. Naab, W. C. Chen, Z. Bao, *Adv Mater* **2017**, 29, 1605166.
- [92] M. Fahlman, S. Fabiano, V. Gueskine, D. Simon, M. Berggren, X. Crispin, *Nature Reviews Materials* **2019**, 4, 627.
- [93] K. Kimura, H. Ohigashi, *Jpn J Appl Phys* **1986**, 25, 383.
- [94] Y. Tajitsu, *Jpn J Appl Phys* **1995**, 34, 5418.
- [95] A. V. Bune, V. M. Fridkin, S. Ducharme, L. M. Blinov, S. P. Palto, A. V. Sorokin, S. Yudin, A. Zlatkin, *Nature* **1998**, 391, 874.
- [96] R. Naber, P. Blom, A. Marsman, D. De Leeuw, *Appl Phys Lett* **2004**, 85, 2032.

- [97] H. Xu, J. Zhong, X. Liu, J. Chen, D. Shen, *Appl Phys Lett* **2007**, 90, 092903.
- [98] T. Furukawa, T. Nakajima, Y. Takahashi, *Ieee T Dielect El In* **2006**, 13, 1120.
- [99] R. Gysel, I. Stolichnov, A. K. Tagantsev, N. Setter, P. Mokrý, *J Appl Phys* **2008**, 103, 084120.
- [100] T. Nakajima, R. Abe, Y. Takahashi, T. Furukawa, *Jpn J Appl Phys* **2005**, 44, L1385.
- [101] D. Zhao, I. Katsouras, M. Li, K. Asadi, J. Tsurumi, G. Glasser, J. Takeya, P. W. Blom, D. M. De Leeuw, *Sci Rep-Uk* **2014**, 4, 5075.
- [102] J. Scott, *Berlin* **2000**.
- [103] T. Ma, J.-P. Han, *IEEE Electron Device Letters* **2002**, 23, 386.
- [104] N. Gong, T.-P. Ma, *IEEE Electron Device Letters* **2017**, 39, 15.
- [105] R. C. G. Naber, C. Tanase, P. W. M. Blom, G. H. Gelinck, A. W. Marsman, F. J. Touwslager, S. Setayesh, D. M. de Leeuw, *Nat Mater* **2005**, 4, 243.
- [106] R. Naber, M. Mulder, B. De Boer, P. Blom, D. De Leeuw, *Org Electron* **2006**, 7, 132.
- [107] R. Naber, B. De Boer, P. Blom, D. De Leeuw, *Appl Phys Lett* **2005**, 87, 203509.
- [108] H. Siringhaus, P. Brown, R. Friend, M. M. Nielsen, K. Bechgaard, B. Langeveld-Voss, A. Spiering, R. A. Janssen, E. Meijer, P. Herwig, *Nature* **1999**, 401, 685.
- [109] S. Steudel, S. De Vusser, S. De Jonge, D. Janssen, S. Verlaak, J. Genoe, P. Heremans, *Appl Phys Lett* **2004**, 85, 4400.
- [110] L. Xiong, Y. Chen, J. Yu, W. Xiong, X. Zhang, Y. Zheng, *Appl Phys Lett* **2019**, 115, 153107.

## Chapter 3. Materials and Experimental Techniques

### 3.1 Employed Semiconductors

#### 3.1.1 Poly (3-Hexylthiophene) (P3HT)

Over the last several decades, soluble  $\pi$ -conjugated polymer semiconductors have attracted considerable attention to replace amorphous silicon as the active layer in field-effect transistors (FETs) because of their interesting mechanical characteristics, remarkable optoelectronic properties as well as low-cost solution processability. The most investigated organic polymer semiconductors are those able to transport holes. In particular, the ones containing a polythiophene backbones, which are relatively stable in air after p-doping, are commonly used in optoelectronic devices.

Among them, poly(3-hexylthiophene) (P3HT) has been the most widely studied compound. P3HT is a polymer composed by thiophene monomers, exposing a short alkyl (i.e. hexyl) side chain on each repeat unit (**Figure 3.1, red box**). P3HT monomers are asymmetric with three different regioisomers that vary in the relative orientation of the two thiophene rings when coupled between the 2- and 5- position, i.e. 2-5' or head-to-tail coupling (HT), 2-2' or head-to-head coupling (HH), and 5-5' or tail-to-tail coupling (TT). Therefore, as shown in **Figure 3.1** the resulting polymers reveal a diverse regiochemistry, i.e. regioregular (RR-P3HT) or regiorandom (RRa-P3HT).

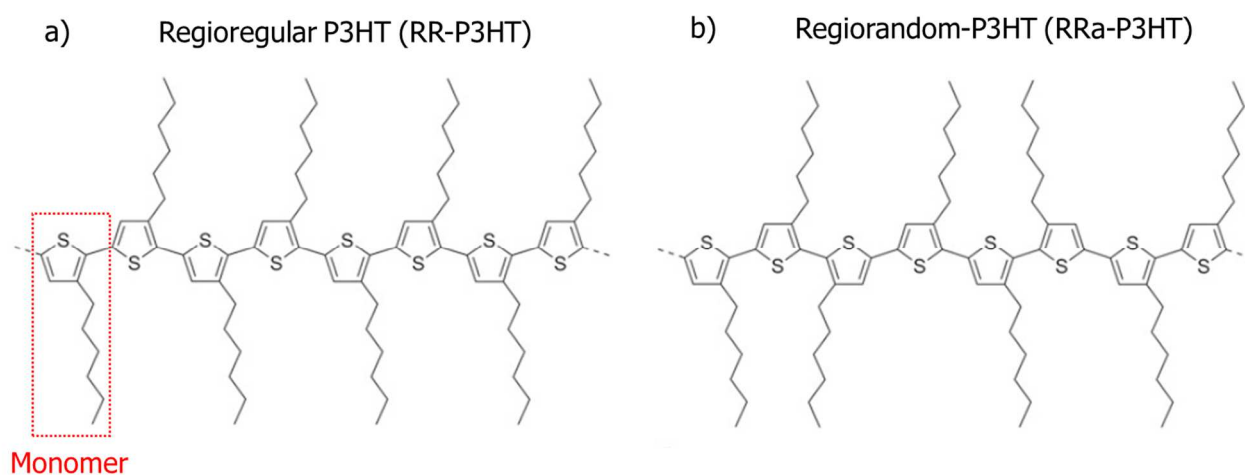


**Figure 3.1:** Structure of a) regioregular P3HT (RR-P3HT) and b) regiorandom P3HT (RRa-P3HT). In the red box the monomeric repeat unit of P3HT is highlighted.

RR-P3HT contains only HT couplings and thus can adopt a planar conformation with an extended  $\pi$  conjugation. On the other hand, in case of RRa-P3HT, as a result of the unfavorable HH coupling, the thiophene units twist away from planarity, resulting into a decrease of conjugation length.

RR-P3HT is highly soluble in organic solvents and one of its most fascinating properties originate from the tendency to form well-ordered crystalline domains.<sup>[1-2]</sup> It exhibits charge-carrier mobilities in the range  $10^{-2} - 10^{-1} \text{ cm}^2 \text{ V}^{-1} \text{ s}^{-1}$ .<sup>[3]</sup> P3HT is known to form two kind of structures within the crystalline domains, i.e. interdigitated and not interdigitated, with a spacing among the lamellar structures that varies between 1.6 and 1.3 nm.<sup>[4]</sup> Such forms usually coexist in a P3HT film and are embedded in amorphous matrixes that generate domain boundaries. In the crystalline domains of P3HT films, the intermolecular distances are reduced and strong intermolecular interactions provide an efficient hopping, respect to the amorphous areas. However, besides increasing the size of crystalline domains to facilitate the intermolecular transport, another key factor is the length of the polymeric chains, to improve the intramolecular transport. Thus, molecular weight ( $M_w$ ) of the polymer is an important parameter regarding the relationship between structure and device performance. The hole mobility has been found to increase with  $M_w$  on a series of P3HT films with  $M_w$  ranging from 20 to 50 kDa, observing a better transport through the chain along the backbone of the polymer, which connects the crystalline areas.<sup>[5-6]</sup> However, at higher molecular weights than 50 kDa, a slight decrease in mobility was observed, which is explained by the entanglement density increase in solution, leading to the formation of a large fraction of amorphous interlamellar regions in the film, featuring reduced interchain and intrachain transport, together with higher trap densities.<sup>[7]</sup> Overall, a decreased thin-film crystallinity severely deteriorates the charge transport performance but a decreased conjugated polymer regioregularity can provide for mechanical flexibility, which is favorable for the fabrication of flexible electronics.

### 3.1.2 Other polymers employed: PDVT-8 and PCD-TPT

Over the past few years, other organic soluble p-type polymer semiconductors have attracted a lot of interest because of their increased air stability and electrical performances, although P3HT is still among the most used. In this thesis, two other thiophene based copolymers, containing alkyl chains to improve the solubility, have been investigated, and their performances compared to that of P3HT: poly[2,5-bis(2-octyldodecyl)pyrrolo[3,4-

c]pyrrole-1,4(2H, 5H)-dione-alt 5,5'-di(thiophen-2-yl)-2,2'-(E)-2-(2-(thiophen-2-yl)vinyl)thiophene] (PDVT-8)<sup>[8]</sup> and poly[4-(4,4-dihexadecyl-4Hcyclopenta[1,2-b:5,4-b']dithiophen-2-yl)-alt-[1,2,5]thiadiazolo-[3,4c]pyridine] (PCD-TPT).<sup>[9]</sup> Their chemical formula is shown in **Figure 3.2**. PDVT-8 and PCD-TPT are donor–acceptor (D–A) type alternating copolymers with an electron-rich unit (donor) and an electron-deficient unit (acceptor) in the polymer backbone which provide low-bandgap.<sup>[10-11]</sup>

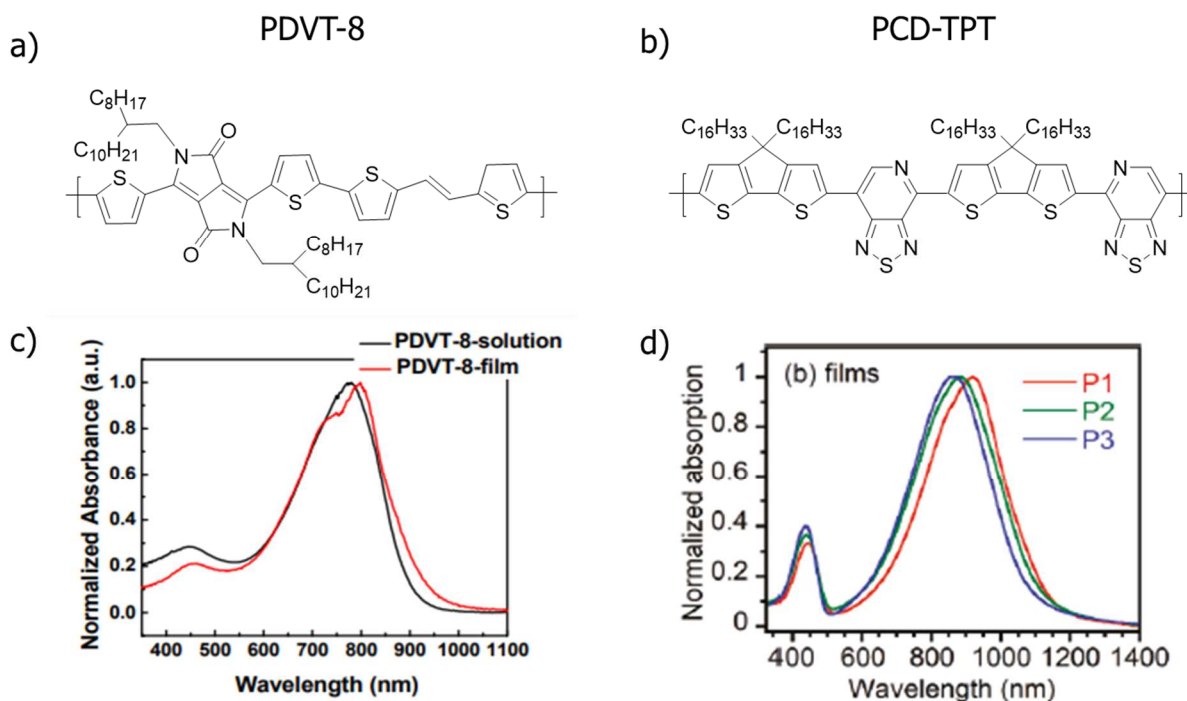


**Figure 3.2:** Chemical formula and absorption spectra of the other two polymers investigated in this work: a, c) PDVT-8, b, d) PCD-TPT. The absorption spectra are taken from literature.<sup>[8, 12]</sup>

The design of PDVT-8 is based on the combination the electron donating (*E*)-2-(2-(thiophen-2-yl)vinyl)thiophene (TVT) (and thiophene unit) block and the electron accepting diketopyrrolopyrrole (DPP) block. Such combination is effective because the polymer can show closer intermolecular  $\pi$ -stacking in view of the attractive forces between the donor and acceptor units, thus improving the crystallinity in the solid phase which as observed for P3HT facilitates the charge carrier transport.<sup>[13]</sup> Moreover, the presence of the DPP unit is advantageous for two main reasons: first, the oxygen atoms can form hydrogen bonds with the  $\beta$ -hydrogen atoms of the neighboring thiophene in the polymer backbone, thus strengthening the coplanarity of the main chains and consequently their intermolecular interactions;<sup>[14-15]</sup> second, the two bridging nitrogen atoms are a versatile center to attach the alkyl solubilizing functionality (2-octyldodecyl sidechains) that can

also tune the interactions of the polymer chains. This polymer has an optimal film-forming ability and highly uniform films can be obtained by simple spin-coating techniques. The reported field-effect mobility is between 2.0 and 4.5  $\text{cm}^2\text{V}^{-1}\text{s}^{-1}$ .<sup>[8]</sup>

PCD-TPT polymer consists of an alternation of dihexadecylcyclopentadithiophene groups (electron donating block), and thiadiazolopyridine units (electron accepting block), forming a thin and rigid conjugated system with two long and non-branched alkyl chains ( $\text{C}_{16}\text{H}_{33}$ ) for each thiadiazolopyridine group. The PCD-TPT polymer solution deposited via spin-casting PCD-TPT polymers generally tends to create uniform film with a fine crystalline microstructure. The reported field-effect mobility is between 0.06  $\text{cm}^2\text{V}^{-1}\text{s}^{-1}$ .<sup>[16]</sup>

Such polymers show better p-type semiconducting performances compared to P3HT as well as some electron-transport properties, thus being slightly ambipolar. Standard solvents used to dissolve both polymers are chloroform and chlorobenzene. The high solubility of these polymers in such solvents allows for an easy fabrication processing as discussed later in this chapter.

## 3.2 Preparation of OFETs and their characterization

### 3.2.1 Methods for solution deposition

Various techniques of deposition are available to obtain thin film materials of organic semiconductors. The technique exploited depends on the type of material as well as on its final application. The most commonly used are solution casting, in case of polymers, and high vacuum sublimation, in case of small molecules. As throughout this thesis, polymeric semiconductors have been used, the following discussion will be focused on solution casting approaches. With this method, in general, the polymer solution in an organic solvent is deposited on a substrate. Solution casting is a quick process since it is performed at ambient pressure, contrary to sublimation which requires vacuum. Nevertheless, there are certain parameters which must be considered to perform a controlled solution casting, including: (i) solvent properties like boiling point, viscosity and solubility of the polymers; (ii) polymer properties such as molecular weight, backbone and side chains type, and regio-regularity; (iii) conditions surrounding processing and post-processing periods, like the deposition environment and post-annealing substrate treatments etc. All these parameters dictate the resulting degree of crystallinity within the deposited film. <sup>[17]</sup>

An elementary solution processing method is drop-casting. Drop-casting is an interesting approach for laboratory experiments as they can be then easily integrated into industrial procedures because of the similarities with ink-jet printing technique. Such method relies on the dropping of the polymer solution onto the substrate. Depending on the size and wettability of the substrate, the volume of drop varies. Then, the solvent either evaporates naturally, or in case of low-volatile solvents, thermal annealing can be used to promote the process and the film is formed. The advantage of this process is that the entire material, which is deposited, remains on the substrate surface. Conversely, the disadvantage involves the limited control over the thickness of the film, its orientation, and uniformity, as the produced films usually remain very thick and inhomogeneous. Moreover, hydrodynamic forces, along with various other reasons, can cause formation of coffee rings during the solvent evaporation process, wherein to replenish the liquid evaporating, there is inducing of capillary flow from the center to the edges, causing accumulation at the boundaries. Coffee rings can be prevented by using a fully soluble solute or an anisotropic material.<sup>[18]</sup>

Spin-coating is the most commonly used method illustrated in **Figure 3.3**, wherein the substrate is held on a spin-coater by vacuum or magnetic forces. For this reason, this approach can only be used for rigid substrates. A drop of the solution or dispersion is applied onto the substrate surface, which is spun with a speed which ranges from a few hundreds of RPM to several thousand turns per minute. In our experimental procedure, the volume was ranging from 100  $\mu\text{l}$  to 250  $\mu\text{l}$  in case of a 225 mm<sup>2</sup> substrate. Depending on the solvent, the rotation speed and acceleration must be adapted because for instance, a small drop of highly volatile solvent could evaporate soon after the deposition. Moreover, most of the solution is swept off the surface and thus might get lost. Nevertheless, the advantage of this method is that the film thickness can be controlled by the concentration of employed solution and the spin-coating speed. Moreover more homogenous films are formed.<sup>[19]</sup> Finally, to completely evaporate the solvent, thermal annealing can be performed on the film, which will also improve the latter's long-range order.<sup>[20]</sup>

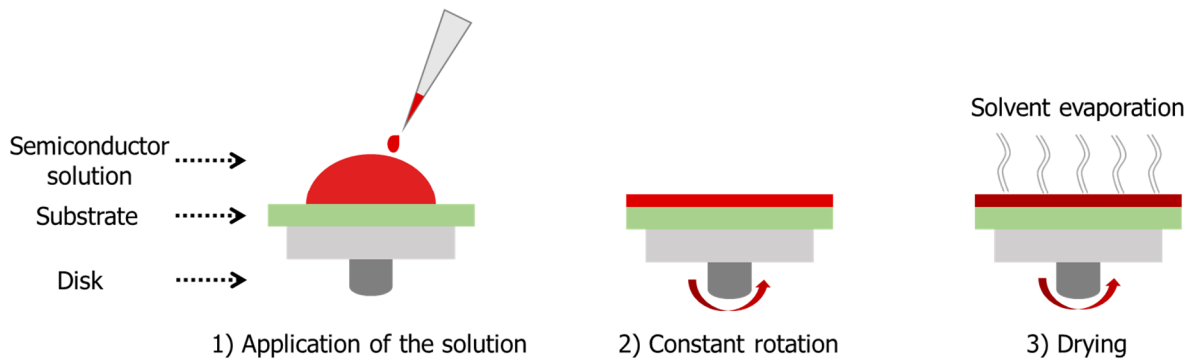


**Figure 3.3:** Schematic representation of the spin-coating method. a) drops of the solution are first deposited on the substrate; b) the disk start to rotate at a constant speed, leading to the covering of the whole substrate; c) still in rotation, the solvent is evaporated and thus the film formed.

### 3.2.2 Substrates for OFET

Basic substrates and pre-patterned substrates are used for the fabrication of bottom-contact, bottom-gate or bottom-contact, top-gate geometry transistors. Both substrates were purchased from IPMS Fraunhofer Institute. They are made of  $n^{++}$ -Silicon covered with 230 nm of thermally grown  $\text{SiO}_2$ , used as gate dielectric (15 nF capacitance). The pre-patterned substrates are provided with interdigitated electrode, with the same channel width  $W = 1$  cm and with four channel lengths:  $L = (20, 10, 5, 2.5) \mu\text{m}$ . In both cases they are treated with hexamethyldisilazane (HMDS) and protected with a layer of dicing resist. The first preparation step involves washing of the sample to remove the dicing resist. Firstly, the sample is rinsed with acetone, followed by complete immersion into an acetone bath. The sample is then placed in an ultrasonic cleaner for 20 minutes. After its removal from the latter, the sample is dried under nitrogen flow, and then immersed in an isopropanol bath inside an ultrasonic cleaner for another 20 minutes. Finally, the sample was removed and dried under nitrogen flow. This procedure leaves the sample free of dicing resist, but still functionalized with HMDS; to remove it, UV-Ozone cleaning must be used.

### 3.2.3 UV-Ozone treatment

In cases where there is adsorption of undesired molecules on the substrate's surface, the sample is placed in a Novascan PSD ozone cleaner and is subjected to intense short ultraviolet wavelengths using a mercury vapor lamp (184.7 and 253.7 nm) in the presence of oxygen. UV-Ozone cleaning is a well-known, simple and cheap method for cleaning insulator surfaces. The ozone cleaning process consists of multiple steps illustrated in **Figure 3.4**. Initially, dioxygen is dissociated into oxygen radicals and ozone molecules, when irradiated at 184.7 nm. Then, under 253.7 nm irradiation, ozone is decomposed, and oxygen radicals are generated. Thus, the oxygen radicals interact with the adsorbed layer on the substrate to produce volatile molecules comprising of  $\text{CO}_2$  and  $\text{H}_2\text{O}$  that leave the surface. Each substrate, after being irradiated for 5 minutes, is allowed 25 minutes of resting time, before being removed from the UV-Ozone cleaner.

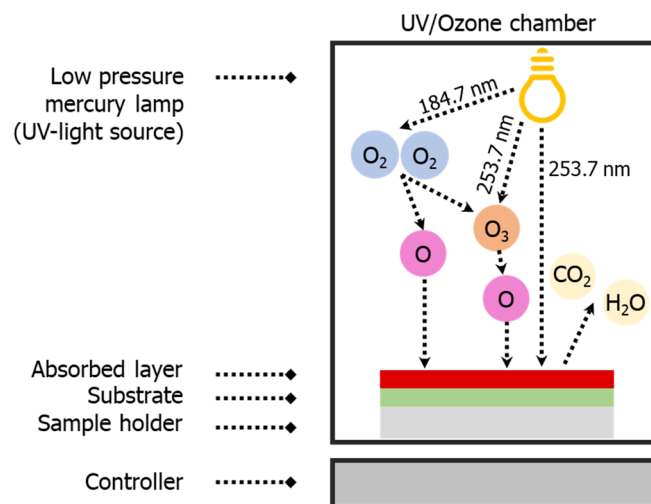


**Figure 3.4:** Schematic representation of an UV-Ozone chamber

### 3.2.4 Design of device's electrodes by photolithography

Photolithography is the main technology employed in microfabrication to precisely pattern device details on a substrate. Such technique is generally used when unconventional motifs need to be fabricated, i.e. when the commercially available shadow masks or already prepatterned devices are not suited for the measurement that needs to be carried out. **Figure 3.5** shows schematically a typical photolithographic process which contains in several steps in sequence. With this method it is possible to create very small patterns, down to a few tens of nanometers in size, with extreme precise control of the shape and

size of the object. The main limit is that it requires a flat substrate as it is not very effective on substrates that are not completely flat.

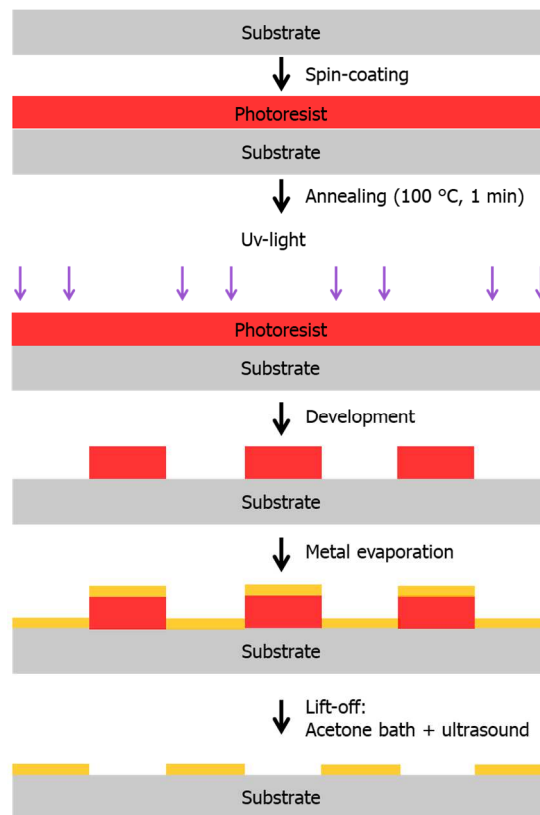


**Figure 3.5:** Fabrication procedure of a device with a positive photoresist with photolithographic process.

First, a photoresist is deposited onto the substrate surface by spin coating (generally at 300 rpm,  $1000 \text{ rpm s}^{-1}$  for 60). The photo resist-coated wafer is then annealed at  $100^\circ \text{C}$  for 1 min, in order to drive off excess of photoresist solvent. Then, a photomask is placed onto the photoresist and the layer is locally irradiated with a LaserWriter at  $\lambda = 405 \text{ nm}$  (LW405-A, Laser Writer from Microtech) which is focalized using a high precision lens with a beam spot of about  $2 \mu\text{m}$ . The energy of the laser beam is an important parameter to set: on the one hand, if the energy is too low, the final pattern will not be completely developed as not enough photons will reach the photoresist; on the other hands, if the energy is too high, the initial shape will be lost because of over-irradiation of the photoresist. Typical energy values to optimize the lithographic process are around  $1 \text{ J/cm}^2$ . There are two types of photoresist, positive and/or negative, depending of their reaction when exposed to UV light. With positive photoresists, UV light hits the part of material that will be removed. Indeed, the chemical structure of the polymer forming the photoresist changes and it becomes more soluble in the photoresist developer. On the other

hands, the areas of the photoresist that are not exposed to the UV light are left insoluble. In such a way, an identical copy of the original pattern is obtained. With negative photoresists instead, only areas that have been exposed to UV-light irradiation remains on the surface while the photoresist developer solution works to remove areas that have not been exposed. In this case, exposure to UV light causes the chemical structure of the photoresist to polymerize, becoming very difficult to dissolve. Hence, an inverse pattern needs to be applied on the wafer. In our case, a positive photoresist was used (AZ1505 from MicroChemicals), which upon irradiation is soluble in the AZ351B developer from MicroChemicals, whereas the non-irradiated part remains not soluble, thus forming an inverse pattern on the substrate. Finally, the metal is evaporated onto the designed surface and the substrate is immersed into a bath of hot acetone with ultrasounds to dissolve the remaining photoresist.

### **3.2.5 Electrodes deposition**

One of the last steps of the device fabrication in top-gate configuration is the deposition of the metallic electrodes (Au, Ag, Cr). To deposit metallic films, a physical vapor deposition setup is used (Plassis ME300B and Plassis ME400B). The desired metal is placed in a crucible (i.e. tungsten boat) in form of pellet while the substrates are fixed on the sample holder together with the shadow mask using small magnets. Basically, the metal is vaporized and allowed to re-condensate on the sample. The process involves pumping the chamber using a rotary pump which is then juxtaposed with a turbo pump, to ensure that the chamber is set into an ultra-high vacuum ( $P < 10^{-9}$  bar). The low pressure allows for the removal of residual gases on the surface, improving the films purity. Moreover, it prevents oxidative processes in case of sensible materials, such as chromium. When the target low pressure is reached, the metal is then heated by the application of a high electric current (typically between 130 A and 200 A) through the tungsten boat, till the metal melting point is reached. To ensure that the film is both homogenous and pure, the evaporation is stabilized at a desirable rate, before opening the shutter which allows the covering of the film. A quartz microbalance is used to examine the variation in mass by reading the frequency changes of a quartz crystal resonator. This allows for the evaluation and the adjustment of the evaporation rate to ensure optimal depositions. For depositing source and drain electrodes over a substrate made of silicon oxide, a thin layer (3 nm) of chromium was first evaporated over the substrate. This intermediate layer promotes optimal adherence of the electrodes onto the substrate. Interdigitated source and drain

electrodes made of gold were evaporated using a shadow mask covering the substrate, with channel lengths of 60, 80, 100 and 120  $\mu\text{m}$  and  $W = 10 \text{ mm}$  or created by photolithography process. Aluminum/gold gate electrodes were evaporated using shadow mask, in the case of top-gate devices. This evaporation process was conducted in a glovebox to avoid any undesired oxygen doping of the organic semiconductor.

### **3.2.6 Self-assembled monolayer functionalization**

Self-Assembled Monolayer (SAM) treatment involves the adsorption of a single layer of molecules on the treated surface. Suitably designed molecules react with solid supporting materials forming spontaneously a well-ordered monomolecular layer. Highly ordered crystalline SAMs can be obtained under thermodynamic control. Molecules employed for SAM treatment need to have an anchoring group which is able to covalently bind to the selected substrate, as well as a core that non-covalently interacts with the closed analogues, thus stabilizing the formed monolayer. Depending on the target surface, the anchoring groups that are needed to bind to gold electrodes and  $\text{SiO}_2$  surfaces are thiol and silane groups, respectively. Each of the SAMs effected the surface differently, particularly impacting the work function and the wetting of the surface. Further, the surface can be made less reactive, and the formation of larger crystal domains can be favored. In case of dielectric treatment, a self-assembled monolayer of octadecyltrichlorosilane (OTS) was used because of its high hydrophobic nature that does not induce almost any doping effect to the semiconductor deposited onto it. The OTS treatment which ran for 12 hours, involved immersion of the ozone-treated wafer into a 10 mM solution of OTS in toluene, which included 30 minutes of heating at 60  $^\circ\text{C}$  when the immersion began. Afterwards, the samples were rinsed multiple times with toluene and were also heated for 60 min at 60 $^\circ\text{C}$ .

### **3.2.7 Preparation of solutions for spin-coating**

Polymer semiconductors (purchased from Sigma Aldrich) were directly moved to a nitrogen-filled glovebox after reception and used as received. Diarylethenes (DAE) were kept in a fridge outside of the glovebox, shielded from light. Organic dielectrics were kept in air atmosphere. After removing potential dust using water and nitrogen flow, vials, caps, spatulas and magnetic stirrers used for solution preparation were also put in the glovebox.

Preparation of the solutions involved adding the selected material into the vial, kept in nitrogen atmosphere, which was previously weighted. After the addition of an adequate

volume of solvent with an Eppendorf micropipette, the vial was weighted again to help calculate the mass of the introduced material. Then, the solution was stirred and heated on a hotplate when applicable. Diarylethenes were weighted in air before their introduction in the glovebox. Blends of solutions were prepared in a vial by mixing separated solution of organic semiconductor material and diarylethene prepared at the same concentration, to obtain the desired ratio. Solutions were then stirred for several minutes before deposition.

Dielectric/ferroelectric materials require several preparation steps (shaking, filtering or crosslinking) which differ depending on the polymer. These steps are described in more details in the result and discussion chapters.

## 3.3 Characterization techniques

### 3.3.1 Surface Characterization

#### 3.3.1.1 Atomic Force Microscopy

Atomic Force Microscopy (AFM) has been exploited in this thesis to characterize the morphology of the films and to gain insight into their surface features. Such technique enables to map a surface with a high spatial resolution by monitoring areas from  $10^2 \text{ nm}^2$  to  $10^4 \text{ }\mu\text{m}^2$ . Differently from an optical or electron microscope, AFM does not create an image by focusing light or electrons onto a surface, but it exploits the van der Waals interactions between the sample surface and a sharp conical tip mounted at the edge of a flexible cantilever to generate a topographical map of the surface with a nanoscale resolution. The schematic representation of an atomic force microscope set-up is shown in **Figure 3.6**. The main components are, beside the sharp tip mounted on an oscillating cantilever, the piezoelectric scanner, the photodiode detector and the feedback loop.

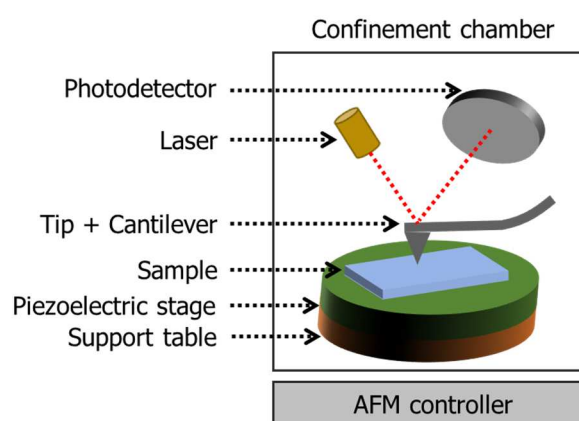


**Figure 3.6:** Schematic representation of an AFM set-up

AFM measurements can be done in two modes, i.e. contact and tapping mode. Because of its less invasive nature, tapping mode is the most common dynamic mode used in AFM when studying organic or polymeric soft materials, because lateral tip-sample forces are avoided. A tip with a canonical shape and a radius of curvature  $< 10 \text{ nm}$  is mounted on an oscillating cantilever. The cantilever is oscillated at (or near) its resonance frequency and scans the sample surface. The cantilever sample distance is controlled by keeping either the amplitude or the phase of the oscillating cantilever constant with a feedback electronic. The movement of the cantilever is read through a laser beam that hits the back side of the cantilever and is focused by an optical system. Its reflection is then recorded by a photo-

diode detector. Upon interaction with the material, Van der Waals forces, electrostatic forces, dipole-dipole interactions, etc., cause the cantilever oscillation amplitude to change. Each time the amplitude is reduced or increased, the tip is automatically raised or lowered, thus avoiding losing contact or damaging both the tip and the sample. Thus, the topography of the surface induces changes in the amplitude of the oscillations. This change is measured point by point. The final image is then obtained upon integration of measurements performed on  $N \times N$  points forming a square array and corresponds to the height of the surface at each coordinate. To control the position of the tip respect to the sample's surface along the X,Y and Z axes a scanner is used. The scanner is made of a piezoelectric material with the property of changing size when exposed to an external electric field. The scanning system consists of integrated 3 scanning elements which control the tip movement in the three directions X, Y and Z. The tip is considered near enough to the surface when completely focused with a CCD camera. It is extremely important to prevent external source of noises, which could result into low quality data. To prevent this, the AFM set up is placed in a Faraday cage, which protects the sample from electrostatic noise and the whole set up is fixed to a table able to provide vibration insulation. Moreover, being the faraday cage sealed, it also protects the AFM from acoustic noise.

AFM experiments in this thesis have been always performed in tapping mode. To increase the quality of the AFM results, each location has been recorded and analyzed twice. Moreover, to make sure that the observed topography is representative of the whole sample, several images have been recorded in different regions of the surface of the sample. On top of this, when AFM has been used to characterize transistors, the surface within the channel between source and drain, i.e. where the charge transport occurs, has been investigated, as it could be different compared to the rest of the device.

As aforementioned, AFM allows for quantitative measurement of the surface topography. Moreover, using the equation below, in which R is the height of the coordinate, the root means square surface roughness ( $R_{rms}$ ) can be calculated.

$$R_{rms} = \sqrt{\frac{1}{n} [(R_1)^2 + (R_2)^2 + \dots + (R_n)^2]} \quad \text{(Equation 3.1)}$$

### ***3.3.1.2 Mechanical contact profilometer***

To quickly measure the thickness of the deposited polymer films or electrodes, a technique generally used is the mechanical contact profilometer. In case of thin film, before starting this kind of measurement, the sample is scratched with a mechanical stylus to create a line by locally removing the deposited film. Such scratched line or the electrode feature is then localized using a camera, which is aligned perpendicular with the length of the profile.

Experiments were performed with a KLA-Tencor Alpha-Step IQ, a scanning instrument with a maximum scan length of 10 mm and a vertical resolution of few nanometers. To detect the vertical motion of the stylus, a transductive sensor is used. As the sensor is extremely sensitive and accurate, it is placed on an isolation table. The sample, which is positioned on a rotating platform, is moved under the stylus. A camera is used to monitor and adjust the sample's position, and the stylus is made to touch the surface of the film. The surface is examined at a high speed of 10-100  $\mu\text{m/s}$  across the gap in the material, and the height is measured using vertical motion sensor.

Post-measurement data analysis allows to set both the sides of the film at the same height ( $h_0$ ) around the gap, or to use the substrate as reference to determine the gap's height ( $h_G$ ). The difference between  $h_0$  and  $h_G$  not only attributes to the depth of the gap but is also equal to the thickness of the probed film. Further, to ensure that the film is uniform in thickness, measurements are taken across the sample and an average value is calculated.

### **3.3.2 Electrical Characterization**

The electrical characterization of all OFET devices was performed in a nitrogen-filled glovebox using a Keithley 2636A Dual-channel System Source Meter with a probe station set up (Cascade Microtech M150). The sample was set on a conductive chuck (sample stage) and two or three tungsten tips were connected to the device, depending on its geometry, and thus electrically connected to the source-meter unit (SMU). The connection was ensured through the mobile sample stage, micro-positioners and a camera integrated to the probe-station. Electrical measurements were controlled by the use of a self-made Matlab software for hysteresis measurements or LabTracer for basic transfer or output characterization.

The electrical characterization during illumination was carried out with the same probe station described above but supplemented by a monochromator Polychrome V, Till Photonics. To control the wavelength and the intensity of the irradiation the software Polycon was employed. The wavelength could be set between 300 and 700 nm, whereas the intensity can be adjusted using filter and the distance of the optical fiber was from the target device. The light exposure could be set with precision of microseconds. In case of short-pulse measurements a laser set-up was used. Irradiation consisted of 3 ns pulses at wavelength which was controllable with an Ekspla NT342. The intensity was  $85 \pm 17 \mu\text{Jcm}^{-2}$  for each 3 ns pulse at 313 nm. More details are provided in the related result and discussion chapter or in Appendix.

## References

- [1] M. Muthukumar, *The European Physical Journal E* **2000**, 3, 199.
- [2] P. J. Brown, D. S. Thomas, A. Köhler, J. S. Wilson, J.-S. Kim, C. M. Ramsdale, H. Sirringhaus, R. H. Friend, *Phys Rev B* **2003**, 67, 064203.
- [3] E. Orgiu, A. M. Masillamani, J.-O. Vogel, E. Treossi, A. Kiersnowski, M. Kastler, W. Pisula, F. Dötz, V. Palermo, P. Samorì, *Chem Commun* **2012**, 48, 1562.
- [4] Y. Olivier, D. Niedzialek, V. Lemaure, W. Pisula, K. Müllen, U. Koldemir, J. R. Reynolds, R. Lazzaroni, J. Cornil, D. Beljonne, *Adv Mater* **2014**, 26, 2119.
- [5] R. Noriega, J. Rivnay, K. Vandewal, F. P. V. Koch, N. Stingelin, P. Smith, M. F. Toney, A. Salleo, *Nat Mater* **2013**, 12, 1038.
- [6] A. Zen, M. Saphiannikova, D. Neher, J. Grenzer, S. Grigorian, U. Pietsch, U. Asawapirom, S. Janietz, U. Scherf, I. Lieberwirth, *Macromolecules* **2006**, 39, 2162.
- [7] A. M. Ballantyne, L. Chen, J. Dane, T. Hammant, F. M. Braun, M. Heeney, W. Duffy, I. McCulloch, D. D. C. Bradley, J. Nelson, *Adv Funct Mater* **2008**, 18, 2373.
- [8] H. Chen, Y. Guo, G. Yu, Y. Zhao, J. Zhang, D. Gao, H. Liu, Y. Liu, *Adv Mater* **2012**, 24, 4618.
- [9] C. Luo, A. K. K. Kyaw, L. A. Perez, S. Patel, M. Wang, B. Grimm, G. C. Bazan, E. J. Kramer, A. J. Heeger, *Nano Lett* **2014**, 14, 2764.
- [10] H. Zhou, L. Yang, S. Liu, W. You, *Macromolecules* **2010**, 43, 10390.
- [11] H. Zhou, L. Yang, S. Stoneking, W. You, *Acs Appl Mater Inter* **2010**, 2, 1377.
- [12] L. Ying, B. B. Hsu, H. Zhan, G. C. Welch, P. Zalar, L. A. Perez, E. J. Kramer, T.-Q. Nguyen, A. J. Heeger, W.-Y. Wong, *J Am Chem Soc* **2011**, 133, 18538.
- [13] H. N. Tsao, D. M. Cho, I. Park, M. R. Hansen, A. Mavrinskiy, D. Y. Yoon, R. Graf, W. Pisula, H. W. Spiess, K. Müllen, *J Am Chem Soc* **2011**, 133, 2605.
- [14] O. P. Lee, A. T. Yiu, P. M. Beaujuge, C. H. Woo, T. W. Holcombe, J. E. Millstone, J. D. Douglas, M. S. Chen, J. M. Fréchet, *Adv Mater* **2011**, 23, 5359.
- [15] Y. Qiao, Y. Guo, C. Yu, F. Zhang, W. Xu, Y. Liu, D. Zhu, *J Am Chem Soc* **2012**, 134, 4084.
- [16] T. Leydecker, M. A. Squillaci, F. Liscio, E. Orgiu, P. Samorì, *Chem Mater* **2018**, 31, 6491.
- [17] J. L. Z. Bao, *Organic Field-Effect Transistors*, CRC Press, New York **2007**.
- [18] S. Pengzhan, M. Renzhi, W. Kunlin, Z. Minlin, W. Jinquan, W. Dehai, S. Takayoshi, Z. Hongwei, *Nanotechnology* **2013**, 24, 075601.
- [19] (Ed: Ossila), Ossila, 2014.
- [20] J. Rivnay, R. Steyrleuthner, L. H. Jimison, A. Casadei, Z. Chen, M. F. Toney, A. Facchetti, D. Neher, A. Salleo, *Macromolecules* **2011**, 44, 5246.

## Chapter 4. Investigation of DAE trapping mechanism using Charge Modulation Spectroscopy (CMS)

By blending diarylethene (DAE) photochromic compounds with P3HT, the output current of a field-effect transistor could be photomodulated upon irradiation at specific wavelengths.<sup>[1-3]</sup> Indeed, photoswitching of the DAE introduced a further remote control to change the device current intensity.<sup>[4-6]</sup>

An open question still holds regarding the nature of the interaction between polarons transported through the conjugated backbone of the host polymer matrix and the DAEs moieties in both their different isomers. Understanding how the electronic charge trapping, i.e. the trapping generated when the DAE is in its closed-isomer form, by the mutual energy level alignment in the DAE/polymer, occurs is of utmost importance to improve optically controlled memory devices.<sup>[3]</sup> A better understanding of polaron-DAE interactions can be investigated by means of charge modulation spectroscopy (CMS). This Chapter is focused on the charge transport modulation in a field-effect transistor due to DAE opening and closure in the channel forming at the interface with the dielectric by s specific attention paid to the comparison of the CMS spectra recorded on P3HT/DAE-Me blends compared to those obtained with neat P3HT transistors.

### 4.1 Charge modulation spectroscopy (CMS): Basic working principles

Charge modulation spectroscopy is an electro-optical spectroscopic technique that allows the *in situ* investigation of the charge carriers present in the conducting channels of an organic field-effect transistors.<sup>[7]</sup> It measures the variation in optical transmittance induced by charges by directly probing the accumulation of charges at the burning interface of semiconductor and dielectric layer where the conduction channel forms.<sup>[8]</sup> Investigation of charge carriers on interfacially doped P3HT films using CMS technique has been reported in different manuscripts.<sup>[9-11]</sup> Effectively, Charge Modulation Spectroscopy is employed as standard characterization technique to investigate semiconductor polymers<sup>[12-14]</sup> and blends.<sup>[15]</sup> The introduction of a charge causes the formation of new states in the band gap of the semiconductor, which can be observed by the changes in the optical absorption spectra. In a metal-semiconductor-insulator structured sample, there is a change observed in the concentration of charge carriers at the semiconductor/insulator's interface, when voltage is applied. A negative voltage applied to

the gate electrode causes holes to gather at the interface of the semiconductor–dielectric. Conversely, a positive voltage at the gate contact increases the depletion layer at the bulk of the semiconductor from the interface. The CMS experiment turns into an electro absorption experiment (EA), when full depletion occurs along the width of the semiconductor. The oscillator strength of the features in the absorption spectra is not affected by charges that are either trapped at the insulator/polymer interface or leak through the insulator.<sup>[16]</sup> A CMS spectrum is used to plot the changes in optical transmission as a result of the changes in the wavelength of the incident light. The spectra are collected using different gate voltages. CMS uses non-polarized light, making this technique sensitive to both transitions along the polymer chain and the direction of the interchain stacking.

Electroabsorption (EA) is the process, wherein when an external electric field is applied on a media, there is a change in its absorption properties which results in a red shift of the absorption edge. This process is related to the Stark effect. <sup>[17]</sup> Both the EA and the CMS processes can be carried out using the same setup. When a device is biased until full depletion, the electro absorption peak dominates the spectra and simultaneously features will disappear. During full depletion, the major focus is on qualitative and quantitative changes in the EA peak due to the field. In this case, the screening of the applied field is weak due to the low charge concentration. In contrast, CMS scrutinizes the absorptions resulted by charges, which are shifted 180° in phase to the EA signal (or opposite sign in the spectra). While charges are being accumulated in the device, the CMS signal rises with the increasing charge concentration.

The absorption of light by a material is described by Lambert-Beer's law:

$$I = I_0 e^{-\alpha d} \quad \text{(Equation 4.1)}$$

where I is the intensity of the light, I<sub>0</sub> is the intensity of the incident light. As in our case we measure transmittance we refer to the intensity of the transmitted light as T and T<sub>0</sub> is the intensity of incident light. α is the absorption coefficient and d is the thickness of the thin film.

The field induced change of the absorption coefficient Δα(E) can be described as the difference between the absorption in the presence of an electric field α<sup>F</sup> and the unperturbed absorption α(E). The field induce change in the absorption intensity ΔI is defined by:

$$\Delta\alpha(E) = \alpha^F(E) - \alpha(E) = -\frac{1}{d} \ln \frac{\Delta T}{T_o} \quad (\text{Equation 4.2})$$

The change in the transmittance is proportional to the actual electric field which is given by the photon energy F dependent imaginary part of the third order non-linear susceptibility  $\text{Im} \chi^{(3)}(E)$ . This can be derived from the dependence of  $\chi$  (susceptibility) on the applied electric field.

$$\frac{\Delta T}{T_o} \sim \text{Im} \chi^{(3)}(E) F^2 \quad (\text{Equation 4.3})$$

When an AC voltage modulating an DC voltage is applied to a semiconductor film, the potential applied to the film can be described by:

$$V = V_0 + V_{AC} \sin(\omega t) \quad \text{with} \quad V_0 = V_{DC} - V_i \quad (\text{Equation 4.4})$$

Where  $\omega$  is the frequency of the AC voltage and t is time. The combination of **equation 4.3** with **equation 4.4** yields

$$\frac{\Delta T}{T_o} \sim \text{Im} \chi^{(3)}(E) (V_0 + V_{AC} \sin(\omega t))^2 \quad (\text{Equation 4.5})$$

$$\frac{\Delta T}{T_o} \sim \text{Im} \chi^{(3)}(E) (V_{DC} - V_i + V_{AC} \sin(\omega t))^2 \quad (\text{Equation 4.6})$$

$$\begin{aligned} \frac{\Delta T}{T_o} \sim \text{Im} \chi^{(3)}(E) & \left( \frac{1}{2} V_{AC}^2 (1 - \cos(2\omega t)) + 2V_0 V_{AC} \sin(\omega t) \right. \\ & \left. + V_0^2 \right) \end{aligned} \quad (\text{Equation 4.7})$$

This last equation can be divided into two parts, one dependent on the first harmonic while the other part is dependent on the second harmonic:

$$\frac{\Delta T}{T_o}(\omega) \sim (V_{DC} - V_i) V_{AC} \sin(\omega t) \quad (\text{Equation 4.8})$$

$$\frac{\Delta T}{T_o}(\omega) \sim V_{AC}^2 \cos(2\omega t) \quad (\text{Equation 4.9})$$

The first harmonic response is proportional to the product of the electric field  $V_0$  and the AC amplitude, the second harmonic signal depends upon the square of the AC amplitude.

## 4.2 Experimental setup and measurement technique

The normalized transmittance variation ( $\Delta T / T$ ), which was the result of a modulated voltage, is measured to collect CMS spectra. The source and the drain electrodes were kept at 0 V during the measurements, while constant voltage  $V$  is applied at the gate electrode together with a modulating voltage  $V_{ac}$  at a frequency  $\sim 1$  kHz. Each sample had different offset voltage and modulation amplitude. A tungsten lamp was monochromated for the probing light. Once the light was focused on the device, a silicon photodiode was used to collect and reveal the transmitted light. A trans-impedance amplifier was used to amplify the electrical signal (Femto DHP-100) which was revealed using a DSP Lock-in amplifier (Stanford Instrument SR830). The sample was placed inside the chamber which was evacuated and was a vacuum ( $\approx 10^{-5} - 10^{-6}$  mbar), inside which the measurements were performed.

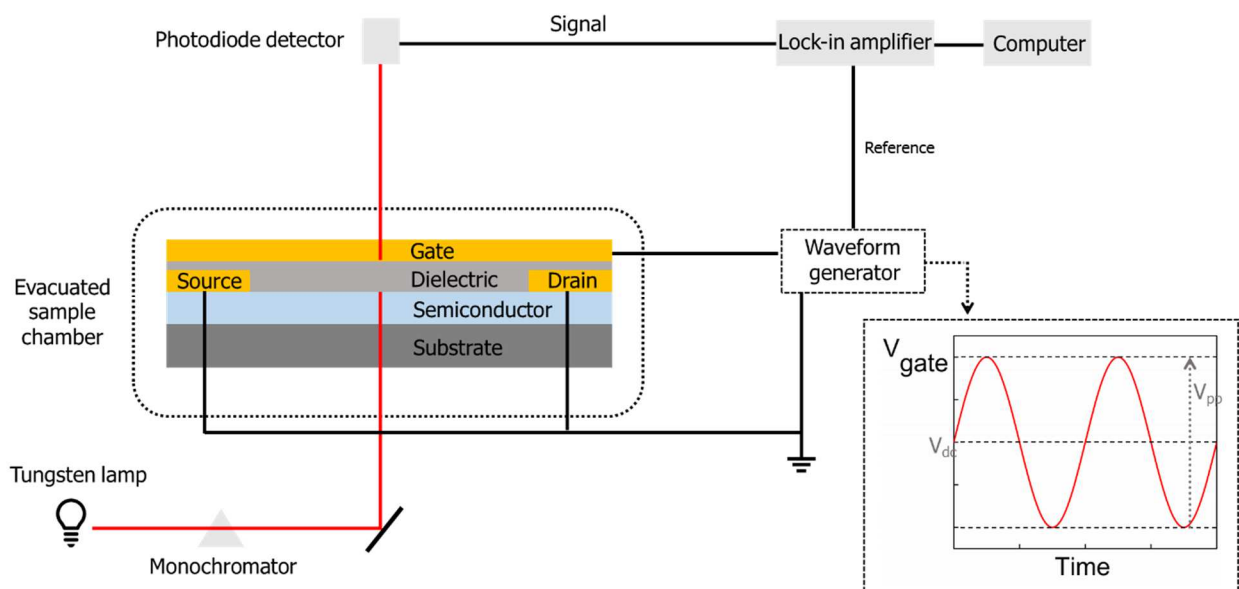


**Figure 4.1:** Schematic sketch of CMS set-up

CMS measurements were carried out in the framework of a secondment at IIT in Milan.

### 4.3 Device fabrication and characterization

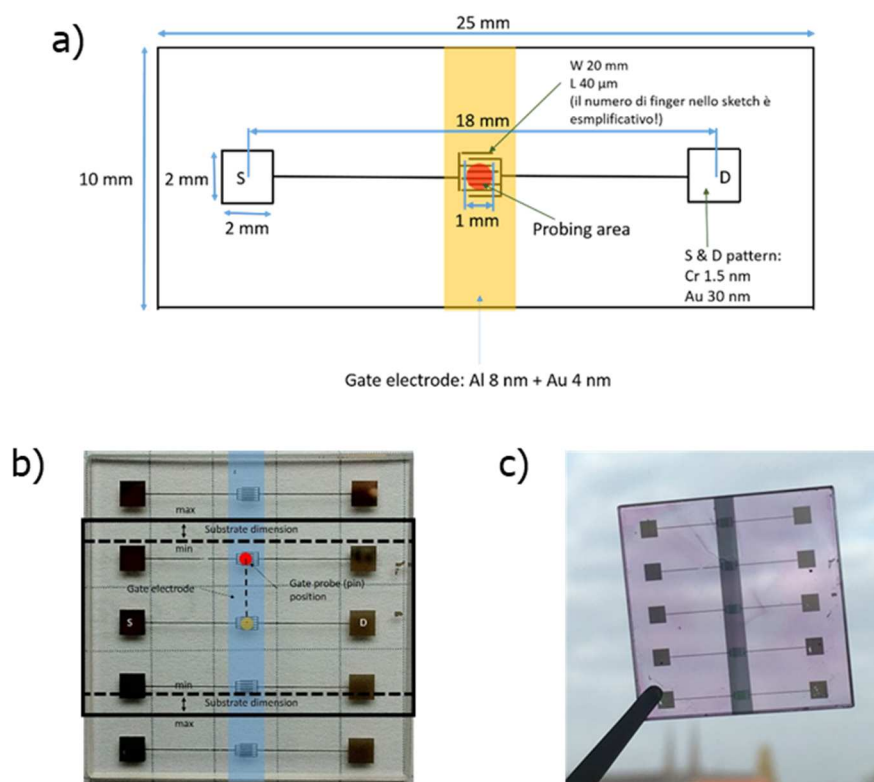


**Figure 4.2:** a) Layout and b) optical images of bottom source and drain electrodes design for CMS measurements and c) picture of the top-gate transistors based on pure P3HT with semitransparent top gate electrodes.

Interdigitated 30 nm-thick Au electrodes ( $W = 10$  mm  $L = 40$   $\mu\text{m}$ ) were fabricated on 25 mm x 25 mm quartz substrate by means of photolithography. The pattern in **Figure 4.2a** was designed to be compatible with the CMS set-up at the Istituto Italiano di Tecnologia (IIT) in Milan. A 10-30 nm thick P3HT layer were deposited by spin-coating in the glovebox. A 700-nm-thick Cytop or 300-nm-thick PMMA film was used as gate dielectric layer because their deposition processes are compatible with the semiconducting layer which is placed underneath. Finally, a top gate (Al 8 nm + Au 4 nm) were evaporated through a shadow mask as described in **Chapter 3**. The thickness of the gate electrode was tuned in order to obtain a conductive layer suitable for gating which is also semi-transparent. The transmittance through the gate electrode is about 20%, enough to perform CMS measurement. The fabrication process was improved by running several trials and fine-tuning the deposition process accordingly to the electrical characterization results.

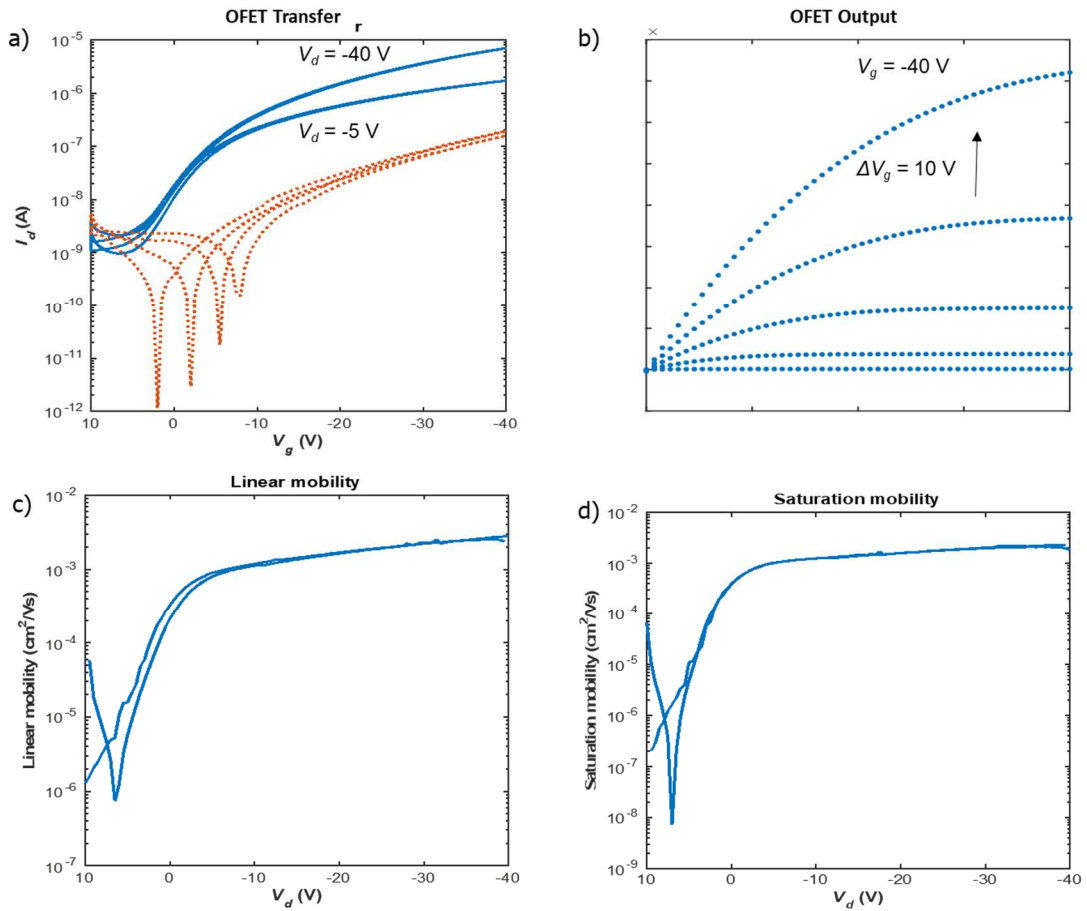


**Figure 4.3:** a) Transfer and b) output characteristics of P3HT FET for CMS measurements. The dotted red line in panel a) is the leakage current. Linear and saturation mobilities are reported in c and d respectively.

The output characteristic of an optimized device is shown in **Figure 4.3b**. No issues with charge injection could be observed since the drain current has a linear behavior close to the 0 V. The transfer characteristic in **Figure 4.3a** exhibits a relatively low  $I_{\text{ON}}/I_{\text{OFF}}$  ratio of approx.  $10^3$ . Top-gate bottom-gate devices are known to have higher leakage current that can lead to reduced  $I_{\text{ON}}/I_{\text{OFF}}$  ratio. In order to exclude that any detrimental oxygen doping effect was affecting device performances, we indirectly checked the doping level by plotting the  $\sqrt{I_{\text{ds}}}$  vs  $V_g$  and analyzed the threshold voltage ( $V_{\text{th}}$ ) shift. A  $V_{\text{th}}$  equals to 0 V is indicating that the doping level is low (virtually zero). Moreover, we cross-checked this result by spin-casting the same P3HT solution on Fraunhofer pre-patterned substrate and testing the electrical performance of this standard configuration. In this latter case, the  $I_{\text{ON}}/I_{\text{OFF}}$  ratio is as high as  $10^5$  meaning that only the leakage current is limiting the OFF current.

#### 4.4 CMS spectra acquired on pristine P3HT-based devices

After electrical characterization, the device is mounted in a vacuum chamber with in-house designed optics for these CMS measurements. Indeed, the vacuum chamber has two opposite quartz windows which allow the monochromatic light to enter and exit the chamber crossing the device and three fixed contact pins matching the device geometry which create electrical contacts with device electrodes allowing to probe the device from the outside. The device was then transferred outside the glovebox onto the optical table where the CMS set-up is sitting. Please refer above for more details on CMS set-up and measurement conditions. Initially, preliminary tests were performed on devices exhibiting lower electrical performances than the devices presented above in the experimental section, resulting in a CMS spectrum dominated by electroabsorption (EA). The electroabsorption signal can be isolated operating the FET in depletion. In depletion, provided that the device is off, the signal can be mainly assigned to EA since negligible charge modulation is expected. **Figure 4.4** shows the CMS spectra measured while probing the device with constant negative bias at -60V and variable  $V_{pp}$  ranging from 20 V to 60 V in comparison with the spectrum measured at constant positive bias, i.e. under depletion regime.

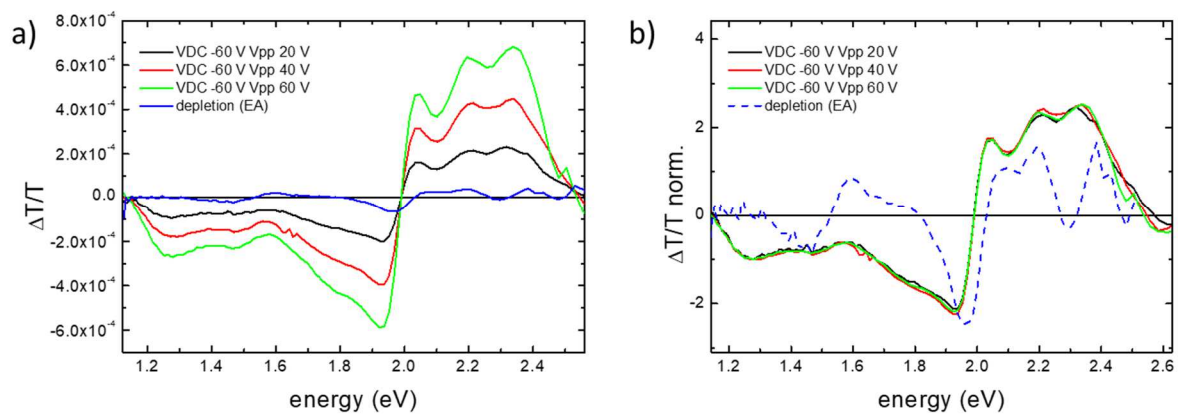


**Figure 4.4:** CMS spectra of the pure P3HT in PMMA transistor. Spectra measured while operating the device in accumulation (-60V) or in depletion (+60V) are compared. The spectra are normalized to allow direct comparison.

When an electric field is applied across a semiconductor, electroabsorption could be induced and hence it could play a role in CMS experiments. Electroabsorption is associated with the Stark effect, which can induce a shift of the material absorbance due to built-in fields or permanent dipole moments. In a  $\Delta T$  experiment, the electroabsorption fits the

first derivative of the absorption spectrum of the semiconductor as already explained in paragraph 4.2. In CMS measurements this means that electroabsorption features can overlap (and cover) with polymer absorption bleaching and charge absorption. This is what happened in the preliminary measurements shown in **Figure 4.4** as a consequence of non-idealities present in the devices, i.e.: photo-oxygen doping, contact resistance, etc. Indeed, the strong EA signal covering polaronic/bleaching features is possibly related to strong contact resistance, small polaronic signal or not fully transparent source and drain electrodes. The fine-tuning of the fabrication process allowed to eliminate these limitations. Spectra acquired on new devices showed neat signals and negligible EA component.

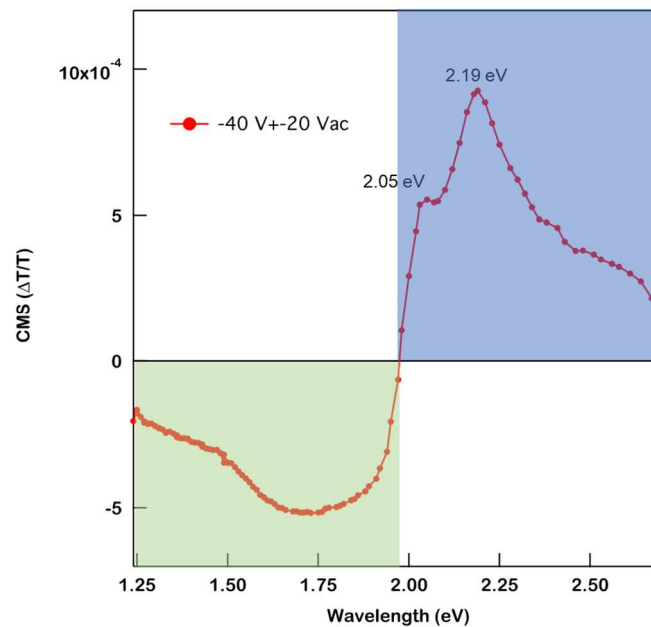


**Figure 4.5:** CMS spectrum of the pure P3HT in Cytop transistor. The applied dc bias was  $-40\text{ V} \pm 20\text{ V}$  ac with a modulation frequency of  $\sim 1\text{ kHz}$ . The blue shaded area highlights the Bleaching of the neutral absorption of P3HT, while the green shaded area the Polaronic charge absorption

The CMS spectrum of a pure P3HT transistor taken in accumulation  $-40\text{ V} \pm 20\text{ V}$  ac at room temperature with a modulation frequency of  $\sim 1\text{ kHz}$  is shown in **Figure 4.5**. The data collected are in agreement with P3HT CMS spectra from literature. <sup>[18]</sup> The part of the spectrum characterized by  $\Delta T/T < 0$  is defined by charge modulation features associated with the charge carriers present in the accumulation layer. The main peak is seen at  $1.65\text{ eV}$  and a shoulder is partially observed at ca.  $1.34\text{ eV}$ . The region of the spectrum at energies greater than  $1.97\text{ eV}$ , where  $\Delta T/T > 0$ , shows the bleaching of the main absorption feature

of the  $\pi$ - $\pi^*$  transition. This increase in transmission is due to the removal of neutral segments from the conjugated backbone and the associated  $\pi$ - $\pi^*$  optical transition upon charging. The bleaching signal shows a structure with features at 2.05, 2.19, whereas the charged features are smooth and structureless. These bleaching features correlate well with P3HT's vibronic features observed in the absorption spectrum of the neutral polymer as reported in literature.[18]

In depletion, the spectra show mainly noise with a little signal centred at 2 eV, as shown in **Figure 4.6b**, while upon complete accumulation, the signal is essentially unaffected by an increase in gate voltage, as shown in **Figure 4.6a**.

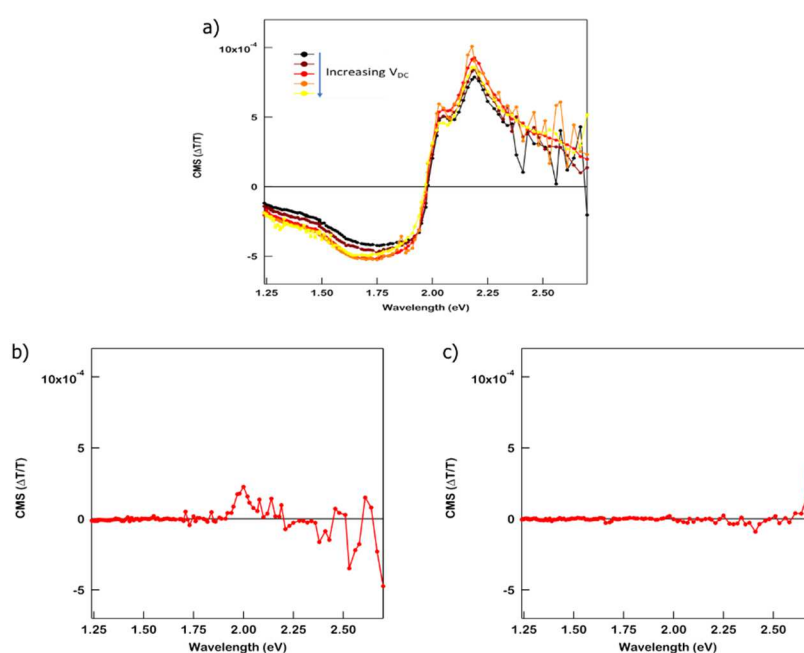


**Figure 4.6:** Charge modulation spectroscopy – a) in complete accumulation varying  $V_{DC}$  b) depletion and c) 2<sup>nd</sup> harmonic

EA on the other hand is meant to increase linearly with the applied voltage. These features, together with a negligible signal in second harmonic (**Figure 4.6c**) provide evidence of negligible electroabsorption. Such observations further support our conclusion that the spectrum above 1.97 eV is related only to the bleaching of P3HT pristine absorption, while the negative absorption is related to polaronic charge absorption.

Fine-tuned fabrication and configuration for pure P3HT devices provided nice trans characteristics and ideal CMS spectra. Following same procedure done for these samples we can therefore analyze the P3HT/ diarylethene blends. Obviously, we need to take into

account the light conversion of the diarylethenes. Experiment details regarding this will be discussed in the following paragraph.

#### 4.5 CMS spectra acquired on P3HT/DAE blends

In order to investigate the effect of the DAE-Me isomerization on the P3HT mobile charge, the CMS spectrum of blend with DAE-Me\_c has to be compared to spectrum acquired on P3HT/DAE-Me\_o devices. Since the CMS measurements require to probe the sample with monochromatic light which spans in energy from UV to visible, the measurement itself modifies the DAE isomerization. Therefore, the sample containing DAE-Me needs to be irradiated with UV light prior to submit the device to CMS measurements. An LED was used to shine 310-nm light directly on the sample inside the glovebox. The device kept in dark condition till that moment was then submitted to CMS measurement. Please refer to paragraph 5.3 for more details on CMS set-up and measurement procedures.

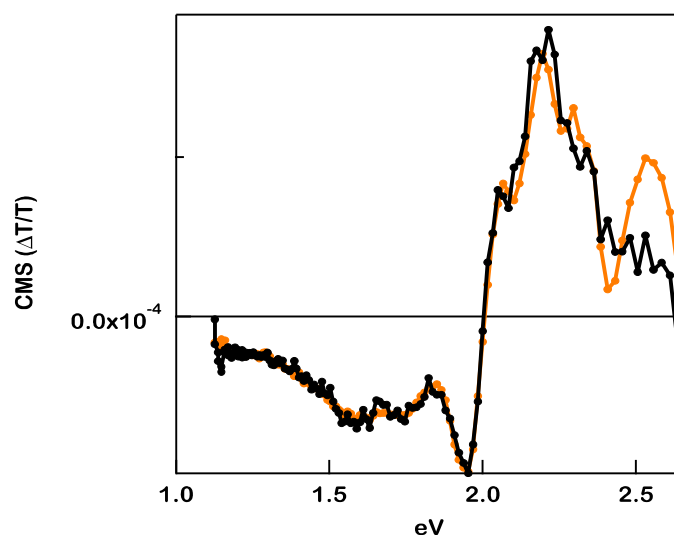


**Figure 4.7:** CMS spectrum of the P3HT:DAE blend in Cytos transistor. The orange line is the spectrum after irradiation at 310 nm. The black line is the spectrum after few cycles of measurement. The device was shone at 310 nm from the backside for 3 min, mounted and left in dark and vacuum for 24 hours before the first measurement.

**Figure 4.7** shows the CMS spectrum immediately after the irradiation (in orange) and after six cycles of probing (in black). The main difference between the two spectra is the presence of a transition peaking at around 2.5 eV (500 nm) for the close structure, which vanishes upon further measurements, i.e. upon VIS light exposures. Considering that the OFETs with DAE-Me\_c show an absorbance that is then vanishing upon irradiation with

VIS light and that the new feature peaks at the absorbance of DAE-Me\_c, a possible interpretation is that the absorbance at  $\sim 500$  nm is a bleaching feature. In principle, it could be associated to absorption of DAE, hence this could be a hint of charges relaxation onto the DAE. Given this first set of data measured, at the beginning we hypothesized that the bleaching at around 2.5 eV could be associated to charge relaxation on the DAE molecule and therefore a direct evidence of DAE trapping mechanism. However, additional measurement on different devices (reported below) has cast some additional light on these observations, showing that this feature can only be indirectly associated to DAE trapping.

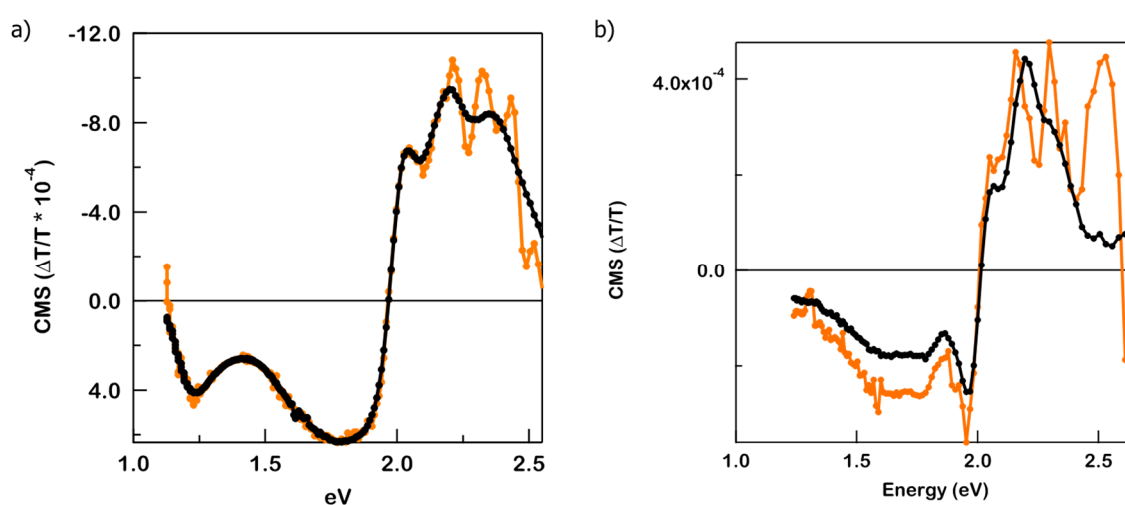


**Figure 4.8:** CMS spectrum of the P3HT:DAE blend in transistor with a)PMMA and b) Cytop as the gate insulator. The orange line is the spectrum after irradiation at 310 nm. The red line represents the second measurement. The black line is the spectrum after few cycles of measurement. The device was shone at 310 nm from the backside for 3 min, mounted and left in dark and vacuum for 24 hours before the first measurement.

In **Figure 4.8b**, the CMS spectra of the P3HT:DAE blend in transistor with Cytop as gate insulator resemble those of devices made of neat P3HT. Minor differences, especially in the bleaching part of the spectrum, are typically associated to batch to batch variation and are often observed also in pure P3HT. On the other hand, more important differences in the charge absorption part can be observed depending on the employed dielectric. As already explained in the **Chapter 1**, the polaronic formation in common semiconducting polymers is associated with the formation of localized intra-gap states. If the polarons are localized onto isolated molecules or polymer chains, two levels are formed in the gap.<sup>[19-22]</sup> In case of strong interchain interactions, which is the case of many polymers, polarons will

undergo a certain degree of delocalization over some molecules chains. This behavior induces the formation of other states and the formation of new optical transitions, with the simultaneous formation of some symmetry forbidden transitions.<sup>[23-26]</sup> In P3HT, a model explaining CMS spectra has been established taking into account the formation of intragap transitions related to intrachain and interchain polymer delocalization.<sup>[27-28]</sup> An interchain transition (C3) and an isolated polymer transition (C2) features the CMS signal of P3HT. Their ratio gives hence an indication of polaron delocalization. For low k dielectrics, the C3 transition is stronger, while for high-k dielectrics the intensity of C2 and C3 is comparable.<sup>[9]</sup> This means that high-k dielectrics increase the energetic disorder in the semiconductor states close to the interface. This is caused by the stronger disorder dipoles present in the dielectric. The increased disorder reduces the ability of the polaron to delocalize. Our PMMA CMS spectra show higher 0-0/0-1 ratio which is in agreement with the picture of a higher localization of the polarons within the polymer chains, besides a shift of the charge absorption towards higher wavelengths (lower energy). This is also in agreement with an increased polaronic localization that increases the shift of the single-chain polaron into the band-gap.<sup>[11]</sup>

Upon photoconversion of the DAE molecules, the CMS spectrum appears affected with the formation in the bleaching part of a highly structured absorption at high energy, while the charge absorption part of the spectrum appears unaffected. The formation of highly structured bleaching cannot be associated with the DAE molecule since the diarylethenes derivatives show a broad, featureless absorption (**Figure 1.7**). Probably these features were not observed in a previous batch (**Figure 4.7**) because of a lower degree of DAE conversion which hence got quickly converted into the open form during the measurement. On the other hand, the latest results can be easily explained considering that P3HT is known to display absorption spectra composed of a number of distinct vibronic features that are very sensitive to structural order, inter- and intrachain interactions and electronic couplings. Typical absorption spectra of this polythiophene derivative show indeed a low energy component dominated by ordered/crystalline regions ruled by weakly interacting H-aggregate states and a higher energy part due to non-aggregated, disordered polymer chains dominated by intrachain states. The specific spectroscopic signatures that we observed in our CMS spectra in the bleaching part could be therefore of vibronic origin. In general, bleaching features of P3HT are redshifted and better resolved compared with the neutral bulk polymer absorption, since charges tend to relax onto the most ordered polymer regions and hence to occupy the lowest energy states. The fine bleaching structure

could then suggest that charges are located in the ordered part of the polymer even upon UV conversion of DAE. Higher energy states, occupied by charges relaxing on more disordered polymer fraction, are however bleached by the interaction with the diarylethene derivative and as a consequence, the conducting pathways are reduced. The charge absorption part of the CMS spectra does not show differences upon DAE conversion, which is somehow puzzling. However, P3HT charge absorption is known to be featureless, hence the absence of vibronic structuring and the intrinsic broadening of the charged transition could bury any spectral evidence of the DAE – P3HT interaction.

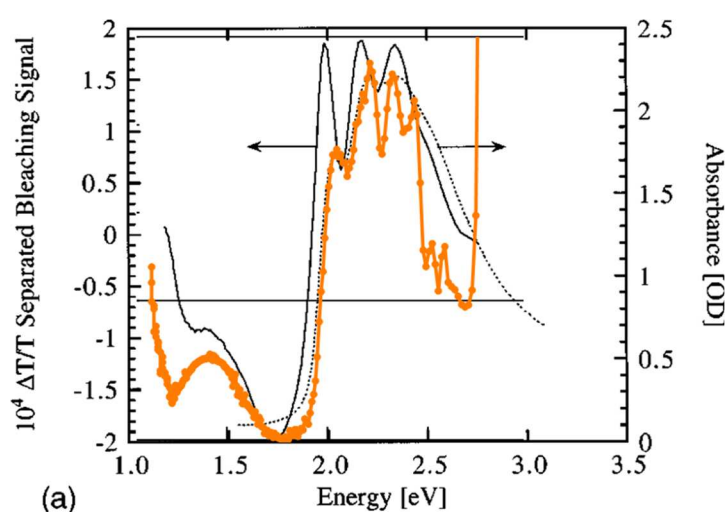


**Figure 4.9:** Comparison between our CMS spectrum of P3HT/DAE-Me\_c at room temperature (orange line) with absorption and CMS spectrum of pure P3HT at low temperature (black line) form ref [18].

Highly structured bleaching spectrum is typically measured for low temperature CMS spectra.<sup>[18]</sup> Our CMS spectrum follows a same behavior as measured for low temperature CMS measurements in literature as shown in **Figure 4.9**. At low temperature charges become more localized and mobility decreases. Therefore, the similarity of the two spectra supports that in our case the reason of charge localization is the interaction between DAE and polymer, with the molecule acting as trap.

## 4.6 Conclusions

In conclusion, we have found indirect spectroscopic evidence that the DAE, intercalated in the least ordered part of the P3HT (the crystalline regions are not accessible), once closed with UV light irradiation limits the charge transfer between ordered areas, thus localizing

more the charge in these. Such observation can be deduced from the variation of the vibronic features of P3HT CMS spectra by interconverting DAE from the close to open form. The analogy with the effect of temperature is that with less thermal energy, charges are forced to populate more ordered polymer regions. In the same way, in our case the charges continue to move in the most crystalline parts of the P3HT, however, the conductive paths are reduced by the trapping effect of the DAE.

In the presence of tie chains, as in this case of the P3HT 50 kDa film, the less ordered regions contribute only partially to the charge transport. Therefore, since the transport takes place preferentially in the most ordered phase, only a small fraction of carriers that also go through the least aggregated phase of the film (where the DAE reside) will be trapped by the photochromic induced states. That is, the DAEs do not necessarily limit the overall charge transfer between ordered areas, but more simply the carriers which end up in the less ordered areas are trapped by the DAEs. For this reason, the conductivity of P3HT/DAE FET never shows a complete modulation upon DAE interconversion (as also reported in the literature). In any case, the charges trapped in the most disordered areas are no longer “read” in the CMS measurements, as shown in **Figure 4.8**, causing as a result the modification of bleaching part of the spectrum.

Although charge trapping, which is capable of induce a change in the bleaching, should also modify the intensity of the absorption band, in our case such variation of intensity is not detectable since we were modulating only a small fraction of carriers, basically leaving the greater portion of carriers unchanged. In fact, the intensity, or the integral in the case of bleaching, does not change as the signal depends on the total amount of modulated charges, which is defined by the capacity and amplitude of the modulation. Since the devices were operated in full accumulation, the resulting signal is the same.

What we observed in the CMS spectra could be related to the Stark effect which is due to the charge trapping. Since this should is a dynamic effect, measurements of spectra at different frequencies are able to confirm this hypothesis. Unfortunately, performing CMS measurements at different frequencies on devices with DAE in closed form is not straightforward, as the DAEs are converted during the measurement itself. Therefore, the measurements at various frequencies would refer to different devices’ states, resulting in an impossible direct comparison.

CMS spectra analysis was able to give us an indirect evidence of the closed DAE molecules with polarons moving in the P3HT matrix. In order to confirm/deny this preliminary result, further investigations which consider the blend morphology and microstructure analysis are required; such study is discussed in the following Chapter.

## References

- [1] T. Leydecker, M. Herder, E. Pavlica, G. Bratina, S. Hecht, E. Orgiu, P. Samori, *Nat Nanotechnol* **2016**, 11, 769.
- [2] E. Orgiu, N. Crivillers, M. Herder, L. Grubert, M. Patzel, J. Frisch, E. Pavlica, D. T. Duong, G. Bratina, A. Salleo, N. Koch, S. Hecht, P. Samori, *Nat Chem* **2012**, 4, 675.
- [3] E. Orgiu, P. Samori, *Adv Mater* **2014**, 26, 1827.
- [4] K. Borjesson, M. Herder, L. Grubert, D. T. Duong, A. Salleo, S. Hecht, E. Orgiu, P. Samori, *J Mater Chem C* **2015**, 3, 4156.
- [5] M. El Gemayel, K. Borjesson, M. Herder, D. T. Duong, J. A. Hutchison, C. Ruzie, G. Schweicher, A. Salleo, Y. Geerts, S. Hecht, E. Orgiu, P. Samori, *Nat Commun* **2015**, 6.
- [6] T. Leydecker, M. A. Squillaci, F. Liscio, E. Orgiu, P. Samorì, *Chem Mater* **2018**, 31, 6491.
- [7] M. Caironi, M. Bird, D. Fazzi, Z. Chen, R. Di Pietro, C. Newman, A. Facchetti, H. Siringhaus, *Adv Funct Mater* **2011**, 21, 3371.
- [8] M. Caironi, Y.-Y. Noh, *Large area and flexible electronics*, John Wiley & Sons, **2015**.
- [9] N. Zhao, Y. Y. Noh, J. F. Chang, M. Heeney, I. McCulloch, H. Siringhaus, *Adv Mater* **2009**, 21, 3759.
- [10] D. Beljonne, J. Cornil, H. Siringhaus, P. J. Brown, M. Shkunov, R. H. Friend, J. L. Brédas, *Adv Funct Mater* **2001**, 11, 229.
- [11] E. Itoh, K. Terashima, H. Nagai, K. Miyairi, *Thin Solid Films* **2009**, 518, 810.
- [12] M. L. Chabinye, *Journal of Vacuum Science & Technology B: Microelectronics and Nanometer Structures Processing, Measurement, and Phenomena* **2008**, 26, 445.
- [13] H. Siringhaus, P. J. Brown, R. H. Friend, M. M. Nielsen, K. Bechgaard, B. M. W. Langeveld-Voss, A. J. H. Spiering, R. A. J. Janssen, E. W. Meijer, P. Herwig, D. M. de Leeuw, *Nature* **1999**, 401, 685.
- [14] E. Itoh, H. Nagai, K. Miyairi, *Thin solid films* **2008**, 516, 2568.
- [15] T. Otsuka, D. Taguchi, T. Manaka, M. Iwamoto, *J Appl Phys* **2017**, 121, 065501.
- [16] Z. Li, G. Wang, N. Sai, D. Moses, M. Martin, M. Di Ventra, A. Heeger, D. Basov, *Nano Lett* **2006**, 6, 224.
- [17] D. Chemla, T. Damen, D. Miller, A. Gossard, W. Wiegmann, *Appl Phys Lett* **1983**, 42, 864.
- [18] P. J. Brown, H. Siringhaus, M. Harrison, M. Shkunov, R. H. Friend, *Phys Rev B* **2001**, 63, 125204.
- [19] D. Fichou, G. Horowitz, F. Garnier, *Synthetic Met* **1990**, 39, 125.
- [20] G. Horowitz, A. Yassar, H. Von Bardeleben, *Synthetic Met* **1994**, 62, 245.
- [21] J. A. van Haare, E. E. Havinga, J. L. van Dongen, R. A. Janssen, J. Cornil, J. L. Brédas, *Chemistry—A European Journal* **1998**, 4, 1509.
- [22] T. Chung, J. Kaufman, *Phys. Rev. B* **1984**, 30, 702.

- [23] K. Kaneto, S. Hayashi, S. Ura, K. Yoshino, *Journal of the Physical Society of Japan* **1985**, 54, 1146.
- [24] Z. Vardeny, E. Ehrenfreund, O. Brafman, M. Nowak, H. Schaffer, A. Heeger, F. Wudl, *Phys Rev Lett* **1986**, 56, 671.
- [25] P. Lane, X. Wei, Z. Vardeny, J. Poplawski, E. Ehrenfreund, M. Ibrahim, A. Frank, *Synthetic Met* **1996**, 76, 57.
- [26] Y. Furukawa, *The Journal of Physical Chemistry* **1996**, 100, 15644.
- [27] D. Fichou, C. Ziegler, *Structure and properties of oligothiophenes in the solid state: single crystals and thin films*, Wiley-VCH: Weinheim, **1999**.
- [28] J. Cornil, D. Beljonne, J. Brédas, K. Müllen, G. Wegner, *Mullen, K* **1998**, 432.

## Chapter 5. A close look at the photo-switching properties of transistors based on a photochromic molecule / p-type polymer semiconductor blend

As previously discussed in **Chapter 1**, one among the greatest challenges in the field of molecular materials is to use their “weak” nature to render them multi-responsive and multifunctional. [1-4] Under this premise, it is important to note that there have been successful efforts to enhance the functionality of solution-processed organic field-effect transistors (OFET) in recent years, through the development of the latest hybrid systems which integrate functional molecules in semiconducting matrices.[5-9] For such newer generation of multifunctional optoelectronic devices, photochromic molecules are suitable to form the functional components as they can be remotely manipulated with high spatiotemporal resolution, without the production of waste products.[10-15] By blending poly(3-hexylthiophene) (P3HT) with diarylethenes (DAEs) organic thin-film transistors (OTFTs) were fabricated that exhibited photo-switching at selected wavelengths with its write/erase states displayed remarkable stability up to several months.[16] These results have recently led to the development of non-volatile 8-bit memory devices with multiple discrete levels. [17] These devices’ functionality and performance are dependent on the charge carriers’ ability to relax on the DAE traps. Therefore, an optimal way to increase the performance of such devices is by improving the efficiency of the blend microstructure, as illustrated in the example of organic bi-component solar cells. [18-19] When DAE molecules are dispersed in the regions of the polymer which are less aggregated, a facilitated energy interaction between the charges and the hole-accepting sites arises, which consequently also boosts the device’s photosensitivity. [20]

Within the framework of this doctoral work, three parameters that could change the film microstructure in P3HT vs. P3HT/DAE films were explored: the polymer’s molecular weight, its regioregularity, and finally the thermal annealing of thin blend films. Regarding the relationship between structure and device performance, the impact of the molecular weight was found to be significant and to play an important role. Experiments conducted on field-effect transistors made with various P3HT films with low  $M_w$  (between 20 and 50 kDa) illustrated that hole mobility can be positively influenced by  $M_w$ . [21-22] Films with higher  $M_w$  displayed reduced crystallinity, as a result of better transport through the chain along the backbone of the polymer connecting the crystalline areas. [23-24] Any further

increase in the molecular weight  $M_w$  (60-331 kDa) leads to a slight decrease in field-effect mobility.<sup>[25]</sup> This can be explained by the detrimental role that the increased average chain length plays by causing a high entanglement density, as a consequence of which a large fraction of amorphous regions is formed. Some studies also revealed that in neat and blend P3HT films, the effect of regioregularity on the packing of the polymer chains is significant.<sup>[26-27]</sup> While using regiorandom (RRa)P3HT as the active layer in transistors leads to low charge carrier mobility, in highly regioregular (RR) P3HT films charge transport is more efficient. Lastly, annealing temperature affects the polymer's microstructure over several length scales.<sup>[28]</sup> The semi-crystalline structure which comprises both lamellar crystals and amorphous regions, can be tuned by thermal annealing. Therefore, determining the optimal annealing temperature leading to the best P3HT morphology, can significantly enhance the device properties.<sup>[29-32]</sup> It was recently observed that when DAEs diffuse in a P3HT matrix, they do not significantly affect the crystalline features of the P3HT film.<sup>[16]</sup> Indeed, when the polymer undergo spontaneous self-assembly, they tend to self-aggregate forming amorphous regions in semi-crystalline P3HT films. Nonetheless, understanding the role of polymer molecular weight, regioregularity, and annealing temperature on the blend morphology will be instrumental towards the enhancement of the DAE dispersion in the film, and consequently the ability of the device to respond to light stimuli.

In this chapter, we will examine the structural, morphological, optical, and electrical properties of DAE-Me blended with P3HT of varying molecular weight (between 20 and 100 kDa), and regioregularity, based on the changes made in the thermal annealing process (rt up to 160 °C), with a special focus on the ability of the bi-component devices to respond to illumination at specific wavelengths.

## 5.1 The role of morphology in optically switchable transistors based on DAE/P3HT blend

**Figure 5.1** portrays the chemical structure of P3HT and DAE-Me<sub>o</sub>, and their energy level diagrams. DAE-Me molecules have been designed, synthesized [16] and used as a starting compound, based on the HOMO level requirement of P3HT. This has been done to ensure that there is electronic interaction between DAE-Me<sub>c</sub> molecules and polaronic charges which are mobile within the P3HT polymer matrix. DAE-Me<sub>c</sub>'s HOMO level is situated in the semiconductor's bandgap, thereby proving to be a driving force leading to the trapping of the holes being transported within the polymer matrix. This also leads to the nullification over photoisomerization to DAE-Me<sub>o</sub> whose HOMO level energy sits outside the bandgap of P3HT.

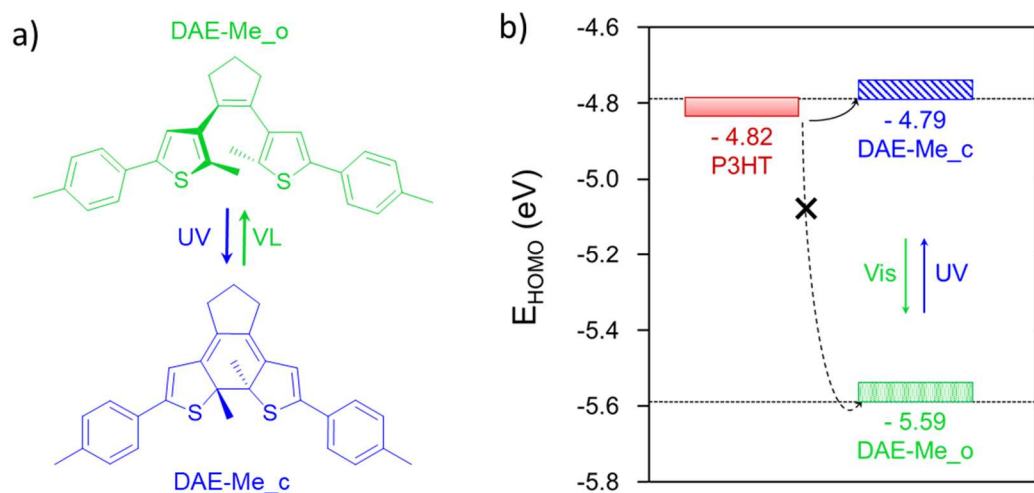


**Figure 5.1** - a) Schematic DAE-Me photo-isomerization between two thermodynamically stable forms. When irradiated with a UV light, DAE-Me molecules can undergo isomerization from an open form (DAE-Me<sub>o</sub>) into a closed one (DAE-Me<sub>c</sub>). The back isomerization, from DAE-Me<sub>c</sub> to DAE-Me<sub>o</sub>, occurs upon irradiation with visible light. b) HOMO energy levels of DAE-Me measured by cyclovoltammetry in comparison with those of P3HT.[20]

Consequently, the photosensitivity of the thin-film transistor is heavily influenced by photochromic molecules' ability of undergoing isomerization. This ability of the photochromic molecules is dictated by the innate photo-responsiveness of the DAE-Me and by the interaction of electronic and structural aspects with the P3HT matrix. The

precise adjustment of the reversible light-response in the current moving through the polymer/DAE-Me hybrid film necessitates that we hold slight control over film structure.

### 5.1.1 Role of molecular weight and regioregularity

In case of a pristine RR P3HT, the morphology of thin films is highly dependent on molecular weight, which also causes changes in field-effect mobility. [33-35] In the case of a P3HT with low molecular weight that goes lower than the critical molecular weight in case of entanglements, i.e. ( $M_{wc}$ ) of  $\sim 35$  kDa, [16, 33] leads to the generation of many isolated crystals which have conformed extended chains which display a paraffin-like structure. [36-37] Conversely, in the case of P3HT with high molecular weight ( $M_w > M_{wc}$ ), the chain's average length is more than the average molecular weight between entanglements, which obviously causes chain folding [38] and a microstructure which is comprised of both ordered and amorphous regions. [23] Once the polymer chain starts to assemble themselves, DAE molecules are more susceptible to station in the polymer matrix which is less aggregated. [16] An effective transport of charges is occurring especially in the ordered regions which are connected by tie-chains which are present throughout the amorphous regions. [24] Thus, it is evident that semi-crystalline structures in DAE-Me/P3HT based transistors will allow for optimal level of high-mobility and light-response.

Three P3HTs with varying molecular weights which are low, medium and high in magnitude ( $M_w \approx 20, 50,$  and  $100$  kDa) were chosen as model semiconducting polymers to help optimize both the electric performance and switching ability of the blend films. Keeping in mind our previous findings, we have focused on DAE-Me/P3HT with DAE-Me at 20 wt% to ensure the production of optimum light-responsive transistors.

Atomic force microscopy (AFM) images of RR P3HT/DAE-Me blends which were taken with multiple  $M_w$  of P3HT are displayed in **Figure 5.2a-c**.

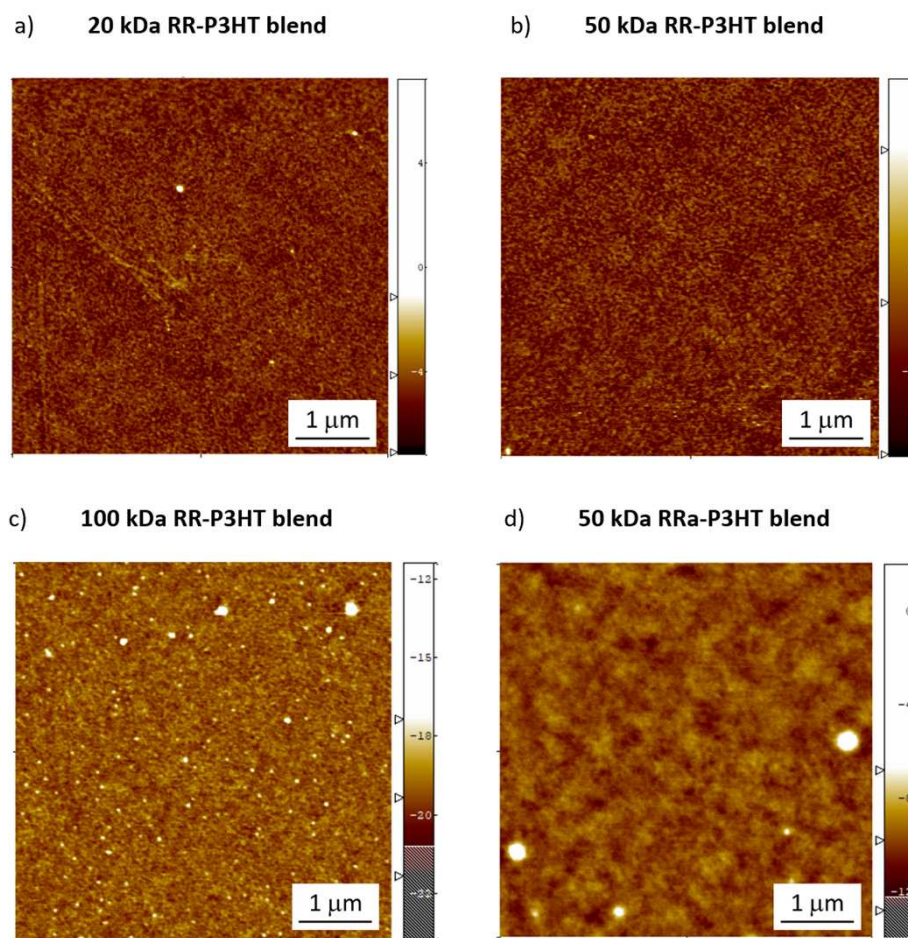


**Figure 5.2:** Height AFM images recorded in tapping mode of a 20 wt% DAE-Me<sub>o</sub> blend with P3HT (a) RR and  $M_w = 20$  kDa, (b) RR and  $M_w = 50$  kDa, (c) RR and  $M_w = 100$  kDa, and (d) RRa and  $M_w = 50$  kDa. Z-scales: (a-c) 6 nm, (d) 10 nm.

These films' surfaces are granular as the crystallites formed are of different sizes, form, structure, and orientation and the evaporation of the solvent significantly impacts them. [39] As  $\text{CHCl}_3$  is extremely volatile, films of RR-P3HT which have high molecular weight do not cause formation of crystalline structures. [40-41] When these films were analysed quantitatively, in areas of  $5.12 \times 5.12 \mu\text{m}^2$ , the root mean square roughness ( $R_{\text{rms}}$ ) varies with the molecular weight. In P3HT with  $M_w = 20$  and 50 kDa,  $R_{\text{rms}}$  was measured to be  $0.50 \pm 0.01$  nm. Likewise, films of P3HT with  $M_w = 100$  kDa displayed an increased  $R_{\text{rms}}$  of  $0.69 \pm 0.09$ . This finding aligns with Ballantyne et al., [42] whose studies found out that blends with high  $M_w$  P3HT ( $M_w = 121$  kDa) containing a small molecule acceptor display rougher surface in comparison to blends with low  $M_w$  (13 kDa). Therefore, we conclude that in **Figure 5.2c**, the observed high roughness, may be due to the self-assembling of DAE-Me molecules which could not sit in between the polymer chains. This can further

be substantiated by the observation of the AFM images of neat P3HT with similar film processing conditions, did not display bright features which are ascribed to DAE aggregates. [21, 43-44] It is also important to note that the films produced using RRa P3HT with  $M_w = 50$  kDa (**Figure 5.2d**) display a completely different structure and morphology. Though the texture displays clusters on the hundreds of nanometer range, the final value of the  $R_{rms}$ , which was found to be  $0.58 \pm 0.10$  nm, is comparable to that of RR films.

**Figure 5.3** portrays the electrical characteristics of the P3HT/DAE-Me blends when subjected to UV and visible light illumination. When  $M_w$  was enhanced from 20 kDa to 50 kDa in the RR P3HT, the field-effect mobility and the light response of the devices were found to increase, especially the latter in terms of cyclability. However, the performance was observed to decrease when 100 kDa RR-P3HT/DAE-Me\_o is used, which could be due to reduced transport of charges as a result of decrease in overlapping of conjugated portions.[42]

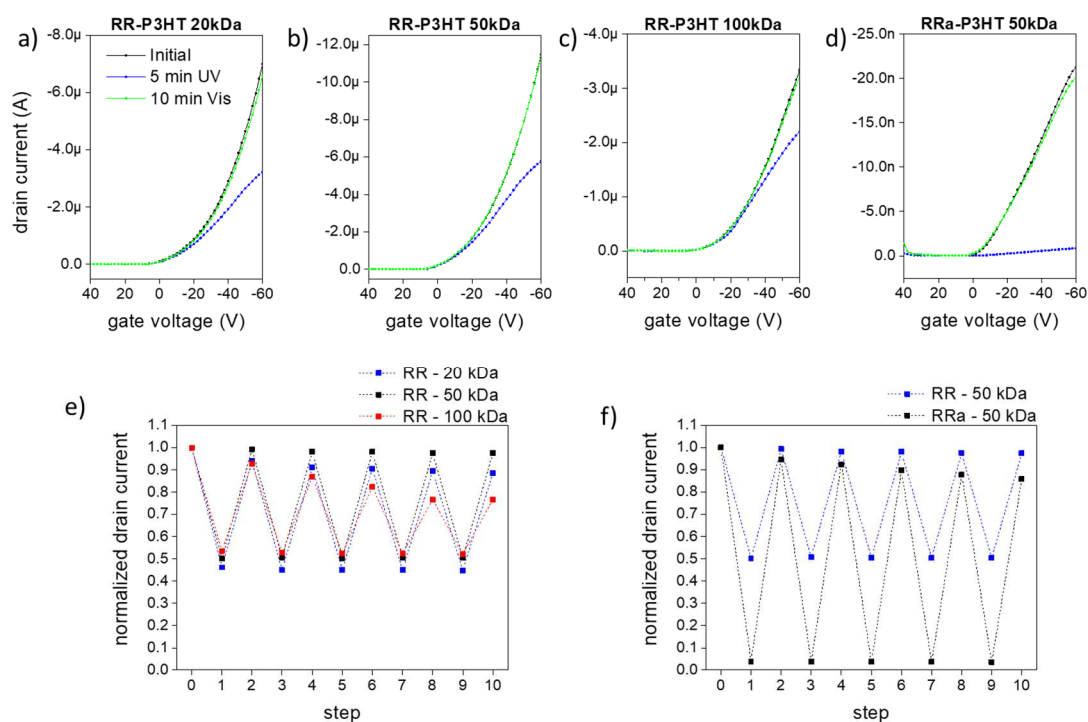


**Figure 5.3** - The photo-reversible transfer characteristics of transistor containing 20 wt% DAE-Me\_o blended with RR-P3HT with  $M_w$  of (a) 20, (b) 50, (c) 100 kDa, and (d) RRa-P3HT  $M_w = 50$  kDa ( $W = 10^4 \mu\text{m}$ ,  $L = 20 \mu\text{m}$ ,  $V_{DS} = -60$  V). Comparative plot of the normalized drain current upon multiple cycles of irradiation with UV and visible light for blends containing (e) RR-P3HT at different  $M_w$ , and (f) regioregular vs. regiorandom P3HT at identical  $M_w = 50$  kDa.

Indeed, a decrease in field-effect mobility is measured in blends with high molecular weight of P3HT (*vide infra*). Further, these devices experience fatigue with respect to optical responses through cycles, which could be a consequence of increased DAE-Me<sub>o</sub> segregation as can be observed from **Figure 5.3e**, in agreement with our AFM data. Instead, when films contain large portions of amorphous regions, it is observed that DAEs are spread out in a relatively homogenous manner within the polymer matrix,<sup>[16]</sup> enabling charges to move and interact with hole-accepting sites upon irradiation with UV light (DEA-Me<sub>c</sub>), specifically when the DAE-Me<sub>o</sub> are well dispersed in the polymer matrix. In such a situation, the lowering of field-effect mobility, causes an enhancement in the light-controlled switching ratio of conductivity. This scenario is especially observed in regiorandom P3HT, whose films are highly amorphous in nature. When **Figure 5.3b** and **5.3d** are compared, it is noticed that the measure of field-effect is three times lower in the case of RRa P3HT, while the switching ratio is seen to be 100% higher, as is apparent in **Figure 5.3f**. Therefore, this observation substantiates that the presence of amorphous regions results in a more homogenous dispersion of DAE-Me in the polymer matrix, which can therefore act as accepting sites for holes.

**Figures 5.5e-f** compare devices with P3HTs of varying molecular weight and regioregularity, in terms of characteristics pertaining to static photo-switching (see Section *Static switching current measurements* in Experimental section of this Chapter). In cases where  $M_w$  is 20 or 50 kDa, the fatigue observed is less. Conversely, in the case of P3HT/DAE-Me<sub>o</sub> blends with 100 kDa, the fatigue is more significant during cycling. These results are in line with what observed in AFM images, shown in **Figure 5.2c**, wherein we can observe DAE-Me<sub>o</sub> phase segregation and aggregation in blends with RR P3HT and  $M_w = 100$  kDa. Though every samples display switching capability, those with 50 kDa exhibit the best device performance when it comes to RR-P3HT. In devices with a blend of RR P3HT ( $M_w = 50$  kDa) and DAE-Me<sub>o</sub>, the observed field-effect mobility is the highest at about  $1 \times 10^{-3} \text{ cm}^2\text{V}^{-1}\text{s}^{-1}$ , along with a photo-induced current change corresponding to 50% of the initial current with complete reversibility over several cycles.

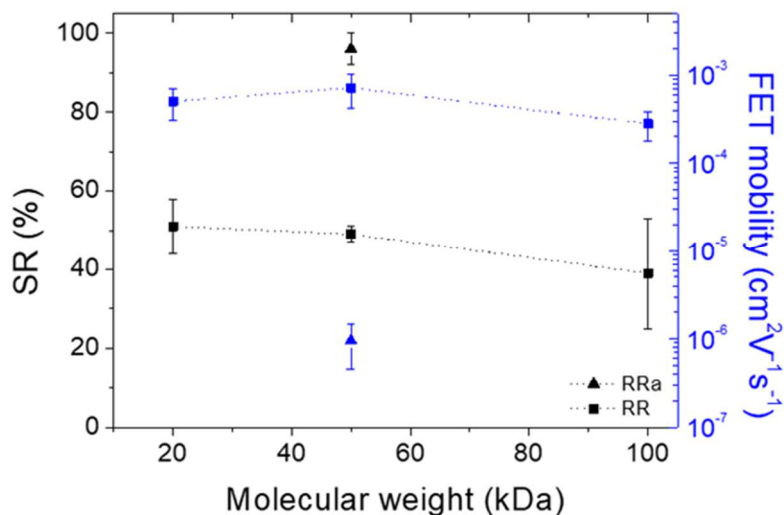


**Figure 5.4:** Switching ratio (SR) of device conductivity as a result of light irradiation and the field-effect mobility of P3HT/DAE-Me<sub>o</sub> blend devices prepared with polymers (a) at different molecular weight, and (b) annealing temperatures (measurements done on blends based on 50 kDa RR P3HT).

In **Figure 5.4**, we can observe that devices made of blends with lower (20 kDa) and higher (100 kDa) molecular weight P3HT tend to exhibit switching ratios which are comparable, i.e.  $SR = |I_{UV,min} - I_{dark}|/I_{dark}$ . However, it is also observed that the lowest field-effect mobility is measured in devices with 100-kDa RR P3HT/DAE-Me<sub>o</sub>, among the three types of regioregular derivatives. Blends with regiorandom P3HT blends exhibit extremely opposite properties, as they have very low field-effect mobility ( $\mu = 2 \times 10^{-6} \text{ cm}^2\text{V}^{-1}\text{s}^{-1}$ ) when compared to the regioregular P3HT-based films, yet they exhibit higher switching ratio, which approaches 100%.

Therefore, it can be concluded that interconnected crystalline domains favour high field-effect mobility of the blends, at the expense of bearing low efficiency of DAE-Me<sub>c</sub> in terms of trapping charges. Films with large fractions of amorphous regions, like RRa P3HT/DAE-Me<sub>o</sub> films, have higher SR due to lower chain-to-chain aggregation capacity with respect to the RR case, causing higher dispersion of the photochromic molecules. In conclusion with respect to the electrical performances, a negligible dependence on polymer molecular weight was observed.

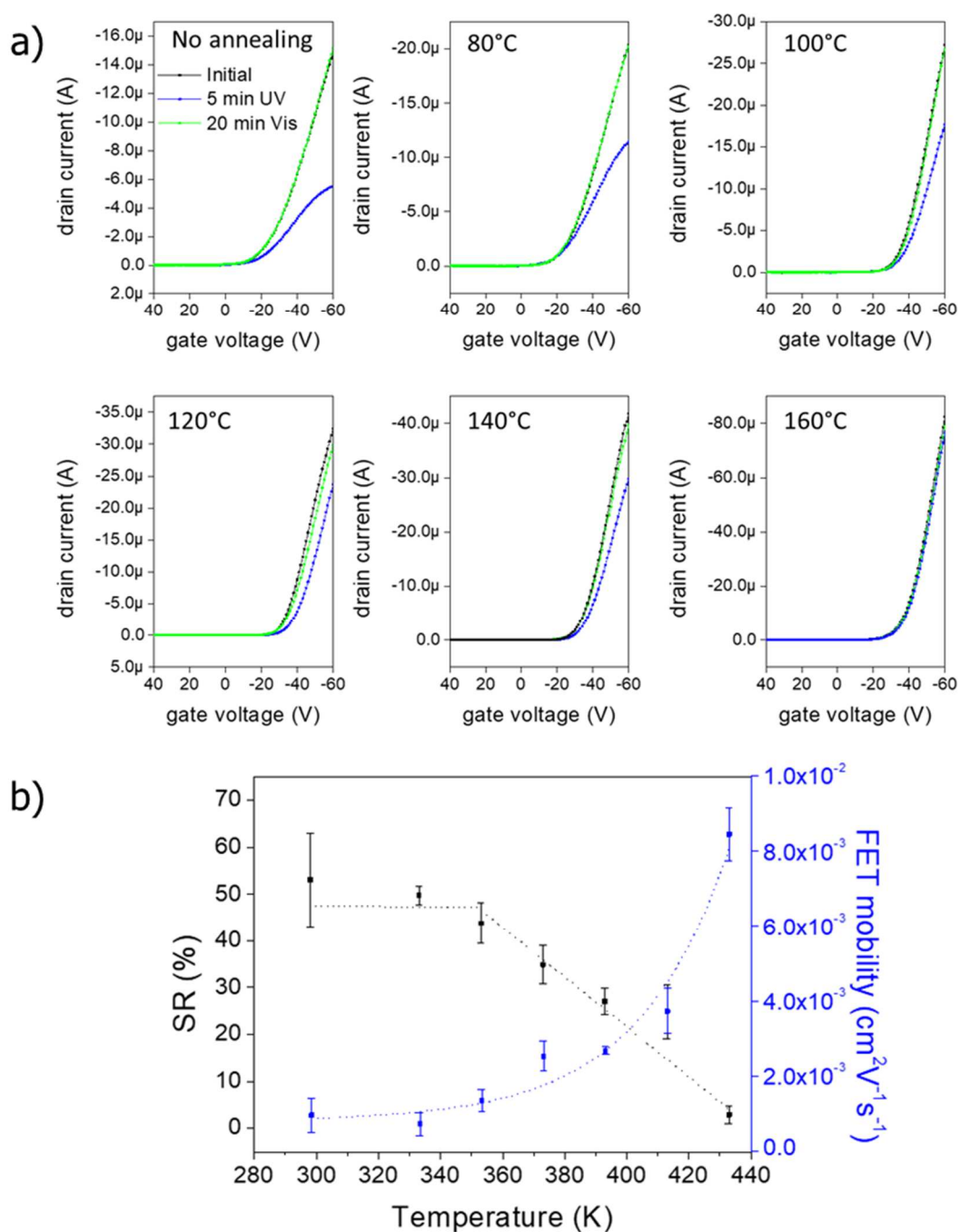
### 5.1.2 Annealing temperature

Having identified the best compromise in terms of high field-effect mobility, high switching ratio and fatigue-free cyclability, we shifted our entire focus to 50 kDa RR P3HT/DAE-Me<sub>o</sub>-based blends. It is well-known that thermal annealing increases the degree of crystallinity in semi-crystalline polymers, as it acts to heal the structural defects in the crystalline portions by enlarging the lateral size of those portions, and in some cases, even increasing the lamellar crystal thickness. These changes are usually beneficial factors for charge transport. Nevertheless, one of the biggest challenges that remains in P3HT/DAE-Me<sub>o</sub> structure control is understanding the relationship between the photoswitching ability of conductivity and degree of crystallinity. Concerning future technological applications, establishing understanding of the behaviour of the device and the material, as a result of the changes in temperature, is rather fundamental as commercial devices typically operate in temperatures ranging from 0 °C to 85 °C.

As already discussed, segregation of DAEs from the polymer matrix would cause considerable decrease of the photo-current variation, as a result of decreased interaction with mobile charges which are transported through the backbone of the polymer. In cases where DAEs are aggregated, extensive fatigue could occur over cycles due to mechanical limitations that the polymer matrix imposes on the DAE-Me ring opening. To better understand the microstructure of P3HT/DAE-Me<sub>o</sub> blend films after annealing, we can correlate the morphological, thermal and structural information acquired on films with the electrical properties of the device.

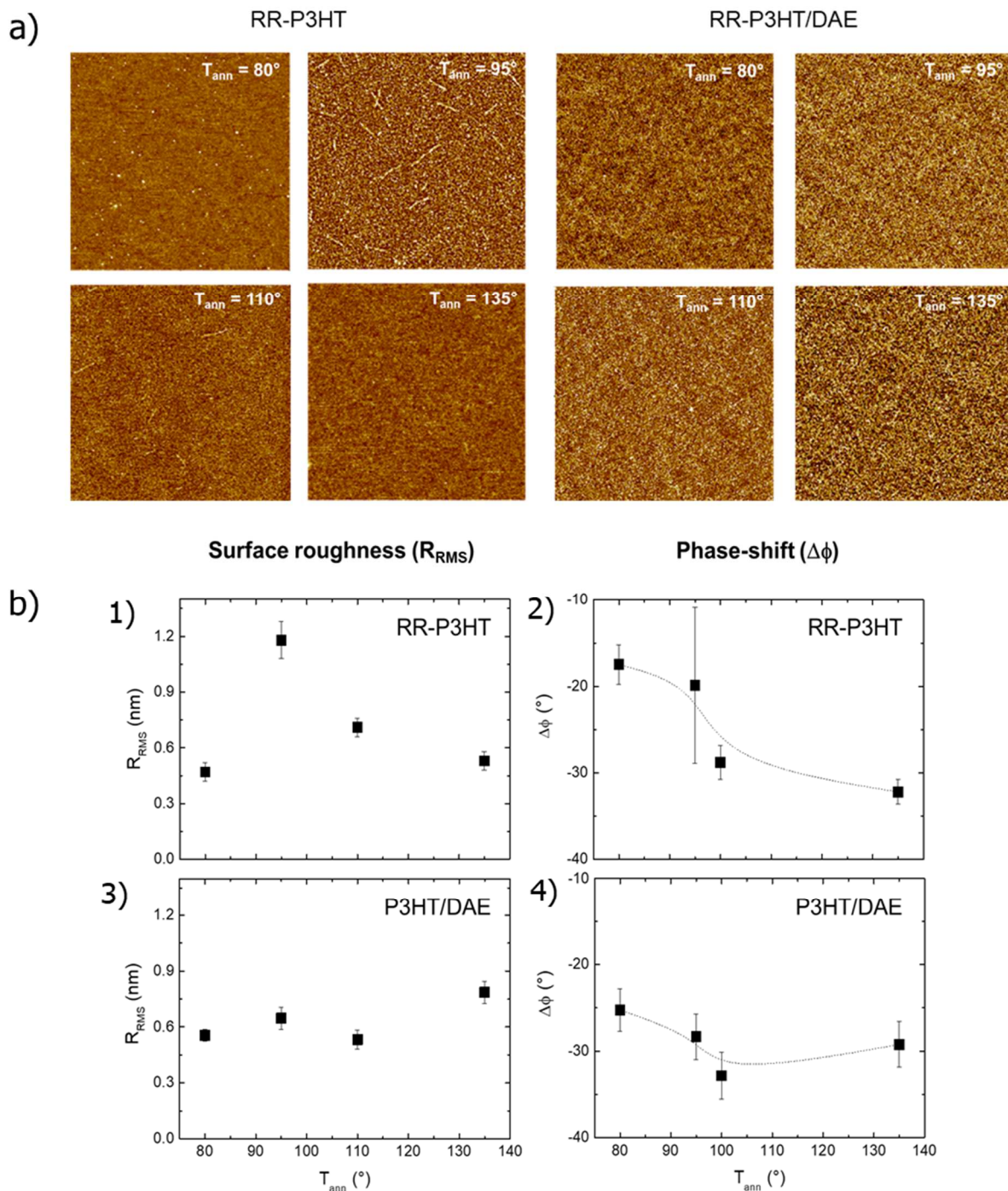
In **Figure 5.5**, we have established the field-effect mobility's dependence on annealing temperature, in the case of blends with 50 kDa RR P3HT. For as-spun P3HT/DAE-Me<sub>o</sub> films, a FET mobility of  $1.0 \times 10^{-3} \text{ cm}^2 \text{V}^{-1} \text{s}^{-1}$  is measured along with a switching transfer characteristic featuring 50% SR which can be regulated completely using light irradiation. These electric characteristics are observed to be similar for annealing temperatures up to 80 °C. In cases of thermal annealing temperature which is greater than 80 °C, there is a considerable effect observed on the current–voltage characteristics and their variation, when irradiated with UV or visible light ( $\lambda=313 \text{ nm}$  with power density =  $0.1 \text{ mW cm}^{-2}$  whereas at  $\lambda=546 \text{ nm}$  the power density =  $1 \text{ mW cm}^{-2}$ ). Finally, when films were annealed at a temperature which was greater than 140 °C, the field-effect mobility of devices was observed to be  $1.0 \times 10^{-2} \text{ cm}^2 \text{V}^{-1} \text{s}^{-1}$ , though SR was found to be substantially lower (see

Figure 5.6a). Therefore, to summarize, thermal annealing, though increases electrical conductivity of the devices, causes reduction in the switching capability.



**Figure 5.5:** a) Optical switching change of transfer characteristics of the 50 kDa RR P3HT/DAE –Me<sub>o</sub> devices upon annealing ( $W = 10^4 \mu\text{m}$ ,  $L = 10 \mu\text{m}$ ,  $V_{DS} = -60 \text{ V}$ ). b) Switching ratio (SR) of device conductivity as a result of light irradiation and the field-effect mobility of P3HT/DAE-Me<sub>o</sub> blend devices prepared with polymers at different annealing temperatures (measurements done on blends based on 50 kDa RR P3HT).

Through AFM investigation, we can see that DAEs significantly impact the properties of the pristine P3HT film. While the  $R_{RMS}$  value of pristine P3HT film depends on the annealing temperature, no remarkable variation is induced up to 135 °C in the blend (Figure 5.6b -1,2). A similar behaviour is noticed in the case of the films' mechanical properties, as performed by AFM phase imaging (Figure.5.6b-2,4).



**Figure 5.6:** AFM analysis of pristine P3HT and P3HT/DAE-Me<sub>o</sub> films. (a,c) surface roughness  $R_{RMS}$  and (b,d) corresponding phase-shift.

Since the measurements of GIWAXS did not reveal any variation in crystallinity after annealing (**Figure 5.7**), the thermal dependency of electrical and optical properties may be ascribed to the possible change in size of the polymer aggregated regions with increasing temperature.

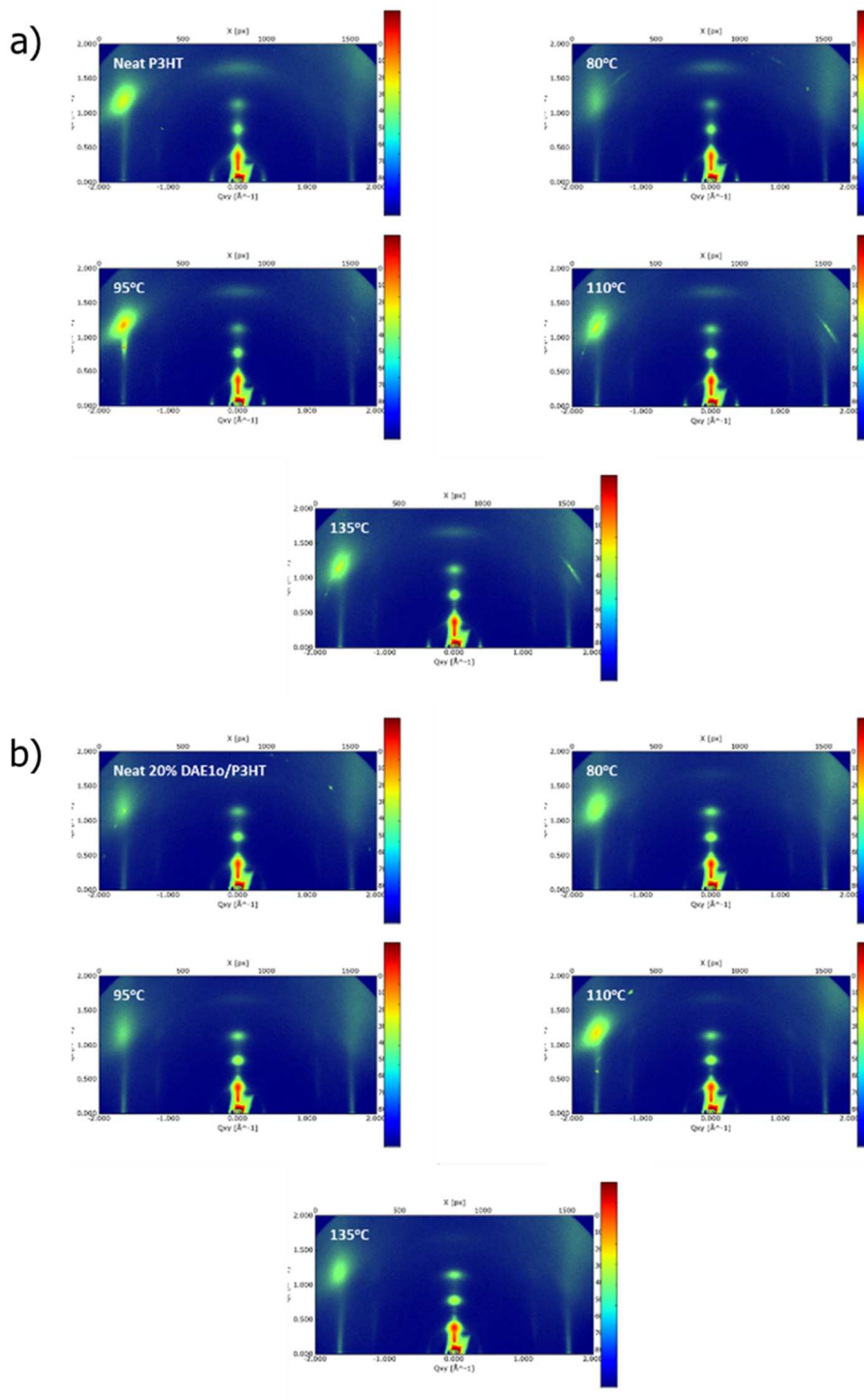


**Figure 5.7:** GIWAXS on neat P3HT films (a) and 20% -DAE-Me<sub>o</sub>/P3HT blend (b).

Linear absorption spectroscopy has been exploited to further examine both the order and the percentage of the aggregated portions of P3HT in blends upon annealing. In **Figure 5.8a-b**, UV-Vis spectra show an increase in aggregation at higher annealing temperatures (decrease of the blue tail in the spectrum) for both neat and blended P3HT. The effects on the excitonic bandwidth are more subtle, however the more pronounced low-energy shoulder in the blended film is an indicator of lower excitonic bandwidth compared to the neat film. The spectrum of absorption of RR P3HT thin films can be extensively elucidated with the aid of weakly interacting H-aggregate model.<sup>[45-46]</sup> When there is a reduction in coupling between the chains due to prominence of 1-D character of the exciton localization, it usually leads to a reduction in excitonic bandwidth,  $W$ , as observed in **Figure 5.8c**.

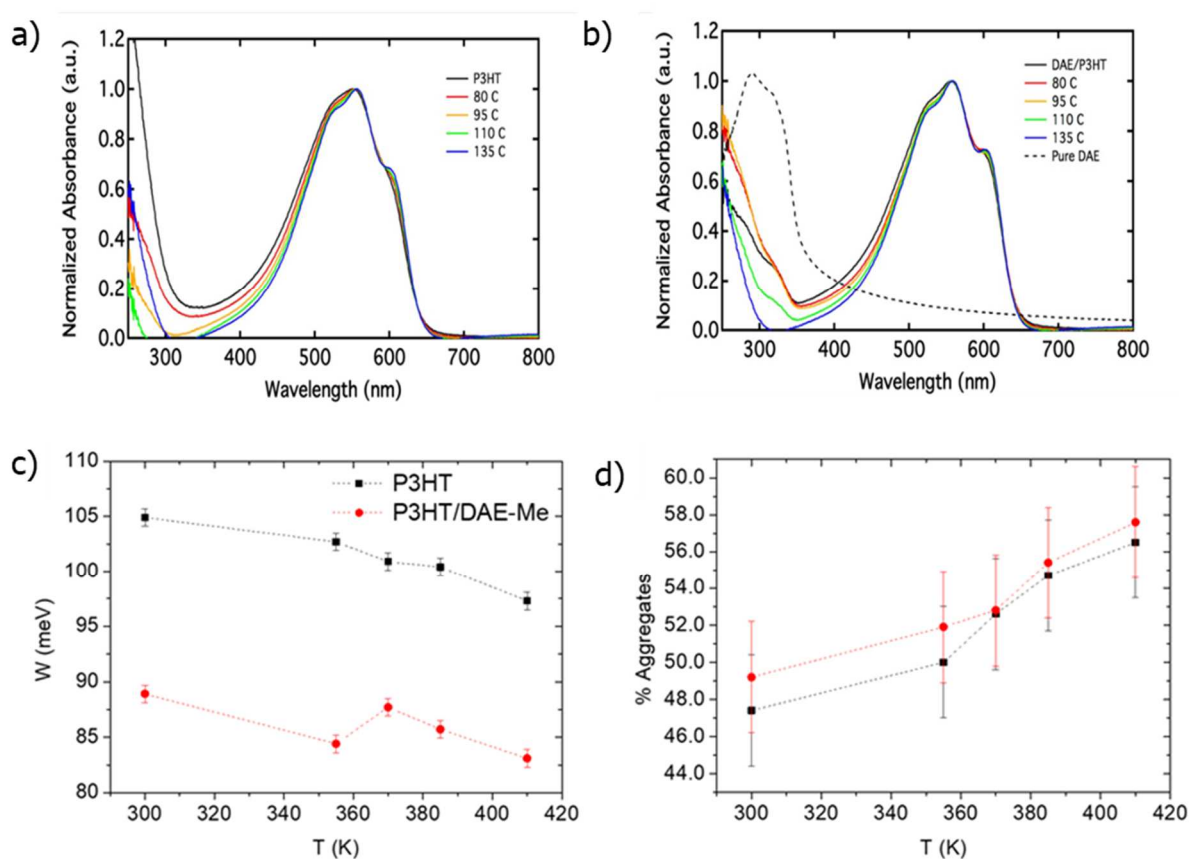


**Figure 5.8:** In the top panel, normalized UV-vis absorption spectra of neat P3HT (a) and P3HT/DAE-Me\_o blend (b) films after thermal annealing, compared to a film before the annealing process (black line). In the bottom panel - Exciton bandwidth (c) and percentage of aggregates (d) in pure and blended P3HT in function of annealing temperature.

The prominence of 1-D character of the exciton localization, suggests higher degree of torsional order, leading to these findings through our experiments: (i) the degree of torsional order typically increased upon annealing in both P3HT and P3HT/DAE-Me\_o

films; (ii) there was a higher degree of order in the case of P3HT/DAE-Me<sub>o</sub> films in comparison to neat polymers. A general trend which was observed for both blended and neat films involves the increase in the percentage of aggregates (**Figure 5.8d**) with the temperature. The increase in percentage of aggregates is comparable for both blended and neat films within experimental error.

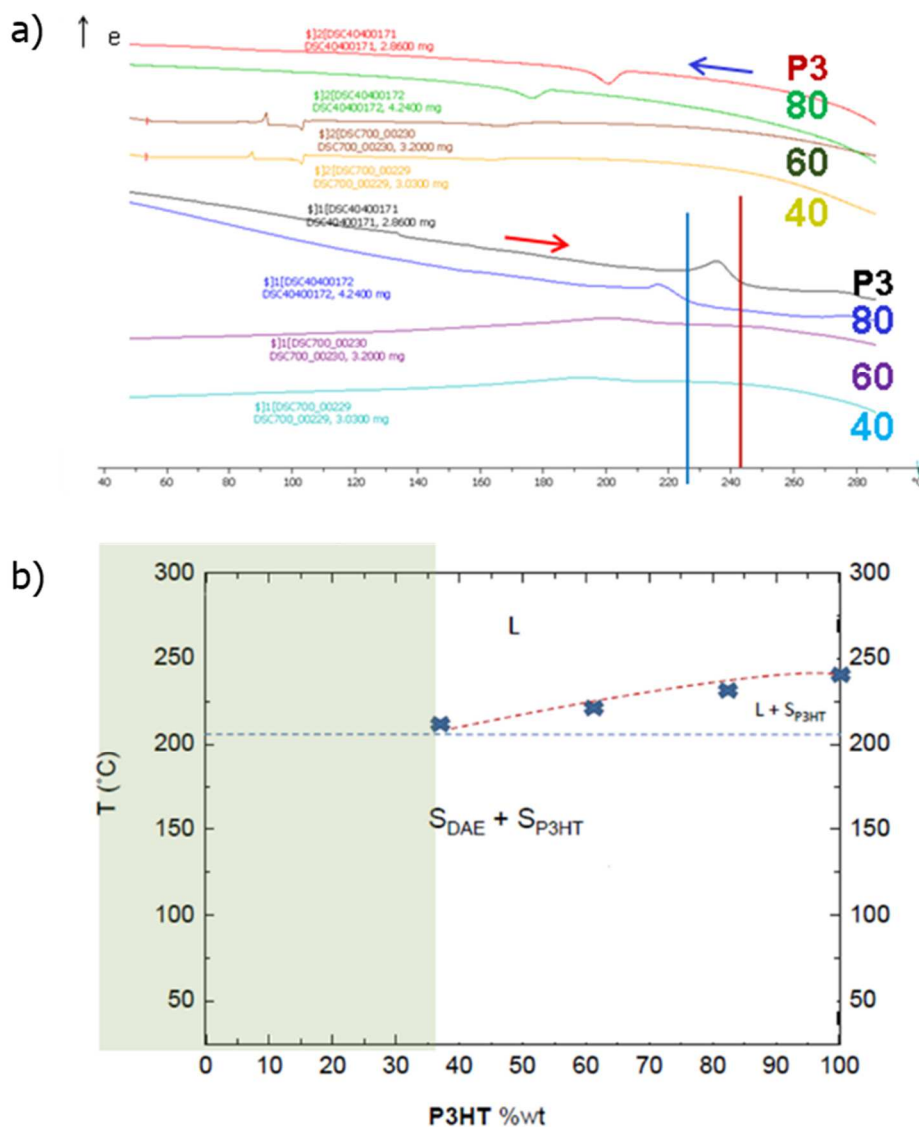


**Figure 5.9:** Bottom - Phase diagram of P3HT/DAE<sub>Me<sub>o</sub></sub> blend. The points are the melting temperature extracted from DCS scans (top).

The increase in the lamellar thickness, which can be induced by a lower torsional backbone disorder in blend vs. neat P3HT films, can be ascribed to the lowered melting point of the P3HT due to the DAEs (**Figure 5.9**) and because annealing is conducted in a semi-liquid state at temperature that is above the melting point of the DAEs; hence, at the same annealing temperature, the P3HT molecules will diffuse more easily than in the neat

material, leading to better order (as already alluded to above). In thin films, there is no evident effect of the annealing temperature (0.31-0.33%) and molecular weight (0.34%, 0.31%, and 0.31% for blends with 20 kDa, 35 kDa, and 100 kDa P3HT, respectively) on the ring-opening quantum yield.

However, as can be observed from **Figure 5.10**, the starting absorbance seems similar in both the room temperature and till temperature up to 80 °C. But there is a sudden noticeable decrease of the absorbance to less than half of the initial value, at 95 °C of annealing temperature, and at temperatures that are higher, there is no noticeable isomerization event. Therefore, we have hypothesized that DAE molecules either start to decompose or reach an aggregated state that is incapable of undergoing photoisomerism, at high temperatures ( $T \geq 95$  °C).

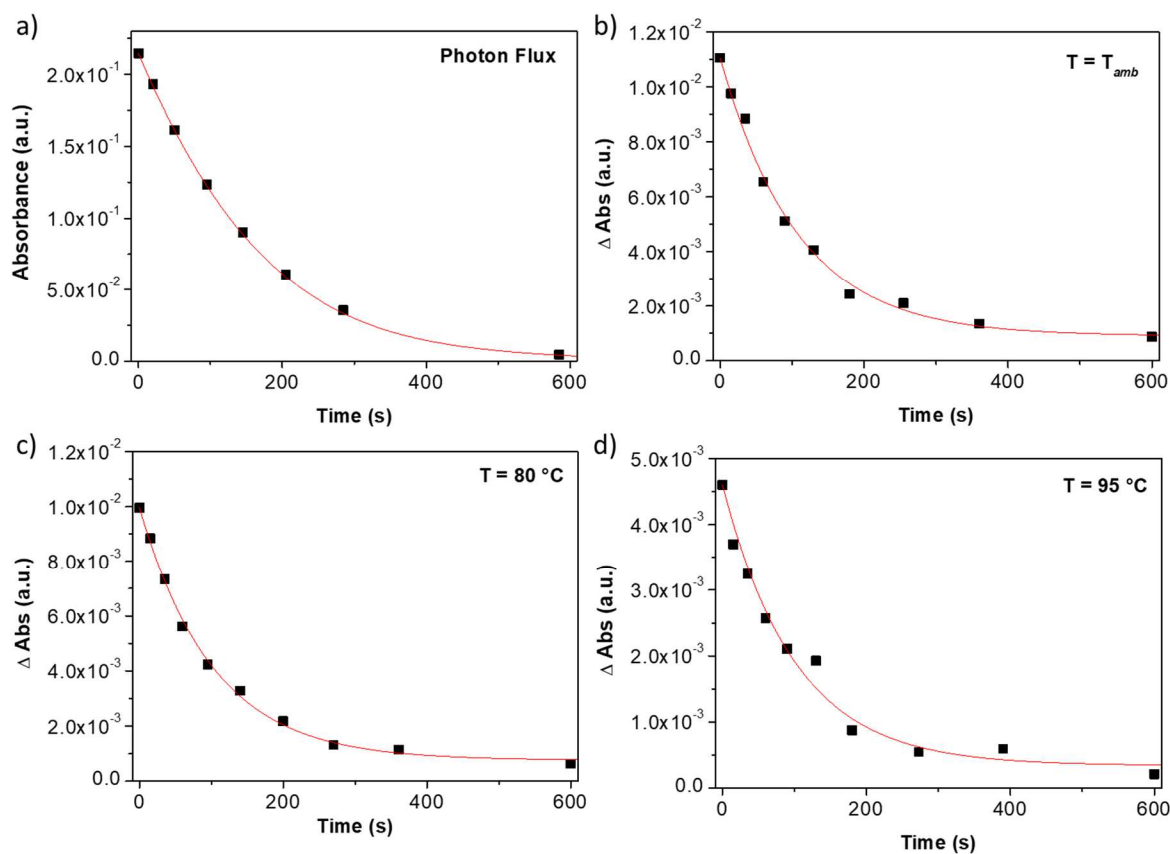


**Figure 5.10:** Absorbance at 535 nm as a function of irradiation times (black squares) and fitted absorbance (red line). In particular photon flux (a), and differential absorbance of P3HT/DAE-Me<sub>o</sub> (20%) films not annealed (b), annealed at 80° C (c) and 95°C (d).

In analogy, by means of electrical response to light stimuli we could not measure any open-to-closed isomerization. Current change upon irradiation turned out to be quenched as

shown in **Figure 5.5**. This effect cannot be ascribed to the DAE molecules degradation. In fact, TG analysis proved that DAE-Me\_o is stable up to 253 °C, after which it decomposes in an exothermic process. Hence, carefully analyzing DTA traces in **Figure 5.11**, a phase transition can be observed at 91 °C, which is therefore the melting point of DAE-Me\_o. This substantiates the decrease in quantum yield and electrical switching, which was observed when films were annealed at 90 °C or at higher temperature.

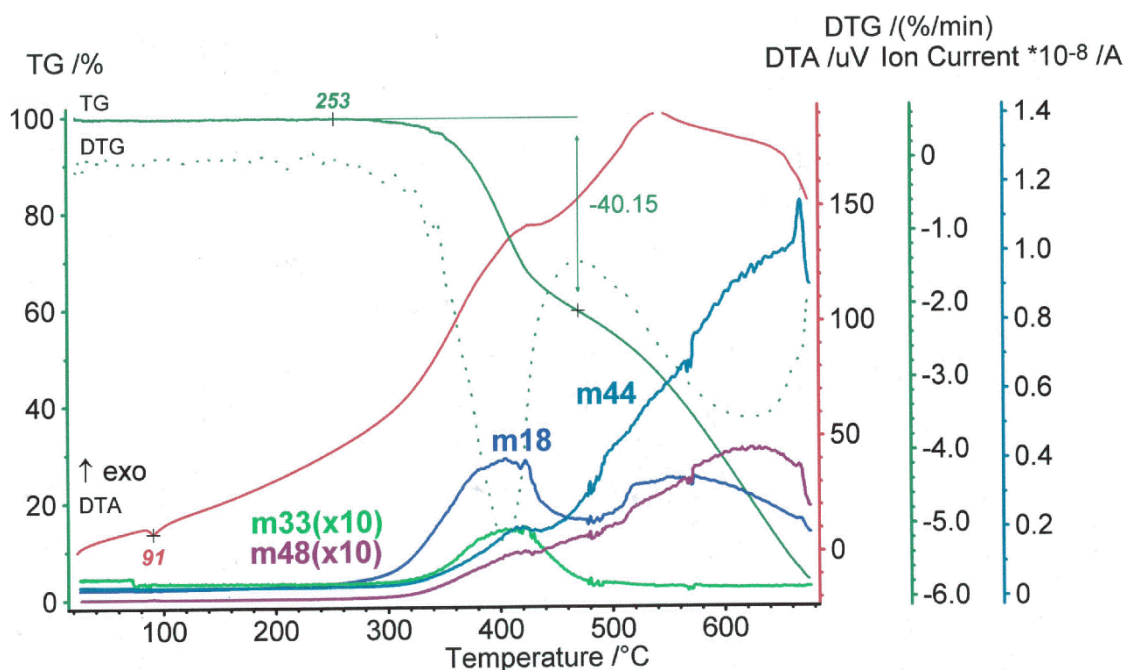


**Figure 5.11:** Combined thermogravimetric and differential thermal analysis of DAE-Me under air (sample mass: 24.72 mg). Thermoanalytical curves (TG, DTA, and DTG) were recorded together with the ion current. Selected  $m/z$  traces ( $m18$ :  $H_2O^+$ ,  $m33$ :  $SH^+$ ,  $m44$ :  $^{12}CO_2^+$ ,  $m48$ :  $SO^+$ ) are shown.

Regarding the switching speed of the device, our study further indicates that QY does not change upon varying the  $M_w$  or upon annealing. Hence, device switching speed will be dominated solely by charge carrier mobility, which did not change significantly with  $M_w$  or increased mildly upon annealing. Therefore, there is no evidence to support that device switching speed will change significantly with respect to earlier report. [16]

## 5.2 Blend of DAE with other p-type copolymers – Preliminary study

Devices based on poly(3-hexylthiophene) (P3HT) with 20 wt% DAE in the blend exhibit good photo-switching capabilities and a very long stability over time, however, they suffer from rather poor charge transport properties, showing a mobility around  $1 \times 10^{-3} \text{ cm}^2/\text{Vs}$ .<sup>[16]</sup> Many other high-performance semiconducting polymers display properties suitable for interaction with DAE in multi-component devices. A first correct assessment of DAE integration requires to test electrically and optically the photo-switching performances of bi-component films allowing to determine the most suitable polymer. In particular, switching amplitude and fatigue with respect to mobility in FET are employed as the major figures of merit to pick the most promising DAE/polymer pair for optoelectronic application. While P3HT remains one of the most used p-type semiconductors for organic electronics and one of the more established building blocks for these applications, in the last few years several materials have successfully challenged it, by displaying greater electrical performances and air stability. Among those, PDVT-8 and PCD-TTP are chosen as alternative host materials since they exhibit a different degree of crystallinity and microstructure than P3HT<sup>[47-48]</sup> and they feature HOMO energy levels that allow electronic interaction with the closed form of DAE-Me (see **Figure 5.12**).

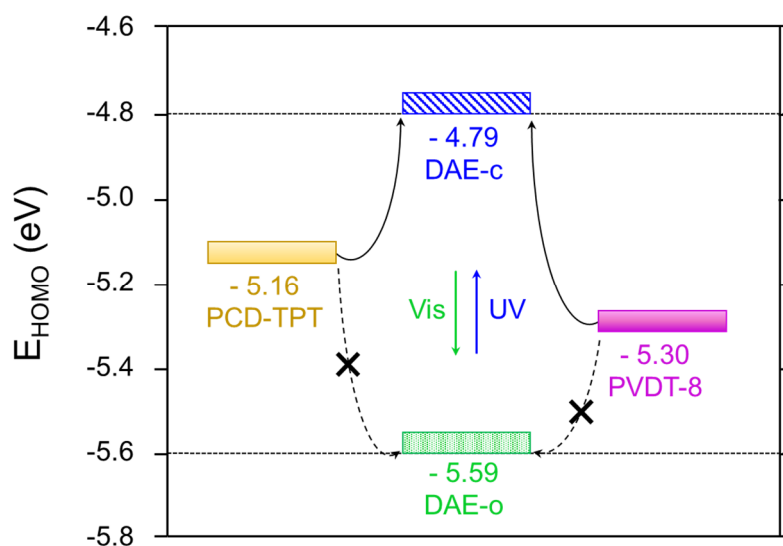


**Figure 5.12:** Energy HOMO levels of polymers in comparison with HOMO levels for DAEs in open and close form.<sup>[47-48]</sup>

Both polymers belong to a new class of high-performance polymers.<sup>[24]</sup> These materials have mobilities comparable to those of semicrystalline polymers ( $\mu_{\text{FET}} \sim 1 \text{ cm}^2 \text{ V}^{-1} \text{ s}^{-1}$ ),

although, morphologically, they are closer to the amorphous materials family. Indeed, their structural disorder is higher than that of semicrystalline polymers, as evidenced by lower diffracted intensities. However, they feature interconnected aggregates exhibiting at least short-range order which is sufficiently pervasive in the thin-film microstructure to provide effective pathways.

For the fabrication of bi-component device, we followed two different preparation procedures. The first is a blend method which has been already reported for P3HT/DAE blend in previous paragraph. The second is an innovative approach called “diffusion method” that consists in a two-step deposition process: (i) the DAE molecules are first deposited by spin-coating on top of a pure polymer layer, then (ii) the polymer is annealed in order to promote the permeation of the DAEs through the polymer matrix (see **Figure 5.13**).<sup>[49]</sup>

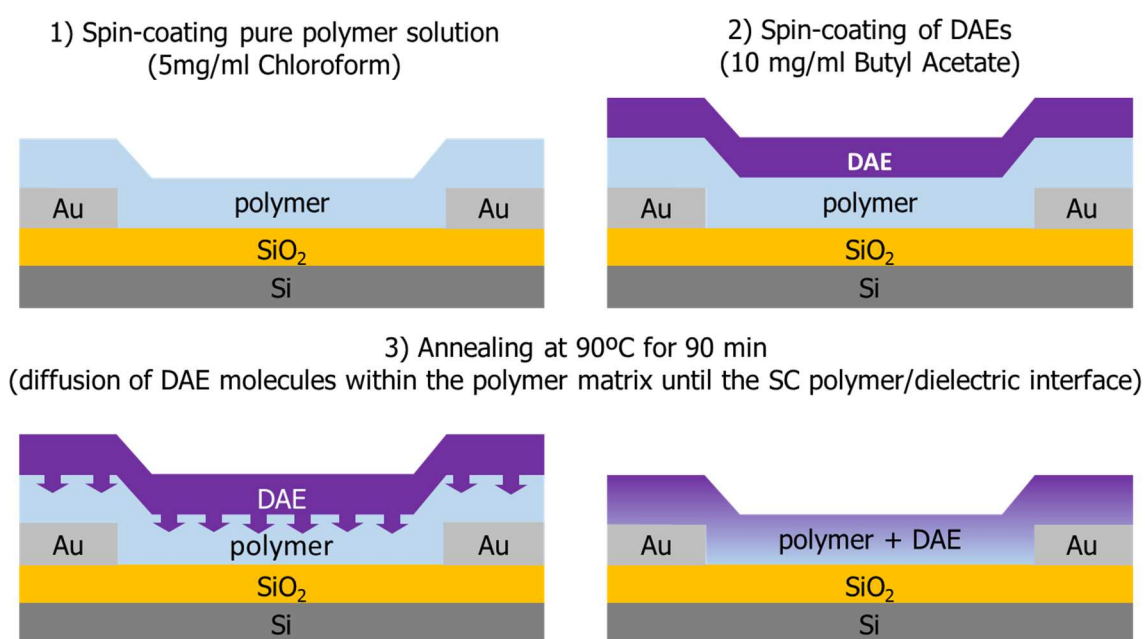


**Figure 5.13:** Schematic representation of the “diffusion method”.

The electrical performances of the transistors fabricated with blend and diffusion methods were compared to devices based on pristine polymers. **Figure 5.14** shows a reduced conductivity upon addition of DAE molecules into the polymer film. This effect is attributed to the distortion of the polymer matrix and the consequent increase of the overall structural disorder when the DAE molecules are included.<sup>[24]</sup> However, the decrease of measured field-effect mobility is slightly different depending on the DAE inclusion method, especially for PDVT-8. In **Table 1**, we can observe that the devices based on

PDVT-8/DAE blend fabricated with “diffusion technique” exhibit one order of magnitude higher field-effect mobility than devices fabricated with the “blend method”. While in the case of devices based on PCD-TPT/DAE blend, the field-effect mobility is less dependent on the fabrication method. The higher electrical performance of PDVT-8/DAE devices fabricated using the diffusion method can be attributed to the effect of the thermal annealing (required for this method) on the film microstructure and molecular arrangements of the polymer. In fact, as reported in literature, PDVT-8 sample increases in the crystallinity of the polymer thin films once thermal annealed.<sup>[48]</sup> Moreover, the thermal annealed PDVT-8 films exhibits a reduced interlayer distance than that of fully extended alkyl side chain, indicating that the side chains are closely interdigitated with the other side chains in adjacent layers; thus leading to an closer interconnection between ordered regions. Additionally, PDVT-8 polymer chains take predominantly edge-on oriented respective to the substrates. On the contrary to PCD-TPT which generally exhibits more amorphous surfaces and requires specific surface treatments/spacers to induce a specific orientation.<sup>[50]</sup>

Polymer	$\mu$ (cm <sup>2</sup> V <sup>-1</sup> s <sup>-1</sup> )		
	Pure	With diffused DAE	With blended DAE
PCD-TPT	0.30	0.005	0.003
PDVT-8	0.28	0.048	0.004

**Table 1:** Table comparing the field-effect mobility values before and after DAE inclusion

**Figure 5.14c-d** show that the drain current in blend devices is controlled not only by the gate-source voltage but also by light irradiations, proving that the DAEs act as photo-modulable trap levels in the semiconductor bulk. Although the optical switching between the more conductive and the more resistive states is observed for both polymers, blend devices based on PVDT-8 shows a higher switching ratio than PCD-TPT. From the absorption spectra reported in Chapter 2, we can observe that both polymers do not absorb light at the specific wavelengths utilized to switch the DAE between closed and open forms. Therefore, the difference in the current modulation is most likely due to the better DAE distribution and ability to interconvert within the one polymer respect to the other. The short-range order of PDVT-8 characterized by edge-on  $\pi$ -stacked aggregates possibly enables a more favorable polymer arrangement for DAE inclusion if compared to PCD-TPT. However, although these observations are consistent with the electrical measurement in **Figure 5.14** and with the structural investigations reported in literature

for pristine polymers, we recognize that are mostly speculations. Further structural characterization of polymer/DAE films is required for understanding the exact interchain organization at the dielectric interface in the FET devices, and how the DAE influences the polymer microstructures.

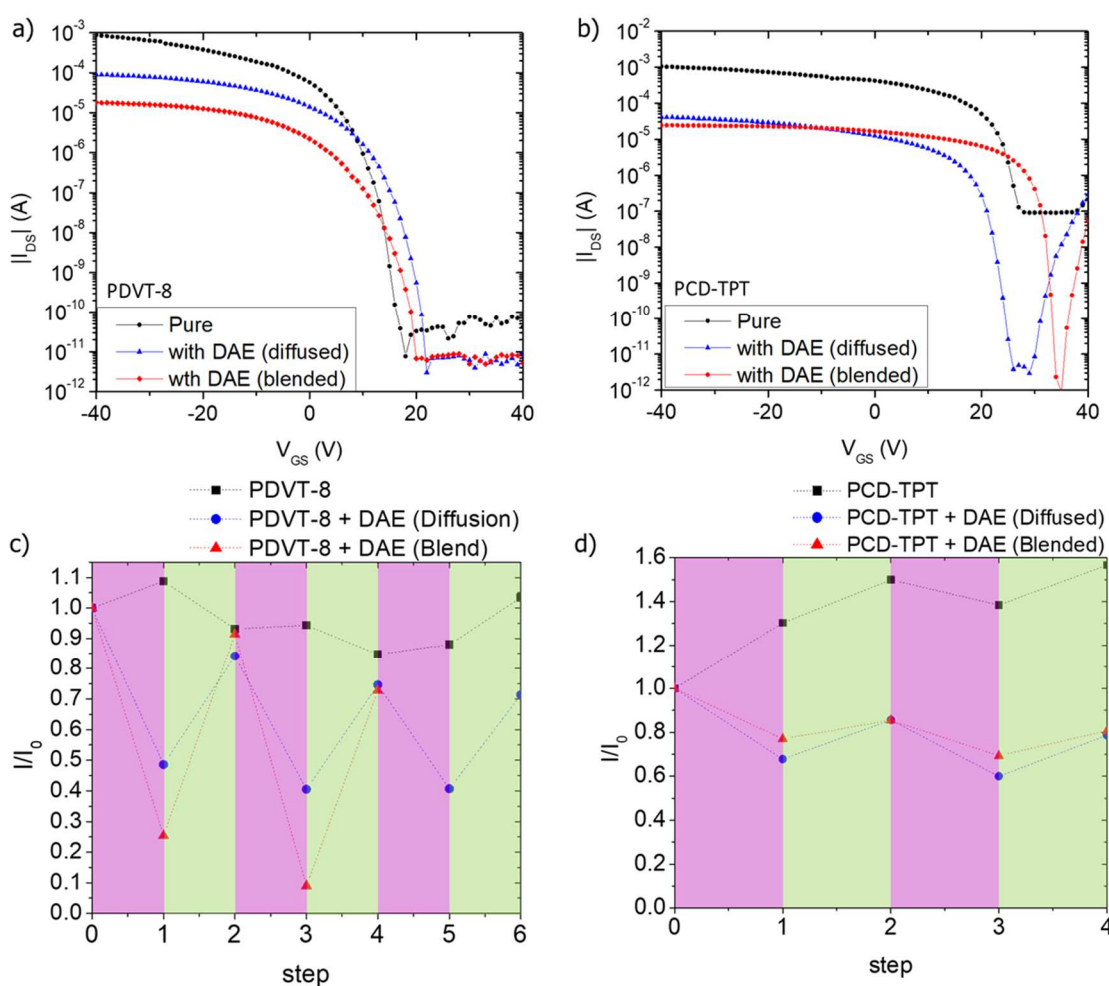


**Figure 5.14:** (a-b) Transfer characteristics of devices based on pure polymer (black), polymer and diffused DAE (red), polymer and DAE blend from solution (blue), at  $V_{DS} = -5$  V. (c-d) Static photo-switching performances at  $V_{GS} = -40$  V and  $V_{DS} = -5$  V. The value of the drain current  $I$  are normalized by the  $I_0$ , which is the value of the drain current measured in the initial step.

In conclusion, PDVT-8 and PCD-TPT are preliminary investigated as possible alternative to P3HT in DAE polymer blend for memory application. Their HOMO energy levels suitable for interaction with DAE-Me<sub>c</sub> and their higher intrinsic mobility led to

interesting results. In particular, devices based on PDVT-8/DAE blend fabricated with the “diffusion method” exhibit a field-effect mobility one order of magnitude higher respect to P3HT based devices and, at the same time, they show a switching ratio (50% of the initial drain current) that is initially comparable to P3HT devices. On the other hand, the higher rigidity of PCD-TPT polymer chain hinders the beneficial effects of “diffusion method” observed in PDVT-8 blends because, possibly, it does not allows the photo-responsive molecules to homogeneously diffuse into the more amorphous parts of the polymer film, maximizing the detrimental effects on both charge transport and photo-responsive properties.

Despite PDVT-8 blends showed high optical modulation, both polymers exhibit an important fatigue after few cycles already, differently from what is observed with devices based on P3HT/DAE blend. Indeed, OFET based on P3HT blend display outstanding photo-switchable capability with the two states being extremely stable over the timescale of several months and showing extremely high cycling resistance. Considering this, P3HT blend is selected as best candidate to fabricated optical controlled memory devices, as described in the following Chapter.

### 5.3 Conclusions

A major challenge for future electronics is the realization of multifunctional devices. A simple way to implement multifunctionality in a single device relies on the combination of different organic components, since each of these components gives a distinct property to the resulting hybrid material. Our approach relies on blending polymer with photochromic diarylethenes (DAE) in order to impart an additional function to organic thin-film transistor. The objective of this study was to optimize light responsive nature to thin-film transistors by dispersing photochromic DAE derivatives into a polymeric semiconducting matrix. Among the studied p-type semiconductors, P3HT blend with DAE-Me molecules leads to the realization of devices which exhibit photo-controlled current levels stable over time and fatigue-free optical cycling. Therefore, P3HT was selected for additional studies. In order to maximize the capability of DAE-Me to trap and de-trap the holes transported within the P3HT matrix when in the closed isomer and in the open isomer respectively, there must not be phase separation at the mesoscale between the two components. Hence, in order to tune the devices' multifunctionality, it is crucial to be able to understand and control those properties which are dependent on the structure and morphology of P3HT/DAE-Me<sub>o</sub> blends. By changing molecular weight and regioregularity of the P3HT in the blend, we were able to conclude that the optoelectronic properties of the bi-functional FET are closely related to the DAE-Me<sub>o</sub> phase separation within a P3HT matrix. P3HT films with higher regioregularity show augmented electrical performance though their photo-response is moderate.

For annealing temperatures above 80 °C, the photo-response reduces. The Spano model together with UV-vis absorption measurements, and quantum yield observations suggests that the reduction of switching performance possibly results because the presence of DAE-Me<sub>o</sub> tends to decrease the melting point of the P3HT, assisting in increasing the lamellar crystal thickness without necessarily affecting the overall degree of crystallinity during thermal annealing. At temperatures which exceeds 160 °C, there is absolutely no photo-response of the transfer curves as DAE-Me<sub>o</sub> melts. Overall, this study is crucial in understanding bi-functional devices exploiting P3HT/DAE-Me<sub>o</sub>. Both the regioregularity and the annealing temperature must be carefully chosen and controlled to ensure that the devices' properties are tuned to our needs. Moreover, future technology which plans on using these blends must consider the temperature window which allows the devices to function while retaining its innate characteristics.

## References

- [1] B. C. Thompson, Y. G. Kim, T. D. McCarley, J. R. Reynolds, *J Am Chem Soc* **2006**, 128, 12714.
- [2] B. Lebeau, P. Innocenzi, *Chem Soc Rev* **2011**, 40, 886.
- [3] I. Ratera, J. Veciana, *Chem Soc Rev* **2012**, 41, 303.
- [4] M. Muccini, *Nat Mater* **2006**, 5, 605.
- [5] W. P. Wu, Y. Q. Liu, D. B. Zhu, *Chem Soc Rev* **2010**, 39, 1489.
- [6] Z. Y. Chen, M. J. Lee, R. S. Ashraf, Y. Gu, S. Albert-Seifried, M. M. Nielsen, B. Schroeder, T. D. Anthopoulos, M. Heeney, I. McCulloch, H. Sirringhaus, *Adv Mater* **2012**, 24, 647.
- [7] Y. L. Guo, G. Yu, Y. Q. Liu, *Adv Mater* **2010**, 22, 4427.
- [8] M. Mas-Torrent, C. Rovira, *Chem Soc Rev* **2008**, 37, 827.
- [9] S. Holliday, J. E. Donaghey, I. McCulloch, *Chem Mater* **2014**, 26, 647.
- [10] R. Gostl, A. Senf, S. Hecht, *Chem Soc Rev* **2014**, 43, 1982.
- [11] L. Wang, Q. Li, *Chem Soc Rev* **2018**, 47, 1044.
- [12] E. Orgiu, P. Samori, *Adv Mater* **2014**, 26, 1827.
- [13] S. Kawata, Y. Kawata, *Chem Rev* **2000**, 100, 1777.
- [14] D. Dulic, S. J. van der Molen, T. Kudernac, H. T. Jonkman, J. J. D. de Jong, T. N. Bowden, J. van Esch, B. L. Feringa, B. J. van Wees, *Phys Rev Lett* **2003**, 91.
- [15] P. Andersson, N. D. Robinson, M. Berggren, *Synthetic Met* **2005**, 150, 217.
- [16] E. Orgiu, N. Crivillers, M. Herder, L. Grubert, M. Patzel, J. Frisch, E. Pavlica, D. T. Duong, G. Bratina, A. Salleo, N. Koch, S. Hecht, P. Samori, *Nat Chem* **2012**, 4, 675.
- [17] T. Leydecker, M. Herder, E. Pavlica, G. Bratina, S. Hecht, E. Orgiu, P. Samori, *Nat Nanotechnol* **2016**, 11, 769.
- [18] M. Campoy-Quiles, T. Ferenczi, T. Agostinelli, P. G. Etchegoin, Y. Kim, T. D. Anthopoulos, P. N. Stavrinou, D. D. C. Bradley, J. Nelson, *Nat Mater* **2008**, 7, 158.
- [19] H. Hoppe, N. S. Sariciftci, *J Mater Chem* **2006**, 16, 45.
- [20] M. El Gemayel, K. Borjesson, M. Herder, D. T. Duong, J. A. Hutchison, C. Ruzie, G. Schweicher, A. Salleo, Y. Geerts, S. Hecht, E. Orgiu, P. Samori, *Nat Commun* **2015**, 6.
- [21] R. J. Kline, M. D. McGehee, E. N. Kadnikova, J. S. Liu, J. M. J. Frechet, M. F. Toney, *Macromolecules* **2005**, 38, 3312.
- [22] A. Zen, J. Pflaum, S. Hirschmann, W. Zhuang, F. Jaiser, U. Asawapirom, J. P. Rabe, U. Scherf, D. Neher, *Adv Funct Mater* **2004**, 14, 757.
- [23] M. Brinkmann, P. Rannou, *Adv Funct Mater* **2007**, 17, 101.
- [24] R. Noriega, J. Rivnay, K. Vandewal, F. P. V. Koch, N. Stingelin, P. Smith, M. F. Toney, A. Salleo, *Nat Mater* **2013**, 12, 1038.

- [25] A. G. Dixon, R. Visvanathan, N. A. Clark, N. Stingelin, N. Kopidakis, S. E. Shaheen, *J Polym Sci Pol Phys* **2018**, 56, 31.
- [26] R. Mauer, M. Kastler, F. Laquai, *Adv Funct Mater* **2010**, 20, 2085.
- [27] H. Sirringhaus, P. J. Brown, R. H. Friend, M. M. Nielsen, K. Bechgaard, B. M. W. Langeveld-Voss, A. J. H. Spiering, R. A. J. Janssen, E. W. Meijer, P. Herwig, D. M. de Leeuw, *Nature* **1999**, 401, 685.
- [28] S. Hugger, R. Thomann, T. Heinzel, T. Thurn-Albrecht, *Colloid Polym Sci* **2004**, 282, 932.
- [29] Y. C. Huang, S. Y. Chuang, M. C. Wu, H. L. Chen, C. W. Chen, W. F. Su, *J Appl Phys* **2009**, 106.
- [30] M. Reyes-Reyes, K. Kim, D. L. Carroll, *Appl Phys Lett* **2005**, 87.
- [31] F. Padinger, R. S. Rittberger, N. S. Sariciftci, *Adv Funct Mater* **2003**, 13, 85.
- [32] Y. Ishiguro, R. Hayakawa, T. Chikyow, Y. Wakayama, *Acs Appl Mater Inter* **2014**, 6, 10415.
- [33] F. P. V. Koch, J. Rivnay, S. Foster, C. Muller, J. M. Downing, E. Buchaca-Domingo, P. Westacott, L. Y. Yu, M. J. Yuan, M. Baklar, Z. P. Fei, C. Luscombe, M. A. McLachlan, M. Heeney, G. Rumbles, C. Silva, A. Salleo, J. Nelson, P. Smith, N. Stingelin, *Prog Polym Sci* **2013**, 38, 1978.
- [34] K. Tremel, S. Ludwigs, *P3ht Revisited: From Molecular Scale to Solar Cell Devices* **2014**, 265, 39.
- [35] D. Chlebosz, L. Janasz, W. Pisula, A. Kiersnowski, *Polimery-W* **2016**, 61, 433.
- [36] M. Brinkmann, *J Polym Sci Pol Phys* **2011**, 49, 1218.
- [37] T. Q. Nguyen, V. Doan, B. J. Schwartz, *J Chem Phys* **1999**, 110, 4068.
- [38] T. Odijk, *Macromolecules* **1983**, 16, 1340.
- [39] J. F. Chang, B. Q. Sun, D. W. Breiby, M. M. Nielsen, T. I. Solling, M. Giles, I. McCulloch, H. Sirringhaus, *Chem Mater* **2004**, 16, 4772.
- [40] J. Clark, J. F. Chang, F. C. Spano, R. H. Friend, C. Silva, *Appl Phys Lett* **2009**, 94.
- [41] H. H. Yang, S. W. LeFevre, C. Y. Ryu, Z. N. Bao, *Appl Phys Lett* **2007**, 90.
- [42] A. M. Ballantyne, L. Chen, J. Dane, T. Hammant, F. M. Braun, M. Heeney, W. Duffy, I. McCulloch, D. D. C. Bradley, J. Nelson, *Adv Funct Mater* **2008**, 18, 2373.
- [43] H. L. Hu, K. Zhao, N. Fernandes, P. Boufflet, J. H. Bannock, L. Y. Yu, J. C. de Mello, N. Stingelin, M. Heeney, E. P. Giannelise, A. Amassian, *J Mater Chem C* **2015**, 3, 7394.
- [44] R. J. Kline, M. D. McGehee, E. N. Kadnikova, J. S. Liu, J. M. J. Frechet, *Adv Mater* **2003**, 15, 1519.
- [45] F. C. Spano, *J Chem Phys* **2005**, 122.
- [46] F. C. Spano, *Chem Phys* **2006**, 325, 22.

- [47] L. Ying, B. B. Hsu, H. Zhan, G. C. Welch, P. Zalar, L. A. Perez, E. J. Kramer, T.-Q. Nguyen, A. J. Heeger, W.-Y. Wong, *J Am Chem Soc* **2011**, 133, 18538.
- [48] H. Chen, Y. Guo, G. Yu, Y. Zhao, J. Zhang, D. Gao, H. Liu, Y. Liu, *Adv Mater* **2012**, 24, 4618.
- [49] W. Rekab, T. Leydecker, L. Hou, H. Chen, M. Kirkus, C. Cendra, M. Herder, S. Hecht, A. Salleo, I. McCulloch, *Adv Funct Mater* **2019**, 1908944.
- [50] C. Luo, A. K. K. Kyaw, L. A. Perez, S. Patel, M. Wang, B. Grimm, G. C. Bazan, E. J. Kramer, A. J. Heeger, *Nano Lett* **2014**, 14, 2764.

## Chapter 6. Optically Switchable Ferroelectric Field-effect Transistors (OS-FeFET) based on P3HT/DAE blend semiconductor layer and organic ferroelectric gate insulator

The ubiquity of information technologies led to the generation of colossal amounts of data, which must be stored and retrieved for very long time.<sup>[1-2]</sup> To address the need for an increasingly larger storage capacity in smaller and more lightweight devices two approaches can be pursued. The former relies on the use of cumbersome lithography-based nanofabrication through which more and more memory cells per unit area can be integrated.<sup>[3]</sup> The latter consists in realization of memory cells with increased storage capabilities, i.e. multilevel memories.<sup>[4]</sup> Such a grand challenge can be faced by exploiting molecular materials which can be made multi-responsive and multifunctional by design, thus opening endless opportunities for multilevel memory applications.<sup>[5-6]</sup> While conventional memories rely on the use of electrical writing and reading, the exploitation of alternative mechanisms to write and read information. In this framework, light writable/erasable memory in which the electrical readout can be photo-programmed promises to address faster writing time and more reliable readout.<sup>[7-8]</sup> In this context, a simple way to implement multifunctionality in a single device relies on the combination of different organic components, with each of them imparting a distinct property to the resulting hybrid material and device thereof.<sup>[9-11]</sup> The functionality of solution-processed organic field-effect transistors (OFET) has been enhanced during the past years with the development of hybrid systems incorporating functional molecules in semiconducting matrices.<sup>[12-13]</sup> In this concern, the possibility of being remotely controlled with high spatiotemporal resolution without generation of waste products, makes photochromic molecules ideal functional components for being integrated in the next generation of optoelectronic memory devices.<sup>[14]</sup> Among various photochromic compounds, diarylethenes exhibit fast photoswitching, high fatigue resistance, thermal bistability, and energy levels that can be tailored through molecular design.<sup>[15]</sup> Another powerful way to increase data storage capacity in a multilevel memory relies on the exploitation of ferroelectricity.<sup>[16]</sup> This can be put in place by using a ferroelectric gate insulator in an organic TFT. One of the most promising organic ferroelectric materials is poly(vinylidene fluoride-trifluoroethylene) (P(VDF-TrFE)) which has several advantageous properties: relatively large fatigue-free remnant polarization,<sup>[17]</sup> modest switching time and good thermal

stability.<sup>[18]</sup> Nevertheless, P(VDF-TrFE) film performance deteriorates upon decreasing the film thickness (i.e. increase of coercive electric field and leakage current).<sup>[19]</sup> Only a few progresses have been reported on overcoming the size effect problem by improving the process and reducing the film thickness.<sup>[20-21]</sup> A strategy to circumvent this problem relies on the use of an increasing number of memory states per memory cell. <sup>[22-24]</sup> On the one hand, multi-layer ferroelectric films separated with an insulator have been exploited. <sup>[25-26]</sup> On the other hand, intermediate polarization states, obtained by applying slightly different voltages in ferroelectric layers, have been also exploited, overall improving the storage capacity per memory cell.<sup>[27-29]</sup> Although the use of either photochromic molecules or ferroelectric polymers for memory applications has been proven successful, a combination of these two strategies in OFETs has never been explored so far.

Here, we demonstrate that fast and robust optical, multi-level, non-volatile memory operations can be achieved in a multifunctional ferroelectric transistor (FeFET). Our approach relies on the use of a blend of a semiconducting polymer with photochromic diarylethenes as active materials capable to impart a photoresponsive nature to an organic FeFET. In our devices, the active layer includes poly(3-hexylthiophene) (P3HT) and ad hoc synthesized diarylethenes (DAE-Me). Organic thin-film transistors (OTFTs) using such bicomponent active layer exhibit outstanding photo-switchable capability with the two states being extremely stable over the timescale of several months.<sup>[30]</sup> In our devices, data are stored in a micrometric transistor memory cell composed of a diarylethene-semiconductor blend film underneath a ferroelectric gate insulator. Information writing into the memory cell can be done independently by either using UV light irradiation or gate voltage sweeps, while the readout of the stored information is carried out by measuring output drain current. The use of fast optical pulses, i.e. on the nanosecond timescale, renders our devices suitable for fast hybrid ferroelectric-optical data storage in electronic circuits.

## 6.1 Results and Discussions

The geometry of our memory cell and the operating building blocks are shown schematically in **Figure 6.1**. The storage of information upon changing the transistor output current occurs through polarization change in the ferroelectric layer (blue region) or by photoactivated trapping and de-trapping in the photochromic/polymer blend (red region).

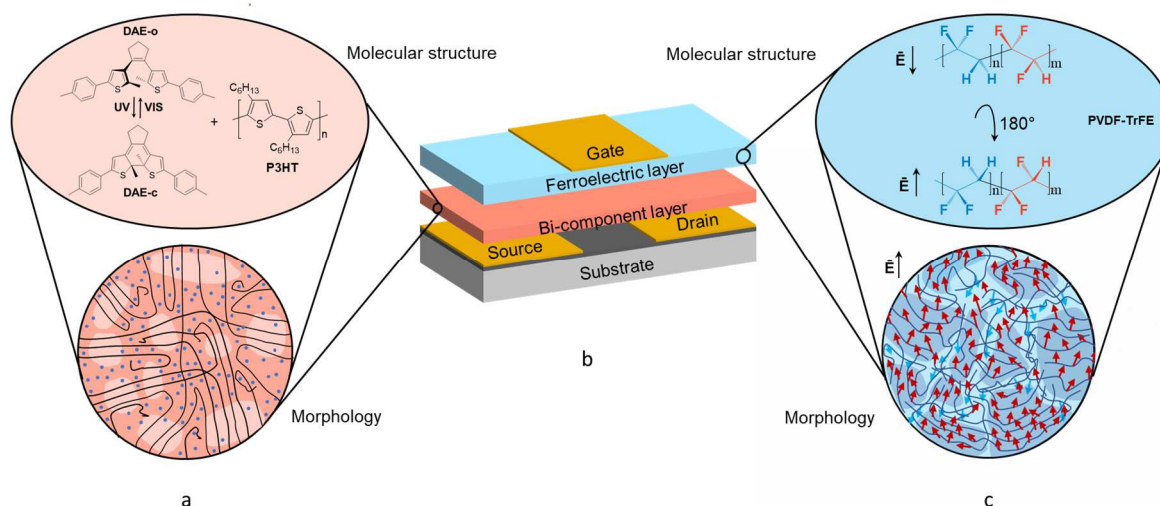


**Figure 6.1: Schematic layout of a optically switchable ferroelectric FET (OSFeFET)** comprising a ferroelectric PVDF-TrFE layer (c – in blue) as gate insulator and a bi-component P3HT/DAE film (a – in red) as semiconducting layer. **c) Ferroelectric polymer layer:** PVDF-TrFE polymer chains can undergo a  $180^\circ$  rotation depending on the intensity of the electric field applied across the dielectric. The morphology influences the capability of the thin film to retain polarization. The ferroelectric  $\beta$ -crystal-phase of PVDF-TrFE is represented as darker blue shadowed area in (c). Negative remanent polarization induces a steady (gate) bias within the semiconductor bi-component layer. **a) Schematic of the microstructure of P3HT/DAE film:** The coexistence of ordered (lighter shaded areas) and amorphous polymer regions allows DAE molecules (blue dots) to be homogeneously dispersed within the polymer matrix. Thus, the energetic interaction between charges moving through conducting paths can be controlled with light.

Irradiation of the device with UV light triggers the DAE isomerization from the open to the close form, the latter acting as hole acceptors in the semiconducting polymer, thereby lowering the net out device current. Hence, data can be written by means of short and low power optical pulses and are encoded in the amount of traps present within the channel.<sup>[30]</sup> On the other hand, the ferroelectric state of the gate insulator layer influences the electrical

field at the interface with the semiconductor in a non-volatile way and therefore the accumulation/depletion state of the device. In this case, writing into the memory or erasing the stored information is achieved by gate voltage sweeps inducing polarization switching. If the voltage applied is high enough to exceed the coercive field, the dipoles align to the external electric field  $E_0$  resulting in a permanent polarization after the removal of  $E_0$ . When the gate field exceeds the coercive field the dipoles in the ferroelectric layer partially align. This enables to reach several partial polarization states which encode multi-level current states. Our device is thus a combination of an optically-controlled memory and a ferroelectric memory, whereby the output current is modulated by varying the electronic states of the material using light or gate voltage pulses, in stark contrast to the physical processes used in conventional electrical or optical storage. In the following we characterized the first example of Optically Switchable Ferroelectric Field-effect Transistor (OSFeFET) device in three distinct and key aspects : (1) program and erase (P/E) cycles of partial non-volatile ferroelectric induced states, (2) light response at fully polarization state, and (3) current modulation induced by light on several polarization states.

As time zero experiments, the OSFeFET needs to be validated in each of its components. While P3HT/DAE-Me blend has been extensively studied in experimental results in Chapter 4 and Chapter 5, the organic ferroelectric layer still requires an optimization. To assure that the desired ferroelectric performances was obtained, the deposition process of the P(VDF-TrFE) and the resulting film properties was initially tested in a capacitor structure, as described in **Appendix A2.1**. Subsequently, OSFeFET were fabricated as described in **Appendix A2.2**.

Firstly, we proved that the OSFeFET conductivity can be modulated in a non-volatile way by partial polarizations of the ferroelectric layer. If the ferroelectric layer is negatively polarized, it can induce a permanent accumulation layer in semiconducting film. This means that when a non-zero drain voltage is applied, a drain current can be measured even if the gate voltage is zero. The electrical programming of the fabricated OSFeFETs was performed by applying an electrical bias sweep between the gate electrode and the source and drain electrodes. The applied erase-programming voltage waveform, which is better described in **Figure A2.3**, goes from +40 V to  $V_p$  (the negative voltage peak) at sweep rate of approx 2 V/s. Therefore, depending on  $V_p = -40$  V, -20 V, -17.5 V, -15 V or -10 V the resulting P/E cycle time  $t_{p-Fe}$  ranges from 30 s to 60 s. **Figure 6.2** shows that five different partial polarization states are achievable.

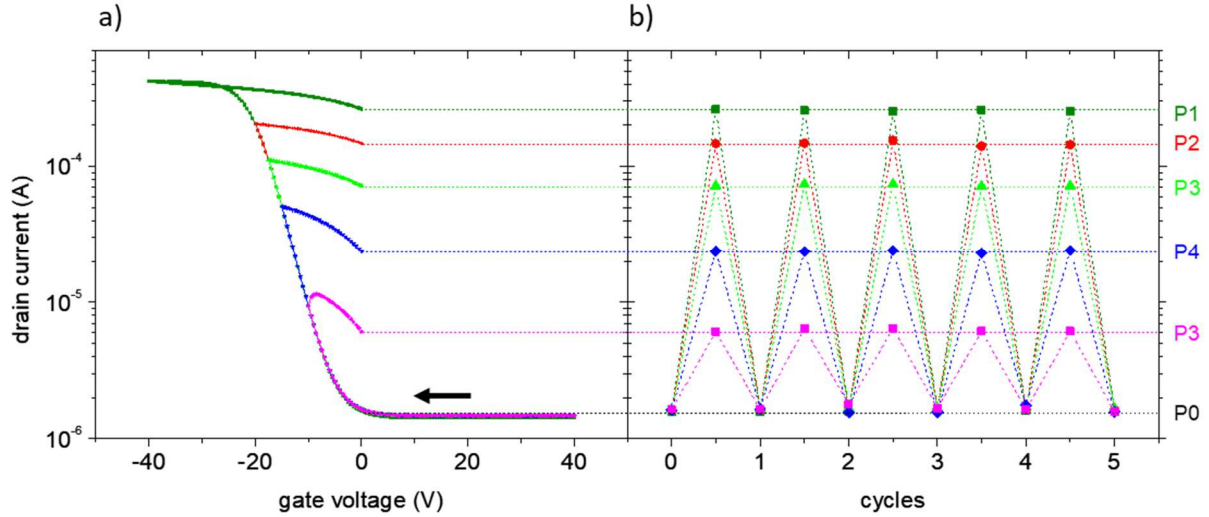


**Figure 6.2: Polarization states and cyclability in P3HT/DAE-Me OSFeFET.** a) Gate voltage sweeps program the ferroelectric OSFeFET into six non-volatile drain current states P0-P5. The writing process starts from -40 V (in order to erase previous polarization state) to negative polarization higher than coercive field: -40 V, -20 V, -17.5 V, -15 V and -10 V and stop at 0 V. This current state is now non-volatile programmed in the memory till an erase cycle is performed and it can be measured just applying a little drain-source voltage as -0.5 V. b) No major fatigue appears over several P/E cycles.

Each of these states corresponds to a different accumulation condition of the FET channel and, therefore, to a distinct FET operational regime. The obtained distinct drain current levels (P1, P2, P3, P4, P5) are reproducible over several cycles and no fatigue is observed, as reported in **Figure 6.2b**. It is known that P(VDF-TrFE) cyclability fatigue occurs because of dehydrofluorination, leading to the release of HF vapors, consequent formation of bubbles in the top metal electrode, and its subsequent delamination.<sup>[17]</sup> However, such delamination and the consequent fatigue is proved to be dependent to the cycles frequency. Although we exploited Au metal layer as top gate electrodes, we do not observe any fatigue over cycles in the polarization states because we used an extremely slow sweep rate during programming operations. Indeed, P(VDF-TrFE) devices operated at low frequency showed a fatigue-free polarization over  $10^7$  cycles.<sup>[31]</sup> On the other hand, increasing the P/E cycle frequency would have mean to damage our devices capability irreversibly hindering any further possible tests and analysis. In order to prevent metal delamination and improve the fatigue endurance at higher frequency, several approaches have been reported.<sup>[17, 31-36]</sup> These methods are fully compatible with the fabrication method of our OSFeFETs, therefore they could be exploited for lowering the  $t_{p-Fe}$  range. However, this

study is not in line with the objective of this work and it will be left for future improvements.

The last step of the electrical characterization for ferroelectric induced properties in OSFeFET requires data retention tests to prove that such devices can be used in memory applications. **Figure 6.3** shows that each current level is stable over time up to several days.

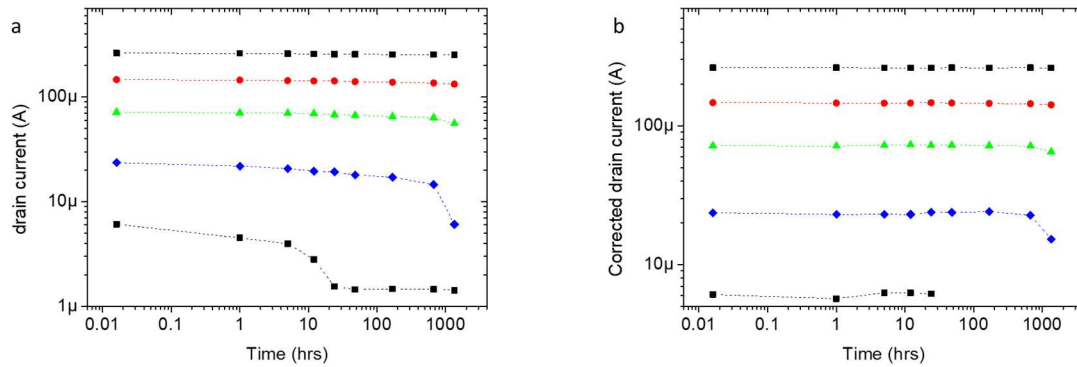


**Figure 6.3:** **a)** Data retention of P1-P5 current states. At time zero, five different FeFETs were programmed according one of the five polarization cycle described in **Figure A2.3** and the readout currents were measured regularly over several days. **b)** Data retention corrected by the electrical disturb induced during read operation

The read operation of the drain current has been repeated nine times over time to test the device capability to retain data. **Figure 6.3a** shows that the drain current readouts of P1-P5 levels. However, before making any conclusion, we need to consider that the readout is affected by the measurement itself. The read operation consists in probing the drain current level by applying  $-0.5$  V as drain-source voltage. Since the gate is connected to the ground together with the source electrode, the low  $V_{DS}$  is enough to slightly perturb the dipole alignment of the ferroelectric layer, resulting in a lowering of the ferroelectric polarization. This means that the retained data is partially lost after each read operation. The absolute current drop induced by the read operation has been calculated and the data retention measurements have been corrected accordingly in **Figure 6.3b**. Corrected drain current is flat proving that devices are able to retain data for long time exceeding previously reported devices performances.<sup>[37]</sup>

$$I_n = n\Delta I_{read} - A(t_n - t_0) \quad \text{(Equation 6.1)}$$

Such effect can be reduced till become almost negligible by reducing the source-drain voltage applied during read operations.

We now take our memory concept a step further by illustrating how the multi-bit ferroelectric device can be also controlled by light. Our approach relies on the wavelength-dependent property of photochromic semiconducting blend, which enables wavelength-selective control on the current of non-volatile memory elements (as demonstrated by Leydecker et al.<sup>[30]</sup> for simple blend optically switchable memories with a storage ‘lifetime’ exceeding 500 days).

**Figure 6.4a** shows the change in output current upon repeated switching from DAE’s open (no electronic interaction with the HOMO of P3HT) to closed state (electronic interaction, with DAE acting as accepting levels for holes). Each optical P/E process that results in a change in device output current (termed ‘optical switching’ hereon) represents the irradiation (310 nm / 530 nm) driven effect in the memory state. The results demonstrate unequivocal multi-level data storage in our photochromic memory transistor, with good signal to noise ratio SNR. As illustrated in **Figure 6.4b**, the switching ratio is proportional to UV light irradiation time and it is highly reproducible with a measured confidence interval of  $\pm 0.5$  %. In order to test the device limit, the fabricated transistor memory elements are operated using an optical pump-probe set-up in combination with a source-meter unit (SMU) as described in the **Appendix A2.4.1**. During such dynamic switching measurements both writing ( $\lambda = 310$  nm) and erasing ( $\lambda = 530$  nm) steps are performed with nanosecond light pulses generated with a laser. The suppression of the pump light and the control of the incident power is achieved by neutral density UV filters with optical densities (OD) of 0.5 and 1.0 OD. The 0.5 filter allows a transmittance of 30.1 % while the OD 1 filter enables a transmittance of 10 % which we had estimated as 33 % and 11 % respectively. The initial high-conductivity state (Level P1) in **Figure 6.4c** is prepared by fully negatively polarizing the ferroelectric layer and fully opening the DAE molecules, in such a way that maximum number of current states is ensured. The absolute current variation per laser pulse is determined by the laser power employed, which defines the amount of DAE molecules that switches inside the blend. To ensure high modulation between the open and closed states we use a transistor of 20  $\mu\text{m}$  channel length. With this device, a change in current readout of 1% is achieved using a single 3 ns write pulse of  $2.17 \times 10^{-7}$  J  $\text{cm}^{-2}$ . Further demonstrations of multi-level current operation were realized by using devices with smaller channel lengths. DAE open to close isomerization exhibits nearly 50 times higher quantum yield than the close to open.<sup>[15]</sup> This conveniently allows the use of pulses with lower incident power when switching from open to close states than for the opposite direction. Initially the pulses induce the isomerization of the DAE

molecules closer to the interface between semiconductor and ferroelectric layer, where the majority of mobile charge pathway resides inducing a higher current drop per laser pulse (see inset 1 **Figure 6.4c**). Therefore, the number of DAE-Me<sub>o</sub> in the channel will progressively lower after each pulse and the current variation will decrease and reach saturation over ~600 irradiation pulses, as shown in **Figure 6.4c**. In total, more than 600 current levels are distinguishable for each ferroelectric polarization state, yielding to a total amount of 3000 levels (>11-bit) if one considers the five ferroelectric polarization states. For the optical Erase process required to go back to Level P1, a consecutive green light irradiation is used, as described in the **Appendix A2**.

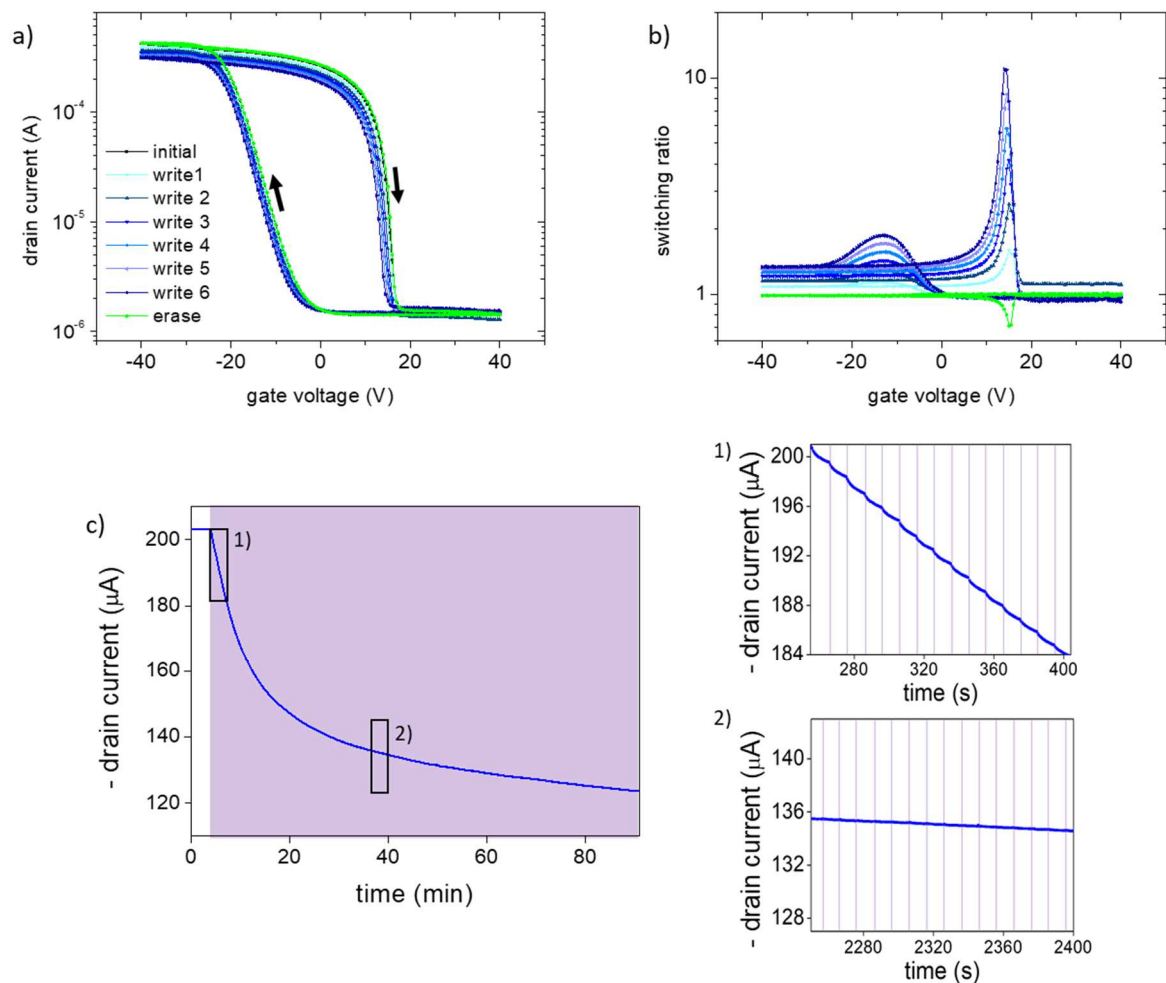


**Figure 6.4: Light response in P3HT/DAE-Me OSFeFET.** a) Full polarization transfer curves related to 6 writing steps using UV light (310 nm for 2 min) and 1 erase step using vis light (530 nm for 5 min). b) Switching ratio ( $I_{D_s,DAE-Me_o}/I_{D_s,DAE-Me_c}$ ) for each irradiation step as function of gate voltage. c) Dynamic drain current response to 0.1 Hz 3 ns UV (310 nm) laser pulses (with incident power  $P_i < 1 \mu\text{J cm}^{-2} \text{s}^{-1}$ ) when ferroelectric layer is fully polarized. Given their short duration (3 ns), illumination steps are not

represented to scale. Insets of Figure 6.4c showing the 3 ns induced steps at different times. After 40 min almost all DAE-Me is in its closed form, thus each 3 ns step induces markedly smaller current drop than at the beginning. Curves were plotted at  $V_{GS} = 0$  V and  $V_{DS} = -0.5$  V.

Besides storage capacity, speed is an integral part of all memory devices, and the speed at which optical Read, Write and Erase operations can be achieved in a single memory element is important. In our memory cell, Write and Erase are linked both to DAE isomerization times, which are intrinsic properties of the DAE molecules and have been reported to take place at picosecond (closure) and nanosecond to sub-nanosecond (opening) timescales, respectively.<sup>[38]</sup> Therefore, we were able to switch with pulses as short as 3 ns. However, to determine how fast the memory might be operated around each polarization state, we monitored the current variation by performing time-resolved measurements during optical switching to extract the optical program time  $t_{p-o}$ . The observed transient behavior is presented in **Appendix A2** where the switching dynamics and the speed of the blend memory were analyzed in detailed. In addition to the length of the Write pulse, the speed of the device is also limited by the post-excitation charge relaxation time (which we call the dead time). This dead time results in a minimum write-read delay on the order of 20 ms, as show in **Figure A2.6**. Further details of this analysis are presented in Appendix. Both the dead time and the readout time are crucially dependent on the device geometry, which determines the duration of the displacement current of non-equilibrium changes induced by illumination or applied voltage.<sup>[39]</sup> The duration is mainly determined by the time-of-flight time, which is the time required for charge carriers to drift across the transistor channel.<sup>[40-41]</sup> In order to speed-up access to the memory, this time can be further reduced by decreasing the channel length. Consequently, in addition to increasing the memory speed, the memory physical dimension could also be reduced, which would enable the stacking of more memory elements per unit area.

We next discuss the potential of our optical cell for future high-density data storage by showing that our memory element is also capable of reversible multi-level storage in a single cell, using simple but extremely effective light Write/Erase cycles for each polarization state. Optical Write/Erase pulses with varying pulse energy we are able to freely and reliably move the current response between intermediate levels (defined by electrical program operation) with high repeatability. This multi-level operation relies on

the freely accessible partial polarization states of PVDF-TrFE as ground levels for intermediate conductivity states due to consequently closure of DAE molecules. These mixed states exhibit current values lying between those induced by the ferroelectric partial polarization shown in **Figure 6.2a**. The number of additional memory levels can be defined by tailoring the amount of DAE (wt%) in the blend and the degree of  $\beta$ -phase crystallization of PVDF-TrFE within a single cell. The number of possible levels in a memory cell is limited by the separation between the highest and lowest current state for a certain partial polarization state and the required confidence interval of an intermediate photo-induced level. The former can be increased by using either a ferroelectric material exhibiting higher remnant polarization or semiconducting polymer with higher mobility. The confidence interval, on the other hand, is mainly limited by the minor variations in the switching and by the signal-to-noise ratio (SNR) of the readout measurement. On one hand, the number of memory levels can therefore be increased by just using a higher readout drain voltage, ensuring a better SNR. On the other hand, as discussed above, a higher drain voltage during read operation would be detrimental for the data retention. Therefore, the right trade-off has to be identified. At selected fabrication parameters, such multi-level operation is demonstrated in **Figure 6.5**.

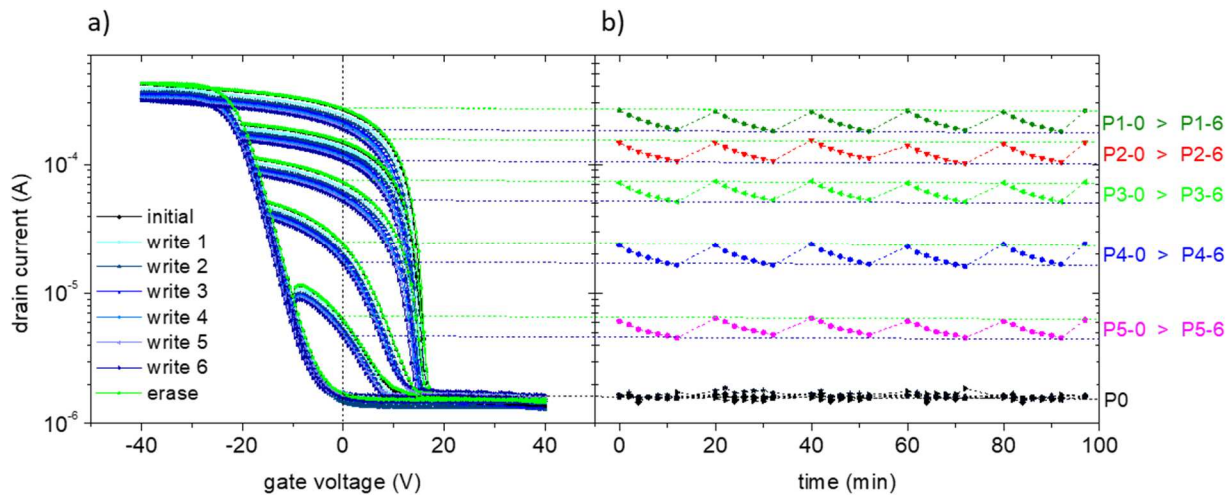


**Figure 6.5:** Current modulation in P3HT/DAE-Me OSFeFET induced by light irradiations on each of the five polarization states. **a)** Light modulation of  $I_{DS}V_{GS}$  curves for 5 ferroelectric polarizations. Writing steps make use of UV light (310 nm for 2 min), while erase step uses vis light (530 nm for 5 min). **b)** Dynamic drain current modulation to P/E steps for each ferroelectric state.

Six distinguishable levels are reached with 2 min UV pulses starting from each main polarization state. These levels were reached in a serial manner and subsequently the Erase operation was carried out from the 6-level to the initial state. These results demonstrate that each level can be reached from both directions, that is, with a closure as well as an opening step. This implies that any level is accessible from all others, with very accurate control of the current levels and remarkable repeatability, just by applying the appropriate Write or Erase electrical or optical program. Such capabilities provide a huge leap forward in terms of functionality and can be crucial for the realization of practicable hybrid memories.

## 6.2 Conclusions and Outlook

In conclusion, we have demonstrated the first prototype of a photochromic-ferroelectric, non-volatile OSFeFET memory that provides multi-level (up to 3000 levels) storage in a single transistor. Our approach uses ferroelectric gate insulator integrated with photochromic molecules embedded in a semiconducting polymer matrix. The memory elements are switched between memory states by orthogonal stimuli: light pulses or voltage sweep, which results in two independent program/erase operations. We have shown that using these program operations we were able to switch readily and directly the memory between the multiple induced current levels, with accurate control of the readout signal and excellent repeatability. We also demonstrate the capability for relatively fast ( $\sim$  milliseconds), low-power ( $< 1 \mu\text{J cm}^{-2} \text{ s}^{-1}$ ) optical write operations of the memory state while maintaining high readout SNR. The major bottleneck for the write operation speed of OSFeFET lies in the ferroelectric switching. Operating the P(VDF-TrFE) device at high frequency can induced a delamination of the top metal electrodes. However, several approaches have been reported to prevent metal delamination and improve the fatigue endurance at higher frequency. Consequently, we believe that improvements in write operation speed can potentially be achieved via a straightforward optimization of the device architecture. In any case, the writing speed of the device is not and does not want to be the key parameters of these memories since the focus is on non-volatility. In fact, non-volatile memories are generally used for applications which require frequently read access to the information which are however rarely modified. Therefore, for non-volatile memories the key requirement is to have short read times. We observed that the readout in OSFeFET can be performed on millisecond timescales, which could be further reduced by decreasing the channel length of the transistor. Consequently, in addition to increasing

the memory speed, the memory physical dimension could also be reduced, which would enable the stacking of more memory elements per unit area. Ferroelectric–photochromic system is fully scalable: the photochromic switching units are just few nm long and they can also be switched individually<sup>[42]</sup> and PVDF-TrFE organic ferroelectric devices have seen an interesting scaling trend in the switching time and the switching voltage as a function of the device area.<sup>[43]</sup> All these attributes, which are essential for the realization of a high-performant memory device are also fully compatible with flexible substrates. Therefore, these very first experimental results demonstrate the higher performance of OSFeFET in term of storage capacity and data retention in comparison with existing multi-component organic memories and they establish the foundations for promising devices in multi-functional opto-electronic application.

## References

- [1] S. Bertolazzi, P. Bondavalli, S. Roche, T. San, S. Y. Choi, L. Colombo, F. Bonaccorso, P. Samori, *Adv Mater* **2019**, 31.
- [2] R. Bez, A. Pirovano, *Materials Science in Semiconductor Processing* **2004**, 7, 349.
- [3] M. Li, *Science China Physics, Mechanics and Astronomy* **2012**, 55, 2316.
- [4] C. Li, W. Fan, B. Lei, D. Zhang, S. Han, T. Tang, X. Liu, Z. Liu, S. Asano, M. Meyyappan, *Appl Phys Lett* **2004**, 84, 1949.
- [5] P. Heremans, G. H. Gelinck, R. Muller, K.-J. Baeg, D.-Y. Kim, Y.-Y. Noh, *Chem Mater* **2010**, 23, 341.
- [6] C. S. Hwang, *Advanced Electronic Materials* **2015**, 1, 1400056.
- [7] M. Gu, X. Li, Y. Cao, *Light: Science & Applications* **2014**, 3, e177.
- [8] M. L. Laliou, R. Lavrijsen, B. Koopmans, *Nat Commun* **2019**, 10, 110.
- [9] Z. Wang, S. R. Zhang, L. Zhou, J. Y. Mao, S. T. Han, Y. Ren, J. Q. Yang, Y. Wang, Y. Zhai, Y. Zhou, *physica status solidi (RRL)–Rapid Research Letters* **2019**, 13, 1800644.
- [10] J. Ouyang, C.-W. Chu, C. R. Szmanda, L. Ma, Y. Yang, *Nat Mater* **2004**, 3, 918.
- [11] J. C. Scott, L. D. Bozano, *Adv Mater* **2007**, 19, 1452.
- [12] Q.-D. Ling, D.-J. Liaw, C. Zhu, D. S.-H. Chan, E.-T. Kang, K.-G. Neoh, *Prog Polym Sci* **2008**, 33, 917.
- [13] S. Möller, C. Perlov, W. Jackson, C. Taussig, S. R. Forrest, *Nature* **2003**, 426, 166.
- [14] H. Ling, K. Tan, Q. Fang, X. Xu, H. Chen, W. Li, Y. Liu, L. Wang, M. Yi, R. Huang, *Advanced Electronic Materials* **2017**, 3, 1600416.
- [15] M. Herder, B. M. Schmidt, L. Grubert, M. Patzel, J. Schwarz, S. Hecht, *J Am Chem Soc* **2015**, 137, 2738.
- [16] W. Y. Kim, H.-D. Kim, T.-T. Kim, H.-S. Park, K. Lee, H. J. Choi, S. H. Lee, J. Son, N. Park, B. Min, *Nat Commun* **2016**, 7, 10429.
- [17] D. Zhao, I. Katsouras, M. Li, K. Asadi, J. Tsurumi, G. Glasser, J. Takeya, P. W. Blom, D. M. De Leeuw, *Sci Rep-Uk* **2014**, 4, 5075.
- [18] R. C. Naber, K. Asadi, P. W. Blom, D. M. de Leeuw, B. de Boer, *Adv Mater* **2010**, 22, 933.
- [19] T. Furukawa, T. Nakajima, Y. Takahashi, *Ieee T Dielect El In* **2006**, 13, 1120.
- [20] A. Gerber, M. Fitsilis, R. Waser, T. J. Reece, E. Rije, S. Ducharme, H. Kohlstedt, *J Appl Phys* **2010**, DOI: 10.1063/1.3437638124119.
- [21] J. Ryu, K. No, Y. Kim, E. Park, S. Hong, *Sci Rep* **2016**, 6, 36176.
- [22] L. Baudry, I. Lukyanchuk, V. M. Vinokur, *Sci Rep* **2017**, 7, 42196.
- [23] D. Ricinchi, M. Okuyama, *J. Phys. D: Appl. Phys.* **2009**, 42.
- [24] A. Ghosh, G. Koster, G. Rijnders, **2016**, 26.
- [25] Woo Young Kim<sup>1</sup>, Hyeon-Don Kim<sup>1,\*</sup>, Teun-Teun Kim<sup>1,2,\*</sup>, Hyun-Sung Park<sup>1</sup>, Kanghee Lee<sup>1</sup>, Hyun Joo Choi<sup>1</sup>, w. Seung Hoon Lee<sup>1</sup>, Jaehyeon Son<sup>1</sup>, Namkyoo Park<sup>3</sup> & Bumki Min<sup>1</sup>.
- [26] G. A. Boni, L. D. Filip, C. Chirila, I. Pasuk, R. Negrea, I. Pintilie, L. Pintilie, *Nanoscale* **2017**, 9, 19271.
- [27] K. Asadi, P. W. Blom, D. M. de Leeuw, *Appl Phys Lett* **2011**, 99, 156.
- [28] B. Kam, X. Li, C. Cristoferi, E. C. Smits, A. Mityashin, S. Schols, J. Genoe, G. Gelinck, P. Heremans, *Appl Phys Lett* **2012**, 101, 033304.
- [29] Z. Dong, **2016**, DOI: 10.1063/1.4953199.
- [30] T. Leydecker, M. Herder, E. Pavlica, G. Bratina, S. Hecht, E. Orgiu, P. Samori, *Nat Nanotechnol* **2016**, 11, 769.
- [31] D. Singh, A. Garg, *Phys Chem Chem Phys* **2017**, 19, 7743.
- [32] J.-W. Yoon, S.-M. Yoon, H. Ishiwara, *Jpn J Appl Phys* **2010**, 49, 030201.
- [33] M. A. Khan, H. N. Alshareef, I. N. Odeh, M. N. Almadhoun, Google Patents, 2018.
- [34] T. Ishida, Google Patents, 2009.
- [35] H. Xu, J. Zhong, X. Liu, J. Chen, D. Shen, *Appl Phys Lett* **2007**, 90, 092903.

- [36] M. Li, N. Stingelin, J. J. Michels, M.-J. Spijkman, K. Asadi, K. Feldman, P. W. Blom, D. M. de Leeuw, *Macromolecules* **2012**, 45, 7477.
- [37] Q. Wu, J. Li, Y. Song, W. Ou-Yang, *Org Electron* **2019**, 105491.
- [38] M. Irie, T. Fulcaminato, K. Matsuda, S. Kobatake, *Chem Rev* **2014**, 114, 12174.
- [39] E. Pavlica, G. Bratina, *Journal of Physics D: Applied Physics* **2008**, 41, 135109.
- [40] L. Dunn, D. Basu, L. Wang, A. Dodabalapur, *Appl Phys Lett* **2006**, 88, 063507.
- [41] F. Otón, R. Pfattner, E. Pavlica, Y. Olivier, E. Moreno, J. Puigdollers, G. Bratina, J. Cornil, X. Fontrodona, M. Mas-Torrent, *Chem Mater* **2011**, 23, 851.
- [42] C. C. Jia, A. Migliore, N. Xin, S. Y. Huang, J. Y. Wang, Q. Yang, S. P. Wang, H. L. Chen, D. M. Wang, B. Y. Feng, Z. R. Liu, G. Y. Zhang, D. H. Qu, H. Tian, M. A. Ratner, H. Q. Xu, A. Nitzan, X. F. Guo, *Science* **2016**, 352, 1443.
- [43] S. Das, J. Appenzeller, *Org Electron* **2012**, 13, 3326.

## Chapter 7. Conclusion and Outlook

Information storage is a basic function required in most electronic devices. Besides large data storage capacity and data retention, future electronic applications for our daily lives shall require additional features such as flexibility and multifunctionality. Organic electronics, as alternative solution to conventional inorganic semiconductor-based electronics, offers unconventional pathways to address such requirements. In this regard, this thesis focuses on the realization of an optically switchable ferroelectric organic field-effect transistor (OSFeFET) device based on a bicomponent semiconductor/photochromic blend that imparts storage capability to the device through a multi-level non-volatile electrical response. Such blend is combined with ferroelectric layer in a non-volatile memory device to boost storage capacity. Our proof-of-concept provides unambiguous evidence for the disruptive potential of multi-component organic devices for the development of a novel generation of low-cost memory technology.

First, the functionality of solution-processed OFETs has been enhanced by incorporating DAE-Me photochromic molecules in a semiconducting P3HT polymer. The nature of the interaction between polarons transported through the conjugated backbone of the host polymer matrix and the DAEs moieties in both their different isomers has been investigated by means of charge modulation spectroscopy (CMS). The comparison of the CMS spectra recorded on P3HT/DAE-Me blends (closed versus open form) together with those obtained with neat P3HT transistors allowed us to observe an indirect spectroscopic evidence that the closed DAE molecules, intercalated in the least ordered part of the P3HT, limit the charge transfer between ordered areas. Such observation is supported by the analogy with the effect of temperature. At lower temperature, charges are forced to populate more ordered polymer regions leading to characteristic features in CMS spectra. Similar features are observed in blend with closed DAE, meaning that the charges continue to move in the most crystalline parts of the P3HT, although the conductive paths are reduced by the trapping effect of the DAE-ME\_c. In tie-chain regime, only the small fraction of carriers that also go through the least aggregated phase of the film (where the DAE reside) will be trapped by the photochromic induced states. For this reason, the conductivity of P3HT/DAE FET never shows a complete modulation upon DAE interconversion. CMS spectra analysis provided the indirect evidence of charge carries

interaction with the closed DAE molecules; however, further investigations which consider the blend morphology and microstructure analysis are required.

Considering that the optical modulation performances are related to the degree of electronic interaction between charge carrier transported in the ordered portions of the film and the accepting DAE levels, the device photoresponse is optimized by investigating the blend microstructure. The correlation between morphology and opto-electronic performance in organic thin-film transistors based on P3HT/DAE blends is investigated by varying molecular weight ( $M_w=20-100$  kDa) and regioregularity of the conjugated polymer as well as the temperature of thermal annealing (rt-160 °C) in thin films. The 50 kDa P3HT has shown the best compromise between field-effect mobility ( $\mu$ ) and switching capabilities, i.e  $1 \times 10^{-3} \text{ cm}^2\text{V}^{-1}\text{s}^{-1}$  and 50% photoswitching ratio, respectively. Higher or lower  $M_w$  than 50 kDa were found to negatively impact both the field-effect mobility and the device current switchability for the several reasons. High-molecular weight P3HT exhibits higher entanglement of polymer chains leading to higher short-range disorder in the  $\pi$ -stacking direction which limits the charge transport. Since the latter is dominated by higher interconnection due to tie-chain, the influence of DAE on the charge transfer between aggregates is reduced compared to lower molecular weights. When films contain large portions of amorphous regions, it is observed that DAEs is homogenously distributed within the polymer matrix, enabling improved interaction with charges. This scenario is especially observed in regiorandom P3HT, whose films are highly amorphous. In this case, the field-effect mobility is three times lower than in the case of RR-P3HT, while the switching ratio is 100% higher. The microstructure of the regioregular P3HT blend was found to be sensitive to the thermal annealing temperature, with an increase in  $\mu$  and a decrease in current modulation being observed as a response to the light-stimulus. The increase in field-effect mobility in both P3HT and P3HT/DAE-Me<sub>o</sub> films has been attributed to the augmentation of the degree of torsional order upon annealing. While the reduced photoresponse measured for annealing temperatures higher than 80 °C was ascribed to the increase of the lamellar crystal thickness, which favors the charge transfer between crystalline aggregates and consequently reduces the chances of electronic interaction with accepting DAE molecules.

Many high-performance semiconducting polymers exhibit properties suitable for interaction with DAE in multi-component devices. Among those, PDVT-8 and PCD-TTP have been tested as possible alternative host materials since they exhibit totally different degree of crystallinity and microstructure than P3HT. Despite PDVT-8 blends showed

high optical modulation, both polymers exhibit an important fatigue after few cycles already, differently from what is observed with devices based on P3HT/DAE blend. Indeed, OFET based on P3HT blend display outstanding photo-switchable capability with the two states being extremely stable over the timescale of several months and showing extremely high cycling resistance. In light of these findings, P3HT-based blends are selected as best candidates to fabricate optical controlled memory devices.

By capitalizing on such knowledge, multicomponent blends comprising a further molecular function has been exploited to realize a new device concept with increased functionality and multi-bit data retention, i.e OSFeFETs. These transistor devices are composed of a P3HT/DAE blend film which is place underneath a ferroelectric P(VDF-TrFE) gate insulator. Information writing into these memory cells can be done independently by either using UV light irradiation or gate voltage sweeps, while the readout of the stored information is carried out by measuring output drain current. At least 5 distinct drain current levels can be programmed in OSFeFET by the partial polarization of the ferroelectric layer. Each current level is stable over time and it is reproducible over cycles. We have shown that by using standard program operations we were able to switch readily and directly the memory between the multiple induced current levels, with accurate control of the readout signal and excellent repeatability. We also demonstrate the capability for relatively fast ( $\sim$  milliseconds), low-power ( $< 1 \mu\text{J cm}^{-2} \text{ s}^{-1}$ ) optical write operations of the memory exploiting a light probe setup. This set-up made it possible also to measure the maximum number of current steps per polarization state. In total, a maximum of 600 current levels are distinguishable for the full ferroelectric polarization state. A combination of optical and electrical write-erase operations defines the memory state and the readout. UV/green light irradiations with defined timescale and intensities are able to reversibly and reliably move the cell status between intermediate levels which are defined by partial polarization states of PVDF-TrFE. These levels were written in a serial manner and subsequently erased to the initial state using green light or erase sweep, demonstrating that each level is freely accessible from all others.

In the era of Internet of Everything in which objects will be seamless connected each other and to humans, the need to store information using poorly invasive inputs such as light on a device supported on a flexible substrate will become a requirement. The continuous interaction between objects and living entities will demand a higher number of sensors to

be embedded in future applications. Considering the additional functionality required for tomorrow's communications, wearable computers, autonomous drones and vehicles, the total memory bandwidth and storage demand is increasing. In this regard, optical data transmission allows faster data rate if compared with its electrical counterpart. Hence, in spite of performances which are still not at the level of those implemented through low-cost silicon-based memory technology, organic electronics holds a great potential for developing memory devices able to act as liaison between electrical and optical stimuli. Our findings demonstrate the paramount importance of understanding the basics of electronic interaction, fine tuning the structure and morphology of bicomponent photochromic films till leveraging them for the realization of multifunctional optoelectronic devices. By blending a semiconducting polymer with a photochromic small molecule and combining the resulting film with an organic ferroelectric material, we were able to realize a three-terminal device with impressive storage capabilities and controllable with light. The long data-retention and good reliability after program/erase cycles makes this approach ideal for non-volatile applications. This thesis has demonstrated the versatility of organic electronics exploiting the blending method as efficient approach to impart additional functionalities to materials, reducing costs and avoiding high process pitfalls. Its content provides a huge leap forward in terms of approach to multifunctionality and will be crucial for the realization of flexible memories for our daily lives.

## Appendix A1- Experimental section of Chapter 5

*Preparation of the P3HT/DAE solutions, device fabrication and electrical Measurements:* Solutions of DAE-Me<sub>o</sub> and regioregular P3HT at several molecular weight (20, 50, 100 KDa) or regiorandom P3HT were prepared at the same ratio 20:80. Four P3HT+DAE-Me<sub>o</sub> solutions (one for each molecular weight/regioregularity) were prepared at the total concentration of 1.2 mg/ml using (high quality) chloroform as a solvent. The whole preparation has been performed in a glovebox.

*Device preparation and electrical measurements:* All devices were prepared on Si n<sup>++</sup> /SiO<sub>2</sub> substrates with pre-patterned Au bottom electrodes, with a P3HT/DAE-Me<sub>o</sub> weight ratio of 4:1 and 70 nm active layer thickness (spin-coated from chloroform).

*Device fabrication:* The resulting solutions were cast by spin-coating in the glovebox at 1500 rpm for 60 sec at 4000 rpm/s on Si n<sup>++</sup> /SiO<sub>2</sub> substrates with pre-patterned Au bottom electrodes. The latter is composed of (i) Si wafer (n-doped  $n \sim 3 \times 10^{17} \text{ cm}^{-3}$ ), (ii) 230 nm SiO<sub>2</sub> dielectric layer, (iii) gold interdigitated source and drain electrodes. Wafers were covered with a dicing resin that needed to be washed off before spin-coating. The cleaning procedure consisted of a first rinsing step with acetone followed by 20 minutes of ultrasound bath with high quality acetone and 20 minutes of ultrasound bath with isopropanol followed by nitrogen drying. When annealing was performed, the sample was placed on a hot plate at a given temperature for 1 hour in inert atmosphere. Films of different thicknesses for absorption experiments are fabricated on glass substrates.

*Electrical characterization:* The electrical measurements were carried out using a Keithley 2636A and contacting the source, drain and gate electrodes via a probe station inside the glovebox. All the transfer curves were accomplished applying a sweep gate voltage from 40 V to -60 V. The value of the drain voltage was set at -60 V.

*Static switching current measurements:* Irradiation was performed with an optical fiber placed at 0.5 cm distance from the sample. The optical fiber was connected to a Polychrome V (Till Photonics) tuneable light source providing a monochromatic beam of  $\pm 15 \text{ nm}$ . Wavelength used were 313 and 530 nm with lamp intensity of 0.5 mW/cm<sup>2</sup> and 19.7 mW/cm<sup>2</sup> respectively. The same irradiation protocol has been used for each sample.

Initial step:

- (i) 15 minutes of green light
- (ii) Electrical measurement

Cycled steps:

- (iii) 1 minutes of UV light
- (iv) Electrical measurement
- (v) 5 minutes of green light
- (vi) Electrical measurement

The initial step was performed to be sure that all the DAEs were in the starting form (DAE-Me<sub>o</sub>) before running the electrical characterization. At the end of each irradiation the light was turned off and the measurement was run after 60 sec. To compare switching capabilities of several devices, the drain current  $I_D$  is normalized by the  $I_0$ , which is the value of the drain current measured in the initial step.

*Absorption measurements:* Spectra are obtained using a Varian Cary 6000i UV-Vis-NIR spectrophotometer and fitted to a modified Spano model to yield the percent aggregate and the excitonic bandwidth  $W$ .

*DSC scans-Phase diagram:* Differential scanning calorimetry (DSC) measurements were conducted under nitrogen at scan rate of 20 °C min<sup>-1</sup> for heating and 10 °C min<sup>-1</sup> for cooling with a Mettler Toledo DSC822 instrument. Neat material and blend powders were produced by preparing homogeneous solutions of 0.5 wt% total material content in chloroform, followed by casting onto glass slides. The solvent was evaporated at ambient pressure in air. 2–4 mg material from such films was used for the DSC experiments. Complete melting of primary crystals as well as melting of the neat materials correspond to the end melting temperatures in the DSC thermograms.

*Photochemical quantum yield in thin films of polymer blends:* The photo-isomerization quantum yields of the closed to open isomerization of DAE-Me were determined by monitoring the absorbance change (at 535 nm; using a JASCO V630 spectrophotometer) of DAE-Me<sub>c</sub> with respect to irradiation time (irradiation wavelength 535 nm; using a

SPEX fluorolog, Horiba). In solution the change in absorbance with respect to time is a function of the photon flux ( $\omega$ ), quantum yield ( $\phi$ ), molar absorptivity ( $\epsilon$ ), length of the optical path ( $l$ ), Avogadro's number ( $N_A$ ), fraction of absorbed photons ( $1-10^{-Abs}$ ), and the volume of the sample ( $V$ ).

$$\frac{dAbs}{dt} = - \frac{\phi \cdot \omega \cdot \epsilon \cdot l \cdot (1 - 10^{-Abs})}{N_A \cdot V} \quad \text{(Equation A1.1)}$$

This equation, which was used to determine the photon flux, can be modified to be applicable on thin films by introducing a unit correction factor (that compensates for the non SI units in the molar absorptivity factor), replacing the volume of the sample with the irradiated area, and by modify the unit of the photonflux from Einstein/s to Einstein/(s\*cm<sup>2</sup>).

$$\frac{dAbs}{dt} = - \frac{\phi \cdot \omega \cdot \epsilon \cdot unit\ correction\ factor \cdot (1 - 10^{-Abs})}{N_A \cdot area} \quad \text{(Equation A2.1)}$$

The photon flux (at 535 nm) was determined using the chemical standard Aberchrome 670, using exactly the same geometry (including a mask with known area) as used when measuring on the films. The molar absorptivity of DAE-Me in blended films was approximated with the solution value (19 000 M<sup>-1</sup> cm<sup>-1</sup>). An in-house MATLAB<sup>®</sup> script was used to fit the absorbance contribution of DAE-Me to theory in which the differential equations where solved in each fitting step.

*Atomic Force Microscopy (AFM):* Topographic and phase-imaging measurements were obtained in air by employing a commercial microscope Multimode 8 (Bruker). In order to obtain a sufficiently large and detectable mechanical deflection, we used ( $k=40$  N m<sup>-1</sup>) silicon tips (NCHV-A, Bruker) with oscillating frequencies in the range between 270 - 400 KHz. The root-mean square roughness ( $R_{rms}$ ) has been estimated by averaging the values obtained on several 5.12×5.12 μm<sup>2</sup> images (1024×1024 pixels) acquired on different regions of the sample (corresponding to about 100 μm<sup>2</sup> of sampled surface). Raw AFM data were treated by using histogram flattening procedures to remove the experimental artefacts due to the piezo scanners. In the phase-imaging mode, the measured phase-shift is the difference between the output and the input signals, mapping differences in mechanical properties of the surface: such as stiffness, rigidity, friction, adhesion.

*GIWAXS characterization:* Polymer thin films for X-ray scattering measurements were prepared by spin-coating a polymer solution onto native oxide silicon substrates. Grazing

incidence wide angle X-ray scattering (GIWAXS) was performed at the Stanford Synchrotron Radiation Lightsource (SSRL) on beam line 11-3 using an area detector (Rayonix MAR-225) and incident energy of 12.73 keV. The distance between sample and detector was calibrated using a LaB<sub>6</sub> polycrystalline standard. The incidence angle was set to 0.1° and was slightly larger than the critical angle, ensuring that we sampled the full depth of the film. All X-ray measurements were performed in a Helium chamber to minimize air scattering and beam damage to samples. Raw data was normalized by detector counts, and reduced and analyzed using a combination of Nika 1D SAXS<sup>[1]</sup> and WAXStools<sup>[2]</sup> software packages in Igor Pro.

*Thermogravimetric analysis of DAE:* Combined thermogravimetric analysis (TGA) and differential thermal analysis (DTA) were performed on a Netzsch STA 409 C Skimmer® coupled to a BalzersQMG 421 mass spectrometer.

TGA curves recorded under an atmosphere of air show no mass loss upon heating the DAE-Me sample up to 253°C. At higher temperatures decomposition starts to occur accompanied by the formation of small molecular fragments (H<sub>2</sub>O, CO<sub>2</sub>, SH, and SO). The DTA trace shows an endotherm at 91°C, corresponding to the melting temperature of DAE-Me

## Appendix A2– Experimental section of Chapter 6

### A2.1 Ferroelectric Capacitor

The main properties of the P(VDF-TrFE) film have been studied characterizing ferroelectric capacitor. Capacitors were fabricated on quartz substrates on which 50 nm-thick Au bottom electrodes were evaporated on a 3 nm Cr adhesion layer through a shadow mask. P(VDF-TrFE) films with a thickness of about 1  $\mu\text{m}$  were spincoated at 2000 rpm from a 10 w% solution in methylethylketone. Finally, the ferroelectric film was sandwiched with a top electrode. A 50 nm thick Au layer was evaporated in glovebox as describe in Chapter 3.

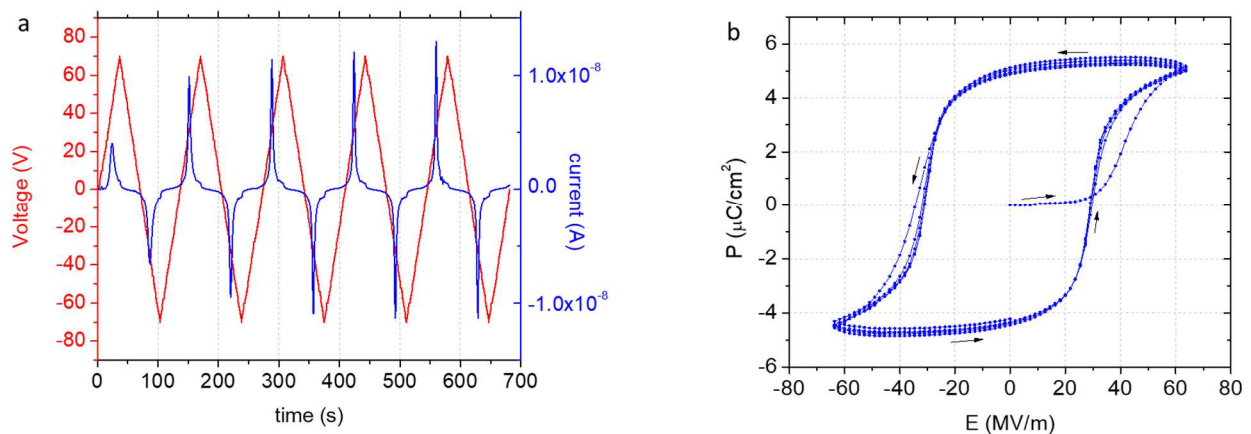


**Figure A2.1:** a) Triangular potential sweep applied to ferroelectric P(VDF-TrFE) capacitor (red) and the resulting measured current response (blue) using a Source Meter Unit (SMU). b) Polarization hysteresis of the ferroelectric film vs applied electric field.

The TVS (Triangular Voltage Sweep method) was used to test the ferroelectric response of P(VDF-TrFE) layer. The TVS method have been used for analyzing dielectric since 1971<sup>[3-4]</sup> and later also for ferroelectric films.<sup>[5-6]</sup> The mechanism of TVS relies on the electrical signals generated from the movement of mobile charges. In this measurement, a positive bias is first applied at one electrode allowing mobiles ions to drift to the other interface. Then the voltage is swept from positive to negative value at fixed frequency, meanwhile the current is recorded. At high frequency, only the electrons can respond to the voltage change, and the measured current is basically due to the displacement current and the leakage current. On the contrary, at lower frequency it can be used to measure the ferroelectric polarization switching. **Figure A2.1** shows five complete cycles of a triangular

voltage wave form the resulting hysteresis switching current for a P(VDF-TrFE) capacitor. To perform the measurement, the bottom contact was grounded while the TVS was applied to the top electrode using a Keithley 2636B Source-Measurement Unit (SMU). The current-time curve is measured as a current response of the ferroelectric capacitor to the triangular signal excitation. The measurement control and data acquisitions were performed using a Matlab home-made software, that allows to change some significant parameters as amplitude, sweep rate and number of cycles of the bipolar triangular waveform. The staircase potential sweep is programmed to maintain constant the sweep rate fixing the apertureTime (the time during which the potential is kept constant before the next step). The maximum applied voltage was approximately  $\pm 60$  V. A single-cycle duration of this measurement was approximately 120 s and the sweeping rate  $dV/dt$  was approximately 1.7 (V/s). It was found that the measured current is maximum when the applied voltage is close to the coercive voltage of the ferroelectric films. These current maxima correspond to the dipole reorientation contribution of the ferroelectric material. The first current spike is lower compared to the other since the ferroelectric film was not initially polarized.

For ferroelectric materials, the basic equation of total current  $I(t)$  is given by:

$$I(t) = A \frac{dD(t)}{dt} + I_l = A \frac{dP(t)}{dt} + C \frac{dV(t)}{dt} + I_l \quad \text{(Equation A2.1)}$$

where  $D(t)$  is the dielectric displacement,  $P(t)$  is the ferroelectric polarization,  $V(t)$  is the applied voltage,  $A$  is the area of the capacitor and  $C$  is the capacitance.

Therefore TVS can help us to distinguish the three main contributions to the current in a ferroelectric capacitor:

$$I = I_s + I_c + I_l \quad \text{(Equation A2.2)}$$

where:

- $I_c$  = capacitance current =  $C \frac{dV(t)}{dt}$
- $I_s$  = ferroelectric switching current =  $A \frac{dP(t)}{dt}$
- $I_l$  = leakage current

The I-V measurement was performed at two different sweep rates. Since the current response is not dependent on the frequency used for TVS, it is possible to conclude that

the contribution of the capacitance current to the measured current is negligible. Moreover, assuming that the leakage current of the device is negligible compared to the ferroelectric switching current, the latter can be considered as the only major contribution of the overall measured current. Therefore, given that  $Q(t) = \int_0^t i(t')dt'$ , the polarization of the organic ferroelectric film can be calculated by:

$$P = \frac{Q(t)}{A} \quad \text{(Equation A2.3)}$$

**Figure A2.1b** shows the polarization loops versus electric field resulting from the TVS measurement of **Figure A2.1a**. The main parameters ( $E_c$ ,  $P_r$ ) resulted to be slightly reduced compare to literature<sup>[7-8]</sup> values mainly due to an over-estimation of both  $A$  and film thickness.

## A2.2 Fabrication of OSFeFET

Following the preliminary results on capacitors, we fabricated top gate ferroelectric FET devices. Ferroelectric spontaneous polarization gives rise to a depolarization field, just like dielectric polarization.<sup>[9]</sup> In the absence of an externally applied field, the depolarization field counteracts ferroelectric polarization. Since this depolarization field ultimately arises from the net charges at the dielectric's surface, to stabilize the polarization one therefore needs to supply compensation charges at the surfaces of the material. This has done by exploiting a conductive substrate which is electrically connected to the gate electrodes. Therefore, silicon/SiO<sub>2</sub> substrates with pre-patterned interdigitated electrodes (described in **Chapter 3**) have been used as substrate in order to reduce the depolarization field. Moreover, the device geometry has been designed with reduced size in order to decrease the leakage current and operating drain voltages. After the standard cleaning procedure with organic solvent and UV-ozone described in Chapter 3, a 2mg/ml P3HT/DAE (4:1) solution in chloroform was cast by spin-coating on the substrates. The devices were then annealed at 60°C in order to remove any solvent residue. Indeed, the solvent residues are inevitably introduced into the semiconducting layers during the device fabrication. These solvent molecules might potentially affect the charge transport and electrical performances of the non-volatile organic field-effect transistor memory.<sup>[10-11]</sup> Then, a P(VDF-TrFE) layer was deposited on the semiconductor layer by spin-coating. In order to avoid the damage of the P3HT/DAE layer, an orthogonal solvent was used for the ferroelectric solution.

Finally, the top gate electrode was patterned using photolithography process in order to reduce any unnecessary overlapping with the underlying interdigitated source and drain electrodes. More details on the photolithography process can be found in **Chapter 3**. A thin (20nm) semi-transparent Au layer was evaporated in order to obtain a conductive electrode which makes light irradiations from the top possible. **Figure A2.2** shows the overall devices architecture.

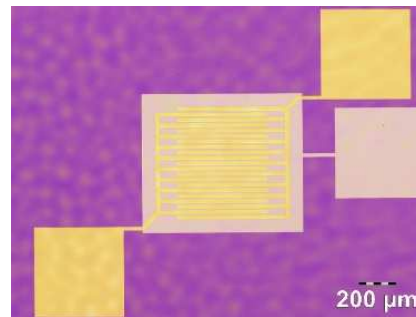


**Figure A2.2:** Optical microscopy image of a P3HT+DAE-Me FeFET. The interdigitated S&D bottom Au electrodes were layer on SiO<sub>2</sub> (channel length = 20 μm) ; (b, d) a P3HT/DAE-Me layer on a PET substrate (channel length = 60 μm).

### A2.3 Electrical Program/Erase (P/E) cycles and electrical characterization of OSFeFETs

The electrical writing (program) process of these photochromic multifunctional memories consists in probing the devices with a triangular waveform potential having fixed sweep rate of 2 V/s, as shown in **Figure A2.3**.

Before every writing operation, the devices need to give a +40 V erase voltage pulse. Five different polarization states are written by sweeping gate voltage up to -40 V, -20 V and -17.5 V, -15 V and -10 V and keeping drain voltage at -0.5V. Reading operation consists in probing the drain current by applying -0.5 V as drain-source voltage. During read operation, the gate voltage is connect to the ground.

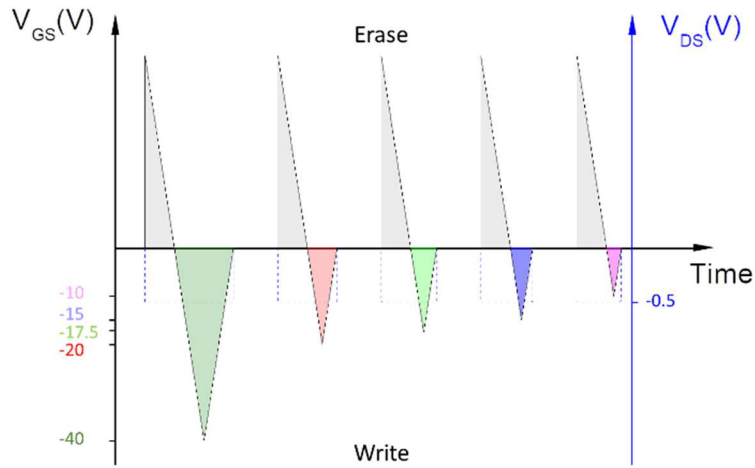


**Figure A2.3:** Schematic diagram of programming different polarization states by triangular voltage sweeps.

### A2.4 Optical P/E operations - Switching in OSFeFET

The electrical writing process of these FeFET memories consists in irradiating the active area with UV (312nm) or visible (540 nm) light. The current change due to light irradiations has been measured for four partial polarization states of the ferroelectric obtained by potential sweeps up to -40 V, -20 V, -17.5 V, -15V or -10V.

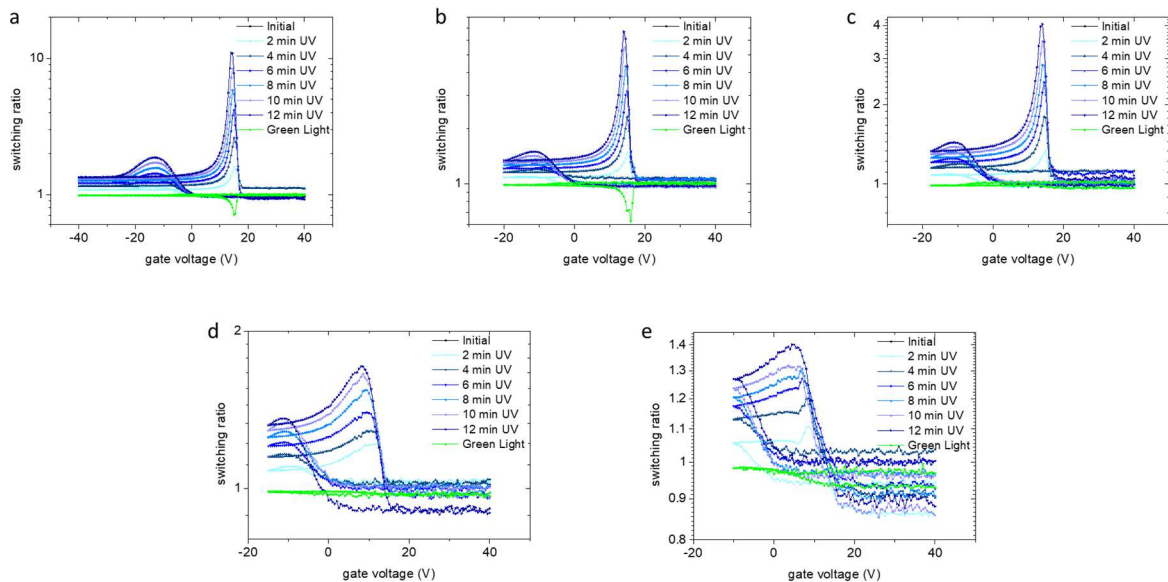


**Figure A2.4:** Optically induced switching ratios for each of the polarization state. The threshold voltage shift and current drops induced by light writing processes are the same for each polarization step (P1, P2, P3, P4 and P5).

### A2.4.1 Time-Resolved Optical Switching

Dynamic switching measurements consist of recording the drain current over time while irradiating the device with 3 ns pulses of UV or visible light at fixed ferroelectric polarization (**Figure A2.5**). A constant bias (typically -0.5 V) was applied across the drain-source terminal and short irradiation steps were repeated every 10 s throughout the measurement. The drain current ( $I_D$ ) was measured with a Keithley 2400 SourceMeter as a source current on the drain terminal. In addition, a resistor was added to the source terminal in order to measure fast transient response of the source current with an oscilloscope. The resistance was negligible compared to the drain-source resistance. The drain current may be slightly affected by bias stress. The latter is attributed to the trapping of carriers into localized electronic states at the interface and it can be explained by multiple trapping-and-releasing model (MTR). Since this trapping mechanism is not related to the bulk trapping induced by DAE, the plots are corrected by the bias stress current drop.

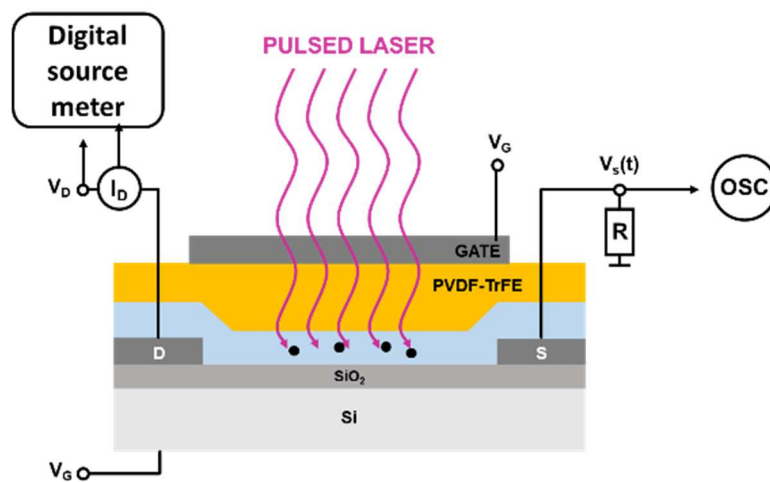


**Figure A2.5.** Experimental setup for the measurement of optical switching with ultra-fast laser pulses. Write pulses were performed by 3 ns 310 nm laser pulses at 0.1 Hz, which induce a stepwise decrease in  $I_D$ . The erasing process was done with either 540 nm laser pulses for a multi-step increase of  $I_D$  or via irradiating the device with green LED for 5 min to achieve a full current reset. The time dependence of  $I_D$  was measured using a Keithley 2400 SourceMeter as a voltage source and ammeter connected to the drain terminal and with an oscilloscope connected to the source-terminated resistor.

In order to estimate the response time of the device, it is necessary to determine the drain current transient dynamics.  $I_D$  exhibits a complex time dependence, which can be resolved

into two decay processes. The fast decay (1 - 10  $\mu$ s), presented in the inset of **Figure A2.6**, is attributed to the displacement current of photogenerated hot carriers, their recombination, and also formation of polarons. The second decay process is visible in the range of milliseconds to seconds. The characteristic timescale of the latter is related to the charge extraction time. The charge extraction time is the time necessary for photogenerated charge carrier within the P3HT/DAE blend to clear the device and is dependent on the device geometry as well as the cross-channel voltage. P3HT typically has a mobility on the order of  $1-10 \times 10^{-3} \text{ cm}^2/\text{Vs}$ , with the slowest carriers exiting the device at  $\sim 10$ -times the transit time. For a 20  $\mu\text{m}$  channel and at 0.5 V drain source bias voltage, this gives an extraction time in the range of 8 - 80 ms. The device response time is limited by the displacement current, which is dependent on two components: the intrinsic hot carrier recombination time ( $\sim 10$ -100  $\mu\text{s}$ ), and the charge extraction time (8 - 80 ms) as demonstrated in **Figure A2.6**. As the extraction time is dependent on the channel width and the drain-source voltage

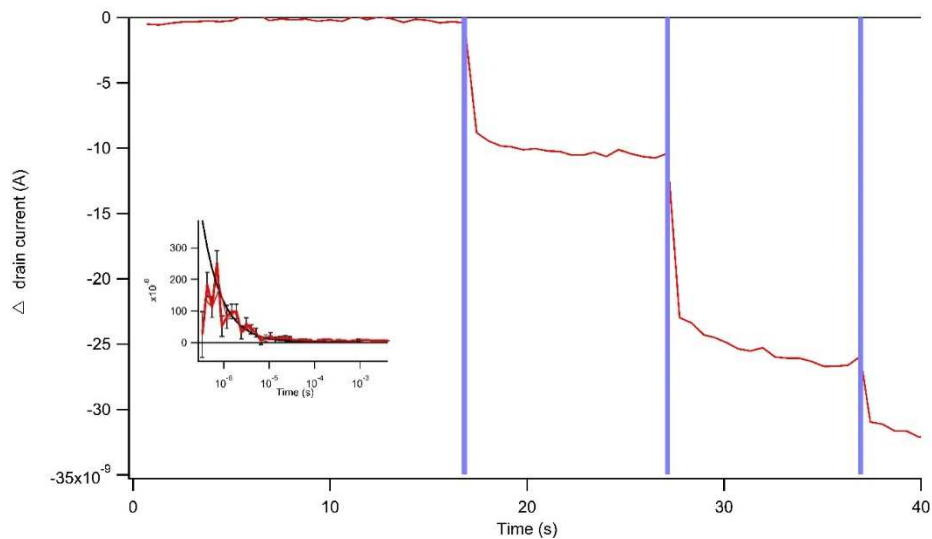


**Figure A2.6.** Decay corrected time resolved current measurements of successive optical switching with the timing of the laser pulses show in purple (laser duration not in scale). Measurement performed on a 20  $\mu\text{m}$  channel device operating at 0.5 V drain-source voltage and partial ferroelectric polarization at -20 V. Insert shows rapid decay of hot carrier in the device.

## References

- [1] J. Ilavsky, *Journal of Applied Crystallography* **2012**, 45, 324.
- [2] S. D. Oosterhout, V. Savikhin, J. Zhang, Y. Zhang, M. A. Burgers, S. R. Marder, G. C. Bazan, M. F. Toney, *Chem Mater* **2017**, 29, 3062.
- [3] M. Kuhn, D. Silversmith, *Journal of The Electrochemical Society* **1971**, 118, 966.
- [4] N. Chou, *Journal of The Electrochemical Society* **1971**, 118, 601.
- [5] B. Melnick, C. P. de Araujo, L. McMillan, D. Carver, J. Scott, *Ferroelectrics* **1991**, 116, 79.
- [6] S. Shunming, T. S. Kalkur, *IEEE transactions on ultrasonics, ferroelectrics, and frequency control* **2004**, 51, 786.
- [7] S. Ducharme, V. M. Fridkin, A. V. Bune, S. Palto, L. Blinov, N. Petukhova, S. Yudin, *Phys Rev Lett* **2000**, 84, 175.
- [8] G. Eberle, E. Bihler, W. Eisenmenger, *IEEE transactions on electrical insulation* **1991**, 26, 69.
- [9] C. Kittel, P. McEuen, P. McEuen, *Introduction to solid state physics*, Wiley New York, **1996**.
- [10] G. Xue, C. Fan, J. Wu, S. Liu, Y. Liu, H. Chen, H. L. Xin, H. Li, *Materials Horizons* **2015**, 2, 344.
- [11] K. J. Baeg, Y. Y. Noh, J. Ghim, B. Lim, D. Y. Kim, *Adv Funct Mater* **2008**, 18, 3678.

## Acknowledgements

As this manuscript is the result of the work carried out with the fundamental support and contribution of many people, I wish to express my gratitude to all of them. This journey in the Nanochemistry Lab has been challenging but rewarding at the same time and has allowed me to learn and meet amazing people.

First, I wish to thank my advisor, Prof. Paolo Samorì for accepting me as a PhD student in his research group and for his supervision throughout the years. It has been a great privilege being a member of the Marie Skłodowska-Curie ITN network “iSwitch”, which gave me the opportunity to travel around Europe and most importantly to meet very brilliant colleagues.

I owe my gratitude to my second advisor Prof. Emanuele Orgiu. I have had the possibility to learn how to work independently, chasing my ideas, while being supported with stimulating discussions and useful advices, even from far away.

I am extremely grateful to Dr. Esma Ismailova, Dr. Dominique Vuillaume, Prof. Thomas Heiser and Prof. Fabio Biscarini for offering their time to review this thesis and accepting of being part of this dissertation committee.

I want to thank all my collaborators Alberto Scaccabarozzi from IIT in Milan and Alex Dixon from University of Nova Gorica. Their contribution to the realization of the different projects has been indispensable, as this work would have not been possible without this precious support.

Very special thanks must go to all the colleagues that over these years have been part of the Nanochemistry Group. You have been an invaluable scientific support and more; thank you for making the Nanochem Lab such a stimulating and enjoyable. Many thanks also to Corinne for her kindness and great support in these years.

I include in these acknowledgements all my friends I have met in Strasbourg outside from the lab who became part of my life, with a special mention to Gianni; a passionate scientist, great guitarist and amazing friend who have taught me the importance of a balanced lifestyle.

Words are not enough to express my deep gratitude to my family who has always supported me throughout this challenge with love and encouragement.

At last, my deepest gratitude goes to Alice - she put up with all my stresses and moans for the past months. Her unconditional support together with her enriching point of view have become my fixed reference for a continuous personal improvement.

# Marco CARROLI

## Dispositifs électroniques multifonctionnels à base organique

### Utilisation d'un mélange organique bi-composant pour des mémoires non volatiles

#### Résumé

Dans cette thèse, la fonctionnalité des OFET traités en solution a été améliorée avec le développement d'un mélange à plusieurs composants incorporant des molécules photochromiques dans un polymère semi-conducteur. La corrélation entre la morphologie et les performances optoélectroniques est étudiée en faisant varier le poids moléculaire et la régiorégularité du polymère conjugué ainsi que la température de recuit thermique dans les couches minces. Le meilleur compromis entre mobilité à effet de champ ( $\mu$ ) et les capacités de commutation a été observé dans les mélanges contenant du RR-P3HT avec  $M_w = 50$  kDa. En exploitant ces résultats, nous démontrons que des opérations de mémoire optique rapide et robuste, à plusieurs niveaux et non volatile peuvent être réalisées dans un FET organique ferroélectrique multifonctionnel optiquement commutable (OSFeOFET) basé sur P(VDF-TrFE). Dans un tel dispositif, l'écriture d'informations dans la cellule de mémoire peut être effectuée indépendamment en utilisant soit rayonnements de lumière UV, soit des balayages de tension de grille, tandis que la lecture des informations stockées est effectuée en mesurant le courant de drain de sortie. Telle preuve de concept ouvre la voie à une complexité fonctionnelle accrue en optoélectronique via l'interfaçage de plusieurs composants dans un seul appareil, dans une technologie à faible coût entièrement intégrée, compatible avec les substrats flexibles.

Mots-clés : OFET, Photochromisme, Ferroélectricité, Mémoire

#### Résumé en anglais

In this thesis, the functionality of solution-processed OFETs has been enhanced with the development of a multi-component blend incorporating photochromic molecules in a semiconducting polymer. The correlation between morphology and opto-electronic performances is investigated by varying molecular weight and regioregularity of the conjugated polymer as well as the temperature of thermal annealing in thin films. The best compromise between field-effect mobility ( $\mu$ ) and switching capabilities was observed in blends containing RR- P3HT with  $M_w=50$  kDa. Leveraging these results, we demonstrate that fast and robust optical, multi-level, non-volatile memory operations can be achieved in a multifunctional optically switchable ferroelectric organic FET (OSFeOFET) based on P(VDF-TrFE). In such device, information writing into the memory cell can be done independently by either using UV light irradiation or gate voltage sweeps, while the readout of the stored information is carried out by measuring the output drain current. Such a proof-of-concept paves the way towards enhanced functional complexity in opto-electronics *via* the interfacing of multiple components in a single device, in fully integrated low-cost technology compatible with flexible substrates.

Keywords: OFET, photochromism, ferroelectricity, memory